Mechanical and electrical properties of dielectric thin films : electrical-nanoindentation experiments and numerical simulations

Morgan Rusinowicz

THÈSE

Pour obtenir le grade de

DOCTEUR DE L'UNIVERSITÉ GRENOBLE ALPES

École doctorale : I-MEP2 - Ingénierie - Matériaux, Mécanique, Environnement, Energétique, Procédés, Production
Spécialité : 2MGE : Matériaux, Mécanique, Génie civil, Electrochimie
Unité de recherche : Science et Ingénierie des Matériaux et Procédés

Propriétés mécaniques et électriques de couches minces diélectriques : expériences de nanoindentation-électrique et simulations numériques

Mechanical and electrical properties of dielectric thin films: electrical-nanoindentation experiments and numerical simulations

Présentée par :

Morgan RUSINOWICZ

Direction de thèse :

Muriel BRACCINI Chargée de recherches, Université Grenoble Alpes	Directrice de thèse
Fabien VOLPI Professeur des Universités, Université Grenoble Alpes	Co-encadrant de thèse

Rapporteurs :

Thomas PARDOEN
PROFESSEUR DES UNIVERSITES, Université Catholique de Louvain
Jean-Luc LOUBET
DIRECTEUR DE RECHERCHE, Ecole centrale de Lyon

Thèse soutenue publiquement le **9 décembre 2022**, devant le jury composé de :

Muriel BRACCINI CHARGE DE RECHERCHE, Grenoble-INP UGA	Directrice de thèse
Fabien VOLPI PROFESSEUR DES UNIVERSITES, Grenoble-INP UGA	Co-encadrant de thèse
Thomas PARDOEN PROFESSEUR DES UNIVERSITES, Université Catholique de Louvain	Rapporteur
Jean-Luc LOUBET DIRECTEUR DE RECHERCHE, Ecole centrale de Lyon	Rapporteur
Alain SYLVESTRE PROFESSEUR DES UNIVERSITES, Grenoble-INP UGA	Président du jury
Frédéric HOUZE CHARGE DE RECHERCHE, Centrale-Supélec	Examinateur

Invités :

Guillaume Parry
MAITRE DE CONFERENCE, Grenoble-INP UGA

À mes parents,
mes ami(e)s,
ma famille.

Remerciements

Ces pages sont peut-être (certainement) les plus importantes du manuscrit puisqu'elles visent à remercier les personnes ayant rendu ces trois années de thèse si belles, riches, instructives, amusantes et épanouissantes sur le plan professionnel comme personnel. Avant d'entrer dans une liste nominative, loin d'être exhaustive, je souhaite donc adresser un GIGANTESQUE premier MERCIIIII à toutes les personnes qui ont participé de près ou de loin à cette SUPERBE AVENTURE.

Tout d'abord, puisque je crois que la vie se construit à partir de rencontres, réduisant à chaque carrefour le nombre de chemins possibles à une voie particulière, je tiens à remercier l'une d'entre elles, et non des moindres : Alexis Deschamps. J'ai rencontré Alexis dès ma première année d'école d'ingénieurs à Phelma durant laquelle j'ai appris à le connaître lors d'un projet portant sur la rupture par choc thermique. Depuis lors, et durant 6 années, ce « grand maître » de la précipitation et des alliages d'aluminium m'a toujours soutenu à TOUTES les étapes de mon cursus pour que j'atteigne mon objectif professionnel, que cela soit à travers mes stages, ma thèse de doctorat (malgré mon déclin d'une proposition de sa part), ou mon post-doctorat. Je suis flatté d'avoir côtoyé un professeur aussi brillant, bienveillant et sympathique, parmi bien d'autres qualités qui seraient trop longues à énumérer. Merci Alexis et au plaisir de te recroiser !

Vient au tour de mes plus sincères remerciements à ma directrice et mon directeur de thèse (oui je n'emploierai jamais le terme de « co-encadrant » !), Muriel Braccini et Fabien Volpi, aka « maman et papa », ou encore « les meilleurs encadrants de thèse de l'univers » (j'arrête les qualificatifs ici pour qu'on ne croît pas que j'en fais trop, mais je pourrais évidemment continuer). Vous m'avez tant appris, soutenu, et communiqué l'amour de votre métier que ça m'a conforté dans mon projet d'entrer dans le monde de la recherche académique comme chercheur permanent. J'espère être à la hauteur des belles valeurs que vous m'avez partagées pendant ces trois années, tant scientifiques qu'humaines. Je me rappellerai notamment de vos multiples appels chaleureux lors de mes (nombreux) covids ou encore de votre soutien sans faille et précieux lors de la rédaction de mon manuscrit, qui s'est superposée avec plein d'autres évènements. Muriel, tu m'as fait confiance en m'offrant une liberté totale sur la manière de mener ma thèse et je suis conscient de la chance incroyable que tu m'as donnée. Ça m'a permis de m'épanouir pleinement dans le vaste océan qu'est la recherche scientifique et de tester tout un tas de disciplines pour trouver celle qui me convenait le mieux, de l'expérimentation à la modélisation, de la mécanique à l'électricité, des matériaux à l'instrumentation. Un extrait (pas tout à fait) caricatural, sans citer les protagonistes :

— « Tu as fait de l'oxydation cette semaine ?
— Euhhh non je finissais un truc...
— Sur l'oxyde de cuivre ?
— Euhhh non sur SiOCH...
— Ah t'as refait des manips ?
— Euhhh non des simus...
— Super montre-moi ! »

Tu as également été, avec brio, la voix de la sagesse quand il fallait prendre des décisions importantes ou parfois même freiner « papa » lorsqu'il se laissait submerger par les « matériaux modèles » qu'il sortait du placard, et dont les études s'avéraient être (beaucoup) plus complexes que prévues. En parlant de Fabien, j'ai eu la chance de côtoyer un expérimentateur de l'extrême comme on n'en rencontre rarement, dont la passion surpasse de loin les problèmes physiques, dans tous les sens du terme : la physique du solide comme les douleurs de dos, le poussant à monter son mur de Keithley dans des positions que je qualifierais « d'artistiques ». Je suis ravi d'avoir pu travailler pendant trois ans avec la personne dont les cours sur les matériaux fonctionnels et les propriétés physiques me plaisaient le plus, bien sûr par le contenu mais surtout par l'enseignant tant investi et passionnant que tu es. Je me souviendrai également de nos sorties à vélo (ne m'en veux pas trop) et de nos randonnées en montagne (avec un ratio neige/équipement pas vraiment en notre faveur), mémorables tout de même ! J'espère que vous renouvellerez ce duo de choc dans l'encadrement de futurs thésards bien chanceux. Un ÉNORME MERCI à vous deux et, en espérant un jour retravailler avec vous quelle que soit la forme de notre collaboration, je vous souhaite tout le meilleur !

Je tiens à adresser mes remerciements aux deux mécaniciens, physiciens et qui ont en fait plein d'autres cordes à leur arc, Guillaume Parry et Marc Verdier. Vous ne faisiez pas officiellement partie de mon encadrement mais c'est à vos bureaux que je venais toquer lorsque j'avais un problème (vous me receviez d'ailleurs toujours avec le sourire sachant que je venais pour des problèmes, c'est d'autant plus appréciable !). Guillaume, merci d'avoir été mon « Maître Jedi », enseignant avec sagesse la « Force » de la simulation numérique à ton jeune « Padawan ». Tu m'as donné goût aux calculs numériques et plus généralement à la mécanique depuis déjà tes enseignements à Phelma. Je retiendrai également nos discussions passionnantes dans les pubs irlandais (avec modération) ainsi que ton imitation de moi en tant que bûcheron lors de ma soutenance de thèse, imitation que même mes parents ont particulièrement appréciée. Marc, je sais qu'on doit refaire toutes les manips de ma thèse avec des pointes sphériques, des coniques d'angles différents, des poinçons plats, des films d'or à la surface des échantillons, en température et tout ça sur la lune... Plus sérieusement, merci de m'avoir ouvert les portes du monde de l'indentation, et communiqué tes conseils précieux, tes innombrables idées, tes propositions pertinentes mais difficilement réalisables et de manière générale une infime partie de ton savoir immense. Merci donc à vous deux qui brillez par votre originalité, mise au service de votre compétence et de votre sympathie.

Je remercie tous les enseignants-chercheurs qui m'ont donné la chance de réaliser des enseignements à Phelma : Annie Antoni, David Jauffrès, Noël Jakse, et Muriel Véron. Ce fut un plaisir de travailler à vos côtés et j'espère être à votre hauteur si je parviens à devenir enseignant-chercheur !

Je remercie plus généralement tous les membres permanents du SIMaP et notamment les membres de l'équipe PM avec qui j'ai quasiment vécu pendant trois ans et qui m'ont rendu la vie agréable. Allez, je me lance dans une liste qui ne sera certainement pas exhaustive, en prenant

le risque de commettre un impair... Sans citer les personnes que j'ai déjà remerciées dans les paragraphes précédents, un merci particulier à Frédéric De Geuser (le grand sage avec qui j'ai eu la chance de travailler durant mon stage de fin d'études), Roberta Poloni (pour ses conseils et les discussions sur les charges électriques dans SiOCH autour de la machine à café du bureau bien sûr), Guillaume Beutier (qui est descendu de sa campagne spécialement pour assister à ma soutenance de thèse), Gilles Renou (pour ses magnifiques manips TEM/ASTAR et surtout pour les diverses discussions toujours très intéressantes), Patricia Donnadieu (pour sa bienveillance et ses formations TEM pédagogiques à la fois théoriques et pratiques), Arthur Després (pour tous les TPs aciers que l'on a enseignés ensemble mais surtout les mémorables microstructures des fontes blanches), Céline Pascal (notamment pour sa gentillesse et sa bienveillance) et Rafael Estevez (dont j'avais grand plaisir de retrouver dans les conférences).

Merci aux personnes qui ont participé à ma formation sur les instruments de mesure, à mes manips et qui m'ont apporté leur aide. Je pense par exemple au personnel du CMTC, en particulier Rachel Martin (qui m'a formé au MEB et qui a toujours été d'une gentillesse extrême), Frédéric Charlot (j'aurais à peu près les mêmes compliments en te remerciant pour les coupes FIB), Francine Roussel (pour les supports multiples, sa bonne humeur et ses encouragements), Stéphane Coindeau et Thierry Encinas (les légendaires X-Men que l'on ne peut pas dissocier, merci pour les manips DRX), sans oublier Florence Robaut (pour avoir extrait une jolie lame TEM mais surtout pour nous réconforter en nous fournissant du bon chocolat au bureau). En plus de Gilles et Patricia que j'ai déjà remerciés pour leurs manips/formations TEM (mieux vaut deux fois qu'une), je remercie également Michel Mermoux, Alexandre Crisci et Grégory Berthomé pour leurs manips, souvent délicates, de Raman, d'ellipsométrie et d'XPS.

Un grand merci aux personnels technique et administratif qui tiennent le labo à bout de bras, à la sueur de leur front, et qui font un travail remarquable ! Merci aux personnes avec qui j'ai eu la chance d'interagir : Magali Morais, Jean-Jacques Franciosi, Laurent Artaud, Nadine Vidal, Marie Dubois, Jacqueline Cuoq et Sylvie Champavier.

Merci à Élisabeth Siebert et Jacques Fouletier, les électrochimistes des solides, pour toutes les discussions intéressantes qui nous ont ouvert à votre monde (qui je l'avoue reste encore un peu obscur pour moi). Et un merci supplémentaire à Jacques qui nous a remonté le moral plus d'une fois par son enthousiasme à tout épreuve et en nous rappelant régulièrement que nos manips étaient géniales.

Je remercie les membres du laboratoire CRISMAT de Caen, Rosine Coq-Germanicus, Sophie Eve et Éric Hug qui, sans que personne ne le voit arriver, m'ont occupé avec un échantillon dont l'étude a durée une très grande partie de ma thèse, y compris dans les multiples confinements.

Merci à Solène Comby-Dassonneville d'avoir si bien travaillée pendant sa thèse pour nous avoir délivré un nanoindenteur fonctionnalisé qui « marche du tonnerre » ! A peu de chose près, les manips sont (presque) faciles.

Merci également à David Mercier pour les multiples discussions très intéressantes menées lors de ma thèse et qui ouvrent de belles perspectives.

Je tiens à remercier tous les membres de mon jury de thèse, le président Alain Sylvestre, les rapporteurs Thomas Pardoen et Jean-Luc Loubet, et l'examinateur Frédéric Houzé, pour leur lecture attentive de mon manuscrit et pour avoir été les moteurs de toute la discussion scientifique passionnante et passionnée que l'on a eu à la suite de ma présentation.

On entre maintenant dans les remerciements des collègues qui sont aussi devenus des ami(e)s puisque je remercie sincèrement tous les thésards/post-docs/stagiaires, des deux générations que j'ai eu la chance de croiser, qui ont rendu mon long passage au labo et à Grenoble plus beau

encore ! Merci donc à (dans un ordre pas forcément logique) mon ami de Phelma Florian qui m'a fait le plaisir d'être présent le jour de ma soutenance de thèse, les génialissimes Melek, Mohammed et Alexandre qui m'ont beaucoup apporté et soutenu sur tous les plans et quelle que soit la période, le « gars sûr » Léo qui venait boire le café quand il entendait ma douce voix dans le bureau voisin (désolé Muriel Véron qui devait aussi l'entendre...), les nouveaux arrivants au bureau Hélène, Thomas et Guillaume qui m'ont supporté dans tous les sens du terme dans ma phase de rédaction, la talentueuse cadreuse et monteuse de ma soutenance de thèse Déborah qui m'a offert un super souvenir mais pas que, la serviable Lucile que j'ai eu le plaisir de recroiser après notre première rencontre à MatéIS et avec qui je prenais plaisir à finir mon tour du 2ème étage, la fondatrice du « Café du Brésil » (comptant aujourd'hui plus de 40000 vues) Marion avec qui je pouvais parler à la fois de « disclinations et disconnections » et de soirées, le fidèle Antoine qui m'accompagnait chercher à manger après avoir reçu un message du genre « chercher manger » sur le groupe WhatsApp et le fêtard Matthieu toujours là pour apporter de la bonne humeur (tous deux partis trop tôt...), bien sûr la team DJ Boutik Pierre et Thomas (aka « Pierro et Tomtom ») avec laquelle j'ai passé d'EXCELLENTS moments, et une longue liste qui prendrait trop de lignes à personnaliser mais ils reconnaitront leur importance : Zélie, Ali, Imad, Fatma, Damien, les deux Lorenzo, Aseem, Angel, Thiam, Luiza, Charline et Maxence. Je tiens à remercier tout particulièrement Chaymaa qui a partagé mon bureau (ou c'est plutôt moi qui ai partagé le sien...) à partir de mon stage de fin d'études jusqu'à ma troisième année de thèse. Merci pour ton aide précieuse dans les manips de nanoindentation-électrique que tu gérais d'une main de maître, pour les indents *post mortem* que tu retrouvais au MEB d'un seul coup d'œil, et surtout pour ta gentillesse légendaire et ton soutien permanent. Ce fut un réel plaisir de partager cette aventure de thèse ensemble ! MERCI à tous et au plaisir de vous recroiser !

Je tiens à adresser un IMMENSE MERCI à mes amis d'enfance, que j'ai du mal à dissocier de ma famille tant ils sont importants dans ma vie. En particulier, merci aux Moulézanais David (aka « Dadou » ou « Blaqué ») et Loïs (aka « Lolo » ou « le suisse ») et au Mauressargois Kévin (aka « Zoz » ou « Zozison »), que j'ai bien rangé en deux catégories sous les conseils de Kévin... mais également à Brenda (aka « Brendoch » ou « Brendoline ») et Amandine (aka « il va vite falloir te trouver un surnom ! »). Vous avez évidemment tous et toutes une place particulière dans cette aventure, mais centrale de par votre simple présence permanente, votre bonne humeur contagieuse, votre sens de la fête remarquable, votre accueil chaleureux chez vous depuis des années voire des décennies, votre suivi bienveillant de l'avancement de ma thèse, et surtout votre amitié fraternelle et indéfectible. Je garderai un superbe souvenir, impérissable, de votre présence à ma soutenance de thèse.

Last but not least, je remercie du plus profond de mon cœur mes parents (les véritables « maman et papa ») sans qui ce parcours n'aurait jamais été possible. Merci de m'avoir infiniment soutenu, encouragé depuis toujours à emprunter le chemin qui me passionnait, et non pas suivre une voie toute tracée qui aurait pu me rapprocher de vous. Merci de m'avoir tant porté, apporté et supporté inconditionnellement durant toutes ces années. Merci d'essayer de suivre mon parcours et mes projets, pas toujours simples à suivre, et qui doivent certainement vous sembler farfelus. Merci également pour votre présence à la soutenance, vous voir au côté de mes amis et de mes collègues restera gravé dans ma mémoire. Je pourrais continuer facilement à développer cette partie mais je m'arrêterai là pour faire en sorte que mes remerciements ne soient pas plus longs que le contenu scientifique du manuscrit...

Bref, MERCI !

Contents

Résumé Étendu

This chapter is an extended summary in French of the manuscript. It presents the scientific methods developed during the present PhD and the main results obtained on the different topics.

Contexte et objectifs

Les dispositifs fonctionnels aux petites échelles (systèmes microélectroniques, capteurs, générateurs ou accumulateurs d'énergie, cellules photovoltaïques, ...) n'ont cessé de se développer depuis plus de six décennies et sont aujourd'hui au cœur de la plupart de nos objets quotidiens (ordinateurs, smartphones, automobiles, panneaux solaires, ...). La réduction de leur taille et la complexification de leur architecture au fil des années a conduit à l'intégration d'empilements toujours plus hétérogènes de matériaux en couches minces comportant à la fois des métaux, des semi-conducteurs et des diélectriques. Or ces matériaux sont soumis à de fortes contraintes mécaniques durant le procédé de fabrication ou la vie du dispositif, pouvant dégrader à la fois l'intégrité de l'empilement (fissuration, délaminage, ...) et ses propriétés physiques (électrique, optique, thermique, ...). La connaissance des propriétés à la fois fonctionnelles, mécaniques et de leurs potentielles interactions, est donc un point clé quant à la fiabilité des dispositifs avancés.

Cette thèse s'inscrit dans ce contexte. Elle a pour objectif d'identifier les comportements mécaniques et électriques de trois systèmes, comparables sur la forme, mais très différents en termes de propriétés et d'applications. Dans les trois cas, il s'agit d'empilements complexes de couches minces céramiques/diélectriques sur des substrats conducteurs :

- Système 1 : Une couche de nitrure de silicium d'épaisseur 1,3 µm sur une couche épaisse d'un alliage d'aluminium (Si_3N_4/AlSiCu). Si_3N_4 est largement utilisé dans les puces microélectroniques comme couche de passivation contre l'humidité et les contaminants ambiants, tandis qu'AlSiCu est la couche de connexion électrique.
- Système 2 : Une couche de verre organosilicate nanoporeuse d'épaisseur 330 nm sur un substrat de silicium (SiOCH/Si). SiOCH est un matériau diélectrique à très faible permittivité utilisé dans les circuits intégrés afin de réduire les couplages capacitifs.
- Système 3 : Une couche d'oxyde de cuivre d'épaisseur 225 nm sur un substrat de cuivre recuit (Cu_2O/Cu). Cu_2O est étudié en vue de son intégration dans un large spectre d'applications potentielles (dispositifs micro- et opto-électroniques, cellules photovoltaïques, batteries, capteurs de gaz, etc.) alors qu'il est particulièrement intéressant pour sa non-toxicité, ses faibles coûts de production, son élaboration relativement aisée et l'abondance de son métal.

La Figure I présente une image en microscopie électronique à balayage (SEM) du système Si_3N_4/AlSiCu (Figure Ia), une autre du système SiOCH/Si (Figure Ib) et une cartographie de phases en microscopie électronique en transmission (TEM) couplée à la méthode ACOM du système Cu_2O/Cu (Figure Ic).

Figure I. Images SEM en coupe transversale des systèmes (a) Si_3N_4/AlSiCu, (b) SiOCH/Si, et (c) cartographie de phases ACOM/TEM du système Cu_2O/Cu.

Le fil conducteur de ce travail de thèse est la caractérisation des propriétés mécaniques/électriques de couches minces céramiques/diélectriques par une approche couplant des expériences de nanoindentation-électrique et des simulations numériques par la méthode des éléments finis.

Expériences de nanoindentation-électrique

Le suivi des réponses mécanique et électrique locales des systèmes introduits a été effectué par nanoindentation instrumentée et nanoindentation-électrique. La nanoindentation instrumentée est une technique consistant à appliquer une charge L avec une pointe très dure et rigide, et à mesurer la profondeur de pénétration h de cette pointe dans l'échantillon. Des courbes de charge (enfoncement de la pointe) et de décharge (retrait de la pointe) sont alors obtenues. La raideur de contact S, correspondant à la dérivée de la courbe $L-h$ aux premiers instants de la décharge, peut également être mesurée en continue grâce à un mode dynamique appelé « Continuous Stiffness Measurement » (CSM). Sur l'appui de modèles analytiques et/ou numériques, l'exploitation des courbes d'indentation $L-h$ et $S-h$ permet d'accéder à diverses propriétés mécaniques locales comme le module d'élasticité, la dureté, la limite d'élasticité, l'exposant d'écrouissage, etc. Cette technique peut être couplée à des mesures électriques fines et prend alors le nom de « nanoidentation-électrique ». Elle consiste à appliquer une différence de potentiel électrique V entre l'échantillon et une pointe conductrice, et à mesurer le courant I traversant la pointe (ou la résistance de contact R) au cours de l'indentation. Comme pour l'exploitation des grandeurs mécaniques de charge $L-h$ et de raideur $S-h$, le traitement des signaux électriques de courant $I-h$ (ou de résistance $R-h$) peut conduire aux propriétés électriques locales du matériau indenté telle que la conductivité, la constante diélectrique, le champ de claquage, etc. La Figure II schématise un essai de nanoindentation-électrique et les courbes mécanique/électrique typiquement obtenues.

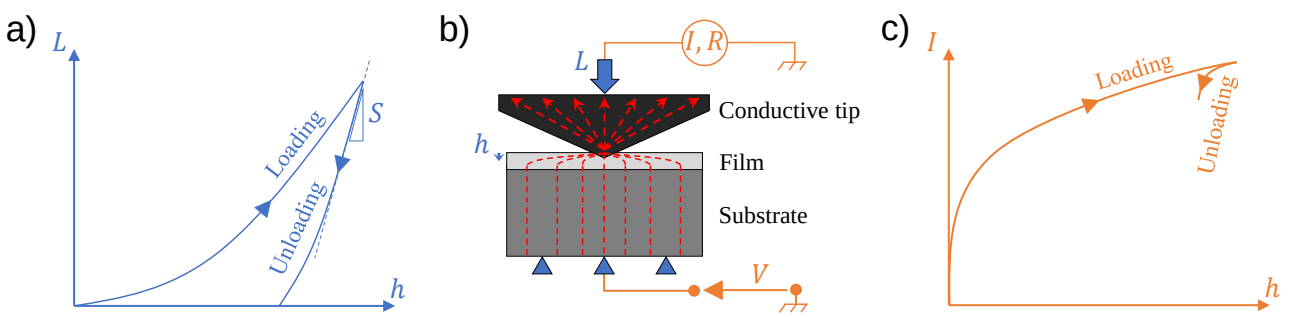

Figure II. Schémas (a) d'une courbe typique de charge-décharge, (b) d'un essai de nanoindentation-électrique et (c) d'une courbe typique de courant.

Les expériences de nanoindentation-électrique ont été réalisées à l'aide d'un dispositif conçu au laboratoire SIMaP, qui combine différents modules commerciaux. La tête de nanoindentation est un actionneur commercial InForce 50 de chez Nanomechanics Inc./KLA-Tencor piloté en force par une bobine électromagnétique, mesurant le déplacement par un système de jauge capacitive, et intégrant la mesure continue de la raideur de contact par le mode CSM. Les pointes d'indentation utilisées au cours de cette thèse sont toutes de géométrie Berkovich fournies par Synton-MDP, composées de diamant dopé au bore dont la résistivité est comprise dans la gamme $[0{,}2 - 2]$ Ω.cm. Elles sont fixées sur une extension en céramique de 3 mm de long, elle-même vissée sur une extension en tungstène de 1,5 cm de long. L'échantillon est monté sur une plaque en époxy à double face revêtue de cuivre. L'extension en céramique et la plaque d'époxy sont nécessaires pour isoler électriquement la pointe conductrice et l'échantillon du bâti mis à la terre. Les contacts électriques (avec la pointe et l'échantillon) sont réalisés avec des fils de cuivre connectés à des prises de courant fixes. Les déplacements de la tête d'indentation et de l'échantillon sont assurés avec des positionneurs linéaires de SmarAct GmbH. Les mesures de courant sont effectuées du côté de la pointe avec un ampèremètre ou électromètre très sensibles (modèle Sub-Femtoamp Remote SourceMeter 6430 de chez Keithley). La polarisation électrique est appliquée à l'échantillon avec une source de tension (soit avec le modèle 6517B de chez Keithley pour SiOCH, soit avec le modèle 6430 pour Cu_2O). Une photo du dispositif de nanoindentation-électrique développé au laboratoire SIMaP est présentée en Figure III.

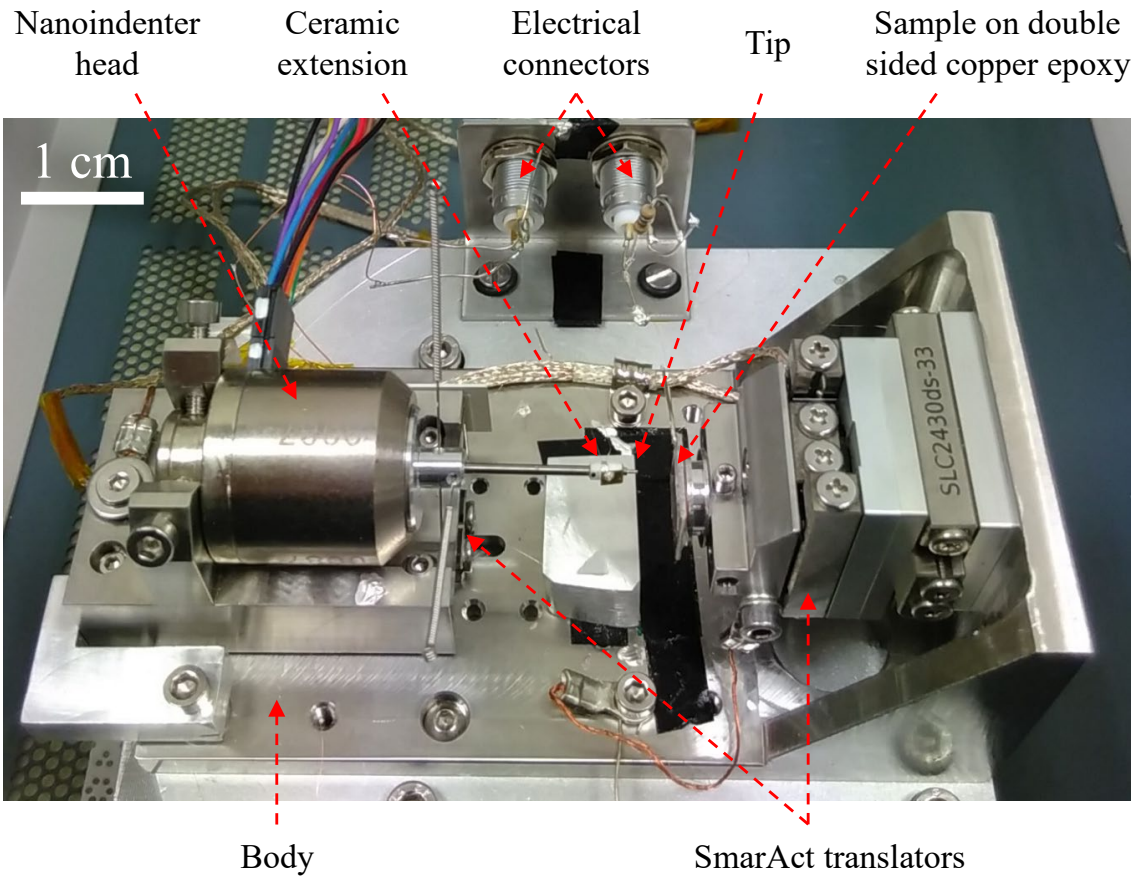

Figure III. Photo du dispositif de nanoindentation-électrique.

Simulations numériques par FEM

Dans ce travail de thèse, les résultats d'indentation ont été traités à l'aide de simulations numériques menées par la méthode des éléments finis (FEM) ce qui a permis d'adopter une approche quantitative pour extraire les propriétés des matériaux. Plusieurs modèles complexes ont été développés comme des modèles mécaniques de fissuration/décohésion intégrant des lois cohésives, des modèles multiphysiques décrivant à la fois le comportement mécanique et le comportement électrique des systèmes, ou encore un modèle particulièrement original couplant la conduction électrique à la plasticité dans les couches minces diélectriques.

Les calculs éléments finis ont été effectués à l'aide du logiciel commercial ABAQUS® avec des modèles établis dans un cadre 2D-axisymétrique (cf. exemple en Figure IV). Les systèmes sont constitués de plusieurs parties : un substrat, une (ou des) couche(s) mince(s) et un indenteur dont la géométrie correspond au profil des pointes Berkovich utilisées expérimentalement. Les lois de comportement et les propriétés associées à chacune des parties dépendent du système considéré mais leur identification pour les trois couches minces étudiées (Si_3N_4, SiOCH, Cu_2O) est au cœur de cette thèse. D'un point de vue mécanique, les simulations consistent à appliquer un déplacement vertical sur la surface supérieure de la pointe pour l'amener en contact avec la surface de la couche supérieure, tandis que la surface inférieure du substrat est encastrée. Ainsi, la distribution des contraintes/déformations dans le système peut être visualisée. La force de réaction est également extraite, permettant de tracer une courbe de charge « force-profondeur ». Concernant l'aspect électrique, une différence de potentiel est appliquée entre la surface supérieure de la pointe et la surface inférieure du substrat tout au long de l'essai d'indentation. Ainsi, la distribution de la densité de courant et du champ électrique dans le système peut être visualisée. Le courant circulant à travers le contact pointe/couche est également extrait, ce qui permet de tracer une courbe électrique « courant-profondeur ». Pour chaque système, la cellule de simulation est suffisamment large afin que les champs mécaniques (et électriques) n'interagissent pas avec les bords, et le maillage est suffisamment fin pour capturer ces champs dans les zones d'intérêt (contact, interface(s), ...). Les calculs ont tous été résolus par des procédures implicites en utilisant le solveur ABAQUS®/Standard.

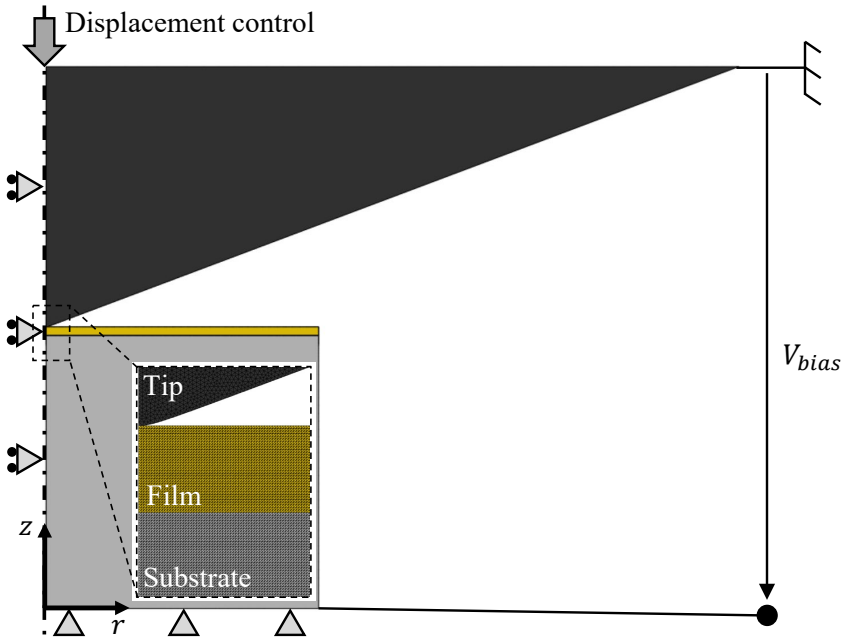

Figure IV. Exemple d'un modèle FEM multiphysique.

I Rupture d'une couche fragile sur un substrat ductile

Note : Cette étude est traitée en détail dans le Chapitre 2.

Le premier échantillon étudié est un empilement de couches multi-matériaux généralement conçu pour les puces microélectroniques. Son élaboration a été gérée par le laboratoire CRISMAT (Normandie Université, France), hors du contexte de cette thèse. D'abord, une couche de silice de 450 nm d'épaisseur a été déposée par dépôt chimique en phase vapeur assisté par plasma (PECVD) sur un wafer de silicium monocristallin de 6" orienté (001). Ensuite, un alliage polycristallin $Al_{98,96}Si_{1,00}Cu_{0,04}$ (AlSiCu) a été pulvérisé sur la surface de la silice, conduisant à une couche de 3,0 ± 0,1 µm d'épaisseur. Finalement, une couche amorphe de nitrure de silicium (Si_3N_4) d'épaisseur 1,3 ± 0,1 µm a été déposée en surface par PECVD à basse température ($\sim$ 400 °C) en utilisant un mélange gazeux SiH_4/NH_3.

Des essais de nanoindentation instrumentée « classiques » ont été effectués sur cet empilement Si_3N_4-1,3µm/AlSiCu/SiO_2/Si, menant à la fissuration de la couche fragile de nitrure et à deux instabilités sur les courbes de charge appelées pop-in (cf. Figure Va). Le processus d'endommagement du multicouche a été entièrement décrit à l'aide de simulations FEM intégrant la plasticité de la couche inférieure d'AlSiCu (loi d'écrouissage puissance) et la fissuration d'à la fois la couche supérieure de Si_3N_4 et de l'interface Si_3N_4/AlSiCu (lois cohésives bilinéaires couplées à la méthode des éléments finis étendus XFEM). Deux types de fissure ont été identifiés comme responsables des évènements mécaniques observés sur les courbes de charge. Le premier pop-in est dû à une fissure conique s'amorçant à l'interface Si_3N_4/AlSiCu et se propageant jusqu'à une zone de compression située sous l'apex de la pointe (cf. ① en Figure V). Le second pop-in est quant à lui induit par une fissure orthoradiale s'amorçant en surface du film de nitrure et se propagent en direction de l'interface Si_3N_4/AlSiCu (cf. ② en Figure V). La méthodologie suivie pour obtenir ces résultats est la suivante.

D'abord, les propriétés plastiques d'AlSiCu ont été déterminées par analyse inverse à partir d'essais d'indentation menés sur un système ne comprenant pas la couche de nitrure.

Ensuite, le processus de fissuration engendrant le premier pop-in a été investigué. Expérimentalement, aucune fissure ni empreinte résiduelle en surface de Si_3N_4 n'a été observée suite au premier pop-in. Dans la couche de nitrure du modèle FEM, des sites d'amorçage de fissure ont été placés à différentes positions dans la zone où la contrainte en tension était maximale (à l'interface Si_3N_4/AlSiCu). Une étude paramétrique sur les propriétés d'endommagement de Si_3N_4, sur celles de l'interface Si_3N_4/AlSiCu et sur la position du site d'amorçage a montré que seuls deux paramètres avaient un impact significatif sur les courbes de charge : la résistance à la traction du nitrure $\sigma^{0,lay}$ et la position de la première fissure r_f. Les couples $(\sigma^{0,lay}, r_f)$ menant à une dissipation maximale de l'énergie causée par la rupture ont alors été sélectionnés (cf. Figure Vb). De manière intéressante, tous les couples obtenus avec cette approche de « dissipation maximale d'énergie » permettent aux courbes numériques de reproduire parfaitement le premier pop-in expérimental.

Finalement, l'étude de la fissuration induisant le second pop-in a fourni des informations supplémentaires pour discriminer parmi l'ensemble des couples $(\sigma^{0,lay}, r_f)$ identifiés sur l'appui du premier pop-in. En effet, seul un nombre limité de couples $(\sigma^{0,lay}, r_f)$ conduisent à la propagation d'une seconde fissure de sorte à ce que les courbes numériques reproduisent le second pop-in.

Cette approche énergétique, basée sur les pop-in d'indentation des empilements « *fragile sur ductile* », donne donc une procédure d'identification des propriétés d'endommagement de

la couche fragile qui pourrait être appliquée à des systèmes similaires. De plus, elle fournit le scénario de fissuration complet comprenant la position des fissures, leur forme, leur longueur, etc. Enfin, elle ne requiert pas l'observation expérimentale des fissures *post mortem* bien qu'elle ait été réalisée dans le cadre de cette étude pour valider la méthodologie présentée (cf. comparaison entre les Figures Vc et d).

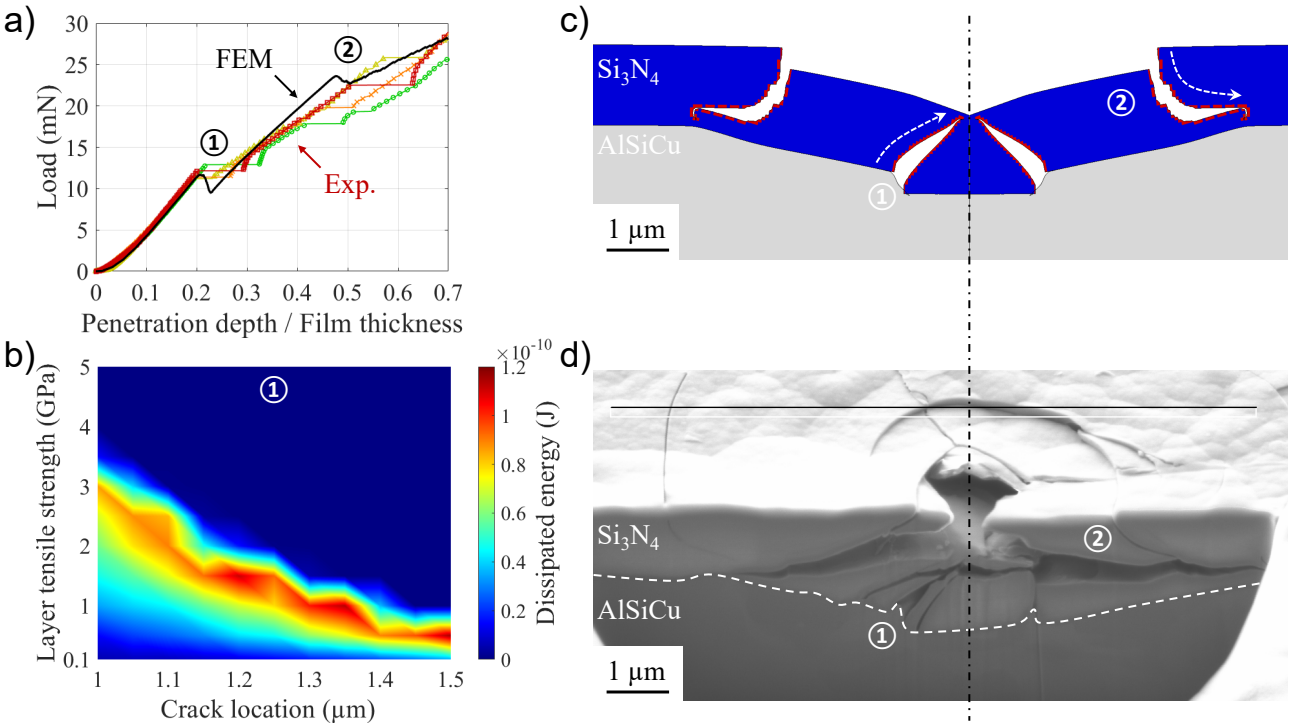

Figure V. (a) Courbes de charge obtenues sur l'empilement Si_3N_4/AlSiCu/SiO_2/Si expérimentalement et par FEM. (b) Cartographies obtenue par FEM de l'énergie dissipée par la première fissure en fonction de sa localisation et de la résistance à la traction de Si_3N_4. (c) Image FEM des deux types de fissure causant les deux pop-in sur les courbes de charge. (d) Image SEM en coupe transversale après abrasion ionique d'une empreinte résiduelle d'un indent effectué à une charge de 45 mN.

Points saillants de cette étude :

- Nouvelle procédure d'identification des propriétés d'endommagement des couches minces fragiles sur des substrats ductiles.
- Méthodologie prédictive quant au processus de fissuration de la couche fragile.
- Application à un système modèle Si_3N_4/AlSiCu.

II Lien conductivité/plasticité dans un diélectrique

Note : Cette étude est traitée en détail dans le Chapitre 3.

Le deuxième échantillon étudié est un système « *couche mince sur substrat* » qui peut être retrouvé dans les circuits intégrés. Il a été élaboré par l'entreprise STMicroelectronics dans le cadre d'une thèse précédente. La couche a été déposée par PECVD à 225 °C avec deux précurseurs et en deux étapes. La première étape consistait à co-déposer une matrice de SiOCH (précurseur diéthoxyméthylsilane) avec une phase organique thermiquement instable appelée « porogène ». La deuxième étape était dédiée à l'élimination du porogène à l'aide de rayons

UV, conduisant à une couche de 330 nm d'épaisseur d'un matériau nanoporeux (20-30 % de porosité).

Des essais de nanoindentation-électrique ont été réalisés sur ce système SiOCH-330nm/Si sur de larges gammes de profondeur ($[0, 700]$ nm) et de tension ($[0, 120]$ V), menant à la plastification de la couche, à sa fissuration et à des fuites électriques.

D'abord, la corrélation entre les défaillances mécaniques et électriques a entièrement été décrite en fonction de la profondeur d'indentation et de la tension appliquée. Cette première étude a révélé l'existence de quatre régimes dont un s'est avéré particulièrement intéressant pour identifier une loi de conduction de la couche de SiOCH sous contrainte ainsi que ses propriétés.

Le domaine d'intérêt se situe aux petites profondeurs (inférieures à ~ 200 nm) et aux fortes tensions (supérieures à ~ 90 V). D'un point de vue mécanique, SiOCH plastifie (sans fissurer) dans cette plage de profondeurs comme en atteste les courbes de décharge non superposées aux courbes de charge en Figure VIa, et les empreintes résiduelles observées par microscopie à force atomique (AFM) en Figures VIb et c. D'un point de vue électrique, les fuites de courant à travers la couche dans cette plage de tensions ont lieu dès l'établissement du contact pointe/échantillon et sont suffisamment importantes (supérieures au femtoampère) pour être détectables par l'équipement de mesure (cf. Figure VId).

De manière contre-intuitive, il a été observé que malgré l'augmentation monotone du champ électrique et de l'aire de contact, le courant saturait et même diminuait au cours de l'indentation. Des simulations FEM multiphysiques mécanique/électrique, intégrant la plasticité de la couche par une loi de Drucker-Prager et sa conduction par une loi de Poole-Frenkel, ont mis clairement en évidence une corrélation entre la déformation plastique et la conductivité électrique. Le modèle de Poole-Frenkel classique a alors été étendu par l'introduction d'une déformation seuil ϵ_{th} à partir de laquelle la conduction locale est réduite par un facteur qui décroît exponentiellement avec la déformation plastique locale ϵ. A travers ce terme exponentiel heuristique, la distribution des lignes de courant se trouve également affectée par le champ de déformation plastique. L'implémentation de cette nouvelle loi dans le modèle FEM conduit à une parfaite correspondance entre les courbes numériques et expérimentales avec très peu de paramètres ajustables, comme visualisé sur la Figure VId.

Bien que l'extension du modèle de Poole-Frenkel soit phénoménologique, elle a été justifiée par une approche physique. La déformation plastique dans ce matériau iono-covalent amorphe peut être la conséquence de rupture de liaisons atomiques, qui sont d'un point de vue électrique des liaisons pendantes capables de piéger des charges. Le stockage de charges pourrait alors créer une charge d'espace répulsive dans la couche de SiOCH, réduisant l'émission de Poole-Frenkel en modérant l'abaissement de la barrière énergétique nécessaire à la conduction électrique. A partir de cette hypothèse, un modèle analytique basé sur l'intégration de la loi de Gauss a permis de relier la densité de défauts à la déformation plastique (cf. Figure VIe).

Finalement, le comportement électrique inattendu de la couche de SiOCH observé à partir de mesures de nanoindentation-électrique a complètement été expliqué à l'aide de simulations numériques et de modèles analytiques. Ces travaux donnent une nouvelle compréhension des couplages mécanique/électrique dans les couches diélectriques, ce qui ouvre des perspectives prometteuses quant aux questions de fiabilité des dispositifs avancés au cœur de la microélectronique moderne.

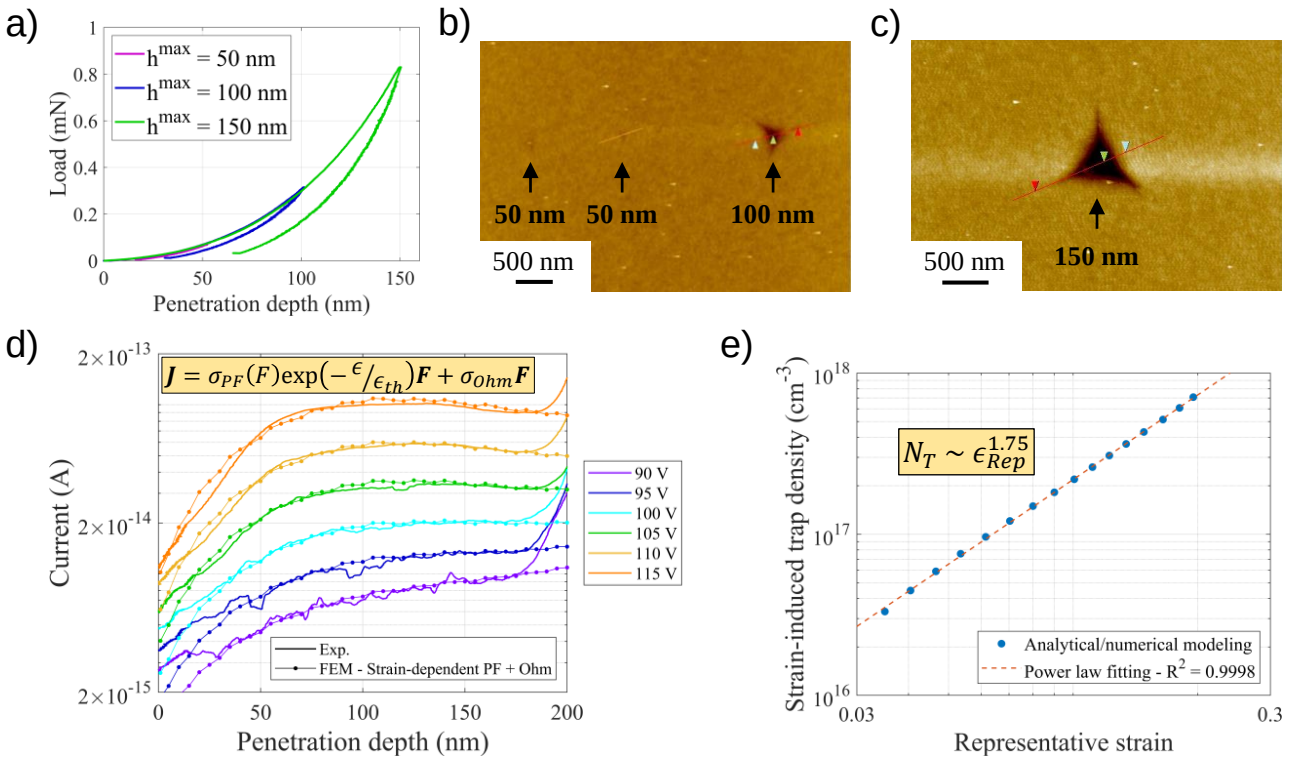

Figure VI. (a) Courbes d'indentation du système SiOCH/Si à des profondeurs maximales de 50, 100 et 150 nm. (b) Images AFM des empreintes résiduelles à 50 nm, 100 nm et (c) 150 nm de profondeur. (d) Courbes électriques expérimentales et numériques après l'implémentation de la loi de Poole-Frenkel étendue. (e) Lien entre la déformation plastique induite lors de l'indentation et la densité de défauts structuraux générés.

Points saillants de cette étude :

- Nouvelle approche permettant de décrire finement les corrélations entre les défaillances mécaniques et électriques des couches minces diélectriques.
- Extension de la loi de conduction électrique de Poole-Frenkel afin de tenir compte de la déformation plastique de la couche diélectrique.
- Application à un système modèle SiOCH/Si.

III Propriétés d'oxydes thermiques de cuivre

Note : Cette étude est traitée en détail dans le Chapitre 4.

Le troisième type d'échantillons étudiés sont également des systèmes « *couche mince sur substrat* » élaborés comme systèmes modèles dans le cadre de cette thèse au laboratoire SIMaP. Du cuivre pur à 99,95 % OFHC (« Oxygen-Free High thermal Conductivity ») sous la forme de plaquette de 2 mm d'épaisseur a d'abord été recuit à haute température (800 °C) sous un flux gazeux Ar/H_2. Le cuivre recuit a ensuite été oxydé thermiquement à 200 °C à l'air ambiant pendant 1 h, menant à une couche d'oxyde Cu_2O nanocristalline de 225 ± 19 nm d'épaisseur. D'autres échantillons ont été élaborés à partir de ce protocole, en particulier : un échantillon de cuivre recuit non-oxydé et deux échantillons de cuivre recuit oxydé à 200 °C avec des durées de 0,5 et 2 h, conduisant à des couches de Cu_2O d'épaisseur 167 ± 32 et 354 ± 44 nm respectivement.

Des essais de nanoindentation-électrique ont été menés sur le système Cu_2O-225nm/Cu,

permettant de suivre l'évolution de la charge mécanique et de la résistance de contact électrique à différentes tensions au cours de l'enfoncement de la pointe (cf. Figure VIIa-haut). A partir de ces courbes et de simulations FEM, les propriétés locales de la couche d'oxyde ont d'une part été déterminées. D'autre part, l'influence de cette couche sur le comportement plastique du substrat de cuivre recuit a été révélée par des expériences complémentaires.

La réponse électrique globale mesurée par nanoindentation-électrique dépend de l'aire de contact pointe/échantillon et du champ électrique, lui même lié à l'épaisseur locale de la couche. La rhéologie du système Cu_2O/Cu durant l'indentation doit donc être connue afin d'extraire les propriétés électriques de la couche d'oxyde. En conséquence, le comportement mécanique des matériaux a d'abord été identifié.

Les courbes de charge sur la Figure VIIa-haut présentent toutes un pop-in. Grâce à des expériences complémentaires, cette instabilité mécanique a été associée à l'amorce de la plasticité dans le substrat de cuivre, qui en d'autres termes correspond à la germination collective et au glissement de dislocations lorsque la contrainte dépasse la résistance théorique au cisaillement du matériau. Ceci a fréquemment été observé dans les métaux contenant une faible densité de défauts. C'est le cas des substrats étudiés qui, après le recuit à 800 °C, ont des grains quasi-millimétriques (assimilables à des monocristaux du point de vue de la nanoindentation) avec une très faible densité de dislocations. Un échantillon de cuivre recuit non-oxydé et trois échantillons de cuivre recuit avec des épaisseurs d'oxyde différentes ont été indentés entre 50 et 150 fois chacun afin de construire une statistique à partir de la charge critique à pop-in (cf. Figure VIIb). Il a été observé une augmentation de cette charge critique en présence de l'oxyde et avec l'augmentation de son épaisseur. Ceci a été expliqué comme une augmentation de la taille équivalente de l'indenteur par le film dur se conformant à sa surface, générant ainsi un début tardif de plasticité dans le substrat de cuivre comme connu pour l'indentation sphérique.

Pour des profondeurs inférieures à celles du pop-in, le substrat de cuivre est donc parfaitement élastique. Or des essais de nanoindentation sur le système Cu_2O-225nm/Cu dans cette gamme de profondeurs ont montré que sa déformation était non-réversible. Ce comportement a été associé à la plasticité du film d'oxyde.

Pour des profondeurs supérieures à celles du pop-in, la dureté du système Cu_2O-225nm/Cu est au moins deux fois plus importante que celle du cuivre recuit non-oxydé juste après le pop-in, puis tendent vers la même valeur pour de très grandes profondeurs (supérieures à ~ 1 µm) comme montré en Figure VIIc. Cet effet a été attribué à un changement de conditions aux limites : en présence d'un film d'oxyde, les dislocations générées dans le cuivre ne peuvent plus glisser librement vers la surface du matériau et s'accumulent donc à l'interface couche/substrat, induisant à la fois un durcissement et un fort gradient de plasticité.

Tous ces comportements mécaniques ont été intégrés dans un modèle numérique FEM, avec une loi de Drucker-Prager pour modéliser la plasticité de la couche d'oxyde et une loi du type Nix-Gao pour modéliser la plasticité à gradient dans le substrat de cuivre après le pop-in. Les paramètres de ces lois ont été déterminés de sorte que les courbes numériques se superposent aux expérimentales (cf. Figure VIIa-haut).

Concernant le comportement électrique de l'oxyde, des caractéristiques courant-tension ont été extraites à différentes profondeurs à partir des courbes de résistance électrique. Leur exploitation a permis d'identifier la loi de conduction de Cu_2O comme étant une loi de Poole-Frenkel. En l'implémentant dans le modèle FEM et grâce à la description du comportement mécanique complexe de ce système menée précédemment, les propriétés de l'oxyde ont été déterminées par une méthode inverse. Il est à noter qu'une loi de Poole-Frenkel classique (non couplée à

la plasticité comme pour la couche de SiOCH) suffit à décrire le comportement électrique de Cu_2O. En effet, ce matériau est un semi-conducteur avec une hauteur de barrière de dépiégeage estimée à 320 meV, contrairement à SiOCH qui est un diélectrique avec une barrière environ trois fois plus haute ($\sim$ 950 meV). Les pièges étant beaucoup moins profonds dans le cas de Cu_2O, le stockage de charges impliquant la génération d'une charge d'espace est peu probable.

Finalement, les comportements mécanique et électrique des oxydes thermiques de cuivre élaborés à basse température ont été complètement décrits par une approche couplant des expériences de nanoindentation-électrique et des simulations FEM. Il a été montré que des effets de taille, déjà connus dans du cuivre non-oxydé, sont renforcés en présence d'une couche d'oxyde à sa surface. Enfin, les propriétés électriques de Cu_2O ont été déterminées ce qui comble des lacunes dans la littérature.

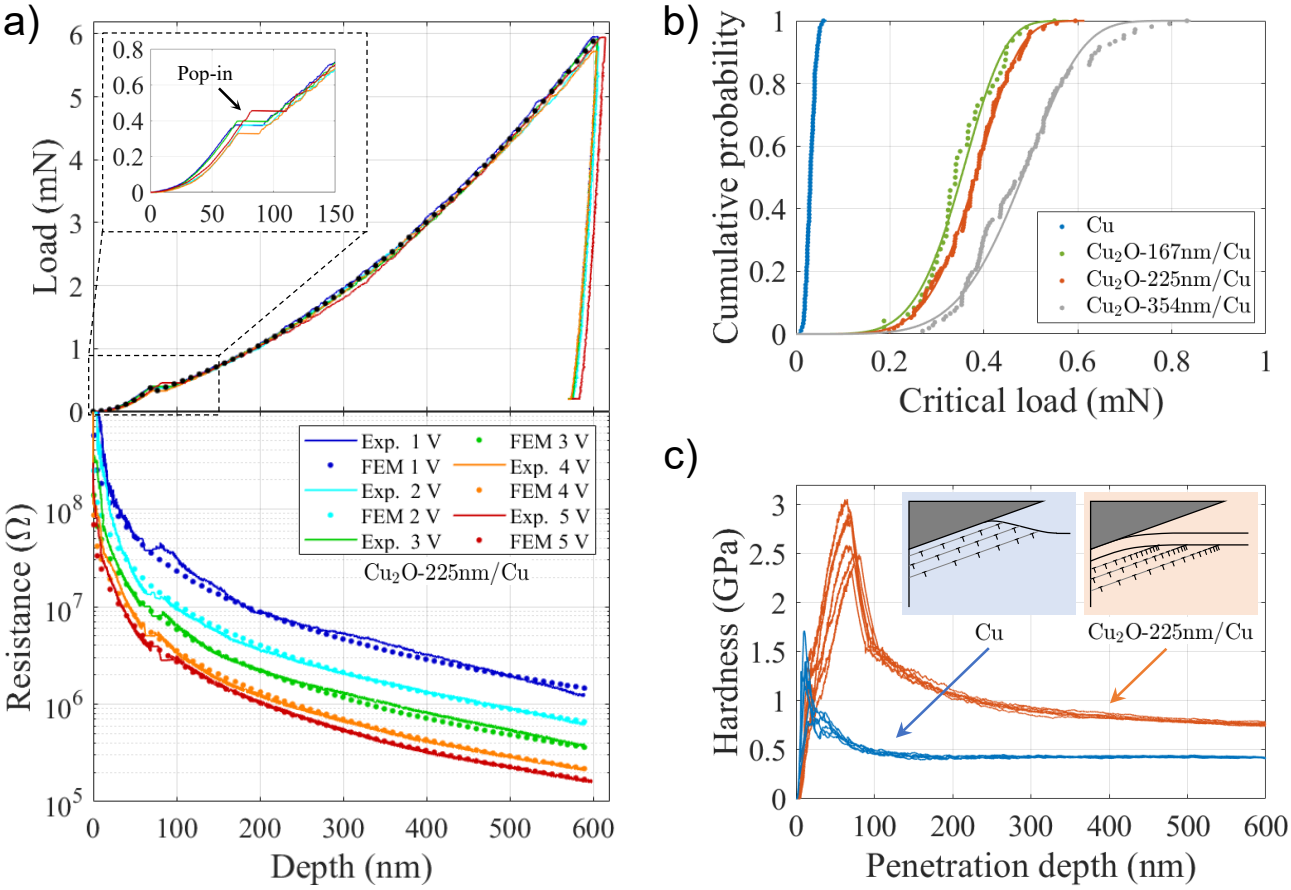

Figure VII. (a) Courbes de charge (haut) et de résistance électrique (bas) obtenues sur le système Cu_2O-225nm/Cu. (b) Statistique à partir de la charge critique à pop-in sur un substrat de cuivre recuit non-oxydé et sur trois autres substrats comportant des couches de Cu_2O de différentes épaisseurs. (c) Courbes de dureté obtenues sur le substrat de cuivre recuit non-oxydé et sur le système Cu_2O-225nm/Cu.

Points saillants de cette étude :

- Détermination des propriétés mécaniques et électriques d'oxide thermique de cuivre Cu_2O en couche mince.
- Renforcement des effets de taille dans les monocristaux métalliques en présence d'une couche d'oxyde à leur surface.

Conclusion

A travers cette thèse, les comportements mécaniques (plasticité, endommagement) et électriques (conduction, diélectricité) de trois couches céramiques sur des substrats conducteurs (Si_3N_4-1,3µm/AlSiCu, SiOCH-330nm/Si, Cu_2O-225nm/Cu) ont été identifiés et leurs propriétés déterminées. Ceci a été rendu possible par une approche couplant des expériences avec une technique de caractérisation avancée (nanoindentation-électrique) et des simulations numériques (méthode des éléments finis). En particulier, plusieurs résultats originaux et d'intérêts à la fois académique et applicatif ont été obtenus :

- une méthodologie basée sur la dissipation d'énergie engendrée par la rupture et utilisant les pop-in d'indentation des empilements « *fragile sur ductile* » a été développée afin de déterminer les propriétés d'endommagement de la couche fragile et d'accéder au scénario de fissuration ;
- la loi de Poole-Frenkel classique régissant le transport électrique de très nombreux diélectriques a été étendue avec l'introduction d'un terme phénoménologique modulant la conduction dans le matériau en fonction de sa déformation plastique ;
- des effets de taille déjà bien connus dans les métaux cristallins (amorce de la plasticité, gradients de plasticité) ont été renforcés en faisant croître une couche d'oxyde à leur surface.

En plus d'accéder à une meilleure compréhension des systèmes étudiés, qui sont au cœur de la microélectronique moderne, ces résultats sont probablement assez génériques pour être applicables à d'autres systèmes similaires. Ils ouvrent notamment des perspectives très intéressantes quant à la fiabilité des dispositifs avancés, devant assurer une ou plusieurs fonction(s) tout en étant sujet à des contraintes mécaniques diverses.

General Introduction

Since the invention of integrated circuits in the late 1950s, the complexity of small-scale devices has never stopped rising, whether they are microelectronic systems, sensors, imagers, solar cells, power sourcing or storage, etc. This increasing complexity has required the integration of thin film materials in the form of ever more heterogeneous stacks, combining metals, semiconductors and dielectrics. Each material has the role of ensuring one or more functions for several years (signal transmission, energy conversion, insulation, ...) of which the most common are based on electrical conduction and dielectric properties. However, the functional reliability of these materials is largely driven by their mechanical strength to the harsh stresses occurring both in the fabrication process and during the lifetime of the device. The development of characterization techniques, and methods for processing their outputs, is therefore necessary to simultaneously determine functional and structural properties of advanced materials at small scales, and potentially identify their interaction.

The present PhD work is part of this context. It consists in identifying the mechanical and electrical behaviors of three functional systems composed of thin film ceramic/dielectric materials on conductive substrates by an approach coupling experiments and numerical simulations.

The studied systems are:

- a 1.3 µm thick silicon nitride film deposited by plasma-enhanced chemical vapor deposition on an aluminum alloy layer (Si_3N_4/AlSiCu);
- a 330 nm thick nanoporous organosilicate glass film deposited by plasma-enhanced chemical vapor deposition on a silicon substrate (SiOCH/Si);
- a 225 nm thick copper oxide film grown by thermal oxidation from an annealed copper substrate (Cu_2O/Cu).

The monitoring of the mechanical and electrical responses of these systems was performed by "electrical-nanoindentation" which is a technique coupling fine electrical measurements to nanoindentation tests initially dedicated to submicrometer mechanical measurements. The processing of the experiments, being neither direct nor trivial for a quantitative approach, was carried out essentially by using numerical simulations by the finite element method to extract material properties.

This thesis is based on articles published or submitted in A-ranked international journals. Consequently, a specific bibliography for each of the systems listed above is included in the introductory section of their respective chapter, followed by the so-called "materials and methods" section.

Four main parts constitute this manuscript:

Chapter 1 is a state-of-the-art on instrumented and electrical nanoindentation. It places these techniques in a historical context and presents the main methods for determining mechanical and electrical properties from indentation tests.

Chapter 2 is a purely mechanical study of the failure of the brittle Si_3N_4 film on the ductile AlSiCu layer. It presents an energy-based methodology using features on the loading curves to determine both the damage properties of the brittle film and the cracking process.

Chapter 3 is a study of the mechanical and electrical couplings in the ultra-low-permittivity SiOCH film. It highlights a plasticity-driven conductivity drop in the dielectric film under mechanical loading and proposes an extension of the Poole-Frenkel conduction law to describe it.

Chapter 4 is a mechanical and electrical study of the Cu_2O semiconductor layer on the annealed Cu substrate. It reveals an enhancement of the mechanical size effects in the copper substrate by the presence of the oxide film and gives the properties of the oxide.

Chapter 1

State-of-the-Art: Instrumented and Electrical Nanoindentation

This chapter is a state-of-the-art review of instrumented nanoindentation and electrical-nanoindentation techniques for the determination of both mechanical and electrical properties of materials. It describes some analytical models and numerical methods widely used to identify, from nanoindentation tests, the material parameters of elastic-plastic, damage or electrical constitutive laws. Special attention is paid to the characterization of brittle/dielectric thin films which are at the heart of this PhD. A specific bibliography for each studied system is presented in the introduction section of their respective chapter.

1.1 Instrumented nanoindentation

1.1.1 Principle of instrumented nanoindentation test

Instrumented nanoindentation is a technique dedicated to the fine and local mechanical characterization of materials, at a micro/nanometric scale. It was developed in the 1980s, notably thanks to the pioneering work of Pethica *et al.* [1] and Loubet *et al.* [2]. The test consists in applying a load L on a hard and stiff tip, and to measure continuously the penetration depth h of this tip in the sample (Figure 1.1a) . Thus, load-depth curves can be obtained during the penetration of the tip in the sample (called "loading curve") or during the withdrawal of the tip (called "unloading curve"). Another magnitude is commonly measured in nanoindentation: the contact stiffness S which corresponds to the derivative of the $L-h$ curve at the beginning of the unloading stage. Since the early 1990s, the contact stiffness can be extracted continuously during the indentation test thanks to the Continuous Stiffness Measurement (CSM) mode [3, 4]. This dynamical mode allows to superimpose a harmonic force on the nominal increasing force. A succession of loading/unloading cycles are performed with an amplitude of the order of 1-2 nm. The contact stiffness is measured at each of these dynamic unloading steps. Figure 1.1b shows a schematic of a nanoindentation load-depth curve gathering all relevant magnitudes.

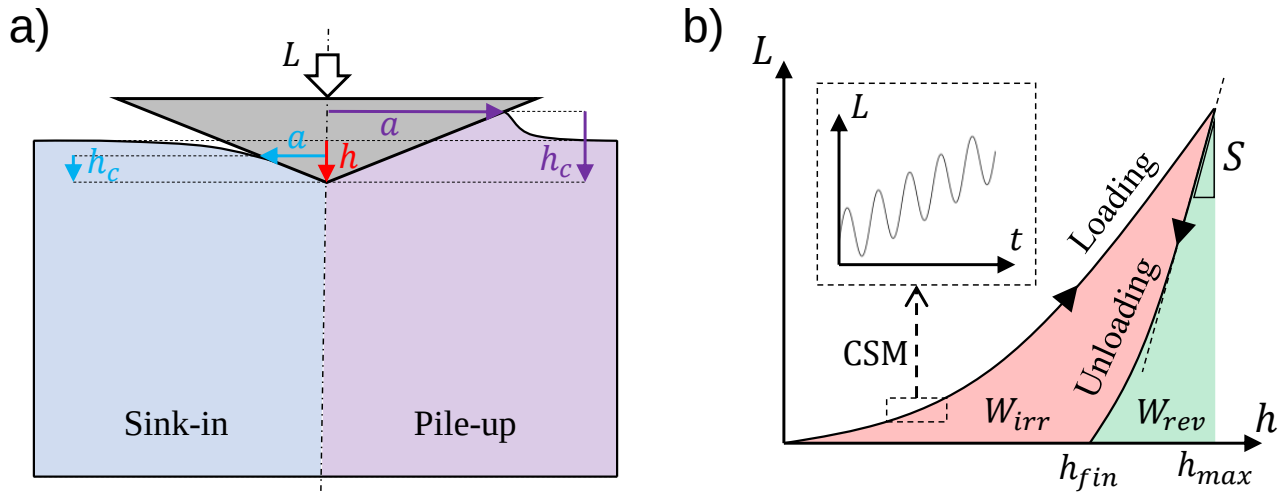

Figure 1.1. Schematics of (a) a nanoindentation test and (b) load-depth curve.

1.1.2 Nanoindentation tips

The nanoindentation tips must be as hard and stiff as possible so that their deformation is negligible compared to that of the sample. They are therefore commonly made of diamond which has a hardness of about 40 GPa and an elastic modulus of about 1140 GPa.

Regarding the geometry of the tips, several types can be used such as flat punches, spherical tips, conical tips or pyramidal tips with different bases. All the work presented in the present manuscript was done with Berkovich tips, which have a pyramidal geometry with a triangular base. These tips are the most commonly used in nanoindentation because they have the same projected surface area at a given altitude as historical Vickers tips (square-based pyramid) while being easier to polish to obtain a sharp apex at small scales (intersection of three planes). Berkovich tips have a face angle of 65.27°, which is equivalent to a conical tip with a semi-angle of 70.32°. The main interest of these indenters is that they are self-similar, i.e. the equivalent

radius of the tip is proportional to its height. This implies that whatever the penetration of the indenter in an isotropic semi-infinite material, the strain and stress fields are geometrically similar. A schematic of a Berkovich tip with the true proportions is shown in Figure 1.2.

In practice, the apex of Berkovich tips is never perfectly sharp and wears out along the indentation tests. However, the geometry of the tips must be known to determine the mechanical properties of the sample, especially the relationship between the projected area A_c and the height of the tip h_c, called "shape function". For this purpose, either the tip can be imaged by Atomic Force Microscopy (AFM) for example, or its geometry can be calibrated using methods based on the indentation of a semi-infinite isotropic reference material whose mechanical properties are well known such as fused silica [4, 5].

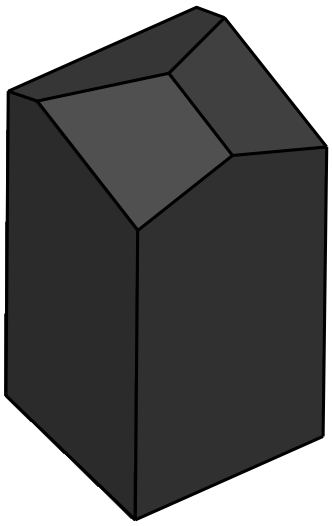

Figure 1.2. Schematic of a Berkovich tip with the true proportions.

1.2 Elastic-plastic laws and properties

1.2.1 Hardness and elastic modulus

In nanoindentation, the hardness H is defined by the Meyer hardness [6] introduced in 1908:

$$H = \frac{L}{A_c} \tag{1.1}$$

and the elastic modulus is generally obtained by the Sneddon equation [7] demonstrated in 1965:

$$E^* = \frac{\sqrt{\pi}}{2}\frac{S}{\sqrt{A_c}} \tag{1.2}$$

where E^* is the reduced modulus:

$$\frac{1}{E^*} = \frac{1-\nu_{tip}^2}{E_{tip}} + \frac{1-\nu_{sample}^2}{E_{sample}} \tag{1.3}$$

with L the load, S the contact stiffness, E_{tip} and E_{sample} the elastic moduli of the tip and the sample respectively, ν_{tip} and ν_{sample} their Poisson's ratio, and A_c the contact area which

corresponds to the projected area of the tip surface in contact with the sample surface. The contact area can be related to the contact radius a by a simple geometrical relation:

$$a = \sqrt{\frac{A_c}{\pi}} \tag{1.4}$$

The contact area depends on both the geometry of the tip and the rheology of the material. A contact area can be associated with a contact depth h_c which is defined by the height of the tip effectively in contact with the sample. For a given tip geometry, h_c can be either smaller than the penetration depth h (called "sink-in" rheology) or greater than h (called "pile-up" rheology) depending of the elastic-plastic properties of the sample (see Figure 1.1a). Extreme cases of rheology are described by analytical solutions of the conical indentation in elastic materials of Sneddon which sink-in [7], and in rigid-plastic materials of Lockett which pile-up [8]. As can be seen in Equations 1.1 and 1.2, the contact area is the only magnitude that is not controlled or measured (assuming known the elastic properties of the tip and fixing the Poisson's ratio of the sample). It is therefore an obstacle to the determination of the mechanical properties of the sample. To access it, several methods exist.

A first method consists in making direct measurements by imaging the residual imprints. This method is the most versatile because it is applicable to most systems, even complex ones (thin films, multiphase alloys, architectural materials, ...). However, only one A_c measurement point per indent can be obtained. The evolution of the contact area with tip penetration requires a large number of indents to be performed at different depths/loads, which can be particularly time-consuming.

A second method relies on analytical models to continuously determine the contact depth h_c during indentation, then access the contact area through the tip shape function $A_c(h_c)$, and finally determine the hardness and elastic modulus of the sample. Two models, valid for isotropic semi-infinite materials, are particularly used. They are both based on the assumption of elastic/plastic partitioning of the indentation depth as initially proposed by Doerner and Nix [9]. The most widely used model is that of Oliver-Pharr [4], which gives the contact depth as:

$$h_c = h - \varepsilon_{OP}\frac{L}{S} \tag{1.5}$$

with ε_{OP} a coefficient depending on the tip geometry ($\varepsilon_{OP} = 0.75$ for a Berkovich tip) obtained by the elastic analysis of the deformation field. However, this model is limited to the description of sink-in rheologies ($h_c < h$). An alternative model that also takes into account pile-up rheology ($h_c > h$) is Loubet's model [5], which gives the contact depth as:

$$h_c = \alpha_{Loubet}\left(h - \frac{L}{S} + h_0\right) \tag{1.6}$$

with $\alpha_{Loubet} = 1.2$ the Loubet coefficient, verified *a posteriori* [10, 11], and h_0 the tip defect determined during the geometrical calibration of the tip [4, 5]. Another method proposed by Volpi *et al.* [12] consists in coupling electrical measurements to the nanoindentation test, typically applying an electrical potential difference between the tip and the sample and measuring the tip/sample electrical contact resistance R during indentation. This method is valid for indentation with an electrically conductive self-similar tip whose resistivity is at least 100 times greater than that of the sample, provided that the tip/sample contact is ohmic. In this case,

the contact depth is expressed as:

$$h_c = \frac{B}{R(h) - A} - h_0 \tag{1.7}$$

with A and B two constants determined by the electrical calibration of the tip and the set-up on a conductive reference sample such as gold, and h_0 the tip defect. This model, less straightforward than the Oliver-Pharr and Loubet models, has the advantage of being applicable whatever the complexity of the sample and boundary conditions (thin films, islands, pillars, multiphase alloys, ...) as long as the contact is ohmic. It is thus particularly well adapted to the characterization of metals.

Concerning the "*thin film on substrate*" systems as presented in this manuscript, the mechanical response obtained by nanoindentation is composite. The complexity lies in the determination of the elastic-plastic properties of the film while avoiding probing the properties of the substrate. For this purpose, there are several methods based on different approaches, often using the ratios a/t or h/t as scale parameters (with a the contact radius, h the penetration depth and t the film thickness).

A first approach is based on a simple analytical description of the problem that consists of expressing the measured composite properties of the sample (E_c, H_c) as a function of the individual properties of the film (E_f, H_f) and substrate (E_s, H_s). It includes:

- various relationships partitioning of the contributions to elastic modulus from the film and substrate [9, 13–15];
- expressions of the form $X_c = X_s + (X_f - X_s)\Phi(x)$ with $X_s = \{E_s, H_s\}$, $X_f = \{E_f, H_f\}$ and Φ a weight function depending on $x = \{a/t, h/t\}$, as in [16, 17] for the elastic modulus and in [18–21] for the hardness;
- laws of mixtures for hardness of the form $H_c = fH_f + (1-f)H_s$ as proposed in [22] where $f = A_f/A_{tot}$ and $(1-f) = A_s/A_{tot}$ are the fractions of the contact carried by the film and the substrate respectively. Another similar law but based on deformed volumes beneath the tip instead of areas was also developed [23], where $f = V_f/V_{tot}$ and $(1-f) = V_s/V_{tot}$ are the fractions of the deformed volumes of the film and the substrate respectively.

A second approach consists in solving the Boussinesq mixed-boundary problem (concentrated force acting on the surface of an elastic half-space) in the axisymmetric framework of the indentation by a rigid body of an elastic film perfectly bound to an elastic substrate. This leads to the resolution of a second kind Fredholm integral equation. Exact solutions to this elastic contact problem have been obtained numerically in the form of Chebyshev series [24] or based on Green's function [25]. The hardness and elastic modulus of the film can then be calculated by different methods. For example, the method of Han *et al.*, which is based on the elastic solutions of Yu *et al.* [24], allows to determine the contact area during indentation and finally the hardness of the film, provided that the elastic properties of the film and the substrate are known *a priori*. Another method based on the elastic analysis of Yu *et al.* [24] is proposed by Li and Vlassak [26]. It allows to estimate the contact area with a method analogous to that of Oliver-Pharr for bulk materials [4] but for the elastic-plastic indentation of a thin film bound to a substrate. Then, both hardness and elastic modulus of the film can be derived.

The last approach that can be reviewed is the numerical approach which essentially consists of parametric calculations by the Finite Element Method (FEM) to reproduce the experimental indentation curves and thus access the properties of complex systems [27–31].

Most of the work resulting from these three approaches requires knowing the properties of

the substrate to determine those of the film, and also having at least one point of contact area measurement by AFM imaging.

1.2.2 Representative stress and strain

Around the 1950s, Tabor [32, 33] proposes a method to determine the mechanical constitutive law (uniaxial stress-strain curve) of materials from indentation tests (load-depth curves). On the one hand, he shows that a representative stress σ_r can be calculated from the hardness H of the material measured by indentation as:

$$\sigma_r = \frac{H}{c} \tag{1.8}$$

with c a constant of about 3 and σ_r corresponding to the yield strength for a rigid perfectly plastic material, where the plasticity domain is located all around the indenter. On the other hand, he introduces a representative strain ϵ_r which in the case of indentation with a self-similar tip (conical and pyramidal indenters such as Berkovich tips) depends only on the semi-angle θ of the equivalent cone:

$$\epsilon_r = 0.2 \cot(\theta) \tag{1.9}$$

The representative strain caused by a self-similar tip is thus constant during the indentation and is about 7 % for a Berkovich indenter. Through this approach, a constitutive law can be derived, but using several tips with different angles in the case of self-similar indentation since a loading curve corresponds only to one point of coordinates (ϵ_r, σ_r) on a stress-strain curve. Tabor's empirical results are also valid for rigid-plastic materials with power-law hardening, as verified by Larson [34] with a finite element study, but are no longer applicable when elasticity has to be taken into account.

Johnson [35, 36] extended this approach to the case of elastic-plastic materials by assuming a spherical expanding cavity under the effect of a hydrostatic pressure. He obtained a new expression where the hardness is function of the yield strength, the elastic modulus and the tip angle.

Following Johnson's work [35, 36], several other models have been developed [37]. For example, Kermouche *et al.* [38] proposed analytical solutions for self-similar indentation of elastic-plastic materials that was validated by finite element simulations. He gives expressions for representative stress and strain as a function of hardness, elastic modulus and tip angle, based on the assumption of defining a linear elastic solid that has the same indentation pressure as the material indented.

Still recently, this concept of representative stress and strain continues to be developed, such as the model of Galanov *et al.* [39] which refines that of Johnson [35, 36] and generalizes it to a wide class of materials.

1.2.3 Inverse analysis

In instrumented nanoindentation, the inverse analysis gathers the methods consisting in identifying the mechanical behavior of the indented material (stress-strain curve) from the experimental indentation curve (load-depth curve). Concerning the determination of the elastic-plastic properties, most of these methods simulate by FEM the indentation test with a consti-

tutive law $\boldsymbol{\sigma} - \boldsymbol{\epsilon}$ representative of the indented material, chosen *a priori*. It is a parametric study on the constitutive parameters (i.e. the mechanical properties to be determined) to obtain a set of indentation curves which are then compared to the experimental one. The material properties are finally deduced from the simulated mechanical responses closest to the experiment.

In sharp nanoindentation (pyramids and cones) of elastic-plastic materials with strain hardening, two types of pioneering work have been done. The first are those of Giannakopoulos *et al.* [40] and Larsson *et al.* [41] around the 1995s, who numerically analyzed indentation tests using FEM. The second are conducted by Cheng and Cheng [42–44] in the late 1990s, who derived scaling relationships between indentation data (stiffness, contact area, hardness, ...) and material properties (elastic modulus, yield strength, strain hardening exponent, ...) by dimensional analysis based on the Π-theorem [45].

In 2001, Dao *et al.* [46] were the first to use an inverse analysis algorithm based on dimensionless functions and FEM simulations to determine the parameters of an elastic-plastic law from the experimental indentation curve. Their study concerns the sharp indentation of materials whose behavior can be modeled by an isotropic linear elastic law for the elastic domain and by a Hollomon-type power-law hardening [47] for the plastic domain:

$$\sigma = \begin{cases} E\epsilon & \text{for } \sigma \leq \sigma_y \\ K\epsilon^n & \text{for } \sigma > \sigma_y \end{cases} \tag{1.10}$$

with E the elastic modulus, σ_y the initial yield strength, $K = \sigma_y(E/\sigma_y)^n$ the strength coefficient and n the strain hardening exponent. The mechanical behavior of such a material is thus fully described with three properties: E, σ_y and n (Poisson's ratio is set). The dimensionless functions of Dao *et al.* [46] relate these properties to quantities that can be extracted from the indentation curve alone (see Figure 1.1b), such as:

- its curvature C assuming that the mechanical response of the material during loading follows Kick's law $L = Ch^2$ [48];
- the contact stiffness $S(h_{max})$ at the maximum indentation depth h_{max};
- the ratio h_{fin}/h_{max} with h_{fin} and h_{max} the residual and maximum indentation depths respectively;
- the irreversible work fraction W_{irr}/W_{tot} where $W_{tot} = W_{rev} + W_{irr}$ with W_{tot} the total work during loading, W_{rev} the released (elastic) work during unloading, and W_{irr} the stored (plastic) work.

Note that the quantities W_{irr}/W_{tot} and h_{fin}/h_{max} are interdependent, but that the first three listed quantities are independent. Thus, at most three material properties could be determined, which would be sufficient for the constitutive laws presented in Equation 1.10.

However, Casals and Alcala [49] show in 2005 that this inverse problem is not bijective and that there are generally not one but rigorously two solutions (two materials with different properties can lead to the same indentation curve). To identify the correct set of properties, they propose an additional enrichment to the indentation curve by verifying the topology of the residual imprint with *post mortem* imaging. Indeed, these two numerical solutions lead to sufficiently different topologies (sink-in or pile-up) to be differentiable from an experimental measurement.

To ensure the uniqueness of the solution, Bucaille *et al.* [50] and Chollacoop *et al.* [51] use an inverse method similar to that of Dao *et al.* [46] but with two conical indenters of

different angles. Bucaille *et al.* [50] suggest to use indenters of semi-angle 70° (equivalent to a Berkovich tip) and 60° which is the limit they estimate below which the tip/sample friction is not negligible anymore. The idea is to associate a representative strain (with the same meaning as Tabor's [33]) to obtain two points on the stress-strain curve. Thus, the effect of the strain hardening n can be easily decorrelated from the effect of the yield strength σ_y.

Since this founding work, the inverse analysis has been extended to other yield criteria than that of Von Mises [52], such as that of Drucker-Prager [53] which takes into account the effect of hydrostatic pressure. It is the case of the studies of Charleux [54] or Seltzer *et al.* [55]. They consider elastic-plastic materials without strain hardening, which results in two plastic properties to be identified, as for a Hollomon-type law with a Von Mises yield criterion. These works, as well as more recent ones, are however based on the same analysis methods as Dao *et al.* [46]: dimensionless functions and FEM simulations with an additional information to the loading curve (setting of the elastic modulus, use of several indenters, *post mortem* imaging of imprints, ...).

Finally, two points are important to keep in mind when using inverse analysis from nanoindentation tests to determine material properties:

- The Hollomon type laws have no physical basis. They just mimic a strain hardening behavior by a power law without giving any information on the physical mechanism of the plastic deformation like dislocations in crystalline metals. However, the indentation test can be simulated by imposing physical constitutive laws and checking that the resulting indentation curve matches the experimental one: this is the so-called direct analysis. Crystal plasticity finite element simulations are for example at the heart of direct methods applied to nanoindentation of crystalline metals [56–60], although they are often restricted to ideal samples (single crystals, FCC structure, ...).
- Size effects can be observed in nanoindentation due to small deformed volumes and/or small sample sizes (pillars, islands, ...), referred to as indentation size effects (ISE). The properties of a material at these scales are not necessarily the same as in the bulk material. This is particularly the case of hardness. For example, crystalline metals with few defects may be subject to late plasticity onset and strain gradient plasticity effects (as discussed in detail in Chapter 4), and brittle materials may exhibit large ductility.

1.3 Damage laws and properties

1.3.1 Fracture toughness

For many years, the indentation technique has been used to assess the damage properties of materials, such as their fracture strength σ_f, critical stress intensity factor K_c or critical energy release rate G_c (K_c and G_c also known as "fracture toughness"). The first studies to determine the fracture toughness from indentation tests date back to the 1970s [61, 62]. They were based on the measurement of the length of the so-called radial cracks (see Figure 1.3a) propagating from the edges of the Vickers or Knoop pyramidal indenters in the context of the microindentation of bulk ceramics. Following these works, the generic expression for the toughness K_c as a function of the maximum applied load L_{max}, the radial crack length c_r and the residual stress σ_{res} was derived by Marshall and Lawn [63], Lawn *et al.* [64] and Anstis *et*

al. [65]:

$$K_c = \chi \left(\frac{E}{H}\right)^m \frac{L_{max}}{c_r^{3/2}} + Z\sigma_{res}c_r^{1/2} \tag{1.11}$$

where :

- E and H are the elastic modulus and hardness of the indented material respectively;
- χ is a calibration coefficient which depends on the indenter geometry ($\chi = 0.016$ usually for a Berkovich tip);
- m is a constant ($m = 1/2$ usually);
- Z is the crack shape factor ($Z = 2/\pi^{1/2}$ usually).

This expression is valid for the Berkovich indentation of bulk brittle materials in the case where the radial cracks are well-developed, i.e. are not confined beneath the indenter ($c_r \gg a$ with a the contact radius). Knowing the elastic modulus and hardness of the indented material (e.g., by the methods described in Section 1.2.1) and the crack length (by microscopy techniques) the plot of $\chi(E/H)^m L_{max}/c_r^{3/2}$ versus $Zc_r^{1/2}$ thus provides easy access to the fracture toughness (the intercept with the ordinate axis) and the residual stress (the slope).

Although in some cases Equation 1.11 can be applied for relatively thick films (a few micrometers thick) by adjusting the empirical constants [66, 67], this is not the case for thin films. Indeed, the influence of the substrate deformation on the radial cracking process can no longer be neglected. Moreover, when the substrate is soft, radial cracks are generally confined within the indentation imprint, making this analytical analysis impossible.

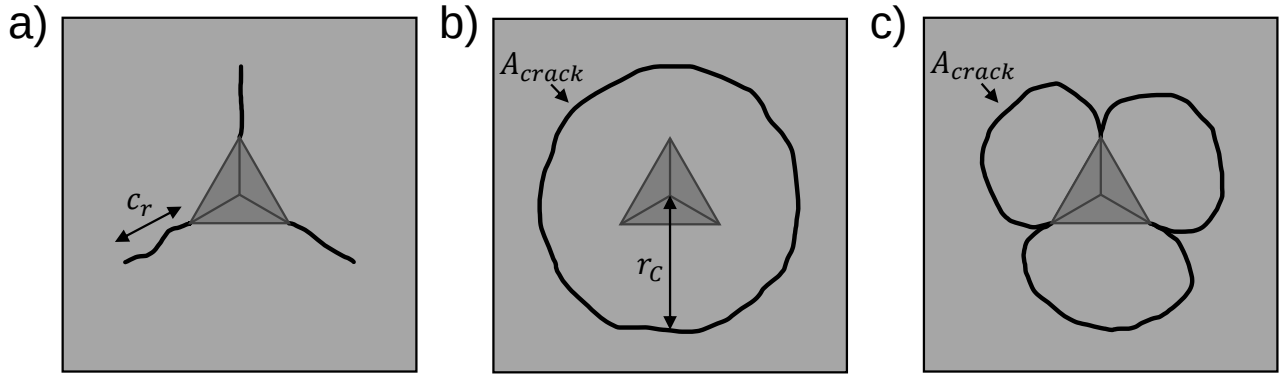

Figure 1.3. Schematics of (a) radial cracks of length c_r generated by a Berkovich tip, (b) unique through-thickness ring-like crack and (c) multiple ring-like cracks.

To overcome this stress field based model which requires empirical adjustments and is difficult to apply to thin film systems, other methods have been developed. This is the case of the energy-based models using the features on the indentation curves generated by the cracking. Indeed, when the tests are load-controlled, cracking can generate a loss of stiffness sufficiently important so that the indentation tip suddenly sinks into the sample. This mechanical instability is visualized on the load-depth curve by a horizontal plateau (displacement jump at a given load) called "pop-in".

A widely used approach is that of Li *et al.* [68, 69], allowing measurement of fracture toughness from through-thickness ring-like cracks as schematized in Figure 1.3b. It was then extended to non-through multiple cracks, which do not propagate perpendicular to the film/substrate interface in spalling events (Figure 1.3c) [67]. The method consists of extrapolating the loading curve between the beginning of the pop-in (supposed to be the onset of fracture) and its end,

as shown in Figure 1.4a. The area ABC is assumed to be the fracture dissipated energy U_{frac}. The toughness K_{Ic} for plane strain mode I fracture can then be calculated by:

$$K_{Ic} = \sqrt{\frac{E_f}{1-\nu_f^2}\frac{U_{frac}}{A_{crack}}} \tag{1.12}$$

with E_f and ν_f the elastic modulus and Poisson's ratio of the film respectively, and A_{crack} the fracture area (for example $A_{crack} = 2\pi r_C t$ for a through-thickness ring crack, where r_C is the crack radius as shown in Figure 1.3b and t is the film thickness).

Nevertheless, the elastic-plastic behavior of the "*thin film on substrate*" system may change due to cracking, which is not considered here. This method was therefore developed by Chen and Bull [70–72] based on the plot of the total indentation work W_{tot} (integral of the loading curve up to a given depth) against the penetration depth h (see Figure 1.4b). First, the $W_{tot} - h$ curve before cracking must be extrapolated from the starting point of the pop-in A to its end point B, to obtain the total work difference BD (fracture dissipated energy plus the work associated with the change in elastic-plastic behavior before and after cracking). Then, the $W_{tot} - h$ curve after cracking must be extrapolated backward from the pop-in end point B to its starting point A, to obtain the work difference AC associated with the change in elastic-plastic behavior before and after cracking only. Finally, the fracture dissipated energy U_{frac} can be calculated by $U_{frac} = BD - AC$, and substituted into Equation 1.12 to determine the fracture toughness. This method has the advantage of being applicable to different types of cracks (ring and radial cracks, delamination, spalling, etc.) but it is subject to several constraints. Indeed, it requires that the fracture generates a pop-in feature, to be able to measure the fracture area, to correctly extrapolate the experimental curves...

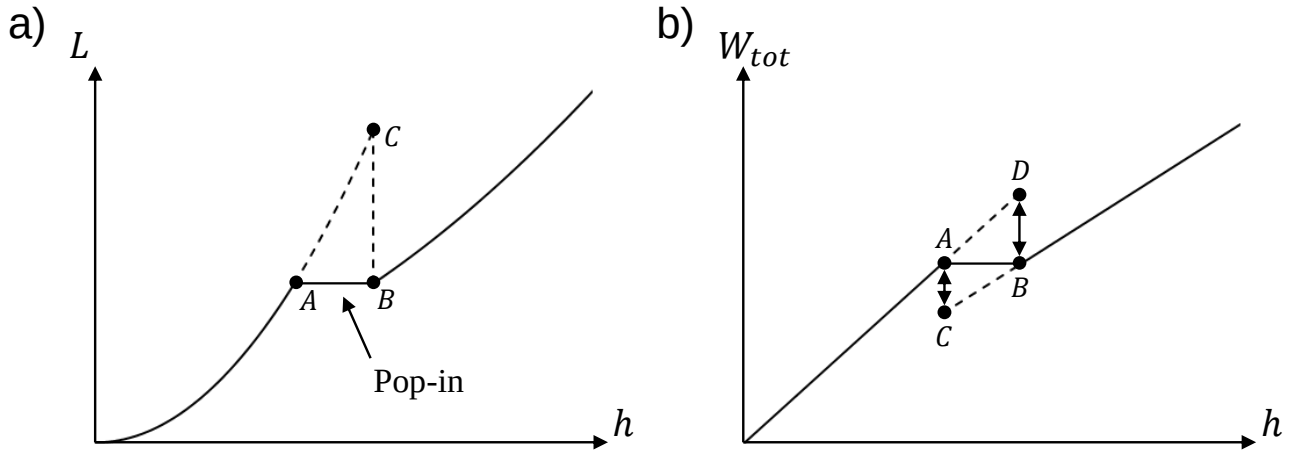

Figure 1.4. Energy-based models for determining fracture toughness based on (a) load-depth curve and (b) total work-depth curve.

Many other analytical models exist, either stress-based or energy-based, to evaluate the fracture toughness of thin films and film/substrate interfaces by nanoindentation [67, 73–75]. However, like the models just described, they present several difficulties such as (not exhaustively): the formation of the crack considered in the model, the measurement of its length or area, the elastic-plastic behavior of the substrate, the multi-cracking of the film, etc. In this context, FEM modeling has been (and still is) widely used to identify the damage properties of thin films.

1.3.2 Cohesive zone models

A very popular computational tool for modeling fracture in FEM simulations are Cohesive Zone Models (CZM), pioneered in the early 1960s by Dugdale [76] and Barenblatt [77], then followed in the early 1990s by Tvergaard and Hutchinson [78], Beltz and Rice [79], and Xu and Needleman [80] among many others [81]. The concept of the CZM is to remove the stress singularity at the crack tip by introducing a zone upstream on which a cohesive force exists and prevents the crack from propagating. This local approach can be physically motivated, for example in brittle materials by considering the surfaces of the crack in the cohesive zone close enough to be regarded as two atomic planes attracted by bonding forces [77]. Constitutive laws called "traction-separation" laws are then defined to describe the evolution of the cohesive traction T as a function of the local separation δ between the cohesive surfaces. They include at least two parameters: the fracture strength σ_f which corresponds to a maximum traction at the onset of damage and the critical energy release rate G_c. From these two material properties, it is possible to calculate a critical separation δ_c from which the cohesive surfaces no longer interact ($G_c = \int_0^{\delta_c} T(\delta)\,\mathrm{d}\delta$). In ceramics, this critical separation is between a fraction and a few nm [82] which corresponds to a cohesive process zone length r_p of several nm [76]. Figure 1.5 presents a schematic of a crack modeled in a cohesive zone model (Figure 1.5a) and an example of a linear traction-separation law (Figure 1.5b). Further details about the cohesive laws are given in Section 2.4.2 of Chapter 2.

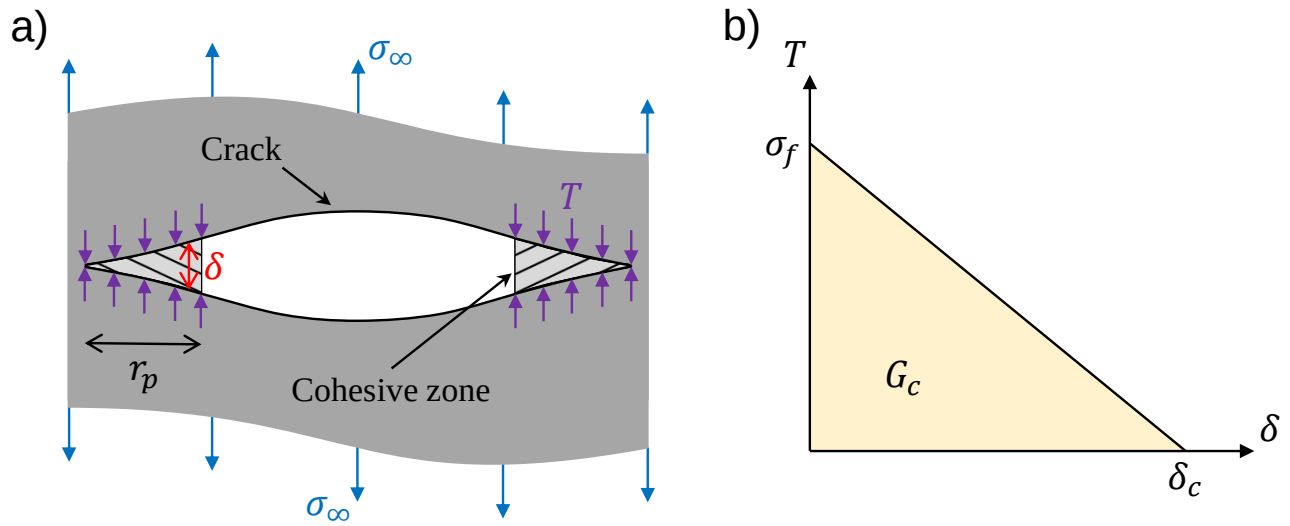

Figure 1.5. (a) Schematic of a crack modeled in a cohesive zone model. (b) Example of a linear traction-separation constitutive law.

These constitutive laws are easily integrable in FEM models when the crack path is predefined, such as at an interface. However, in many cases in nanoindentation, multiple cracks develop in the bulk with unknown trajectories. The treatment of this problem by the conventional finite element method would then require remeshing at each crack advance to match the geometry of the discontinuity. In this context, the eXtended Finite Element Method (XFEM) introduced in 1999 by Belytschko and Black [83] allows to handle dynamic cracking with the same mesh throughout the simulation. It is an extension of the finite element approximation space by local enrichment functions which capture both the singularity (stress around the crack tip) and the discontinuity (jump in displacement across the surfaces), this makes the crack geometry independent of the finite element mesh. XFEM-based cohesive behavior can thus be

used to simulate crack initiation and propagation along an arbitrary solution-dependent path in the bulk materials. Since the 2000s, CZMs integrated in FEM or XFEM simulations have become a standard way to determine the damage properties (typically σ_f and G_c) of thin films from nanoindentation measurements, usually by inverse methods based on the comparison of predicted loading curves with experimental ones [84–90].

1.4 Electrical-nanoindentation

Since the 2000s, many developments have been made to expand the capabilities of instrumented nanoindentation by coupling it to other techniques [91]: Scanning Electron Microscope (SEM) [92, 93] and Transmission Electron Microscope (TEM) [94–96] imaging, high-temperature measurements [97–100], electrochemical analysis [101], multi-field testing [102], etc. Among these advances, the coupling of nanoindentation with through-tip electrical measurements has emerged. This technique (referred to as electrical-nanoindentation, resistive-nanoindentation, conductive-nanoindentation or nano-ECR) was developed in 2007 by Ruffel *et al.* [103] in collaboration with Hysitron Inc. (now acquired by Bruker USA). It consists in applying an electrical potential difference V between the sample and a conductive tip and to measure the current I flowing through the tip, or the contact resistance R, continuously during the indentation. The electrical signals of current $I - h$ or resistance $R - h$ can therefore be monitored simultaneously with the mechanical magnitudes of load $L - h$ and stiffness $S - h$.

Individual contributions to the total measured contact resistance must be identified to quantitatively analyze data from an electrical-nanoindentation test. As long as the electronic transport remains in the diffusive regime, the contact resistance R is the sum of several resistances in series, as shown in Figure 1.6 [12, 103, 104]. In the case of the indentation of a "*thin film on substrate*" system, it can be expressed by the following expression:

$$R = R_{Tip} + R_{Film} + R_{Substrate} + R_{Set-up} \tag{1.13}$$

where:

- R_{Tip} is the resistance of the tip. Generally, electrical-nanoindentation tips are made of Boron-Doped Diamond (BDD) which ensures an ohmic behavior with a resistivity in the range $[0.1, 10]$ Ω.cm. In the case of self-similar geometries such as the Berkovich one, the tip resistance is proportional to the ratio of its resistivity to the contact radius [105].
- R_{Film} and $R_{Substrate}$ are the resistances of the film and substrate respectively. Their evolution during the indentation and their value depend on the electrical behavior of the materials composing the film and the substrate.
- R_{Set-up} is the resistance of the set-up. This is a constant resistance during the indentation that comes from the experimental set-up (wires, connectors, tip brazing, etc.).

In the case of indentation of insulating thin films on conductive substrates, the resistances of the substrate and the tip can be neglected. This makes the electrical-nanoindentation technique sensitive only to the electrical properties of the film and the rheology of the "*film on substrate*" system. It is on this principle that the analysis of the electrical behavior of the films studied in the present PhD is based.

The motivations for coupling nanoindentation with through-tip electrical measurements are numerous and cover a wide range of applications, as evidenced by the recent (2021) and comprehensive review of George *et al.* [106]. Non-exhaustively, it can be mentioned the local

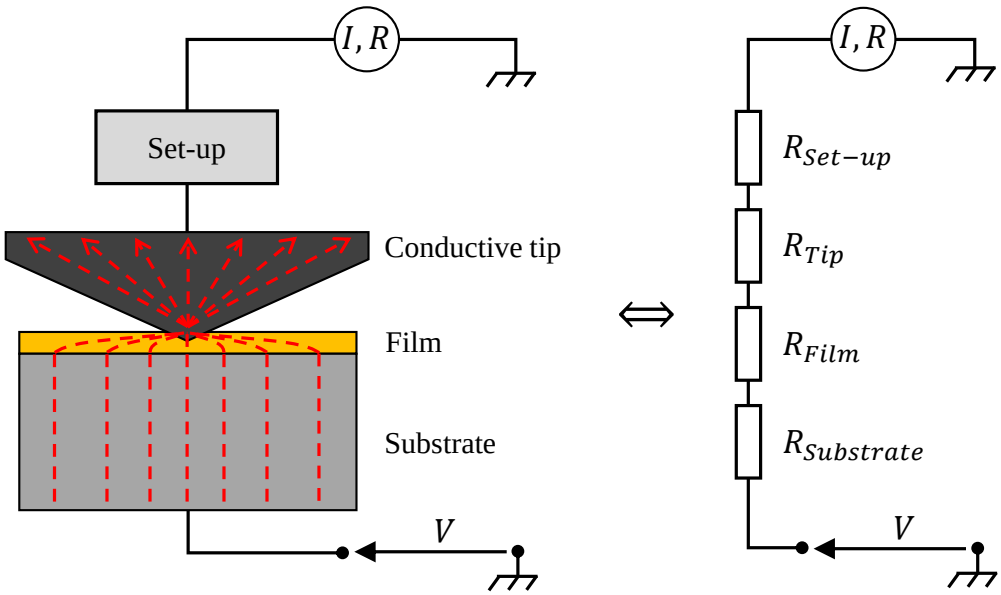

Figure 1.6. Schematic of the individual contributions to the measured contact resistance and the equivalent electrical circuit diagram of the series arrangement of resistances for the indentation of "*film on substrate*" system.

monitoring of phase transformations [103, 107], the study of fracture [108] and delamination [109] of ceramic films, the characterization of piezoelectric materials [91, 110–112], the local measurement of dielectric properties of thin films [113], or the computation of contact area during indentation tests [12, 104, 114] as discussed in Section 1.2.1.

Among all these applications, a few allow the estimation of dielectric material properties such as the effective piezoelectric coefficient [112] or the dielectric constant [113]. However, none of them allow the identification of constitutive laws of electrical conduction (relations between the current density $\boldsymbol{J}$ and the local electric field $\boldsymbol{F}$ [115]) and their parameters. A large part of this PhD work is therefore devoted to this, in an analogous way to the identification of $\boldsymbol{\sigma} - \boldsymbol{\epsilon}$ mechanical constitutive laws, by an approach coupling nanoindentation experiments and FEM simulations.

Chapter 2

Failure of a Brittle Layer on a Ductile Substrate: Nanoindentation Experiments and FEM Simulations

This chapter is based on the following paper published in the "*Journal of the Mechanics and Physics of Solids*":

M. Rusinowicz, G. Parry, F. Volpi, D. Mercier, S. Eve, U. Lüders, F. Lallemand, M. Choquet, M. Braccini, C. Boujrouf, E. Hug, R. Coq Germanicus, M. Verdier. Failure of a brittle layer on a ductile substrate: Nanoindentation experiments and FEM simulations. *Journal of the Mechanics and Physics of Solids* **163** (2022), 104859.

It reports the mechanical study of a microelectronic-dedicated stack of a silicon nitride (Si_3N_4) passivation layer deposited on a thick aluminum alloy (AlSiCu) electrical connection layer. An energy-based methodology using features on the loading curves is proposed to determine the damage properties of the brittle film and elucidate the cracking process.

This work is the result of a collaboration with the CRISMAT laboratory of the Normandie Université (France). On the one hand, the processing of the multilayer system, the measurement of the thickness of the films and the verification of their chemical composition were managed by the CRISMAT lab outside the context of this thesis. On the other hand, the nanoindentation tests, the imaging of the residual indent imprints and the numerical simulations were carried out within the framework of the present PhD at the SIMaP laboratory.

2.1 Introduction

In the field of functional applications, devices are manufactured using planar technologies that proceed with successive cycles of film deposition, patterning and etching processes. This process flow results in complex stacks of thin films that combine different families of materials (semiconductors, dielectrics, metals) with dissimilar properties. A typical example of such multilayer stacks can be found at the top surface of most microelectronic chips, where a silicon nitride (Si_3N_4) film is generally deposited on top of the whole device stack at the final processing step. This layer is an efficient passivation layer against moisture and ambient contaminants [116–120]. In standard process flows, it is deposited by Plasma Enhanced Chemical Vapor Deposition (PECVD) [119, 121, 122], and fully covers the wafer surface. Depending on the device layout, the dielectric Si_3N_4 film can be locally deposited on top of a metallic alloy ("*brittle on ductile*" stack) or another dielectric film ("*brittle on brittle*" stack). During processing, wafers are subjected to mechanical stresses induced by packaging processes (grinding, dicing, bumping, ball dropping, cleaving or sawing) [123, 124] and to thermal stresses that build up during device operation [125–127]. These stresses may initiate and propagate some mechanical cracks that can lead to device failures. Preventing stress-induced failures requires to properly apprehend the mechanical behavior of multi-material stacks. Especially, a robust design of these systems requires the quantitative knowledge of the fracture properties of constitutive layers. In the literature, the mechanical properties of Si_3N_4 layers with different under-layers have been explored for mechanically hard sub-layers (silicon, fused silica, germanium and sapphire) [128], owing a strong influence of the substrate on hardness measurements. To the best of our knowledge, the mechanical properties on mechanically soft under-layers were studied only very scarcely. Scafidi and Ignat [129] have studied the crack propagation with *in situ* tensile tests of PECVD Si_3N_4 deposited on Al substrates, focusing on the different steps of the damage using a simplified analytical approach with a shear lag model. Nevertheless, in the context of high-integrated microelectronic devices, for optimizing the process flow, investigation is needed to determine the critical tensile stress of deposited Si_3N_4 as coating layer.

The mechanical behavior of thin film stacks is a cornerstone question that numerous application fields have to address, as for the development of microelectronic chips, solar cells, embedded power devices, optical lens functionalization, thermal barrier coatings, and surface hardening of cutting tools. However, measuring material properties of such structures remains a difficult task, because of their composite response. In terms of experimental means, nanoindentation is a mechanical testing technique well suited for the determination of the intrinsic mechanical parameters of single materials [130] or thin films deposited on a substrate [26, 70, 131, 132]. Nanoindentation shows to be particularly useful for investigating the properties of multiple stacks [72, 133]. The measurement of hardness and elastic modulus from nanoindentation can be obtained in both cases of "*hard coating on softer substrates*" [134] and of "*soft coating on harder substrates*" [135], but numerical simulations are required to identify the material properties from experimental data [30, 136]. The problem of determining the fracture properties (i.e. fracture strength, fracture toughness) of coatings is even more challenging. Although there is no standard test procedure to date, there are however several methods to access these quantities, either stress-based or energy-based [137]. Indenting the coating to propagate cracks is maybe the most widely used method but has some inherent difficulties such as (non exhaustively) the formation of the precrack, the determination of the crack length, the critical failure stress, and the development of plastic deformations in the substrate during loading

process. In this context, modeling by the Finite Element Method (FEM) can be used to simulate crack initiation and propagation during indentation, and to compare the loading curves obtained numerically to the ones obtained experimentally, for identifying key parameters such as the fracture toughness of the coatings [85, 87, 138].

In the present study, the analysis of the fracture behavior of a Si_3N_4/AlSiCu/SiO_2/Si multilayer system under nanoindentation is reported. The evidence of successive displacement bursts ("pop-in") can be observed on the loading curves. Numerical FEM calculations are carried out accounting for: (i) plastic deformation in the AlSiCu layer, (ii) crack initiation and propagation inside the Si_3N_4 layer, using eXtended-FEM (X-FEM) combined with a cohesive behavior of the cracks, (iii) a possible delamination at the Si_3N_4/AlSiCu interface using a cohesive zone model. The behavior of the AlSiCu underlayer in the plastic deformation regime is also identified by fitting parameters in FEM simulations using nanoindentation results and *post mortem* images of imprints.

The various stages of the damage process occurring in the Si_3N_4 layer are elucidated thanks to numerical simulations, showing in particular the occurrence of a first crack in the region underneath the indenter (hence not visible by a surface observation), followed by a second crack forming on the top surface of the layer, further from the indenter. Moreover, a novel procedure for the identification of the Si_3N_4 layer tensile strength is presented, using an inverse method based on FEM simulations and experimental data. This approach uses the distance of the first crack to the indenter axis as well as the tensile strength as parameters involved in the optimization procedure. The consistency with experimental data is extremely good and allows to narrow down the possible values of the tensile strength. Finally, the results of simulations (cracking patterns and crack locations) are also further validated using a Scanning Electron Microscope (SEM) cross-section view of the sample. The identification procedure is quite generic and can be adapted to other systems showing similar multiple-cracking patterns under indentation.

2.2 Experimental details

2.2.1 Samples

The investigated structure is a multi-material film stack usually designed in microelectronic chips for high-integrated systems. The starting material is a (001)-oriented 6" single crystal silicon wafer with a thickness of 675 µm. After substrate cleaning, a 450 nm thick SiO_2 layer was deposited by PECVD followed by the sputtering of $Al_{98.96}Si_{1.00}Cu_{0.04}$ (AlSiCu) polycrystalline metallic alloy. Finally, a Si_3N_4 amorphous film was deposited by PECVD at low temperature (about 400 °C) using a SiH_4/NH_3 gas mixture. The deposition rate was about 0.2 µm/min with a SiH_4/NH_3 flow ratio of 0.15. The RF power was optimized at 400 W with a chamber pressure of 2.7 Torr. The layer thickness and chemical compositions were verified by SEM and Energy Dispersive X-ray (EDX) analysis. A SEM cross-sectional view of the sample is shown in Figure 2.1. The thickness of the deposited AlSiCu and Si_3N_4 films were 3.0 ± 0.1 µm and 1.3 ± 0.1 µm, respectively.

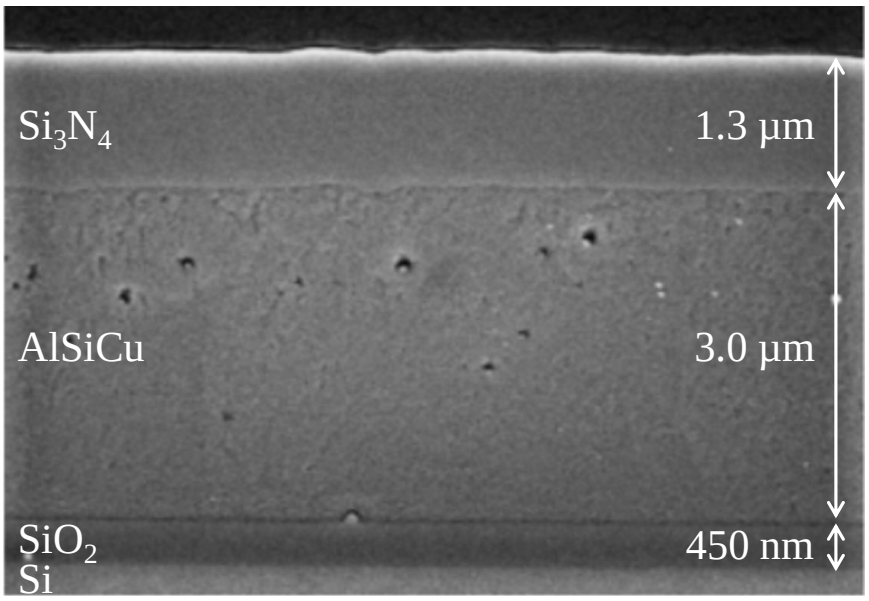

Figure 2.1. Cross-sectional SEM view of the investigated structure.

2.2.2 Experimental techniques

Two nanoindentation systems were used. The first apparatus was an InForce 50 actuator (from Nanomechanics Inc./KLA-Tencor) integrated into a home-made set-up and the second one was an MTS Nano Indenter XP. Both apparatuses operate in a load-controlled mode. The tests were performed at a strain rate of 0.05 s^{-1} with diamond Berkovich tips (nominal tip radius of ≈ 20 nm) and Continuous Stiffness Measurement (CSM) mode, the latter allowing continuous hardness and elasticity extraction during indentation. Spacing between indents was fixed to several tens of µm, thus avoiding any overlapping of deformation fields. The displacement data were corrected from drift rate which was re-evaluated before or after each test. Residual nanoindentation imprints were essentially observed by SEM, before or after Focused Ion Beam (FIB) milling. Two systems were used: a FIB Cross Beam NVision 40 from Carl Zeiss (Ga source with an acceleration voltage of 30 kV and current intensity of 300 pA) and a SEM Zeiss Supra 55 operated at 5 kV. Imprint observations were also performed by Atomic Force Microscopy (AFM) on an AFM ICON (Bruker, Corporation, USA) in the scan-asyst mode.

2.3 Experimental results

2.3.1 Nanoindentation tests

Figure 2.2 shows representative loading curves obtained from the indentation of the Si_3N_4/ AlSiCu/SiO_2/Si stack (load versus penetration depth normalized by the Si_3N_4 film thickness). Figures 2.2a and 2.2b report the data from tests performed at maximum loads of 15 mN and 45 mN, respectively. Significant displacement jumps at constant load, called "pop-in" events, can be observed on these curves. As nanoindentation tests are performed in a load-controlled mode, these horizontal plateaus correspond to abrupt displacement bursts of the indenter into the sample when the sample compliance suddenly changes. Two pop-ins can be distinguished in Figure 2.2b. The first pop-in starts for a critical (depth, load) dataset of ($h_{c1} = 266 \pm 21$ nm, $L_{c1} = 11.8 \pm 1.1$ mN) and ends at a final depth of $h_{f1} = 356 \pm 46$ nm. For the second pop-in, values are much more dispersed: $h_{c2} = 694 \pm 116$ nm, $L_{c2} = 23.1 \pm 3.6$ mN, $h_{f2} = 790 \pm 86$ nm.

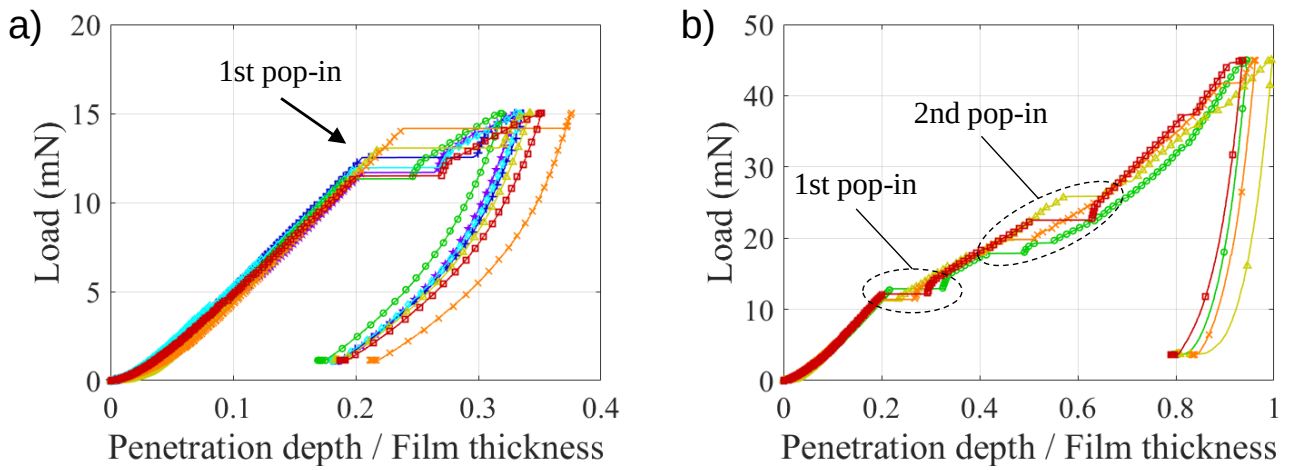

Figure 2.2. Representative experimental nanoindentation curves revealing large pop-in events. (a) Maximum load = 15 mN. (b) Maximum load = 45 mN.

2.3.2 SEM observations

Generally, pop-in events can be the signature of different phenomena such as the onset of plasticity [139], stressed-induced phase transformation [140], twinning [141], or film cracking [68, 70]. In "*brittle film on elastic-plastic substrate*" stacks, pop-in events are often caused by the fracture of the film and/or of the film/substrate interface. *Post mortem* images of indented zones were taken to identify which cracking mechanism occurred. Figures 2.3a and 2.3b present SEM top-views of indented zones with maximum loads of 15 mN and 45 mN, respectively. From Figure 2.3a, no signature of the indent can be observed for tests performed at 15 mN. On the contrary, a complex residual imprint is observed after 45 mN tests (Figure 2.3b): a central hole is surrounded by peripheral cracks. A cross-section of this imprint obtained by FIB-milling along the dotted line (Figure 2.3c) clearly revealed the damage of the Si_3N_4 film by cracking. The cracks, which display a concentric distribution centered on the indentation axis, can be classified into two types:

- ① cracks between the Si_3N_4/AlSiCu interface and the tip apex imprint. Located at about $1.0-1.5$ µm from the indentation axis at the Si_3N_4/AlSiCu interface, they converge towards the tip apex imprint without emerging at the film surface;
- ② orthoradial cracks visible on the film surface and extending into the film thickness with a "comma-shape".

The objective of the study is to identify by FEM modeling the origin of the two pop-ins observed on the nanoindentation curves and to relate them to the cracks observed on the cross-section view. More generally, this work aims at defining a methodology to determine the damage properties of a "*brittle film on ductile substrate*" from the experimental loading curves only.

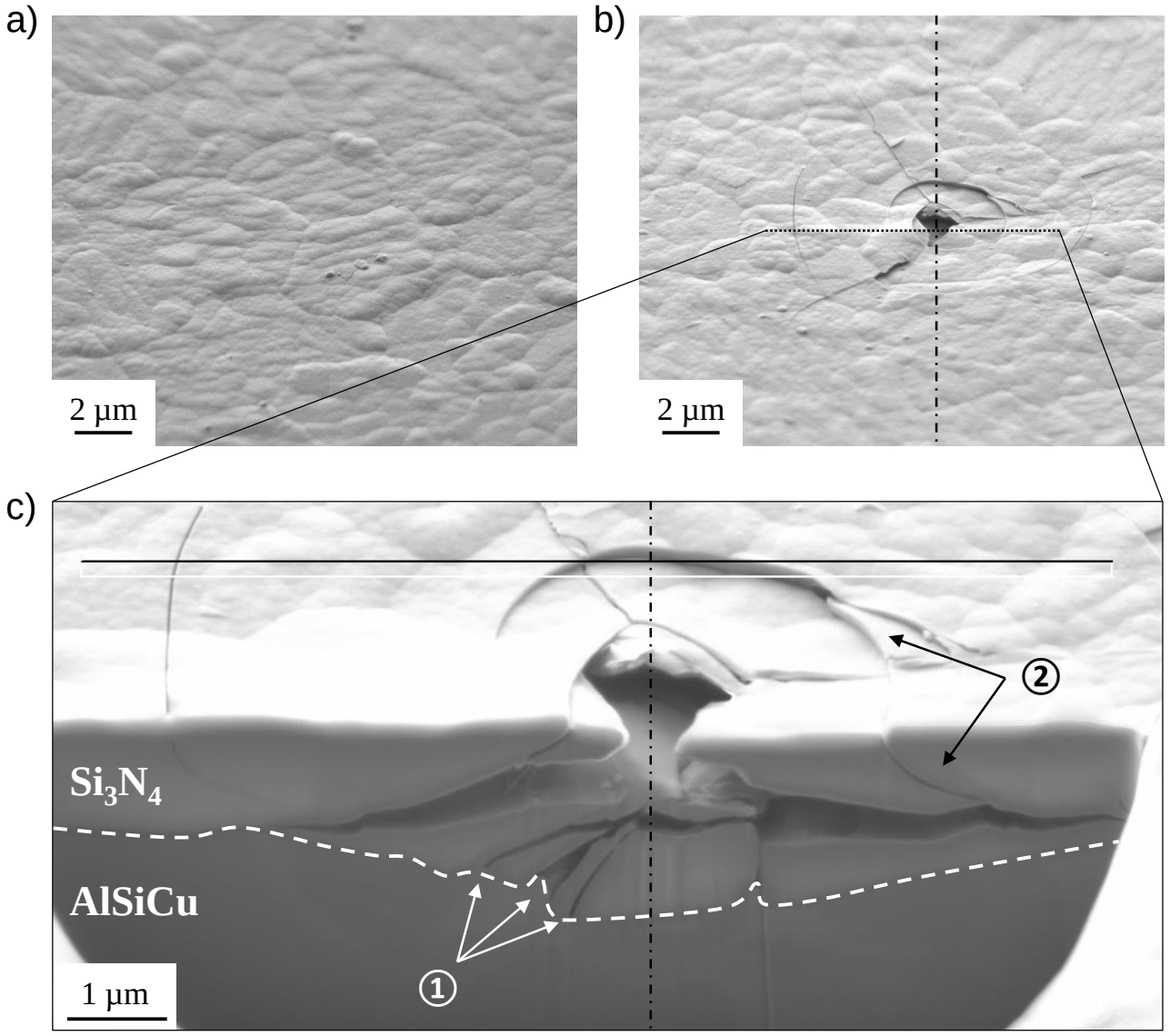

Figure 2.3. SEM views of residual imprints of indents corresponding to the loading curves of Figure 2.2. (a) Top-view after an indent up to 15 mN. (b) Top-view after an indent up to 45 mN. (c) Cross-section view after FIB-slicing of imprint of Figure 2.3b.

2.4 FEM modeling of cracking under nanoindentation

2.4.1 Global presentation of the FEM model

The mechanical model is set up in a 2D axisymmetric framework. It consists of one "indenter" brought into contact with the "sample" by a prescribed displacement applied to the indenter (the model is depicted in Figure 2.4). With this approach, the nanoindentation tests are performed in a displacement-controlled mode. The indenter is modeled as an analytical rigid body. Its conico-spherical profile is designed to fit the area shape function $A_c(h_c)$ of a Berkovich indenter (where A_c is the indenter section at a distance h_c from the tip apex). The opening angle of the indenter is 70.32°.

The sample is modeled as a stack of three layers and a substrate which are (from top to bottom in Figure 2.4):

- A 1.3 µm thick Si_3N_4 layer, with an isotropic linear elastic behavior.
- A 3 µm thick AlSiCu layer, elastic–plastic. It is assumed to be isotropic linear in the

elastic regime. In the plastic regime, an isotropic hardening is considered, following a Hollomon type power law:

$$\sigma_y = \sigma_{y0} + k(\epsilon_p^{eq})^n \tag{2.1}$$

- A 0.5 µm thick SiO_2 layer, with an isotropic linear elastic behavior.
- A 6 µm thick Si substrate, with an isotropic linear elastic behavior.

The simulation cell was taken wide enough so that the stress/strain fields generated inside the sample during indentation do not interact with the outer boundary (global radius of 15 µm, as reported in Figure 2.4). Moreover, it was checked that taking a thickness of 6 µm for the Si wafer in the computation cell was sufficient (due to the high rigidity of this substrate).

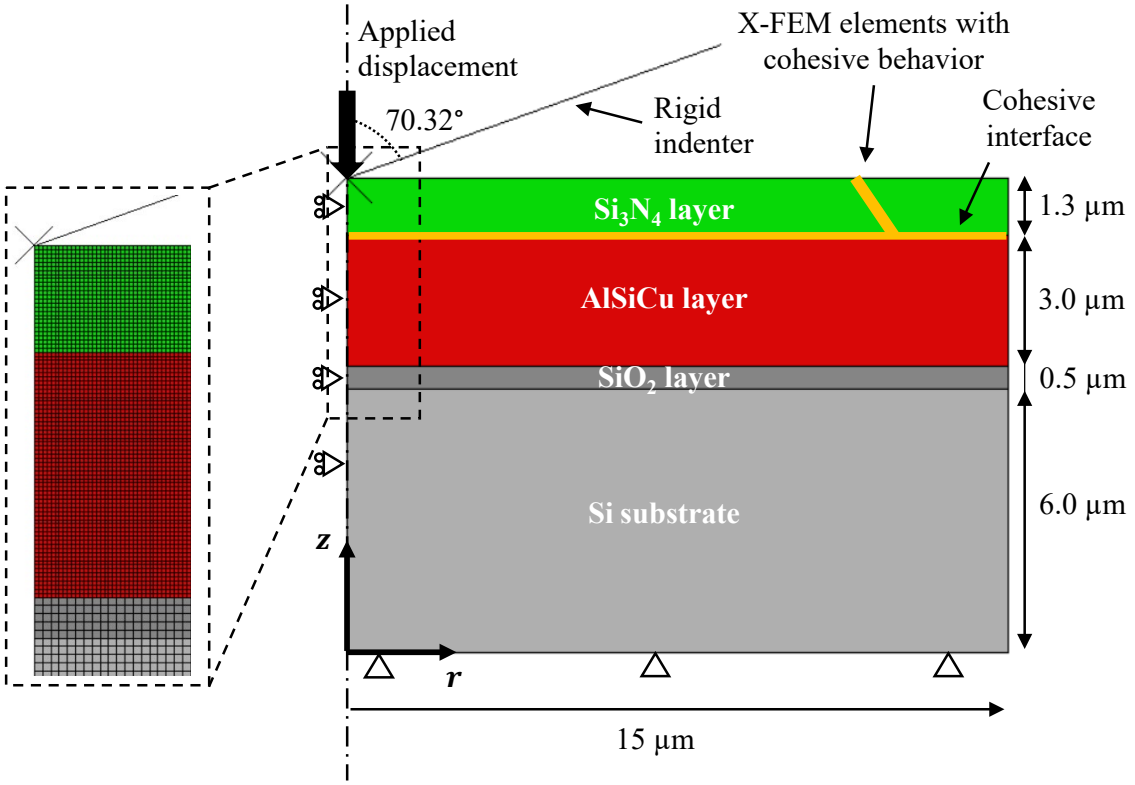

Figure 2.4. Model for the FEM calculations of cracking under nanoindentation.

2.4.2 Structure cracking: cohesive zone modeling

In addition to elastic and plastic material behaviors, crack initiation and propagation were accounted in the calculations, both inside the Si_3N_4 layer and at the Si_3N_4/AlSiCu interface. The fracture was described using a cohesive zone model (e.g. among many others: Tvergaard and Hutchinson [78] and Xu and Needleman [80]).

The cohesive behavior of cracks is characterized in our case by an irreversible bilinear softening model (Figure 2.5): when opposite crack faces in the cohesive zone undergo relative normal displacement δ_n, a normal traction $T_n = K\delta_n$ develops at the interface where K is the stiffness (pure mode I). Given the cohesive traction T_n^0 and the work of fracture G_{Ic}, the displacement at full fracture δ_n^f is defined by $G_{Ic} = 1/2\ T_n^0\delta_n^f$. Adhesion irreversibility is modeled by a damage variable d which increases monotonically from 0 to 1 as the maximum interfacial displacement δ_n^{max} increases from $\delta_n^0 = T_n^0/K$ to δ_n^f. Damage affects the cohesive zone by reducing the stiffness by a factor $1-d$ so that $T_n = K(1-d)\delta_n$ which is zero if the surfaces are brought back into

contact after full fracture (simple frictionless unilateral contact). A similar model is applied for pure mode II, with work of adhesion G_{IIc} and cohesive traction T_t^0. In our case, the total work of fracture G_c, which is the sum of G_{Ic} and G_{IIc}, is assumed to be independent of the mode mix (i.e. the dissipated energy associated with full crack opening always takes the value G_c that we prescribe, irrespective of the particular way this opening is performed).

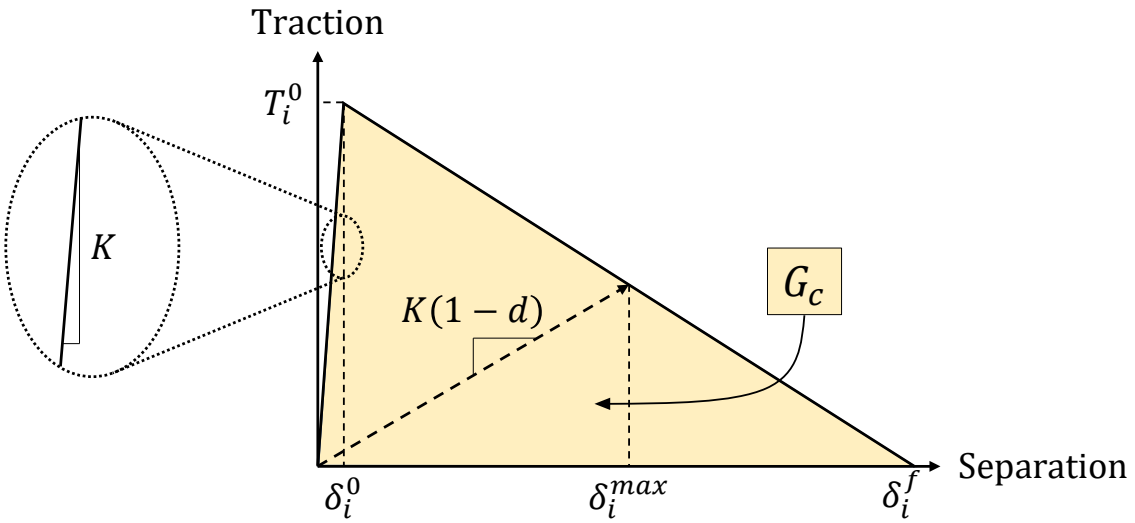

Figure 2.5. Traction versus separation law for the cohesive zone description of fracture ($i = n$ for mode I and t for mode II).

For the Si_3N_4 layer, as well as for the Si_3N_4/AlSiCu interface, the three material parameters to be defined are T_n^0, T_t^0 and G_c. These quantities will be denoted $T_n^{0,int}$, $T_t^{0,int}$, G_c^{int} for the interface and $T_n^{0,lay}$, $T_t^{0,lay}$, G_c^{lay} for the Si_3N_4 layer.

The finite elements implementation of the above described mechanical model was carried out with the FEM software ABAQUS®. The crack propagation was implemented using a Cohesive Zone Model (CZM), within a "cohesive interaction" framework. Instead of using cohesive elements, this technique uses a contact algorithm including the definition of a cohesive behavior (as defined above). This is hence a surface to surface interaction. The crack initiation criterion chosen for the interface is a quadratic criterion on the traction components:

$$\left(\frac{T_n}{T_n^{0,int}}\right)^2 + \left(\frac{T_t}{T_t^{0,int}}\right)^2 = 1 \tag{2.2}$$

Regarding the crack in the Si_3N_4 layer, the "cohesive segments method" implemented in ABAQUS® was used. This approach is developed within the framework of X-FEM, based on classical shape functions enriched with the Heaviside step function across the crack surface. The crack opening follows the cohesive traction-separation law described above. The maximum principal stress criterion was chosen for crack initiation:

$$\frac{< \sigma_{max} >}{\sigma^{0,lay}} = 1 \tag{2.3}$$

The $< . >$ symbol means that the crack is only triggered if σ_{max} is positive (tensile stress). The main advantage of this method is that the crack path does not have to be pre-defined. Indeed, once the maximum principal stress criterion is reached within an element, a crack is initiated in the direction normal to the maximum tensile stress direction. In this case, $\sigma^{0,lay}$ is actually introduced as a material parameter, whereas $T_n^{0,lay}$ and $T_t^{0,lay}$ are subsequently

computed at the increment when the criterion is met. This crack description allows both crack initiation and propagation. However, an initial location of an enriched feature is sometimes defined to study the influence of crack location.

The problem contains four sources of non-linearities: (1) in geometry, due to large deformations (particularly underneath the indenter), (2) in the AlSiCu material behavior due to plasticity, (3) for the contact developing between the indenter and the surface of the Si_3N_4 layer and (4) due to the loading path dependent crack propagation. An implicit dynamic time integration procedure is therefore used to calculate the quasi-static response of the system, using the ABAQUS®/standard solver. A Hilber-Hughes-Taylor time integration procedure is carried out (an extension of the Newmark β-method). The Hilber-Hughes-Taylor operator is implicit. The set of simultaneous non-linear dynamic equilibrium equations are solved iteratively using Newton's method. Finally, the elements are 4-node bilinear, reduced integration with hourglass control (CAX4R in ABAQUS®), possibly enriched in the Si_3N_4 layer to model cracks. Elements size in the Si_3N_4 and AlSiCu layers is set at 50 nm.

2.4.3 Identification of the parameters for AlSiCu plasticity

Nanoindentation tests were performed directly on the AlSiCu film after removal of the Si_3N_4 film to access the AlSiCu mechanical properties. A typical experimental loading curve is reported in Figure 2.6a. The AlSiCu behavior was identified on this experimental curve. The system without the Si_3N_4 was modeled similarly to the method presented in Section 2.4.1. A schematic is depicted in Figure 2.7. The plastic behavior of the AlSiCu film is described by a Hollomon-type power law expression, as specified in the previous section (see Equation 2.1). Three scalar parameters (σ_{y0}, k and n) have to be identified to accurately model the material work-hardening. For this purpose, loading curves are obtained from FEM numerical simulations, and compared to the experimental one (Figure 2.6a). The loading and boundary conditions used in these calculations are quite similar to those described in Figure 2.4, except that there is no Si_3N_4 top layer, hence no crack modeling. The three plastic parameters were obtained using the least-squares method to minimize the summed square of residuals between the experimental and simulation load-displacement curves [142]. Those parameters are provided in Table 2.1. Finally, it was checked that the contact area between the nanoindentation tip and the AlSiCu layer is consistent between experimental and numerical data (Figures 2.6b and 2.6c).

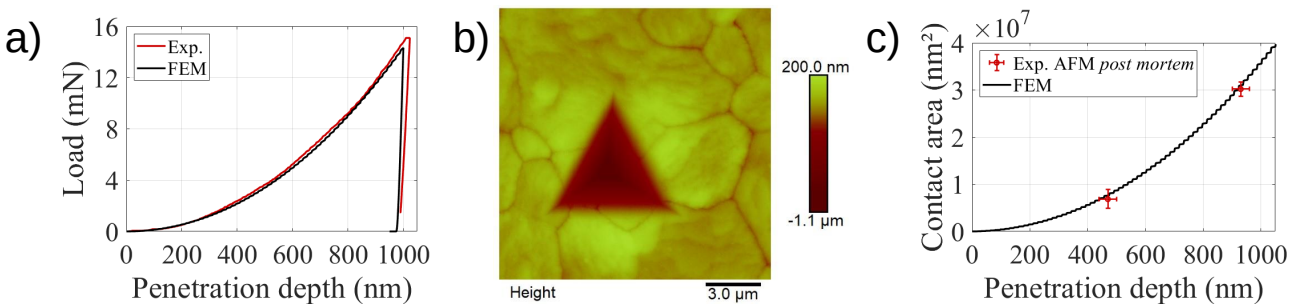

Figure 2.6. (a) Load versus displacement curve for a nanoindentation test carried out on the AlSiCu/SiO_2/Si stack (comparison between experimental and numerical data for the best fit). (b) AFM topography of a residual imprint after a 1 µm-deep indentation test, the scan size is 15 µm×15 µm (512 × 512 pixels). (c) Verification of the good agreement between the experimental contact area measured *post mortem* by AFM and the numerical contact area.

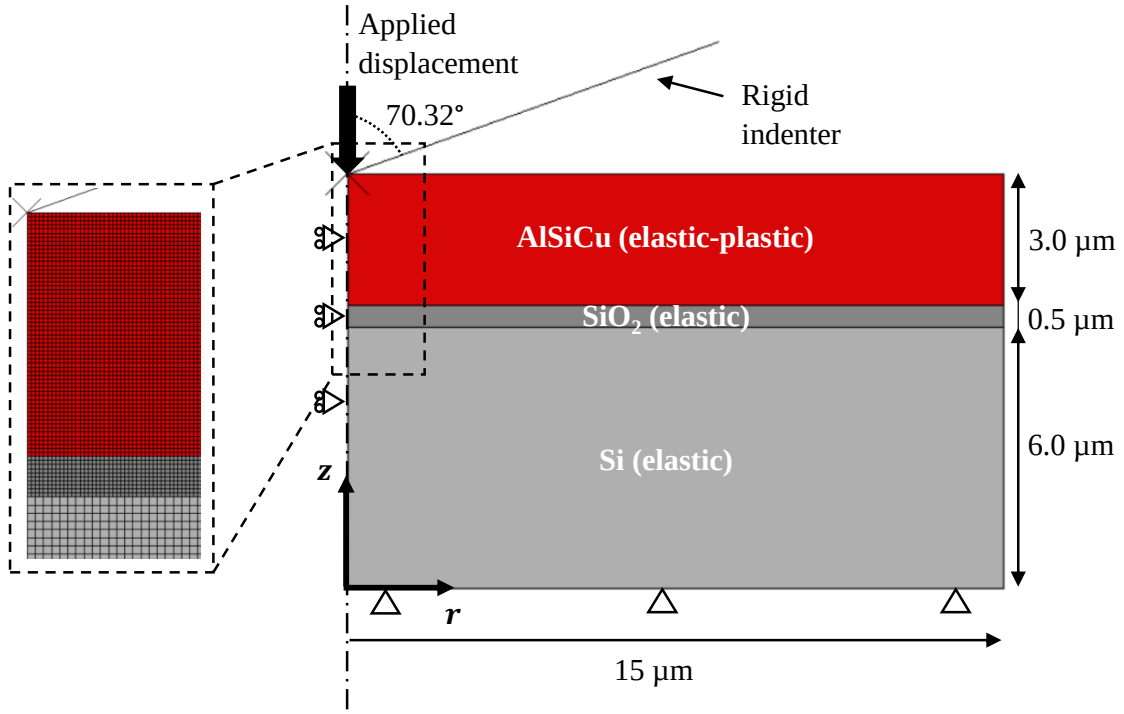

Figure 2.7. FEM calculation cell used for AlSiCu plastic behavior identification.

Material	Si_3N_4	AlSiCu	SiO_2	Si	Unit
Elastic Behavior	$E_1 = 160$ $\nu_1 = 0.27$	$E_2 = 50$ $\nu_2 = 0.3$	$E_3 = 68$ $\nu_3 = 0.17$	$E_4 = 165$ $\nu_4 = 0.22$	GPa –
Plastic Behavior	None	$\sigma_{y0} = 61.8$ $k = 113$ $n = 0.09$	None	None	MPa MPa –
Cohesive Behavior	$\sigma^{0,lay} = 2.5$ $G_c^{lay} = 1$	None	None	None	GPa J/m^2

Table 2.1. Material properties used in FEM simulations.

2.5 Simulation of the first pop-in

Pop-in events during the indentation of "*brittle layers on ductile substrates*" have been widely reported [87, 143, 144], with some mechanical analysis carried out by FEM (with the use of X-FEM [87]). The experimental observations and FEM results of these studies focused in cracks occurring outside the contact edge of the indenter, caused by high tensile radial stress on film surface. The value and position of the maximum tensile stress was shown to be affected by the size of the plastic zone in the substrate beneath the indenter. However, the mechanism of a first crack triggering underneath the indenter (not visible from the sample surface), responsible of the first pop-in, has not been described.

In ceramics, the opening at complete separation (previously denoted δ^f in Section 2.4.2) is known to be of the order of nanometers, and the peak traction values (previously denoted T^0) are ranging between a few hundreds of MPa to a few GPa [145–147]. By using the FEM simulations and comparing their results to the experimental data, these values can be determined.

2.5.1 Overall stress distribution

The results of a FEM calculation simulating the indentation of the whole system can be analyzed, without accounting for fracture, to have an idea of the stress distribution into the system as the indenter is progressively driven down into the sample. The distribution of the maximal principal stress component inside the system is plotted in Figure 2.8 for an indentation depth $h = 300$ nm, which is the depth for which the pop-in event is experimentally detected (Figure 2.2). The maximum tension area appears in light gray, above the Si_3N_4/AlSiCu interface, and extends up to 1300 nm away from the axis. A lower tensile stress threshold of 3 GPa was arbitrarily fixed for this gray area, for the sake of representation. Admitting that the pop-in event is associated with the propagation of a crack, the crack can be assumed to be initiated within the gray region. Moreover, since there is no visible sign of crack propagation on the experimental loading curve prior to this loading threshold, it may be assumed that the crack nucleates and propagates for this loading. This provides an estimate of the peak mode I traction $\sigma^{0,lay}$ around 3 GPa that should be applied to the cohesive behavior of the Si_3N_4 layer. In the same way that a correct value of $\sigma^{0,lay}$ should be clearly identified to match the critical load L_c for which the horizontal pop-in plateau is observed, the length of this plateau should depend on G_c^{lay}, the toughness of the Si_3N_4 layer. Thus, a set of $(\sigma^{0,lay}, G_c^{lay})$ should be chosen to reproduce in the closest way the experimental loading curve. Note the presence of a compression dominated area just underneath the indenter apex (dark gray area in Figure 2.8).

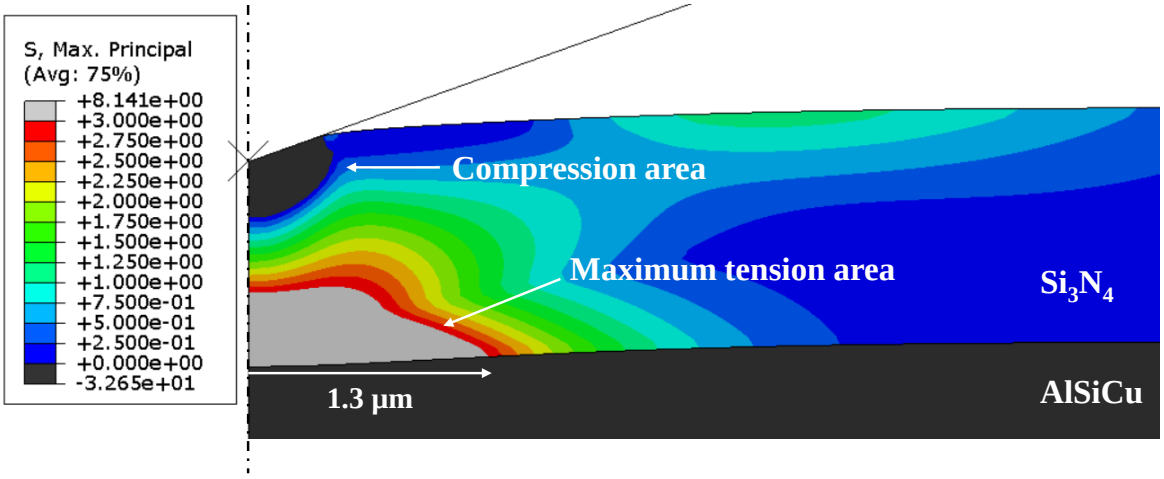

Figure 2.8. Distribution of the maximal principal stress component (in GPa) inside the system, for an elastic Si_3N_4 layer and an elastic–plastic AlSiCu layer (without crack or delamination). Results were obtained for an indentation depth $h = 300$ nm (for which a pop-in event is experimentally detected). Gray area indicates the maximum tension area.

2.5.2 Procedure to model the first pop-in event

Although cracks are susceptible to nucleate wherever in the domain of maximal tension just identified, a location within this area where a crack is more likely to nucleate is assumed to exist. We will denote by r_f the optimal location of this crack (distance of the crack to the axis). Several simulations were carried out to determine values of r_f and to show its dependence on the material properties. The material data describing the fracture properties $(\sigma^{0,lay}, G_c^{lay})$ were fixed. As delamination of the Si_3N_4/AlSiCu interface was allowed, the interface cohesive parameters $T_n^{0,int}$, $T_t^{0,int}$ and G_c^{int} were also kept identical. In each simulation, an initiation site

is introduced at a distance r_{ini} of the axis, under the form of a 100 nm long enriched feature (i.e. already initiated crack). The feature is long enough to cross two elements but small compared to the layer thickness (1300 nm). This initial crack, vertical just above the interface, is depicted in Figure 2.9.

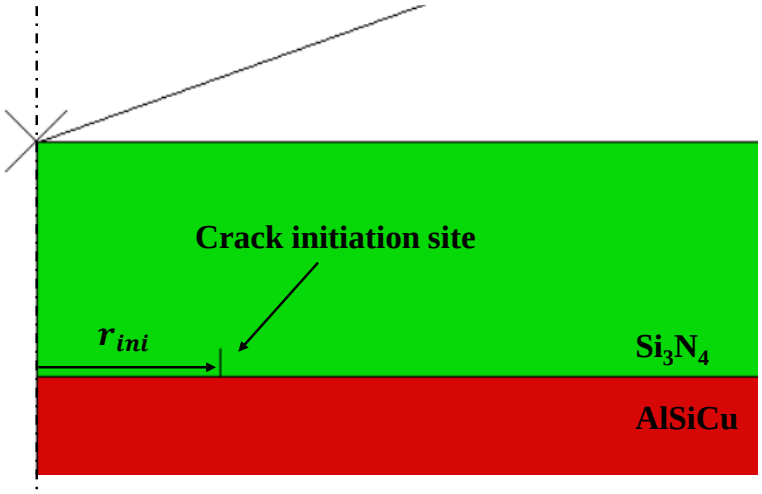

Figure 2.9. Crack initiation site for the calculation of the optimal crack propagation location.

2.5.3 Structure cracking for different initiation site locations

A set of simulations with fixed material properties and with varying locations of the initiation site is provided in Figure 2.10. On the left side, the state of the system for a penetration depth of $h = 400$ nm (depth at which the first experimental pop-in ends) is shown for various values of r_{ini} (increasing from top to bottom). It is clear that the crack propagates inside the Si_3N_4 layer quite differently for different r_{ini}. On the right side of Figure 2.10, the energy dissipated in fracture is represented as a function of the penetration depth normalized to the film thickness h/t, as well as the corresponding loading curve. For an initiation site far from the axis (Figure 2.10d), no propagation is observed and no pop-in is visible on the loading curve. For smaller distances, as in Figure 2.10a and 2.10b, although crack propagation is observed, no pop-in is visible on the loading curve either. In these three cases, crack propagation dissipates only a small amount of energy. On the contrary, for an initiation site at intermediate location, the effect of crack propagation is clearly visible on the loading curve (right side of Figure 2.10c), as a double elbow feature which is the signature of a snap-through instability (detailed below). In this configuration, a large amount of energy is seen to be dissipated by the cracking event. In terms of crack travel, whatever the initiation site location, if the crack initiates (Figure 2.10a, 2.10b and 2.10c), it propagates towards the indenter apex. By comparing these figures to Figure 2.8, it can be seen that the crack actually stops when reaching the compression zone underneath the indenter apex. Finally, some interface damage is visible at the vicinity of the crack when it propagates. It will be later shown that the interface damage has very little influence on the load versus penetration depth response of the system.

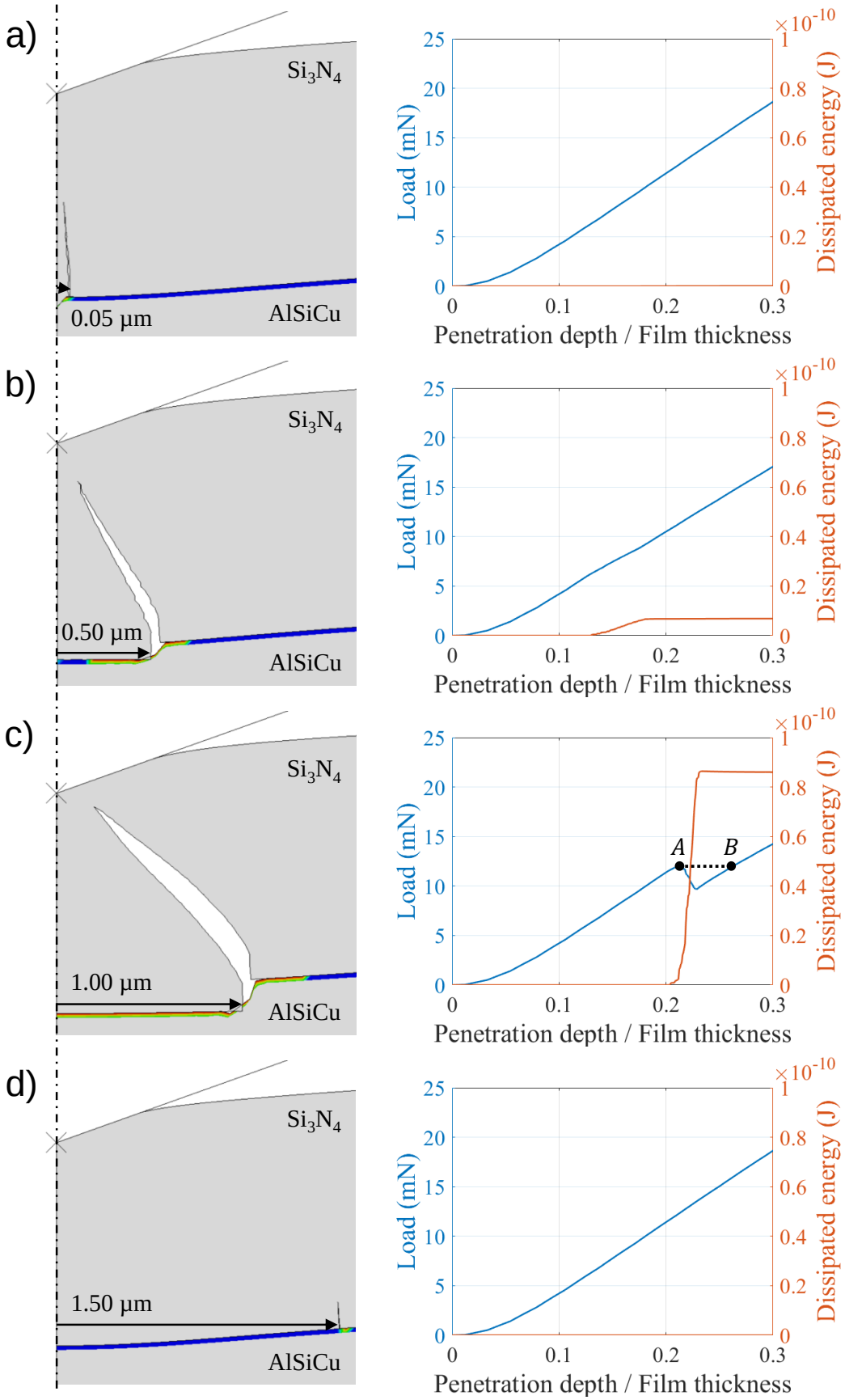

Figure 2.10. Crack propagation in Si_3N_4 for nucleation sites at various distances from the axis. (a) $r_{ini} = 0.05$ µm, (b) $r_{ini} = 0.50$ µm, (c) $r_{ini} = 1.00$ µm, (d) $r_{ini} = 1.50$ µm. Left: crack as observed for an indentation depth $h = 400$ nm. Contour plots show the damage parameter of the Si_3N_4/AlSiCu interface ($d = 0$ in blue and $d = 1$ in red). Right: plot of the energy dissipation and reaction force on the indenter as a function of h/t during indentation. The damage properties are fixed: $\sigma^{0,lay} = 3$ GPa, $G_c^{lay} = 1$ J/m^2, $\sigma^{0,int} = 100$ MPa, $G_c^{int} = 1$ J/m^2.

2.5.4 Snap-through instability

The double elbow feature observed in Figure 2.10c is the signature of a snap-through instability. Given that the loading in the numerical simulation is performed in a displacement-controlled mode, the force decrease at the elbow feature simply indicates that a significant loss of stiffness of the system is associated to the crack propagation. Thus, as the indenter is pushed deeper into the sample, the reaction force first decreases, then increases again, and the mechanical equilibrium is maintained at every step of the loading. However, in the experiment, the load is imposed in a monotonically increasing way on the indenter (load-controlled mode). Thus, when the upper point of the first elbow is reached (point A in Figure 2.10c), a displacement jump is observed on the loading curve, as the next equilibrium point that is accessible for a slightly larger force is point B. This is the origin of the experimental pop-in.

2.5.5 Mapping of crack parameters

In practice, the actual crack location is assumed to be at the distance $r_{ini} = r_f$ that maximizes the energy dissipation. According to Figure 2.10, the critical value of r_{ini} for each value of $\sigma^{0,lay}$ can be identified. Even though this critical value r_f is *a priori* a function of $\sigma^{0,lay}$ and G_c^{lay}, the influence of G_c^{lay} is rather small (as discussed later). A map of the dissipated energy during crack propagation in a $(r_{ini}, \sigma^{0,lay})$ space is displayed in Figure 2.11, with a value of G_c^{lay} fixed to 1 J/m^2. The distance of the crack to the axis is represented on the horizontal axis, and the layer tensile strength $\sigma^{0,lay}$ on the vertical axis. The red front characterizes the maximum dissipation. For each value of $\sigma^{0,lay}$, a critical value r_f can then be identified. For instance, as seen in Figure 2.10, the maximum dissipation at $\sigma^{0,lay} = 3$ GPa is obtained for the configuration depicted in Figure 2.10c, at $r_{ini} = 1$ µm. Consequently, Figure 2.11 becomes an universal map to relate the material properties to the crack location.

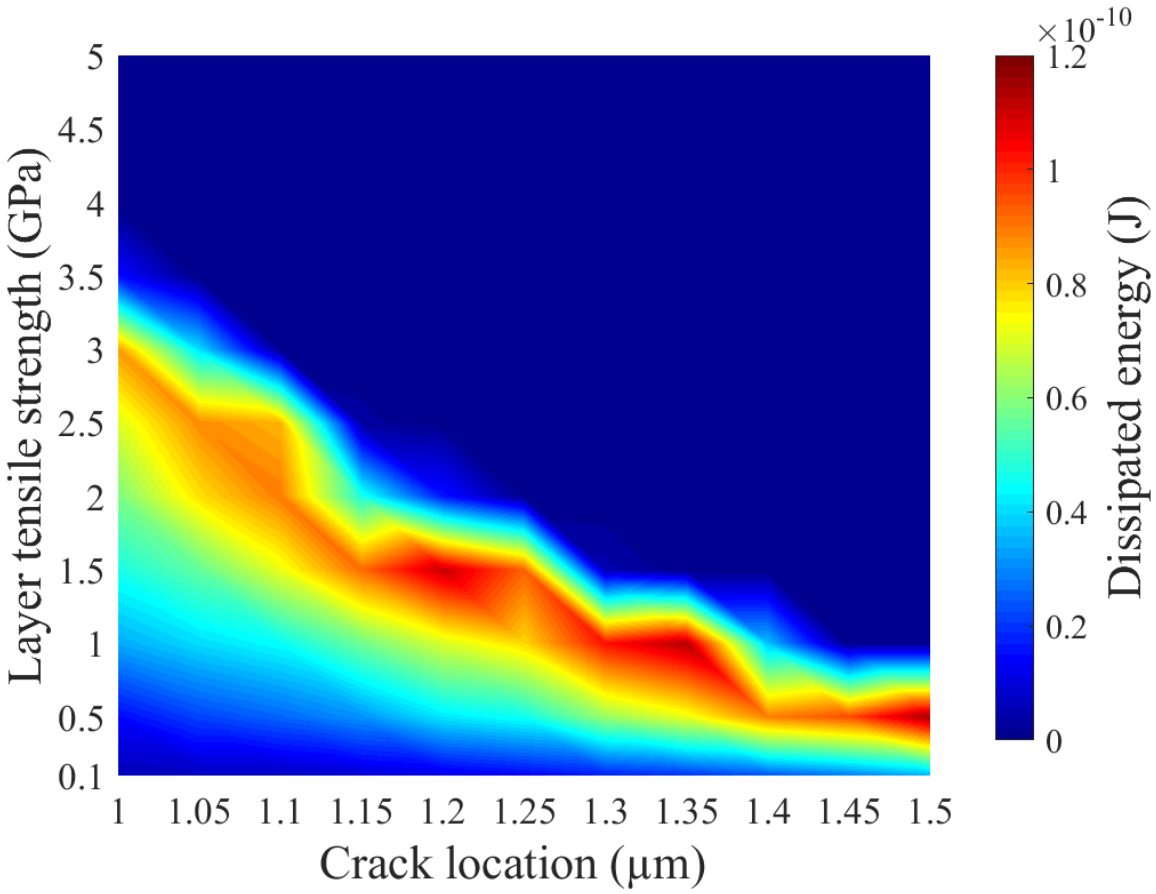

Figure 2.11. Map of the dissipated energy during the propagation of the "first" crack (the one propagating in the area underneath the indenter). Horizontally: distance of the crack to the axis; Vertically: layer tensile strength $\sigma^{0,lay}$. This map gathers the results of 121 simulations, with horizontal and vertical grid steps of 50 nm and 0.5 GPa, respectively.

2.6 Analysis of the first pop-in event

2.6.1 Tensile strength values of Si_3N_4 obtained from the first pop-in

As the pop-in events observed on the experimental loading curves can be well represented using our FEM numerical simulations, we now want to use the pop-in characteristics as a signature to identify the cohesive parameters of the Si_3N_4 layer. The procedure is based on an inverse method, similar to the one that was used to identify the hardening properties of AlSiCu, previously described in Section 2.4.3. The identification procedure is based on:

- the critical loading state for which the plateau is reached, formed by the couple (h_c, L_c), respectively the critical depth and critical load at which the pop-in occurs;
- the length of the plateau itself, further denoted Δh_c.

A set of experimental loading curves (out of a matrix of 12 indents) are displayed in Figure 2.12a. A relatively good reproducibility can be observed regarding the load at the pop-in plateau, as well as the length of this plateau.

The loading curves obtained numerically with six sets of $(\sigma^{0,lay}, r_f)$ data allowing the maximum energy dissipation (see Section 2.5.5) are displayed in Figure 2.12b. The average and standard deviation values of both load and depth observed experimentally were also represented in Figure 2.12b. All couples lying between (3.0 GPa, 1.00 µm) and (0.5 GPa, 1.50 µm) are found to generate loading curves falling within the range of experimental output. A curve obtained from the FEM showing values of L_c and Δh_c within the experimental range is also reported in Figure 2.12a and compared to the set of experimental curves. To narrow down the interval of tensile fracture strength values $\sigma^{0,lay}$ identified from the simulation, the second pop-in must also be exploited.

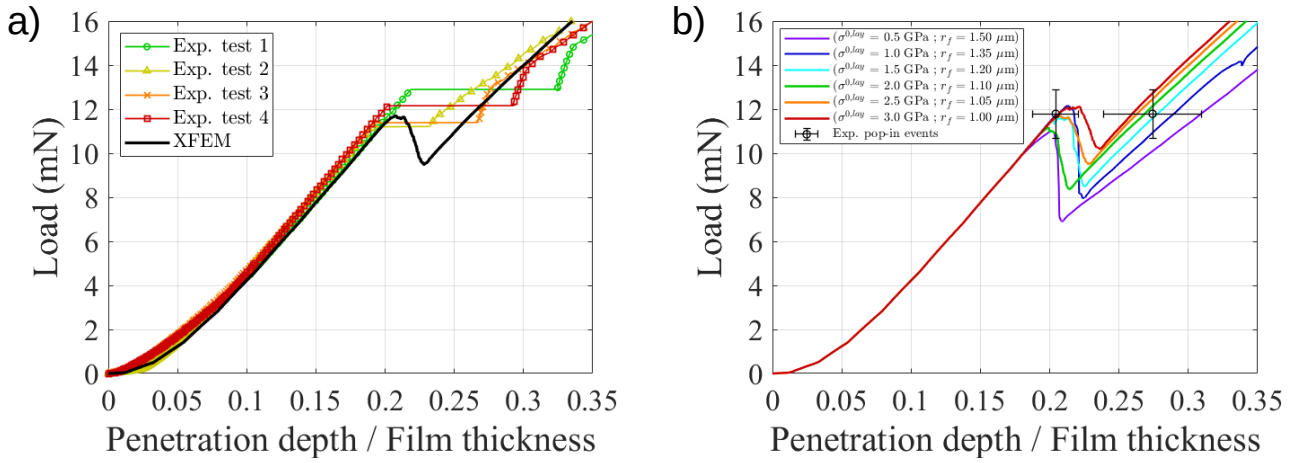

Figure 2.12. Loading curves versus penetration depth. (a) The experimental data from various indents are gathered. One of the best fit FEM simulations results is plotted (black curve with double elbow) with $\sigma^{0,lay} = 2.5$ GPa and $r_f = 1.05$ µm. (b) Sets of $(\sigma^{0,lay}, r_f)$ data providing loading curves within the experimental data range (experimental error bars indicated).

2.6.2 Influence of G_c^{lay}

To assess the role of G_c^{lay}, the loading curves obtained numerically for 3 sets of $(\sigma^{0,lay}, G_c^{lay})$ values matching the same pop-in plateau $L_c = 12$ mN were reported in Figure 2.13. The values of G_c^{lay} vary in a ratio of 1000, while the tensile strength values $\sigma^{0,lay}$ only vary in a ratio of 1.4. A similar double elbow feature is observed on all curves. Changing G_c^{lay} does not affect the pop-in initial and ending points, thus showing the lesser role of G_c^{lay}. This indicates a fracture mechanism that is essentially stress-controlled in the sense that, once the initiation criterion is met, the crack is able to propagate over a long distance due to a large energy release rate. It only stops when the crack fronts enter a compression-dominated area (i.e. just underneath the indenter).

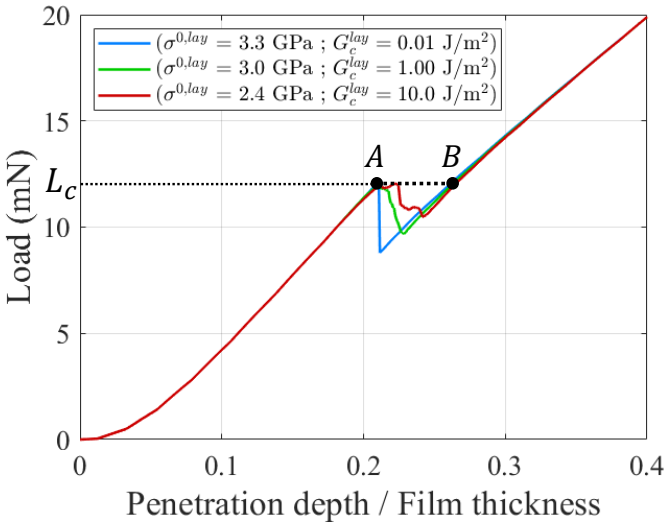

Figure 2.13. Influence of the two layer parameters $\sigma^{0,lay}$ and G_c^{lay} on the value of the pop-in load plateau L_c. The values of $\sigma^{0,lay}$ necessary to trigger the pop-in at this value of L_c show little variation as G_c is varied of a thousand-fold (for $r_{ini} = 1$ µm).

2.6.3 Cohesive behavior of the interface

The parameters of the interface cohesive behavior have been introduced previously: the peak traction components in the normal and tangential direction (respectively $T_n^{0,int}$ and $T_t^{0,int}$) and the adhesion energy G_c^{int}. Because the crack in Si_3N_4 is connected to the interface, a shear loading develops at the interface in the vicinity of the crack. Thus, the shear traction component ($T_t^{0,int}$) is the dominant parameter for the initiation of interface delamination. Regarding the value of the shear strength at a ceramic coating/metal interface, values of the order of a hundred MPa can be found [148, 149]. However, the experimental values for G_c^{int} found in the literature must be interpreted with care. Indeed, the energy measured experimentally during interface separation often involves a significant amount of plastic work in the metal, which should not be implemented as interface adhesion energy in the simulation parameters. Calculations of adhesion at metal/ceramic interfaces based on first principle calculations estimate G_c^{int} around 1 J/m^2 [150, 151] or even less.

A range of interface property values were tested in the FEM calculations, with $T_t^{0,int} \in [100, 500]$ MPa and $G_c^{int} \in [0.01, 10]$ J/m^2 (Figure 2.14). In all cases, there was no influence on the loading curve (the pop-in load was the same), as illustrated in Figure 2.14a. The damage distribution along the interface is also plotted in Figure 2.14b. Three cases are observed: (i) for high $T_t^{0,int}$ and moderate G_c^{int}, the interface is damaged only at the crack location, (ii) for moderate $T_t^{0,int}$ and moderate G_c^{int}, some interface damage by shear can form between the crack and the axis of symmetry and (iii) for moderate $T_t^{0,int}$ and small G_c^{int}, the interface can be damaged by shear on a wide area extending far from the axis of symmetry. This last case is unrealistic, as it requires a very small value for G_c^{int}.

The main information resulting from the parametric study concerning the interface is that the pop-in response identified on the loading curve is not affected by the various interface damage processes. This indicates that it is not possible to collect informations about interfacial fracture properties from the indentation test as it is carried out in this study. However, it also simplifies the identification of the tensile strength of the Si_3N_4 layer.

Finally, to obtain more precisely the strength of the Si_3N_4 layer, the interval of values of

the $(\sigma^{0,lay}, r_f)$ couples can be identified using the experimental data from the second pop-in.

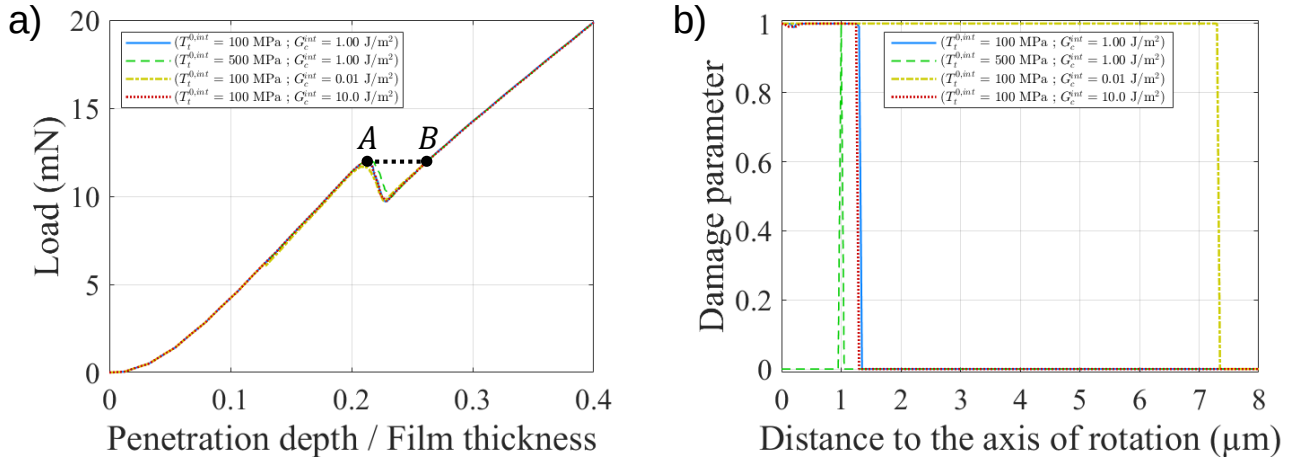

Figure 2.14. Influence of the interface strength and toughness on the calculations results. (a) Load versus penetration curve obtained during the simulation of nanoindentation, for a large spectrum of values of the interface shear strength $\sigma_t^{0,int}$ and toughness G_c^{int}. (b) Damage parameter along the interface, for the same sets of interface strength and toughness values.

2.7 Study of the second pop-in event

A FEM calculation was performed for each couple of $(\sigma^{0,lay}, r_f)$ satisfying the maximum energy dissipation and providing results consistent with the experiments (see Figure 2.12b). For these tests, the loading was pursued after the first pop-in event (up to 900 nm depth). In addition to the first crack responsible for the first pop-in, cracks are also allowed to nucleate and propagate anywhere else in the layer. The interface strength and toughness parameters were fixed to 100 MPa and 1 J/m^2 respectively, consistently with data from the literature.

The numerical results are displayed in Figure 2.15, as well as the experimental data scattering (black crosses). The experimental characteristics of the second pop-in (pop-in plateau load L_{c2} and displacement jump Δh_2) are found to be much more scattered than those of the first pop-in. Interestingly, contrary to the first pop-in, the second pop-in is very dependent on the chosen $(\sigma^{0,lay}, r_f)$ couple. The valid data $(\sigma^{0,lay}, r_f)$ are those for which the simulated second pop-in plateau lies within the experimental scattering interval (level of pop-in load). Thus, the relevant range for these magnitudes becomes possible to identify. From the data represented in Figure 2.15, it can be concluded that 2.0 GPa $\leq \sigma^{0,lay} \leq$ 3.0 GPa and 1.0 µm $\leq r_f \leq$ 1.1 µm.

The sensitivity of our results to material parameters can be discussed, as well as the possible role of uncertainties, whether they are "epistemic" (i.e. possible to be reduced by gathering additional data or refining the model) or "aleatory" (i.e. no possibility is seen of reducing them) [152, 153]. Up to this point, our approach was rather focused on the understanding of the failure mode and the measure of the layer strength, but the latter is likely to be affected by aleatory uncertainties related to local heterogeneities (small-scale defects, interface coherences, etc.). In terms of experimental characteristics, the first pop-in displays a very small experimental dispersion (Figure 2.2a) while the second pop-in presents much more scattered features (Figure 2.2b). In terms of numerical results, the impact of these two cracks on the loading curve is also drastically different: for the first pop-in, the locus of the fitting parameters that maximize the energy release (very sharp and stretched area in Figure 2.11) shows that the

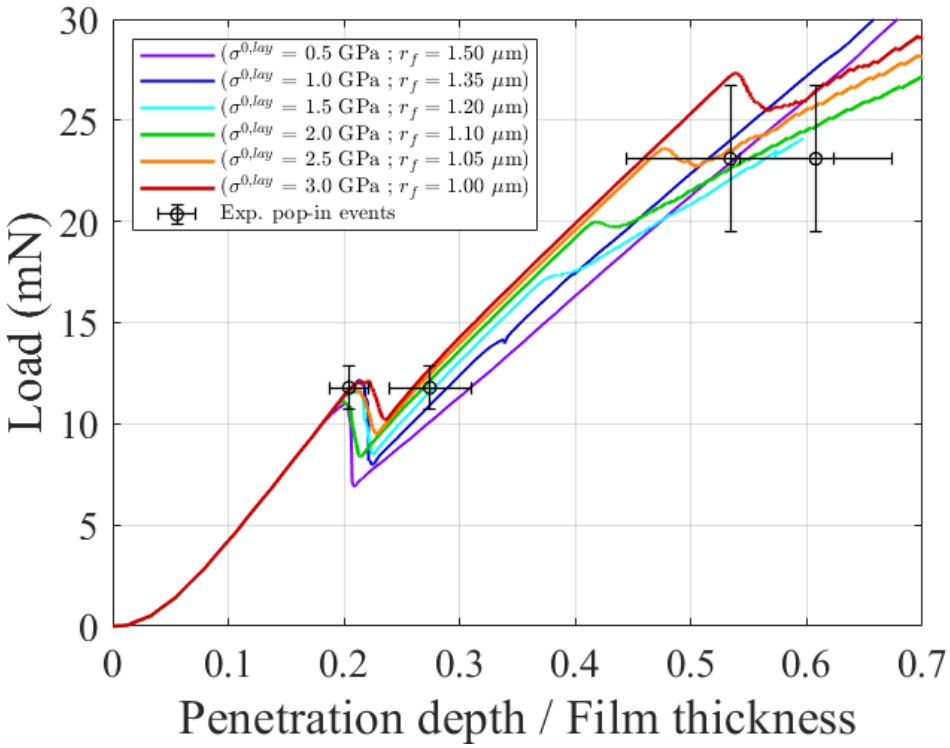

Figure 2.15. Simulated loading curves reported for $(\sigma^{0,lay}, r_f)$ couples allowing maximum dissipation for the first crack. Experimental data scattering is also reported (black crosses).

description of this first crack is highly sensitive to numerical inputs (small changes in numerical strength or crack location induce a large deviation in dissipated energy) even though a wide range of $(\sigma^{0,lay}, r_f)$ couples can fairly describe it. This latter point actually prevents the direct identification of the actual layer characteristics solely from the first pop-in. On the contrary, for the second pop-in, despite the dispersed experimental characteristics, only a limited range of numerical inputs allow the overall description of the experimental results.

As the presence of defects can influence the location of crack nucleation, a sensitivity study of the problem regarding the location of cracks was carried out. The variations of dissipated energy versus the crack locations are reported in Figure 2.16a. For all the simulations, the strength $\sigma^{0,lay}$ is fixed to 2.5 GPa, for which the optimal crack locations (i.e. associated with the highest release of energy) are $r_1^* = 1.05$ µm and $r_2^* = 3.9$ µm for the first and second crack, respectively. The corresponding released energies are denoted E^* and E (positive values) for the optimal and tested crack locations, respectively. The quantities plotted in Figure 2.16a are relative to the optimal parameters: $(E - E^*)/E^*$ as a function of $(r - r_1^*)/r_1^*$ (first crack) or $(r - r_2^*)/r_2^*$ (second crack). The variation of the energy release with respect to the first crack location shows a sharp peak at the optimal value, so the system is not expected to deviate much from this value, whatever the distribution of structural defects within the material. This point explains the small dispersion on the first pop-in features. On the contrary, the variation of the energy release with respect to the second crack location is quite weak, with a 5 % variation in energy over a 45 % range of crack location span. So the location of the second crack is more likely to be sensitive to structural defects. To further understand the nucleation process of this second crack, the numerically computed distribution of maximum principal tensile stress component in the Si_3N_4 layer just before crack initiation was plotted versus crack location (Figure 2.16b). It appears that the stress value does not decrease quickly in the vicinity of the peak. In fact, it only varies from 5 % over a 1 µm span from the peak. Of course, in calculations

the crack forms at the peak value of the stress. However, this is where the "aleatory" defects in the "real" layer may take a part, as the weakest defects may trigger cracks not exactly at the numerically-predicted location, but rather in a close vicinity of this stress peak. This finally sheds light on the experimental dispersion on the loading curve for the second pop-in, as both tensile stress and released energy vary very weakly over a large region of the film during the phenomenon.

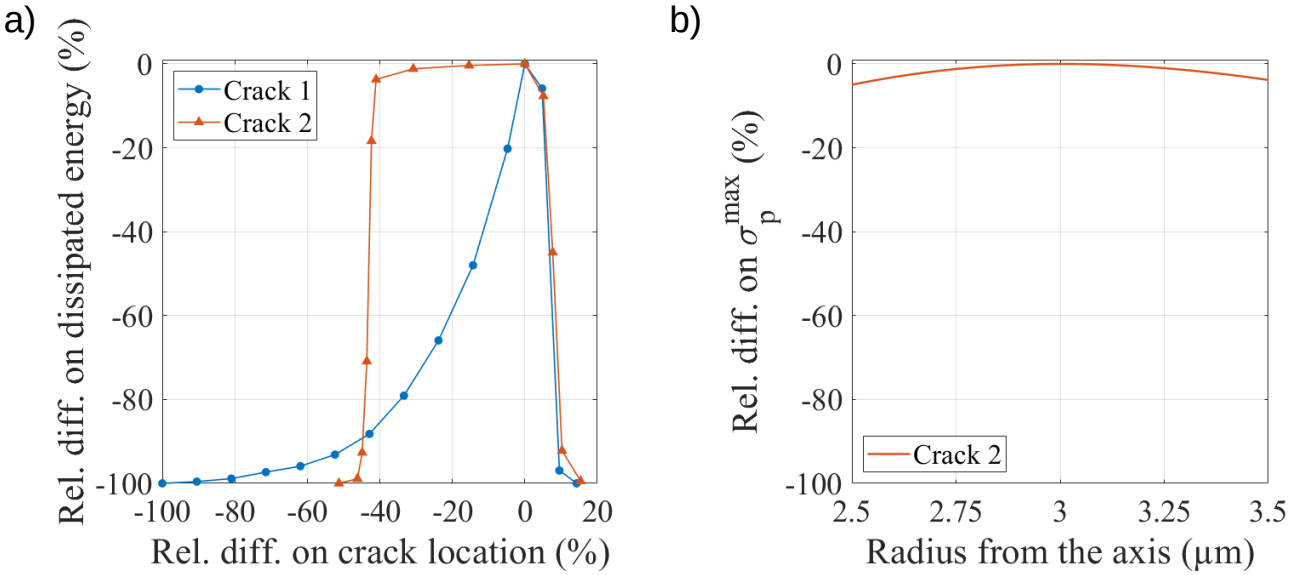

Figure 2.16. (a) Variations of dissipated energy with respect to crack locations. The quantities plotted are relative to the optimal parameters: $(E - E^*)/E^*$ as a function of $(r - r_1^*)/r_1^*$ (first crack) or $(r - r_2^*)/r_2^*$ (second crack), with optimal values $\sigma^{0,lay} = 2.5$ GPa, $r_1^* = 1.05$ µm and $r_2^* = 3.9$ µm. (b) Numerically computed distribution of tensile stress in the Si_3N_4 layer just before the crack initiation (indenter depth $h = 580$ nm).

The result of the calculation for $\sigma^{0,lay} = 2.5$ GPa and $r_f = 1.05$ µm is shown Figure 2.17a. A radial crack forms at a distance $r = 3$ µm of the axis, starting from the surface, propagating down into the layer, kinking from an initially vertical to horizontal propagation direction. The simulated loading curve was reported in Figure 2.17c, with an experimental curve. A second pop-in event is clearly observed on the FEM curve, associated with the propagation of the second crack. A similar second pop-in feature can be observed on the experimental curve.

Since the loading curve only gives information about the global response of the sample, complementary data can be obtained from the direct observation of the fracture pattern on the SEM cross-section view taken after FIB-milling of a residual imprint (as shown in Figure 2.3c). To compare experimental observations to simulation results, this SEM cross-section view is reported again in Figure 2.17 with its numerical counterpart. The corresponding pop-ins are recalled on the experimental and numerical loading curves (Figure 2.17c). Remarkably, the two main cracks that were identified in the simulation as causing the first and the second pop-in events can be observed on the image, at locations that are consistent with the numerics (respectively ~ 1 µm and ~ 3 µm from the axis for the first and the second crack). Likewise, the experimental crack paths were also correctly predicted by simulations: while cracks ① nucleate at the Si_3N_4/AlSiCu interface and propagate up to the indenter apex, cracks ② kink from a vertical to an horizontal direction, going away from the indenter. All these observations confirm the ability of the model to be predictive and bring confidence to the reliability of the data values determined for the Si_3N_4 tensile strength.

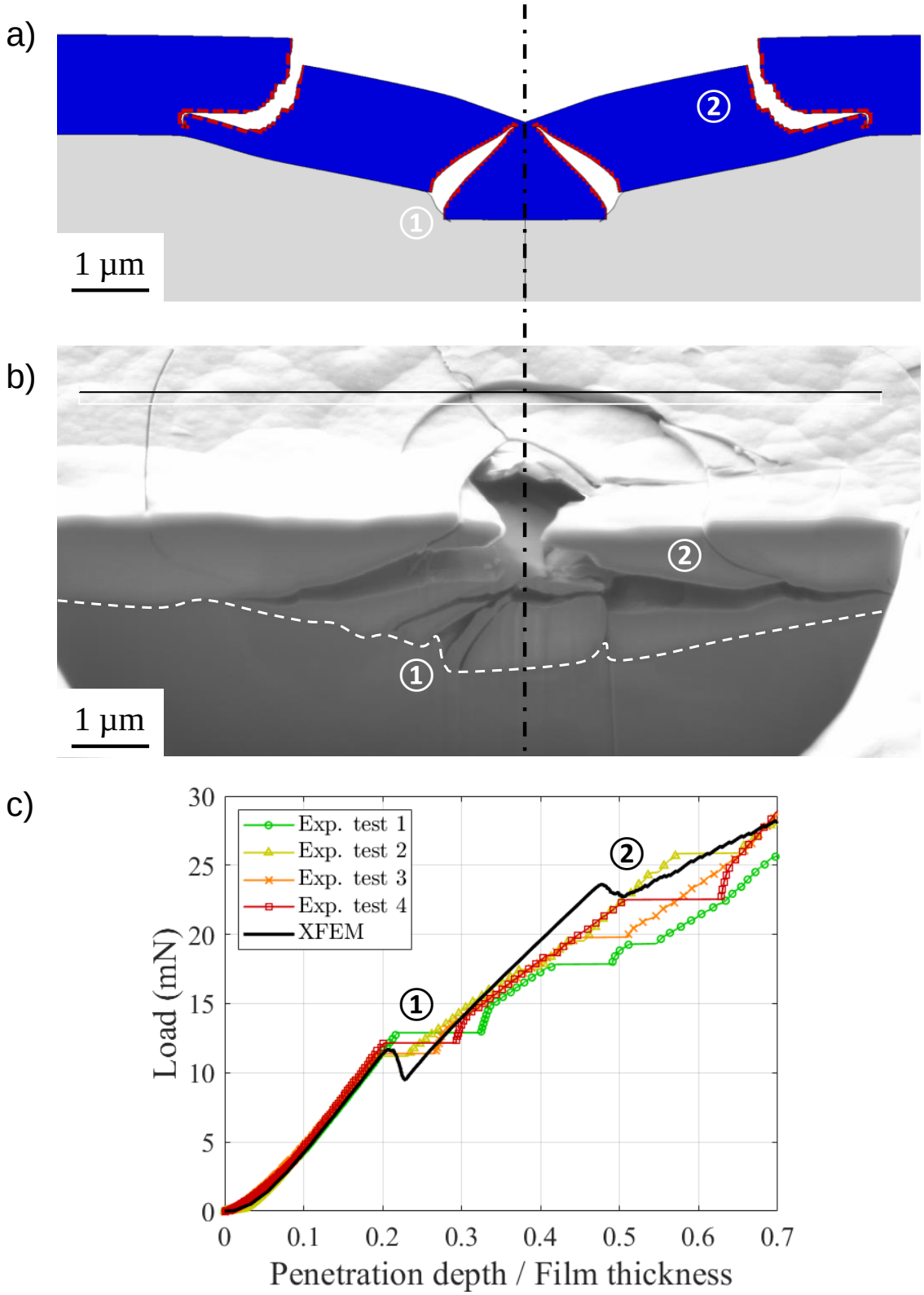

Figure 2.17. Comparison between the numerically predicted crack pattern (a) and the experimental one (b). The experimental and numerical loading curves are recalled (c). The cracks associated to the first and second pop-in events are labeled, respectively, ① and ②.

2.8 Conclusion

The formation of multiple cracks during the nanoindentation of a stack composed of a silicon nitride (Si_3N_4) layer deposited on top of a ductile metallic alloy (AlSiCu) layer was investigated. The complete damage process of the multilayer during indentation was analyzed using FEM, accounting for plasticity in AlSiCu and crack propagation in the Si_3N_4 layer. The various stages of the damage process occurring in the Si_3N_4 were elucidated, showing in particular:

- The initiation/propagation of a crack of conical shape, nucleating from a location along the interface and propagating towards the apex of the indenter. The crack does not reach the surface, as it is stopped in a compression zone underneath the indenter. It explains why this crack cannot be observed on the sample surface. However, observations of a sample cut reveals its presence.
- A second crack initiation and propagation following the first one, but this time propagating from the top surface of the layer down towards the Si_3N_4/AlSiCu interface.

Moreover, a novel procedure for the identification of the Si_3N_4 layer tensile strength is presented, using an inverse method based on FEM simulations and experimental data. The procedure is composed of two steps:

- Step 1: Fitting on the first pop-in. Only two physical magnitudes are adjustable parameters for this fitting step: the layer tensile strength $\sigma^{0,lay}$ and the distance of the crack to the indenter axis r_f. A collection of these parameters able to match the first pop-in was identified as follows: for each value of $\sigma^{0,lay}$, the value of r_f maximizing the energy dissipation is selected. The characteristics of the first pop-in on the experimental loading curves (critical load and depth) are fully reproduced by the numerical curves obtained with this "maximum energy dissipation" approach.
- Step 2: Fitting on the second pop-in. Within the collection of $(\sigma^{0,lay}, r_f)$ couples identified at Step 1, only a limited set of couples are able to reproduce the second pop-in behavior: critical load and depth, snap-through feature, ...

The strength of this two-step procedure relies on its ability to narrow down the identification range for the layer properties. Indeed, at Step 1, all the $(\sigma^{0,lay}, r_f)$ couples maximizing the energy dissipation result in similar characteristics of the simulated first pop-in (critical load and depth). Consequently, the fitting of this first pop-in is not sufficient to discriminate a tensile strength value by itself. By contrast, the characteristics of the simulated second pop-in are much more sensitive to the $(\sigma^{0,lay}, r_f)$ couples, opening a way for a closer identification of the layer property. The experimental dispersion on this second pop-in is small enough to allow this identification. This implies that a remarkably good estimate of the layer tensile strength can be achieved by the method described here.

Finally, this double pop-in phenomenon is probably very generic to brittle layers deposited on ductile underlayers, and is indeed observed in other works (see e.g. Lofaj and Németh [87]), but up to now, each pop-in had not been clearly attributed to a first crack forming underneath the indenter before a circumferential crack, probably due to the difficulty that the first crack cannot be spotted from surface observations, and is more likely attributed to a circumferential crack. In our case, the FIB observation clearly confirmed the existence of this under-surface crack. Because our modeling approach is very general as it involves only a few influential key parameters to describe fracture and plasticity, the identification procedure that we propose should be quite generic to systems of brittle/ductile layers showing similar multiple-cracking patterns under indentation.

Chapter 3

Evidence of Plasticity-Driven Conductivity Drop in an Ultra-Low-k Dielectric Organosilicate Glass

This chapter is based on the following paper published in the journal "*Advanced Functional Materials*":

M. Rusinowicz, F. Volpi, G. Parry, M. Braccini, C. Boujrouf, M. Verdier. Evidence of Plasticity-Driven Conductivity Drop in an Ultra-Low-k Dielectric Organosilicate Glass. *Advanced Functional Materials* **32** (2022), 2207354.

It presents a study of mechanical and electrical couplings in a nanoporous organosilicate glass (SiOCH) ultra-low-permittivity dielectric film deposited on a silicon (Si) substrate. A plasticity-driven conductivity drop is revealed in the SiOCH thin film under mechanical loading and fully described both analytically and numerically, in particular by establishing an extension of the standard Poole-Frenkel electrical conduction model.

This work was carried out using SiOCH samples processed by the STMicroelectronics company in the framework of a previous thesis. As for Chapter 2, the nanoindentation experiments, the imaging of the residual indent imprints and the numerical simulations were performed in the present PhD.

3.1 Introduction

For more than six decades, the semiconductor industry has extensively developed and integrated innovative materials capable of meeting challenging technical requirements for the fabrication of integrated circuits. These requirements have imposed cross-related conditions on both functional (electrical conduction or insulation, thermal conduction or insulation, transparency or opacity, thermodynamic stability, etc.) and structural properties (stiffness, hardness, toughness, etc.). These material-based improvements have applied concomitantly to the active devices fabricated directly on semiconducting substrates (transistors, diodes, sensors, etc.) and to the upper interconnect structure allowing these devices to communicate with each other. This interconnect structure is a complex architecture of metal lines surrounded by a composite dielectric matrix. However, as the dimensions of devices have shrunk, these interconnect metal lines have moved closer, thus increasing the intrinsic delay of signal propagation within the structure [154–157]. After the replacement of aluminum by copper, which reduced overall interconnect resistance, major improvements in the performance of the interconnects have involved upgrading the dielectric material, which has evolved continuously from dense SiO_2 to nanoporous organosilicate glasses (OSG) [157–163]. The driving force for this evolution in dielectric material was to decrease its permittivity k to reduce capacitive coupling between the metal lines. In terms of chemistry, this lowering of permittivity was driven by the Clausius-Mosotti relation: it was first obtained by partially replacing highly-polar Si-O bonds by Si-C bonds (methyl groups were then introduced into the SiO_2 backbone), leading to dense SiOCH low-k dielectrics. Further lowering of permittivity was achieved by introducing nanoporosity (obtained by UV curing after the incorporation of organic porogens), leading to nanoporous SiOCH ultra-low-k dielectrics [164–166]. Nevertheless, these performance improvements were accompanied by a drastic decline in reliability [155].

From the mechanical point of view, modifications in SiOCH chemistry and density lowered its effective Young's modulus, hardness and toughness [163, 167–174], thus reducing the ability of such structures to sustain mechanical stresses during processing or operation [123, 124, 126, 127, 175, 176]. The mechanical properties of low-k dielectrics were essentially measured on full-sheet specimens by bulge testing or by nanoindentation [168, 169, 172, 177, 178].

From the electrical point of view, the introduction of porosity and organic groups led to a dramatic increase in current leakages [179–181], and dielectric breakdowns have become the most important failure mechanisms in interconnects [182–188].

The strong interplay between SiOCH chemistry and electrical failures has been extensively studied [184, 185, 189–193], including the effect of metallic contamination [194, 195]. In comparison, the interplay between mechanical stresses and electrical failures has been more rarely addressed. Most attempts have focused on the effect of mechanical stresses on the dielectric breakdown of ultra-thin oxide films [196–199], demonstrating the synergistic effect of mechanical and electrical stresses on bond breaking. Conversely, it has been reported that electrical current initiates mechanical delamination [200, 201]. More recently, the effect of mechanical stresses on trap-assisted conduction mechanisms has been studied: within the reversible domain, it has been shown that mechanical stresses lower/increase the trap energy barrier reversibly when tensile/compressive, respectively [202, 203]. The latter trend has been shown to depend strongly on the chemistry of the dielectric material [204]. Despite all these studies, a thorough understanding of the effect of mechanical damages on the electrical conduction of ultra-low-k dielectrics still seems to be lacking. Yet this point is crucial for the modeling of time-dependent

dielectric breakdown (TDDB) phenomena and for the prediction of device lifetime [184, 195, 205–207].

In the present work, a nanoporous SiOCH film deposited on silicon substrate was nanoindented with a home-developed device able to monitor simultaneously and continuously both the electrical and mechanical responses of the film during indentation [12, 112, 113]. Nanoindentation is a well-established technique dedicated to the local mechanical testing of materials at nanoscales [1, 2], and is well suited for thin film characterizations [70, 208]. The coupling of this technique with electrical measurements allows the analysis of the mechanical and electrical behaviors of thin film materials as well as their interaction. In this study, such "electrical-nanoindentation" tests (performed under biases ranging from 1 to 120 V) enabled to monitor the leakage current from the earliest stages (at the fA level) up to film failure (dielectric breakdown or film cracking). Different mechanical/electrical regimes were observed and could be explained thanks to *post mortem* analysis and numerical modeling. In particular, a correction to the original Poole-Frenkel law is proposed to account for the film plasticity that occurs continuously during indentation, thus leading to a full description of the evolution of the electrical conductivity. A physical interpretation of this strain-dependent correction is given in terms of plasticity-induced space-charge. This case study of electrical/mechanical experimental monitoring and numerical modeling paves the way for identifying correlations between structural and functional properties that would otherwise be inaccessible.

3.2 Experimental and numerical details

3.2.1 Sample

The sample was a simple stack consisting of a thin nanoporous SiOCH film on a (001)-oriented silicon substrate. Nanoporous SiOCH is one of the silicon based ultra-low-k materials and belongs to the organosilicate glasses (OSG). It contains a silica backbone and characteristic Si-CH_3 terminating groups [160, 164]. Film was deposited by Plasma Enhanced Chemical Vapor Deposition (PECVD) at 225 °C with two precursors and two steps. The first step consisted in co-depositing the SiOCH matrix (diethoxymethylsilane precursor) with a thermally-unstable organic phase called porogen [209]. The second step was dedicated to porogen removal using UV rays [210, 211], leading to a porous material (20-30 % of porosity) with a dielectric constant of 2.5. The film was 330 nm-thick. The Si substrate was p-type with a resistivity of 20 Ω.cm.

3.2.2 Experimental techniques

The experimental electrical-nanoindentation set-up combined various commercial modules with customized adaptations. A more detailed description of the set-up is given in [12, 112]. The nanoindentation head was a commercial actuator (InForce 50 actuator from Nanomechanics Inc. / KLA-Tencor) that enabled continuous stiffness measurement (CSM) for hardness and elastic modulus monitoring [212]. All the experiments presented in this chapter were performed with boron-doped diamond (BDD) Berkovich tips with resistivity in the range of $[0.2-2]$ Ω.cm supplied by Synton-MDP. It was decided to use this reference geometry as it is comparable with most works already reported in the literature, but any other tip geometries can be used (flat-punch, cube-corner or spherical tips). The actuator and samples were displaced with linear positioners from SmarAct GmbH. The whole electrical measurement chain was fully guarded

up to the tip, leading to ultra-low set-up leakage (in the fA range). The set-up leakage was measured before each test in an open-circuit configuration, thus the current offset can be annulled by simple subtraction. The set-up shielding resulted in a noise RMS-amplitude of circa 3 fA. Ground planes were used to prevent spurious capacitive couplings. Different electrical magnitudes could be measured with this set-up: leakage current, quasi-static resistance, dielectric capacitance, piezoresponse, etc. In the present case, the focus was on electrical conduction: only currents were monitored. Current measurements were conducted at the tip side with a highly-sensitive ammeter (sub-femtoamp 6430 model from Keithley, with a current sensitivity as low as the fA range with an integration time of 40 ms). Current compliance was set to 100 nA. In this configuration, electrical bias was applied to the sample with a voltage source (6517B model from Keithley), while tip bias was set at ground level.

Residual nanoindentation imprints were observed by Atomic Force Microscopy (AFM) and Scanning Electron Microscopy (SEM). The AFM apparatus was a NanoObserver AFM from CSI/Scientec, and the SEM apparatus was a Gemini SEM 500 from Carl Zeiss. Cross-views were taken after focused ion-beam (FIB) milling, using a FIB Cross Beam NVision 40 from Carl Zeiss (Ga source with an acceleration voltage of 30 kV and current intensity of 300 pA).

3.2.3 Finite-element modeling

Numerical calculations were carried out by the Finite Element Method (FEM) using the ABAQUS® software within the framework of a 2D axisymmetric model. The model is composed of three parts, consisting of deformable bodies:

- The substrate. It has a cylindrical shape with a radius and height of 10 µm. These dimensions are chosen to be sufficiently large compared to the maximum indentation depth (200 nm) to avoid any interaction of the stress/strain fields generated in the material with the outer boundary of the sample (and also so that the electric fields do not interact with the edges).
- The film. It has a thickness of 330 nm and a radius equal to that of the substrate (10 µm). It is fully tied to the substrate (i.e., nodes of the film and the substrate are merged along the film/substrate interface), which ensures perfect continuity of the mechanical and electric fields between these two parts.
- The indenter. It has a cono-spherical geometry, chosen to match the profile of the experimentally used Berkovich tip (i.e. its area function relating the section of the tip to the distance from its apex). Its height is 10 µm, chosen for the same reasons as for the substrate.

The goal of the simulations is to reproduce electrical-nanoindentation tests for capturing both the mechanical and electric fields in the SiOCH film (stress/strain and current density/electric field distributions). They are divided into three steps in which the bottom surface of the substrate is always mechanically fixed and the top surface of the tip is at zero voltage. In the first step, a small downward displacement of one nanometer is applied to the upper surface of the tip to bring it into contact with the film surface. In the second step, a voltage is applied incrementally to the bottom surface of the substrate until the desired voltage for the electrical-indentation test is reached. Finally, in the third step, a displacement of the tip on the film surface continues to be applied incrementally to a maximum depth of 200 nm, while maintaining the desired voltage constant. The elements available in the ABAQUS® software do not combine mechanical and electrical physics in a 2D axisymmetric framework. A coupled

thermal-stress analysis is therefore performed, in which the mechanical and thermal equations are solved simultaneously. The idea is to make an analogy between heat transfer and electrical conduction in a stationary state. Throughout this study, the temperature is thus assimilated to the electric potential and the heat flux density is assimilated to the electric current density.

The calculations are carried out in the framework of large displacements. A steady-state coupled temperature-displacement analysis is performed using the ABAQUS®/Standard solver. "Temperatures" (i.e. values of the potential) are integrated using a backward-difference scheme, and the nonlinear coupled system is solved using Newton's method.

The indenter/film mechanical contact is defined as "hard" and "frictionless", which means that the penetration of the film surface into the tip surface is minimized. Concerning the electrical contact, the conduction is defined as "infinite" ("conductance" of 10^{23} $\Omega^{-1}.cm^{-2}$) when the distance between the surfaces of the indenter and the film is zero ("clearance" of 0 nm) and the conduction is specified as nil when the clearance is 1 nm or more.

The elements used to mesh the three parts are 3-node axisymmetric linear interpolation for displacement and temperature elements (CAX3T in ABAQUS®) with a size of 10 nm in the film and near the indenter/film and film/substrate interfaces. A convergence study (not shown) was carried out in order to check that the mesh was fine enough so that the results obtained were independent of the element size.

The post-processing consists of calculating mainly two quantities during the indentation: the mechanical force and the electrical current. The reaction force of the substrate to the displacement of the indenter (boundary condition) is determined by summing the vertical nodal reaction force components of the bottom surface of the substrate. The current induced by the electric potential bias (boundary condition) corresponds to the current flux crossing the film/indenter interface. Thus, both "force-displacement" mechanical loading curves and "current-displacement" electrical curves at fixed voltage can be plotted, as in the case of an experimental electrical-nanoindentation test.

A schematic summarizing the model parts, dimensions, boundary conditions and mesh is shown in Figure 3.1.

Concerning the mechanical behavior of the materials, the boron-doped diamond indenter and the (001)-oriented silicon substrate are assumed to be isotropic linear elastic. The Young's modulus and Poisson's ratio of these materials are well known and were fixed in the numerical model. The film is assumed to be elastic-plastic since residual imprints were measured by AFM even before the mechanical cracking associated with the first pop-in (see Section 3.3.2), which is the signature of a non-reversible deformation. Its elastic regime is described by an isotropic linear elastic law with a Poisson's ratio fixed at 0.2 [213]. As SiOCH undergoes non-reversible deformation under shear during mechanical loading, as well as nanoporosity densification under the effect of hydrostatic pressure, a yield criterion taking into account both effects is needed to properly model its plastic behavior. This is why a Drucker-Prager yield criterion was chosen. In the ABAQUS® software, we chose a linear Drucker-Prager law, with the yield surface defined as:

$$\sigma_{eq} - p\tan(\beta) - d = 0 \tag{3.1}$$

with p the hydrostatic pressure:

$$p = -\frac{1}{3}\mathrm{Tr}(\boldsymbol{\sigma}) \tag{3.2}$$

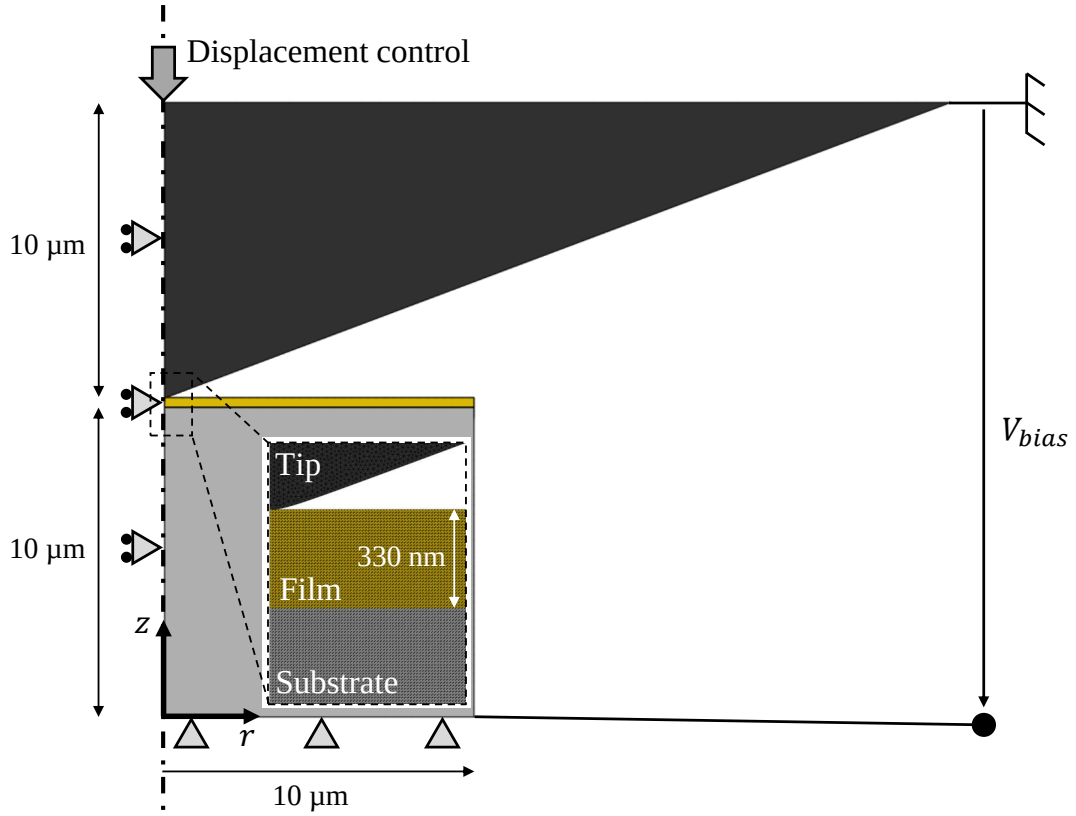

Figure 3.1. Numerical model for the FEM simulations.

and σ_{eq} the Mises equivalent stress:

$$\sigma_{eq} = \sqrt{\frac{3}{2}(\mathbf{S} : \mathbf{S})} \tag{3.3}$$

where $\mathbf{S}$ is the stress deviator:

$$\mathbf{S} = \boldsymbol{\sigma} + p\mathbf{I} \tag{3.4}$$

β is the slope of the linear yield surface in the $p - \sigma_{eq}$ stress plane (also called the internal friction angle of the material). Finally, d is called the cohesion parameter:

$$d = \left(1 - \frac{1}{3}\tan(\beta)\right)\sigma_c \tag{3.5}$$

where σ_c is the uniaxial compression yield stress.

Thanks to an inverse analysis methodology based on the experimental loading curves the following film properties were determined: its Young's modulus E, its friction angle β and its uniaxial compression yield stress σ_c.

First, the friction angle was determined by a method proposed by [54] which relates β to the irreversible work fraction W_{irr}/W_{tot} measured from the area under the experimental loading/unloading curves. Thus, an angle of 30°was identified.

The other two parameters (E and σ_c) were determined by fitting the simulated load versus penetration curve to the experimental one. However, if we consider σ_c to be independent of the plastic strain (i.e. plasticity without hardening), two problems seem to appear after the inverse analysis:

- The Young's modulus is out of the range estimated in the literature for a SiOCH film of a few hundred nanometers thickness with ~ 25 % of nanoporosities ($E \sim 8$ GPa according to [213]).
- The value of the uniaxial compression yield stress does not allow the material to enter its plastic domain from a few tens of nanometers of indentation as experimentally observed by AFM (see Section 3.3.2).

This is explained by the phenomenon of densification-induced hydrostatic hardening, which is known for amorphous silica [214, 215]. In our simulations, this effect is incorporated by using a linear hardening law relating the uniaxial compression stress σ_c to the equivalent plastic strain ϵ_{eq}^{pl}, such that:

$$\sigma_c = \sigma_{c0} + K\epsilon_{eq}^{pl} \tag{3.6}$$

with σ_{c0} the initial uniaxial compression yield stress and K the hardening modulus.

The σ_{c0} value was arbitrarily set at a low value of 100 MPa so that the material undergoes non-reversible deformations from the first tens of nanometers of indentation. Furthermore, it was noticed that for a Young's modulus varying around 8 GPa, the value of the hardening modulus also varied around this value. These moduli were therefore assumed to be equal. By adjusting them until the difference between the experimental and simulated load-depth curves is minimized, we obtained $E = K = 7.6$ GPa.

For understanding the value of K, note that the mechanisms governing plastic deformation in amorphous materials are quite different from those arising in metallic solids. In the latter case, the mechanisms are well known and rely on the pinning of dislocations, or the interaction between dislocation systems, resulting in shear-hardening slopes two orders of magnitude lower than the elastic modulus. In the case of amorphous silica, K and E have been found to be of the same order [214], so it is not surprising to reach a similar conclusion in our case.

Concerning the electrical behavior of the materials, that of the boron-doped diamond indenter and the (001)-oriented silicon substrate is assumed to be ohmic, while that of the SiOCH film is what we seek to identify. Nevertheless, the results are not sensitive to the electrical constitutive laws and properties of the indenter and the substrate because the film is much more resistive than the materials composing these two systems. Electrical transport is therefore limited by the film and not by the indenter or the substrate.

Table 3.1 gives all the material properties implemented in the numerical model.

By default, the steady state conduction law in ABAQUS® is Fourier's law, i.e. Ohm's law with our thermal-electrical analogy. The UMATHT subroutine was used to change this constitutive law in the SiOCH film. In this subroutine, two relations have to be defined: the heat flux density vector (current density vector) with respect to the spatial gradients of temperature (spatial gradients of electric potential) and the variation of this vector with respect to the gradients. Concerning the dependence of the conduction law on the mechanical strain, the USDFLD subroutine was also used. It allows the strain (defined at the element integration points) to be used as a field variable, to store it as a solution-dependent state variable, and finally to pass it into the UMATHT subroutine to integrate it into the conduction law.

Part / Material	Elastic properties		Plastic properties			Electrical properties
	E (GPa)	ν (-)	β (°)	σ_{c0} (MPa)	K (GPa)	σ_{Ohm} (Ω^{-1}.cm^{-1})
Indenter Boron-doped diamond	1140	0.07	None	None	None	0.1
Substrate (001)-oriented silicon	130	0.28	None	None	None	0.1
Film Nanoporous SiOCH	7.6	0.2	30	100	7.6	In this chapter

Table 3.1. Material properties used in FEM simulations.

3.2.4 Statistical analysis

The original sample was a 300 mm large microelectronic-type sample, which was cut into several 1×1 cm^2 pieces. The experiments were repeated several times (approximately 3-5 times, depending on the test under consideration) on multiple locations ($\sim$ 3-5 locations/pieces) on 4 different pieces. All raw results were similar, but the fine trends shown in this chapter could only be discriminated when comparing the results obtained on the same piece during the same experimental run. Comparison of "electrical" curves were only made on tests were the "mechanical" curves were identical. The extraction of the critical electrical and mechanical depths (Figures 3.4 and 3.5) were performed from graphical analysis, the reported data are the mean values over at least three tests carried out for each voltage, and error bars are calculated by standard deviation on these three values. The numerical fitting of the electrical curves (Figures 3.6 and 3.7) was performed by manual iteration until the maximum relative deviation falls below 10 % for each value of voltage and penetration depth. For each curve, the RMS relative deviation between numerical and experimental data was circa 5 % over the 30-180 nm range.

3.3 Results and Discussion

3.3.1 Electrical-nanoindentation experiments: overall description

Figure 3.2 reports a typical set of electrical-nanoindentation tests performed on the SiOCH/Si stack with a Berkovich tip under different voltages (from 1 to 100 V). For these tests, the maximum load was set to 45 mN, leading to typical penetration depths h of 700 nm. A schematic of the experiment defining the relevant dimensions is shown in Figure 3.2a. The lower part of Figure 3.2b reports the loading curves (load vs penetration depth) and the upper part reports the evolution of current flowing through the dielectric during indentation. For these experiments, the ammeter was set to "current autorange" mode so that the current would rise to compliance if needed (100 nA). During indentation, both the contact area A_c and the electric field $\boldsymbol{F}$ continuously increase: A_c increases because of the pyramidal shape of the tip but the case of $\boldsymbol{F}$ is slightly more complex. For a given penetration depth, $\boldsymbol{F}$ gradually decays along the tip radius (from the apex to the edge), but its maximum is always located at the tip apex,

where it strengthens during indentation because of the decrease in distance d. The initial electric field $\boldsymbol{F_0}$ can be defined as the electric field at the tip apex when indentation starts. Thus, $\boldsymbol{F_0}$ is the ratio between the applied voltage and the film thickness.

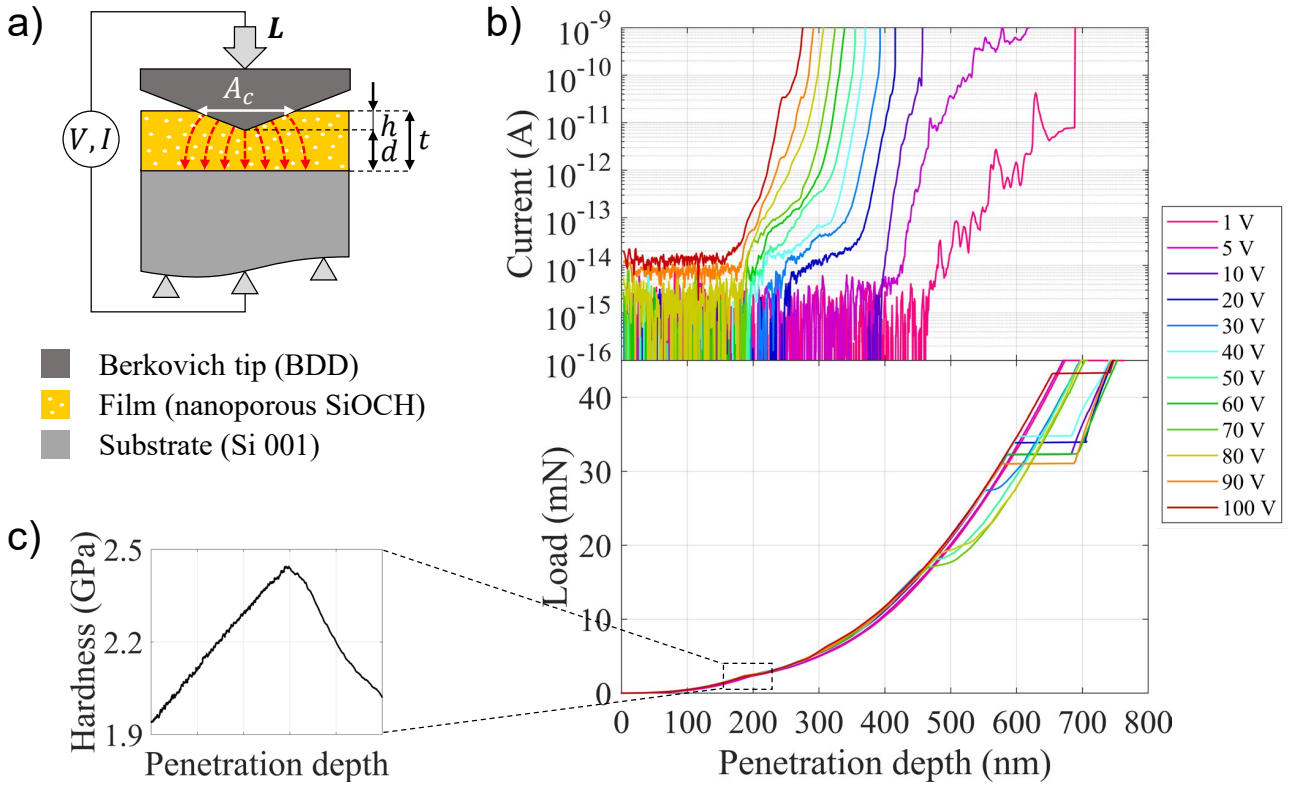

Figure 3.2. (a) Schematic of the electrical-nanoindentation experiments. The dotted red arrows represent the current lines, $\boldsymbol{L}$ is the applied mechanical load, h is the penetration depth of the tip into the material, A_c is the contact area, d is the distance between the tip apex and the substrate during indentation, and t is the initial thickness of the pristine film, 330 nm. (b) Upper curves: raw current-depth curves (before withdrawal of the open-circuit current) with the current scale cut off at 1 nA (i.e. before 100 nA compliance). Lower curves: corresponding load-depth curves. (c) Example of a hardness-depth curve on the first pop-in. Each electrical-nanoindentation curve represents a set of 5 tests.

3.3.2 Mechanical behavior and film damaging

From the mechanical point of view, two distinct stages can be identified on the loading curves:

- Stage 1. From 0 to $\sim$ 190 nm ($\sim$ 55 % of the film thickness), the loading curves are highly reproducible and follow a given curvature up to a slope change circa 190 nm. This curvature change (usually referred to as a "pop-in" feature) is the signature of a non-reversible mechanical event (brittle cracking, dislocation bursts, phase transformations, etc. [216, 217]). This pop-in is clearly observed on the hardness curves, where hardness drops sharply at pop-in (see Figure 3.2c). The onset of this pop-in is highly reproducible from test to test.
- Stage 2. From $\sim$ 190 nm to the final load, continuous loading with a lower power-law dependence is observed. This second stage is finally marked out by a second pop-in of much larger amplitude (abrupt tip penetration into the sample) and with more dispersed

characteristics (onset depth, amplitude, ...).

Dedicated indentations with intermediate final penetration depths were performed (Figure 3.3) to identify the mechanisms driving these loading curves. The series of tests were stopped: either before the first pop-in (at 50, 100 and 150 nm, left), after the first pop-in (at 200 nm, middle) or after the second pop-in (at 500 nm, right). The corresponding loading curves are given in Figures 3.3a,d,g, the residual imprints of shallow indents observed by AFM are shown in Figures 3.3b,c, and the residual imprints of deep indents observed by SEM after FIB-slicing in Figures 3.3e,f,h,j.

Figures 3.3b,c present the residual imprints of indents stopped before the first pop-in (50 and 100 nm on Figure 3.3b, and 150 nm on Figure 3.3c). The profiles of these imprints were measured by AFM over $2-3$ tests for each maximum depth. The residual depths of these imprints are $1-2$ nm for the 50 nm indentations, $9-11$ nm for the 100 nm indentations, and $25-35$ nm for the 150 nm indentations. The existence of residual imprints after tip removal means that non-reversible deformation of the SiOCH films is initiated at the earliest stages of indentation (at least from 50 nm of penetration depth). The non-reversibility is confirmed by the hysteretic behavior of the loading/unloading curves in Figure 3.3a. In the following, we will refer to this non-reversibility by the term "plasticity", which here gives no information on the irreversible deformation mechanism.

Figures 3.3e,f present the residual imprints left right after the first pop-in (final penetration depth of 200 nm). The three-pointed star shape of the imprint (enclosed in an area of typically 1 µm radius) shows that the mechanical event responsible for this first pop-in is a crack in the SiOCH film initiated along the indenter edges. This observation is in accordance with the reported data [167, 169, 218]. Figure 3.3d magnifies the pop-in feature shown in Figure 3.3b.

Figures 3.3h,i present the residual imprints after the second pop-in (final penetration depth of 500 nm). These images show spalling of the SiOCH film, as reported in the literature [70, 218, 219]. Furthermore, the SiOCH material at the indent center remained trapped by the indenter apex (indicated on Figure 3.3i). Finally, the underlying Si substrate remained in its elastic domain throughout the test, as no residual plastic deformation is observed.

3.3.3 Electrical response

In terms of electrical response, all the current curves of Figure 3.3.3b can be described as follows. First, the current remains quite steady at a low base level (in the range of several fA), then it increases continuously over several decades, and it finally undergoes a steep rise. In the initial regime, the steady state current is actually equal to the set-up open-circuit current. This open-circuit offset will be withdrawn from the raw data in the following analysis. Within this initial regime, the actual leakage current that flows through the SiOCH film is concealed by this base level. This is no longer the case during the second regime, where leakage through the film overtakes this open-circuit base level. It can be clearly seen that the higher the voltage, the earlier the detection of this leakage current. Moreover, the apparent slopes gradually increase with the applied voltage: from 3 decades/100 nm to 3 decades/200 nm from 1 to 100 V, respectively. Finally, current reaches the apparatus compliance level (100 nA) shortly after the final steep rise. This "compliance" saturation cannot be seen in the figure as the graph scale is cut at 1 nA in order to emphasize the low-level signals.

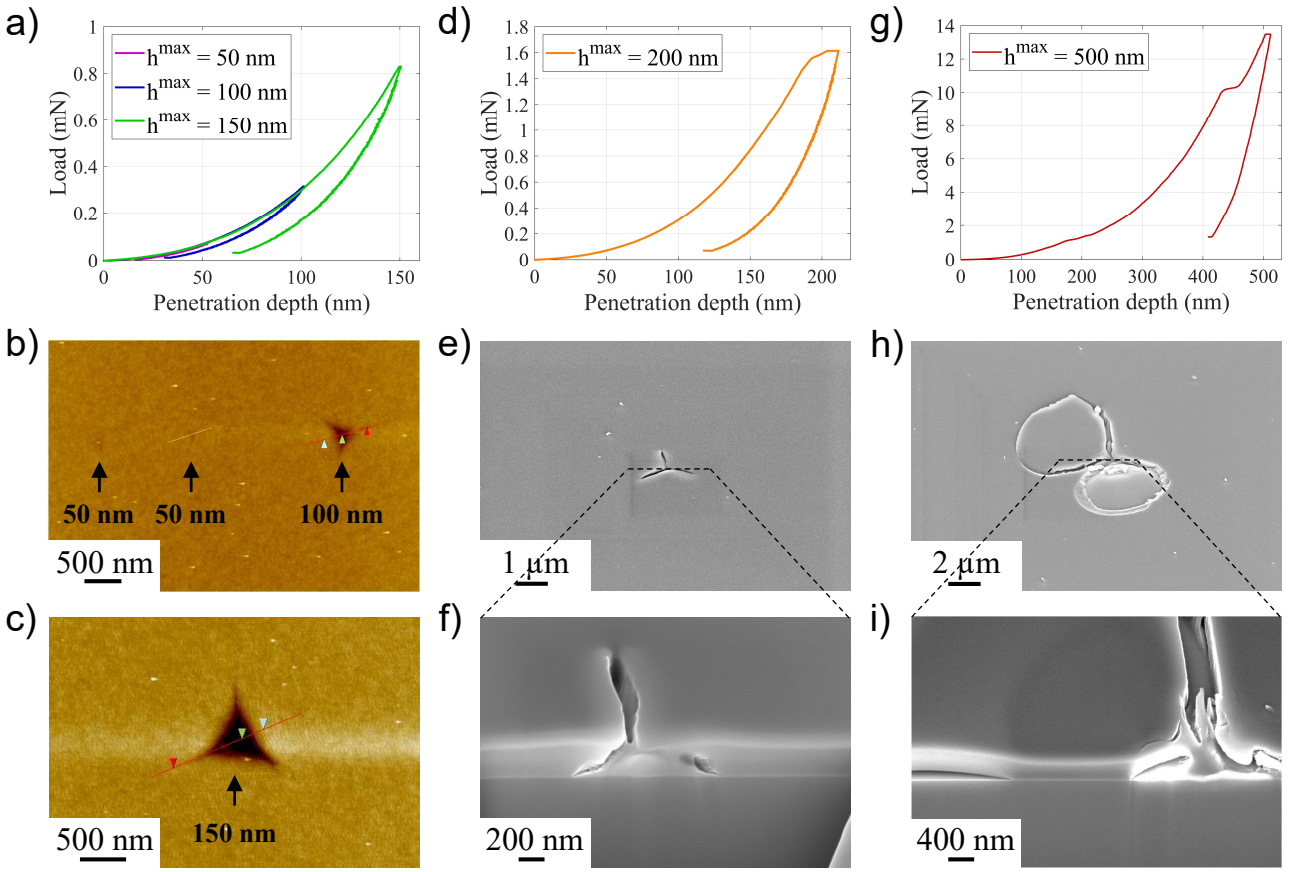

Figure 3.3. (a) Load-depth curves for maximum indentation depths of 50, 100 and 150 nm. (b) AFM image of the residual indents for indentation depths of 50, 100 nm and (c) 150 nm. (d) Load-depth curve for a maximum indentation depth of 200 nm. (e) SEM image of the residual indent at 200 nm indentation depth viewed from the surface and (f) in cross-section after FIB-slicing. (g) Load-depth curve for a maximum indentation depth of 500 nm. (h) SEM image of the residual indent at 500 nm indentation depth viewed from the surface and (i) in cross-section after FIB-slicing. Each loading curve represents a set of 5 tests.

3.3.4 Correlation between mechanical damage and electrical leakage

Another set of experiments was performed with the ammeter in a "fixed current range" mode (from 1 to 1000 fA, depending on the test conditions) to finely distinguish the onset of electrical and mechanical failures at the earliest indentation stages. Under such conditions, current cannot be explored up to the compliance level (it is only limited by the current range) but the signal-to-noise ratio is improved by one order of magnitude. Voltages between 1 and 120 V were applied in steps of 5 V. Each indent, at fixed voltage, was repeated 3 times to ensure good reproducibility. In each test, the open-circuit current was measured before the tip reached the sample surface and was subtracted from the current measured during indentation. Current curves were finally smoothed by a moving average over 300 points (i.e. about 20 nm of penetration depth).

As an illustration, Figure 3.4 reports the current-depth and load-depth curves for indentations performed under 5 V (Figure 3.4a) and 70 V (Figure 3.4b). Both the mechanical and electrical responses display sharp changes on their related curves: a pop-in feature on the mechanical curve and a significant current rise on the electrical curve. Consequently, two critical depths can be defined:

- Critical mechanical depth h_C^{Mech}. This critical depth corresponds to the first pop-in depth, i.e. to the onset of mechanical failure of the film. h_C^{Mech} is highly reproducible from test to test and equals $\sim$ 190 nm. For the sake of precision, h_C^{Mech} was extracted at the hardness peak (Figure 3.2c).
- Critical electrical depth h_C^{Elec}. This critical depth corresponds to the depth from which leakage current overtakes the base level. h_C^{Elec} depends strongly on the applied voltage as shown in Figure 3.4, where $h_C^{Elec} \sim 285$ nm under 5 V (i.e. greater than h_C^{Mech}), while $h_C^{Elec} \sim 110$ nm under 70 V (i.e. lower than h_C^{Mech}).

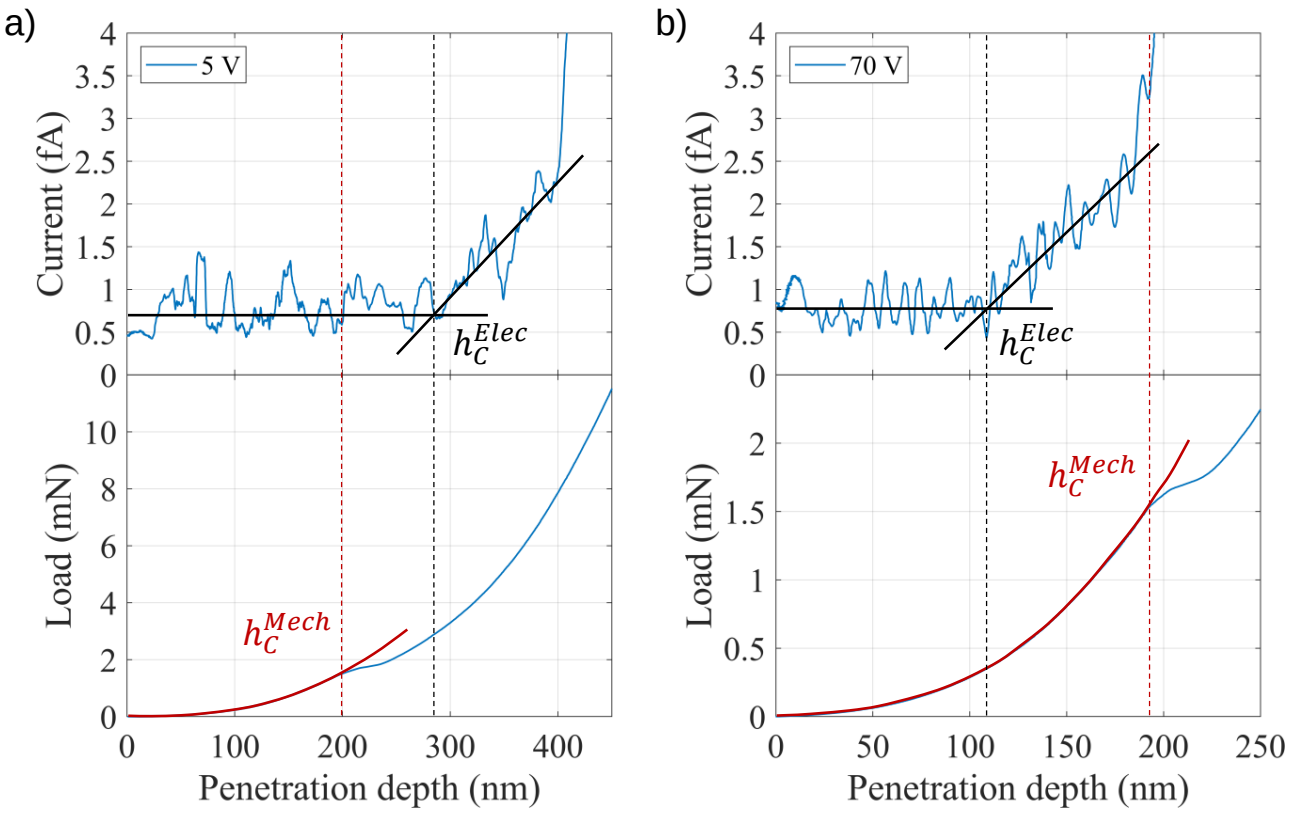

Figure 3.4. Changes in current and load versus penetration depth (a) for a voltage of 5 V (case where $h_C^{Elec} > h_C^{Mech}$) and (b) for a voltage of 70 V (case where $h_C^{Elec} < h_C^{Mech}$).

After extraction of h_C^{Elec} and h_C^{Mech} for each indentation test (i.e. for each voltage), their difference $h_C^{Elec} - h_C^{Mech}$ can be plotted against the applied voltage (Figure 3.5). With this representation, leakage onset and mechanical failure can be related to the electric field applied. Four cases can be identified (described below from small to large voltages).

- From 1 to 10 V: $h_C^{Elec} > h_C^{Mech}$. With low voltages, current leakage through the dielectric is detected after the film cracking along the tip edges (Figure 3.3e). Note that the higher the applied voltage, the earlier the leakage current is detected, which is consistent with an increase in leakage currents under larger electric fields.
- From 10 to 50 V: $h_C^{Elec} = h_C^{Mech}$. In this voltage range, a zero-dwell is observed: film cracking actually triggers leakage currents through the dielectric. This leakage triggering can be attributed to the multiplication of electrical traps that form conduction paths along the crack side-walls.
- From 50 to 90 V: $h_C^{Elec} < h_C^{Mech}$. In this voltage range, leakage current through the SiOCH film is detected before the first pop-in occurs. As in the low voltage range, the higher the applied voltage, the earlier the onset of leakage. Furthermore, two different curvatures can be observed, with a slope change occurring at 75 V. This point will be fully explained in Section 3.3.11 in terms of damage and current line distributions in the SiOCH film.
- From 90 to 120 V: $h_C^{Elec} = 0$. In this high voltage range, leakage current through the SiOCH film is detectable as soon as tip/sample contact is established. As both h_C^{Elec} and h_C^{Mech} are constant in this case, their difference is also constant and equal to ~ -190 nm. This range is of particular interest as it can be used to drive a detailed description of the electrical conduction regime (large analyzable indentation range, no mechanical instability such as film cracking, etc.). The following description of electrical conduction analyses this voltage range, even though the results will explain Figure 3.5 as a whole.

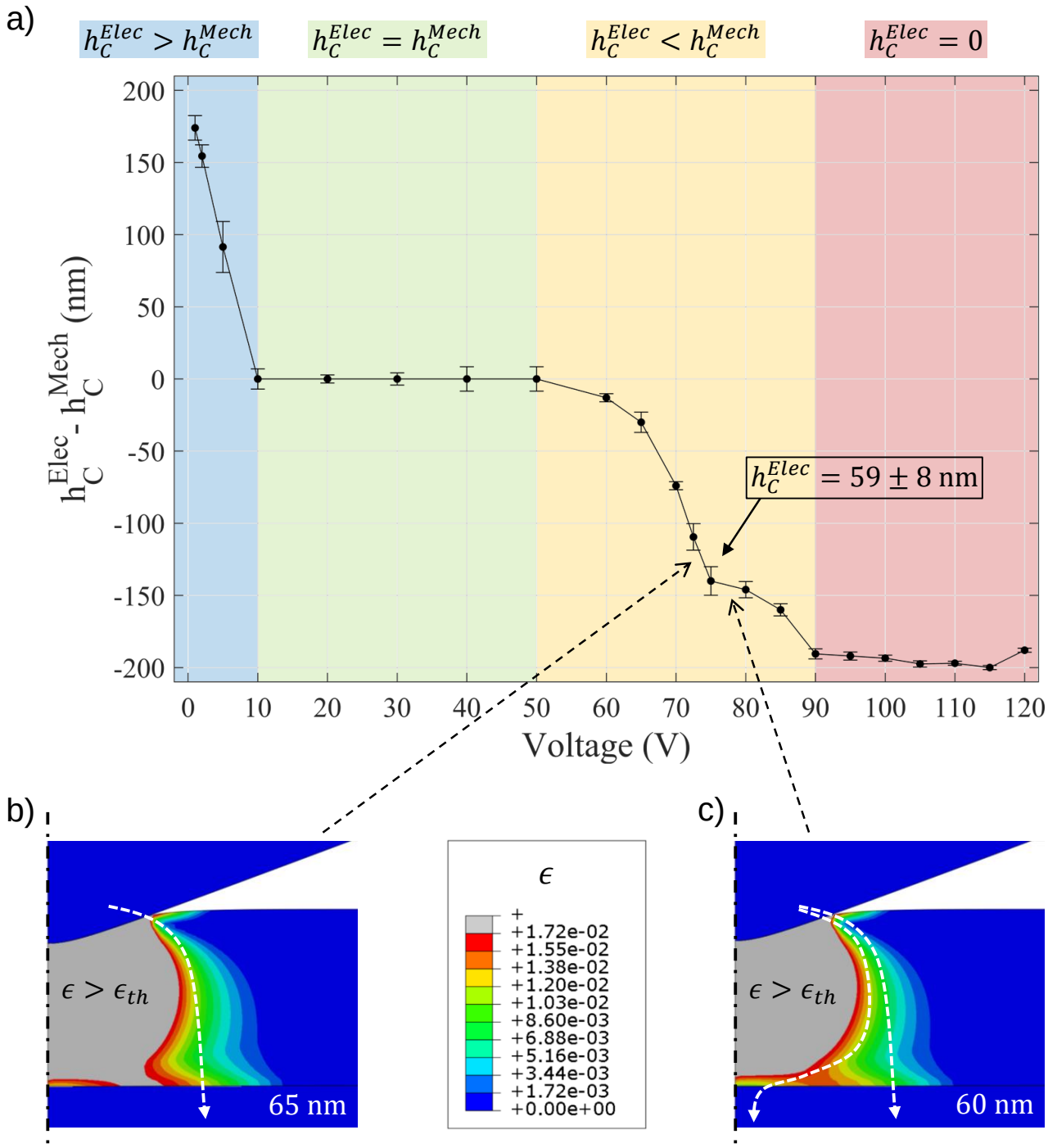

Figure 3.5. (a) Difference between electrical and mechanical critical depths versus the applied voltage. Each point is the average over three tests carried out for each voltage, and error bars are calculated by standard deviation on these three values. (b) Snapshot at 65 nm depth of the maximum principal plastic strain in the film, thresholded so that the gray area corresponds to the area where strain exceeds the threshold strain ϵ_{th}. Current lines (white dashed arrow) follow a unique path. (c) Snapshot at 60 nm depth of the maximum principal plastic strain in the film, thresholded so that the gray area corresponds to the area where strain exceeds the threshold strain ϵ_{th}. Current lines (white dashed arrows) follow two possible paths.

3.3.5 Electrical conduction behavior at high electric fields

Figure 3.6 reports the current-depth curves obtained by indenting the SiOCH film under voltages between 90 and 115 V. The solid lines are experimental data. In this voltage regime, the initial electric field F_0 ranges from 2.6 to 3.5 MV/cm. Data are only represented up to 200 nm, as the response beyond mechanical cracking (circa 190 nm) is of no interest for this analysis. On all the curves, a significant increase in current is observed at the earliest stages (up to $60 - 70$ nm). The trend is consistent with the increase in both the contact area and the electric field. Then, current further increases but with a gentler slope, or even saturates at the highest voltages ($105 - 115$ V) before decreasing. This behavior is unexpected as both the contact area and electric field carry on increasing during indentation. Finally, beyond 190 nm, the current sharply increases due to film cracking.

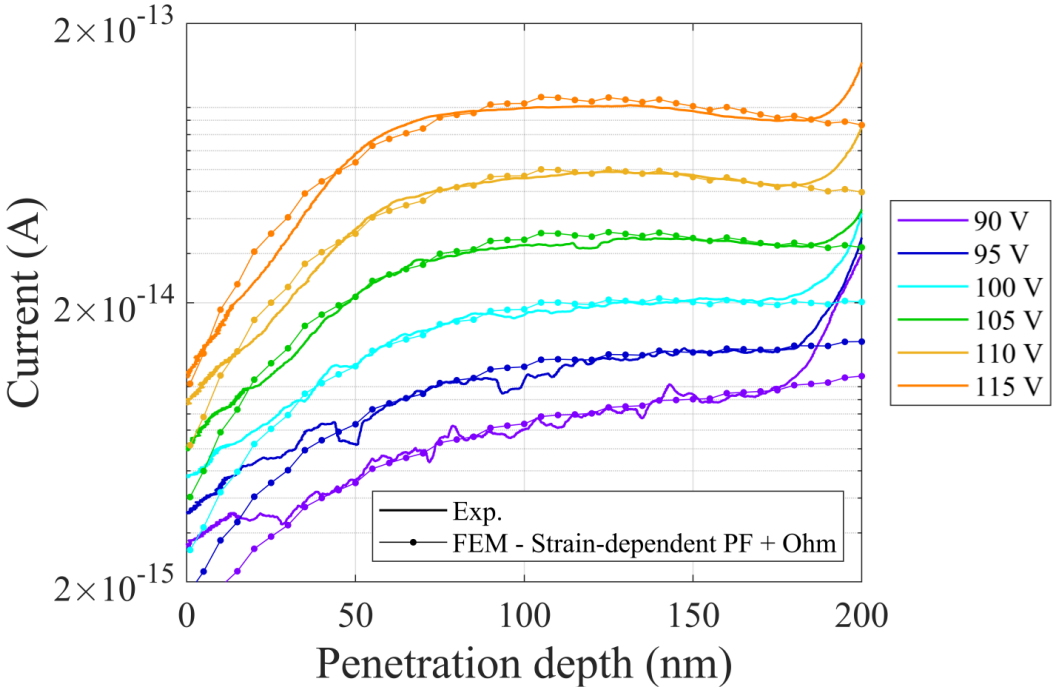

Figure 3.6. Comparison of experimental and numerical current-depth curves, with the model taking into account both strain-dependent Poole-Frenkel and Ohmic conduction, for applied voltages between 90 and 115 V. For each curve, the RMS relative deviation between numerical and experimental data was ~ 5 % over the 30-180 nm range.

3.3.6 Conduction mechanism modeling

Electrical conduction mechanisms in dielectric films have been widely studied in the literature [115, 220, 221]. The most widely reported mechanisms for electrical transport in ultra-low-k films are essentially Ohmic, Poole-Frenkel or Schottky conductions depending on the electric field range, the chemistry of the injecting electrode or the dielectric barrier, ... [188, 189, 222] Ohmic conduction is usually observed in low field ranges [201, 223, 224]. It only depends on the constant carrier density and mobility, leading to a linear relationship between current density and electric field. In contrast, Poole-Frenkel and Schottky conductions are highly non-linear: the emission of free carriers is promoted by the local electric field through the lowering of an energy barrier. In the case of Poole-Frenkel conduction, carriers are emitted from traps in the

dielectric bulk, while Schottky conduction is an interface-controlled mechanism. The following analysis will focus on Poole-Frenkel conduction, as it is widely accepted to be the driving mechanism in porous SiOCH films at high electric fields. Poole-Frenkel conduction is described by the following relationship between current density $\boldsymbol{J}$ and electric field $\boldsymbol{F}$ (Equation 3.7).

$$\boldsymbol{J} = C \exp\left(-\frac{\Phi}{r k_B T}\right) \exp\left(\frac{q^{3/2}/\sqrt{\pi \varepsilon_0 k}}{r k_B T} \sqrt{\|\boldsymbol{F}\|}\right) \boldsymbol{F} \tag{3.7}$$

In this equation: C is a coefficient that depends essentially on the elementary electric charge, the carrier mobility, the effective density of states and the donor-like and/or acceptor-like trap density; ε_0, k_B, and T are the vacuum permittivity, the Boltzmann constant and the temperature respectively; Φ is the zero-field trap barrier; k is the relative dielectric constant; r is the compensation factor between 1 and 2 [225–227]; the second exponential factor represents the lowering of the Poole-Frenkel barrier, expressed as the square-root of the electric field.

This analytical law was implemented in the numerical model presented in the Section 3.2.3 to describe electrical conduction through the SiOCH film. In the numerical simulations, mechanical displacement and voltage are imposed, while mechanical load and electrical current are extracted. The zero-field trap barrier and the dielectric constant values were set to 0.95 eV and 2.5 respectively, in accordance with previous studies [184]. The compensation factor r, which must be physically between 1 and 2, was initially set to 1.5. Finally, the C factor was chosen arbitrarily to match the current level at the beginning of indentation (i.e. before any mechanical/electrical damage). Figure 3.7a compares the experimental and simulated current-depth curves under 115 V (solid line and markers, respectively). The modeled Poole-Frenkel current (i) increases monotonically throughout indentation, and (ii) increases much faster than the experimental current. Even though this fast current increase is explained by the exponential dependence of current density on electric field (Equation 3.7), the authors propose that the steep fall in conduction between the experimental data and the standard Poole-Frenkel model is due to mechanical degradation of the SiOCH film. For testing this hypothesis, the ratio between the experimental and calculated currents (referred to hereafter as "current ratio") was extracted at different depths (from 40 to 160 nm) and then plotted against a "representative strain" ϵ_{Rep} (Figure 3.7b). An exponential relationship is clearly observed. The significance of this "representative strain" must now be given. During indentation, the film undergoes gradual plastic deformation (Figure 3.3) described by an extended maximum principal plastic strain field at a given depth. To represent this heterogeneous strain field with a simple scalar quantity, the maximum of this mechanical field was extracted from the FEM results and then modulated by a numerical factor, which leads to our "representative strain". The choice of the maximum principal plastic strain as indicator to quantify the impact of plasticity on conductivity and the methodology used to determine the numerical factor for the representative strain are discussed in Sections 3.3.7 and 3.3.8 respectively. The strong correlation between electrical conduction and mechanical deformation having been identified, a correction of the original Poole-Frenkel law is proposed by the authors (Equation 3.8). It is a threshold constitutive law based on the maximum principal plastic strain ϵ: if this exceeds a threshold strain ϵ_{th}, then the original Poole-Frenkel law is scaled by a decreasing strain exponential $\exp(1 - \epsilon/\epsilon_{th})$.

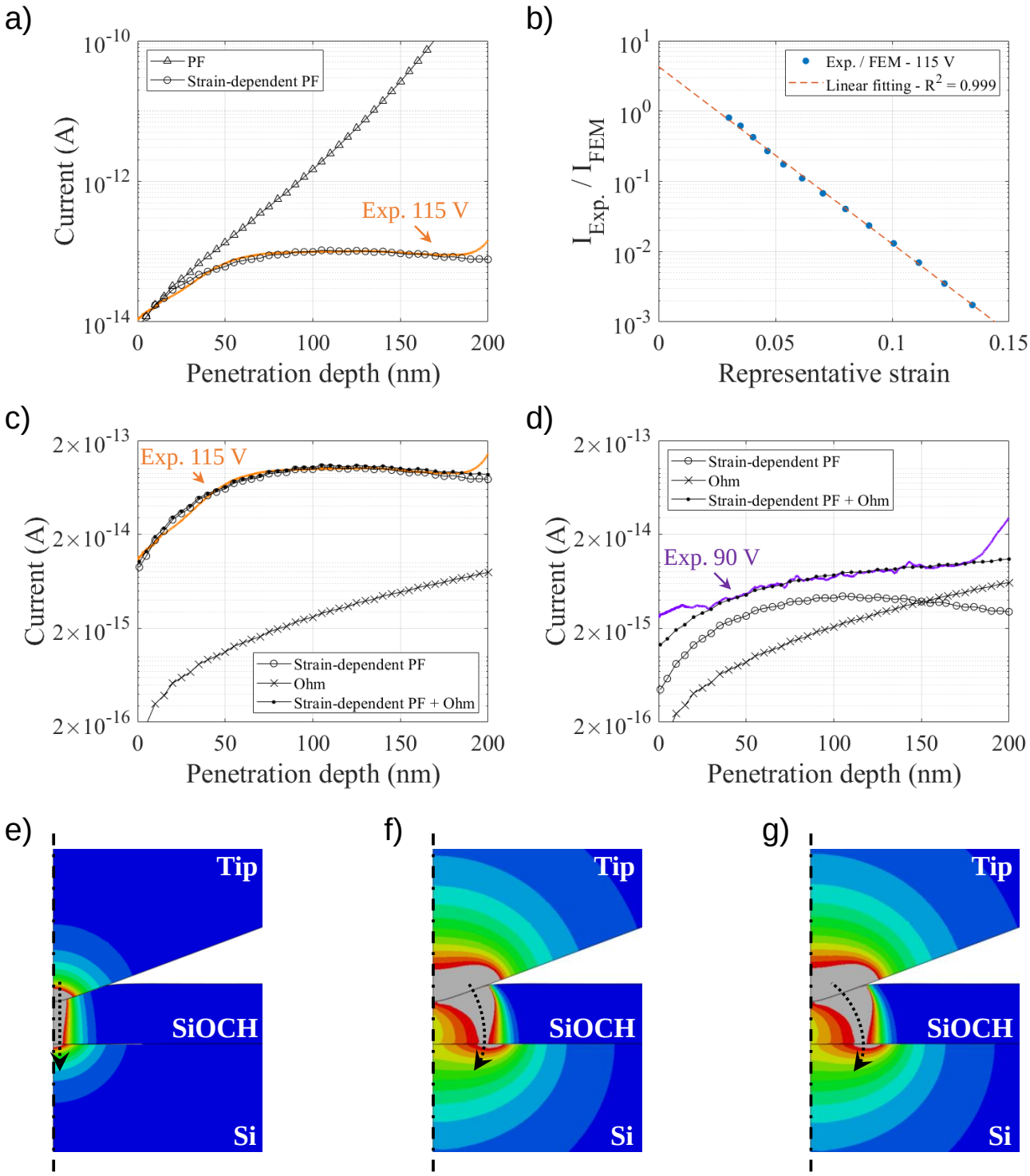

Figure 3.7. (a) Comparison of experimental and numerical current-depth curves with the "Poole-Frenkel" and "Strain-dependent Poole-Frenkel" models for an applied voltage of 115 V. (b) Linear fitting of the "current ratio" logarithm as a function of the representative strain. (c) Comparison of experimental and numerical current-depth curves with the "Strain-dependent Poole-Frenkel", "Ohm" and "Strain-dependent Poole-Frenkel + Ohm" models for an applied voltage of 115 V and (d) for an applied voltage of 90 V. (e) Current line distribution (shown by the black dashed arrows) at 100 nm indentation depth for the "Poole-Frenkel", (f) "Strain-dependent Poole-Frenkel" and (g) "Strain-dependent Poole-Frenkel + Ohm" models. These current density maps are arbitrarily thresholded so that the gray areas are those in which the majority of the current lines flow. On (a), (c) and (d), the RMS relative deviation between numerical and experimental data is ~ 5 % over the 30-180 nm range.

This phenomenological law was implemented in the FEM numerical model. The resulting current curve corresponds to the circular markers denoted "Strain-dependent PF" in Figure 3.7. The only new adjustable parameter is the threshold strain ϵ_{th} which reflects the curvature of the current-depth curve. An optimized threshold strain of 0.0172 was obtained, leading to a typical relative deviation between calculation and experiment below 10 %.

Such a simple modification of the Poole-Frenkel law reproduces the unexpected current decrease at deep penetrations.

If $\epsilon > \epsilon_{th}$:

$$\boldsymbol{J} = C \exp\left(-\frac{\Phi}{r k_B T}\right) \exp\left(1 - \frac{\epsilon}{\epsilon_{th}}\right) \exp\left(\frac{q^{3/2}/\sqrt{\pi \varepsilon_0 k}}{r k_B T} \sqrt{\|\boldsymbol{F}\|}\right) \boldsymbol{F} \tag{3.8}$$

Equation 3.8 is then introduced in the numerical model where, for a given indentation depth, the strain ϵ is no longer chosen arbitrarily from the entire strain field, but corresponds to the local strain defined in each element integration point.

3.3.7 Choice of the strain measurement criterion

Figures 3.8a,b,c,d represent the strain fields at 120 nm indentation depth of maximum principal strain, maximum principal elastic strain, maximum principal plastic strain and equivalent plastic strain respectively.

First, the elastic strain level is $\sim$ 10 % of the plastic strain and the distribution of the maximum principal strain is largely driven by that of the maximum principal plastic strain (see the comparison between Figures 3.8a,b,c). The impact of the elastic contribution can therefore be safely neglected, which is in agreement with the literature [202, 203] where only weak modulations of conductivity have been reported in the reversible domain.

Then, the choice that was made between maximum principal plastic strain and equivalent plastic strain as a criterion for strain intensity measurement can be discussed. Figure 3.8c shows that the maximum principal plastic strain field has a notable particularity: it is always in tension (i.e. $\epsilon > 0$), which corresponds to the radial component of the strain tensor in an axisymmetric framework. On the one hand, this tensile plastic strain is believed to contribute to the breaking of atomic bonds in the porous material through nanopore growth and/or nucleation. Those dangling bonds, in turn, will interfere with the conductive mechanism as discussed in Section 3.3.9. On the other hand, equivalent plastic strain (Figure 3.8d) is a measure of shear, which can also lead to the generation of dangling bonds. By comparing Figures 3.8c,d, the FEM calculations indicate that the maximum principal plastic strain and equivalent plastic strain distributions are similar and their levels are close. Moreover, Figure 3.8e shows that all "plastic approaches" reproduce the experimental curve by adjusting the threshold strain by less than 10 %. It is therefore impossible to determine which one prevails.

Finally, the exact mechanism that produces these dangling bonds (shear or nanopore growth and/or nucleation) cannot be identified at this point. The authors chose the maximum principal plastic strain on the hint that the porous nature of the material might play a role in the observed behavior.

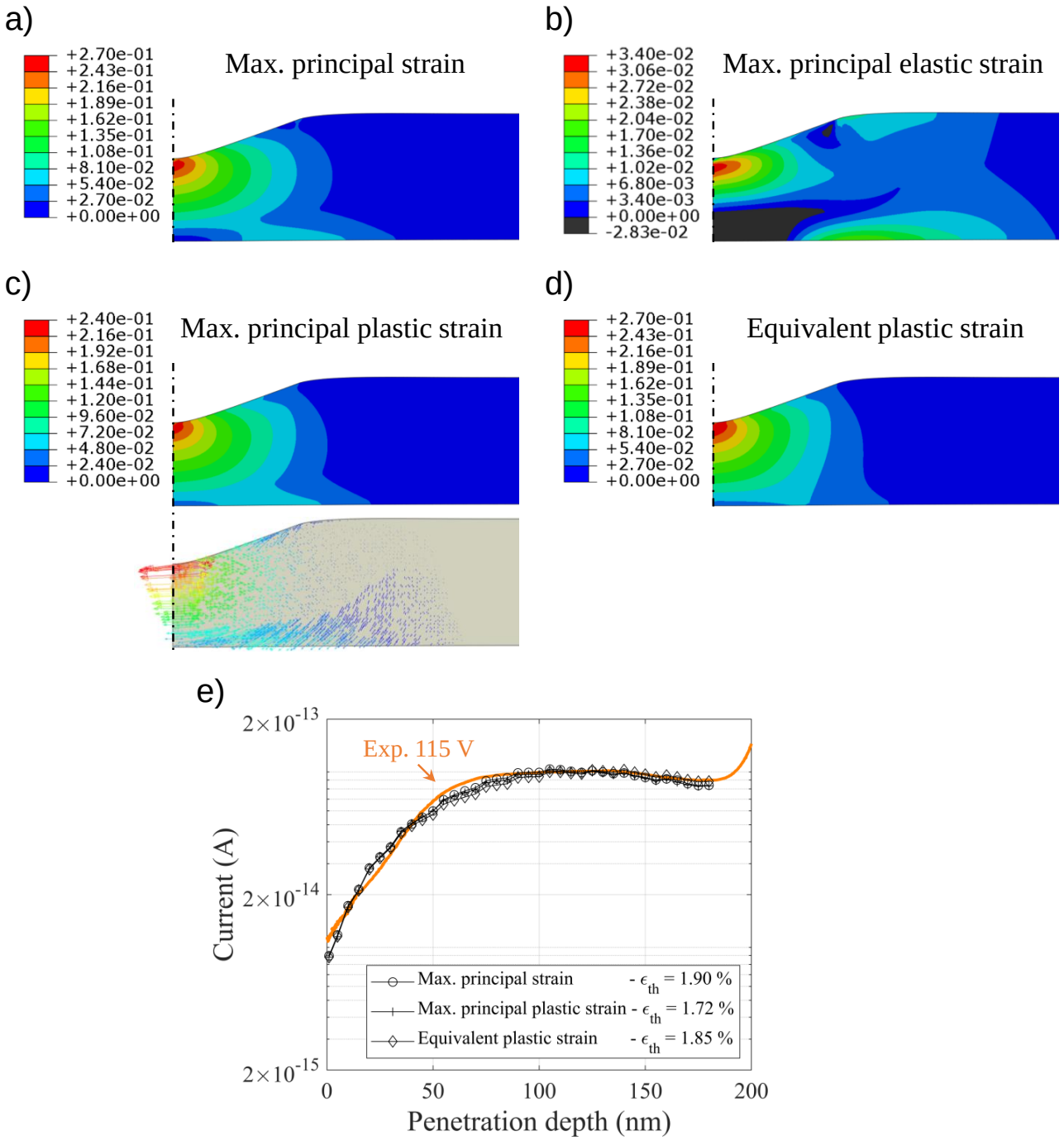

Figure 3.8. Strain fields at 120 nm indentation depth, representing (a) the maximum principal strain, (b) the maximum principal elastic strain, (c) the maximum principal plastic strain and (d) the equivalent plastic strain. (e) Calculations from the strain-dependent Poole-Frenkel model considering different strain fields (maximum principal strain, maximum principal plastic strain, equivalent plastic strain), all matching the experimental current-depth curve at 115 V by adjusting the threshold strain by less than 10 %.

3.3.8 Meaning of the representative strain ϵ_{Rep}

At each indentation step, the strain field underneath the indenter is fully determined by numerical modeling. Consequently, the maximum value of this strain field can be easily extracted, and the plot of the "current ratio" against this maximum strain at each step can be performed (Figure 3.9). However, this maximum strain is not the most relevant magnitude

as it does not represent trustfully the strain field. A more physical approach is to modulate this magnitude by a numerical factor to obtain a representative scalar for this strain field. Any numerical factor would be acceptable and would not change the physical meaning of the present rationale. Among these factors, the 2.56 figure allows the slope of the "current ratio vs strain" curve to match the threshold strain of 1.72 % extracted independently.

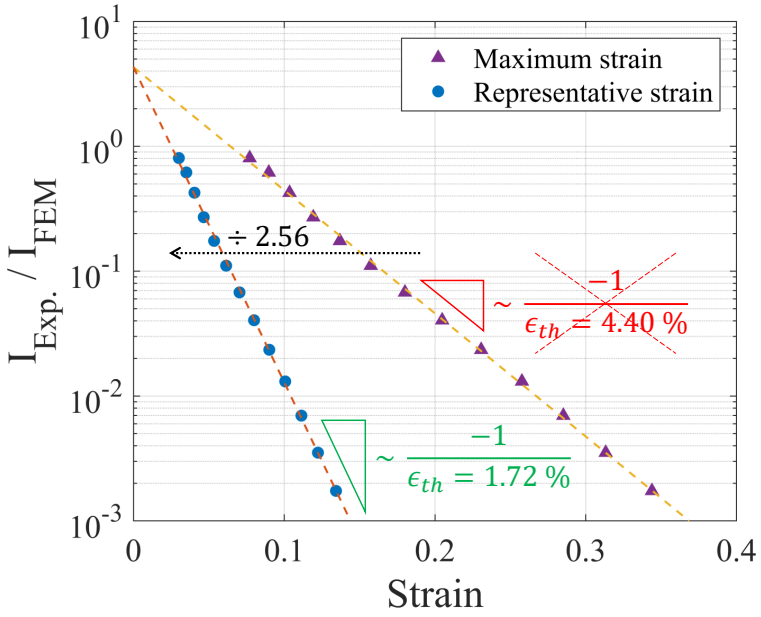

Figure 3.9. "Current ratio" vs the "maximum strain" (triangular markers) and the "representative strain" (circular markers).

3.3.9 Meaning of the strain-dependent Poole-Frenkel correction

The impact of mechanical stress on trap-assisted conduction mechanisms has been rarely explored in the literature. In most studies, applied stresses were kept within their reversible domain, and tensile stresses were found to increase the leakage current (with the notable exception of [228]). The reasons given for this tendency were either the lowering of the trap energy barrier [202, 203], or the change in apparent band gap [229, 230]. In contrast, in the present case, the mechanical stress level goes beyond the reversible regime (plasticity is triggered at the earliest stages of indentation) and conduction is seen to decrease when tensile stress increases. The authors propose that the production of structural defects is the origin of this electrical conduction drop.

As already discussed, indentation induces large plastic strains within the dielectric film (Figure 3.3). In crystalline materials, plastic deformation relies on the gliding of dislocations, while it occurs through the breaking of atomic bonds under shear and/or tensile stresses in amorphous iono-covalent solids [231–233]. From the electrical point of view, these dangling bonds are known to behave as electron/hole traps in dielectrics [189, 202, 234, 235]. These defects are gradually added to the defects already present at low densities [191, 229, 236]. In the present system, when a positive voltage is applied to the p-type silicon substrate, holes are injected into the SiOCH and flow all through the film up to the grounded p-type diamond tip. As holes travel through the dielectric, some are trapped by these dangling bonds, thus leading to a build-up of the space charge. This current-induced space charge finally modifies the electric field distribution within the SiOCH film [237]. Figure 3.10a presents the band diagram of the

Si/SiOCH/C system under a bias of 100 V. It was calculated analytically from the integration of Gauss's law with or without space charge, i.e. with or without charged traps (dashed or solid lines, respectively):

$$\mathrm{div}(\boldsymbol{F}) = \frac{\rho}{\varepsilon_0 k} \tag{3.9}$$

and from the relationship between potential and electric field:

$$\boldsymbol{F} = -\mathbf{grad}(V) \tag{3.10}$$

with $\boldsymbol{F}$ the electric field, ρ the local charge density, k the SiOCH relative permittivity and V the electrostatic potential. The local charge density is controlled by the trap density N_T:

$$\rho = eN_T \tag{3.11}$$

The external bias V_{App} is applied to the silicon substrate, while the reference bias 0 is applied to the diamond tip.

The system boundary conditions are in 0: $V(0) = V_{App}$; and in t: $V(t) = 0$.

Finally, one can obtain the following expressions:

$$F(x) = \frac{V_{App}}{t} + \frac{eN_T}{\varepsilon_0 k}\left(x - \frac{t}{2}\right) \tag{3.12}$$

$$V(x) = V_{App} - F_0(N_T)x - \frac{eN_T}{2\varepsilon_0 k}x^2 \tag{3.13}$$

with:

$$F_0(N_T) = \frac{V_{App}}{t} - \frac{eN_T}{\varepsilon_0 k}t \tag{3.14}$$

The impact of the trap density on Poole-Frenkel emission should be calculated at the vicinity of the injecting electrode (silicon substrate). Several distances to this electrode were tested, leading to similar results. The results presented here were obtained at a distance where electrical screening fades, at the Debye length λ_D:

$$\lambda_D = \sqrt{\frac{\varepsilon_0 k k_B T}{e^2 N_T}} \tag{3.15}$$

Finally, the increment in Poole-Frenkel barrier lowering due to the traps was calculated from the difference between the actual barrier lowering (with space charge) and the original Poole-Frenkel barrier lowering (without space charge):

$$\Delta\Phi_{SC} = \sqrt{\frac{eF(\lambda_D)}{\pi\varepsilon}}e - \sqrt{\frac{eV_{App}/t}{\pi\varepsilon}}e \tag{3.16}$$

A trap density N_T of 2×10^{17} cm^{-3} was considered. The introduction of this space charge adds a quadratic contribution to the initially linear hole energy profile. As can be seen in Figure 3.10b, this quadratic term reduces the slope of the band bending in the vicinity of the Si/SiOCH interface, where holes are injected. This reduction in slope corresponds to the

decrease in local electric field. In other words, hole conduction is hampered when trap density increases. This hampering process promotes better conduction along other paths (where trap density is lower) or low-electric field conduction mechanisms (such as Ohmic conduction). We will now focus on the hole-trap interaction energy at atomic scale (Figure 3.10c). The Poole-Frenkel mechanism relies on the lowering of the effective trap barrier by the local electric field [238]. However, if the local electric field decreases (because of the space charge effect), barrier lowering also decreases (by an amount $\Delta\Phi_{SC}(N_T)$, indicated in Figure 3.10c), thus leading to an apparent decay of Poole-Frenkel emission. This trend is in full agreement with Figure 3.7a: Poole-Frenkel conduction tends to weaken as indentation proceeds. The authors believe that the strain-related scaling factor $\exp(1-\epsilon/\epsilon_{th})$ introduced in Equation 3.8 is behind this alteration in conduction. In this equation, if the first two exponentials are merged, the ϵ/ϵ_{th} term appears as an apparent increase in the trap barrier, as shown in Equation 3.17 and Equation 3.18 ($\epsilon > 0$ as strain is tensile).

$$\exp\left(-\frac{\Phi}{rk_BT}\right)\exp\left(1-\frac{\epsilon}{\epsilon_{th}}\right)=\exp\left(1-\frac{\Phi+\Delta\Phi_{Strain}(\epsilon)}{rk_BT}\right) \tag{3.17}$$

with:

$$\Delta\Phi_{Strain}(\epsilon)=rk_BT\frac{\epsilon}{\epsilon_{th}} \tag{3.18}$$

These two approaches can now be related: the strain-related scaling factor (with $\Delta\Phi_{Strain}(\epsilon)$ obtained by FEM) and the space-charge-related decay of Poole-Frenkel emission (with $\Delta\Phi_{SC}(N_T)$ obtained by integrating Gauss's law). To do so, the following procedure was applied. First, the "representative strain" ϵ_{Rep} was extracted from the FEM calculations at every 10 nm of indentation (from 50 to 200 nm). Then it was converted into $\Delta\Phi_{Strain}(\epsilon_{Rep})$ thanks to Equation 3.18. Additionally, the analytical space charge approach was used to calculate $\Delta\Phi_{SC}(N_T)$ throughout the SiOCH film, and then extracted at a short distance from the Si/SiOCH interface (at the Debye length, where electrical screening fades). Finally, by simple inverse analysis, the trap density N_T required to equalize $\Delta\Phi_{Strain}(\epsilon_{Rep})$ and $\Delta\Phi_{SC}(N_T)$ was extracted by iteration. Consequently, the dependence of trap density N_T on the "representative strain" ϵ_{Rep} can be plotted (Figure 3.10d in log-log scale). A simple power-law relationship is clearly observed, with a power exponent $n = 1.75$ (Equation 3.19).

$$N_T \sim \epsilon_{Rep}^{1.75} \tag{3.19}$$

In terms of defect density, the order of magnitude for N_T falls within the $10^{16}-10^{18}$ cm^{-3} range, which is in close agreement with previously reported data for comparable leakages, thus supporting the relevance of the present procedure [191, 192]. In our approach, the production of defects by electrical stress was not considered [192, 239, 240]. Indeed, the electrical stress conditions (charge fluence, current density, electric field, ...) in these works were much more severe than in the present work, where the production of defects by mechanical stress should prevail. Finally, this proposed apparent barrier increase with defect density is opposite to the trend observed with the overlap of neighboring potential fields [223, 241]. This point is coherent with our considerations: while these works consider the ability of carriers to hop from full-site to empty-site, we consider the effect of space-charge on the emission barrier.

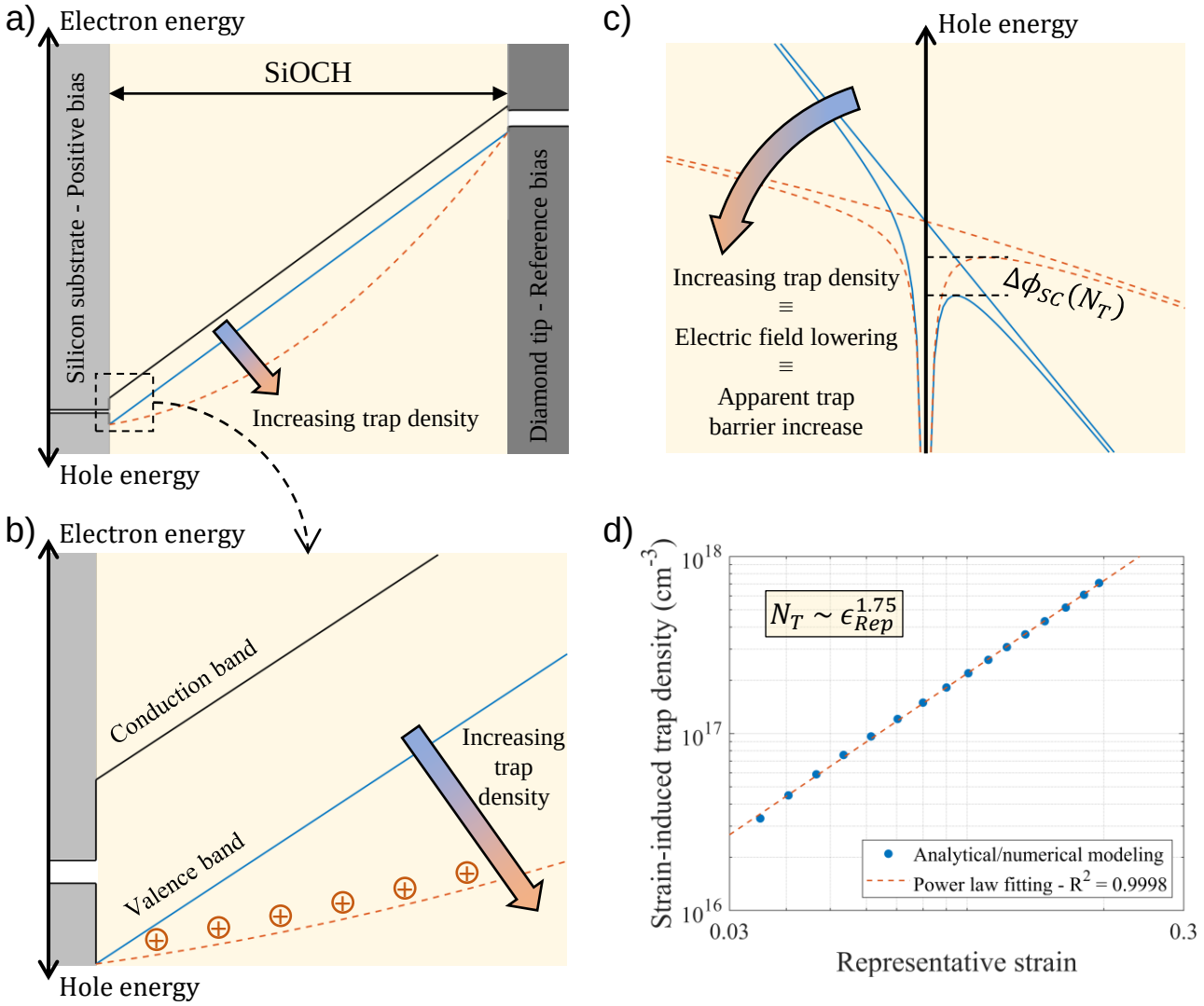

Figure 3.10. (a) Band diagram of Si/SiOCH/C system under a bias of 100 V. (b) Zoom-in on the band diagram close to the SiOCH/Si interface. (c) Hole-trap interaction energy profile. (d) Analytically calculated strain-induced trap density versus numerically calculated representative strain.

3.3.10 Additional contribution of Ohmic conduction

As already stated, the space charge that builds up within the dielectric affects the electric charge transport in two ways. First, the current line distribution is forced to change radically during indentation. Although the electric field is initially maximum vertically at the apex of the tip (Figure 3.10e), it tends to decrease in this axial zone due to the large quantities of defects that are continuously generated. Consequently, Poole-Frenkel conduction progressively drifts away from the contact center to the contact periphery, where defect density is lower (Figure 3.10f). Secondly, in this axial zone, the decay of the electric field tends to promote low-electric field conduction mechanisms, such as Ohmic conduction for instance. To consider this effect, an Ohmic contribution was implemented in the numerical model (Equation 3.20). The numerical results and experimental data are compared in Figures 3.10c,d, where only the extreme voltages of this range (115 and 90 V) are shown, for the sake of clarity. As expected, Ohmic conduction affects the overall current more strongly at low voltages (as Ohmic transport prevails where Poole-Frenkel is absent). But it can also be observed that for a given voltage

(90 V for instance) this Ohmic contribution has a greater effect on the deep stages when the widely-extended defect distribution hampers Poole-Frenkel conduction. The proposed model (strain-dependent Poole-Frenkel mechanism and Ohmic contribution) perfectly reproduces the experimental data, as shown by the scatter markers in Figure 3.6. The optimized parameters are the following: $C = 3.8 \times 10^{-11}$ S/cm, $r = 1.5$, $\epsilon_{th} = 0.0172$, $\sigma_{Ohm} = 1.1 \times 10^{-13}$ S/cm.

If $\epsilon > \epsilon_{th}$:

$$\boldsymbol{J} = C \exp\left(-\frac{\Phi}{r k_B T}\right) \exp\left(1 - \frac{\epsilon}{\epsilon_{th}}\right) \exp\left(\frac{q^{3/2}/\sqrt{\pi\varepsilon_0 k}}{r k_B T} \sqrt{\|\boldsymbol{F}\|}\right) \boldsymbol{F} + \sigma_{Ohm} \boldsymbol{F} \tag{3.20}$$

This additional Ohmic contribution is further confirmed when considering conduction in the low-field range (below 10 V, Figure 3.5). The numerical extrapolation of these current curves to this low-field range matches the experimental data without any adjustment of the parameters (Figure 3.11). This point confirms the predominance of Ohmic conduction at low fields.

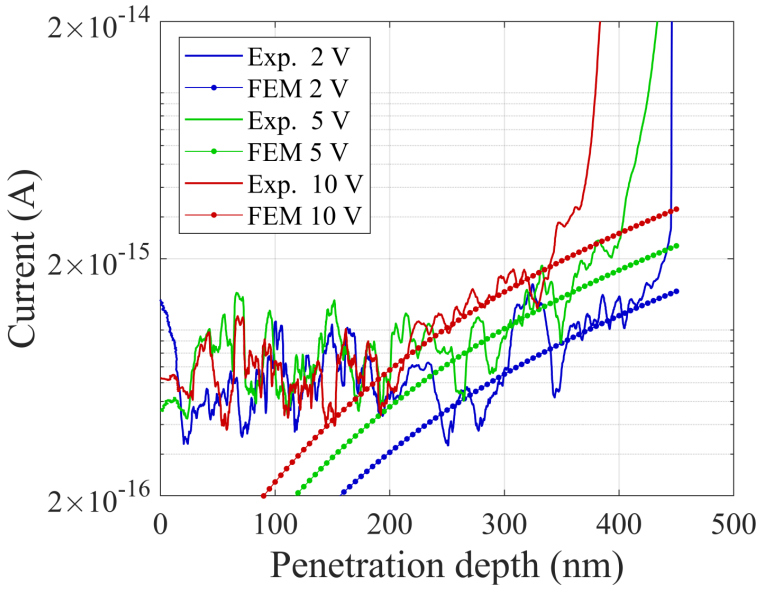

Figure 3.11. Comparison of the experimental and numerical current-depth curves for voltages of 2, 5 and 10 V. The FEM curves come from the "strain-dependent PF + Ohm" model with the properties given in this chapter, but here they are fully driven by the ohmic regime.

3.3.11 Relevance of the threshold strain

A final argument that supports the model proposed above is its ability to explain the change in slope in Figure 3.5 (voltage range between 50 and 90 V, where $h_C^{Elec} < h_C^{Mech}$). The slope change is observed at 75 V, which corresponds to a critical electrical depth h_C^{Elec} of 59 ± 8 nm. If one focusses on the strain field distribution in the SiOCH film (Figures 3.5b,c), it can be seen that this depth corresponds to the percolation limit for the threshold strain ϵ_{th}: before percolation, Poole-Frenkel conduction can reach the silicon substrate close to the tip apex (red arrows), while it is repelled to the periphery beyond percolation. In the latter case, the apparent resistance of the film is greater than in the former case, thus delaying the onset of large leakage currents.

3.4 Conclusion

In summary, our work provides a comprehensive understanding of the interplay between the mechanical and electrical behaviors of an ultra-low-k dielectric film by both experimental and numerical means. A recently developed technique (electrical-nanoindentation) is first used to correlate the electrical and mechanical failures of an SiOCH film: onset of leakage current, dielectric breakdown, plasticity, film cracking, ... Most importantly, electrical-nanoindentation tests reveal a counterintuitive trend: even though both electric field and contact area increase, current is seen to saturate and even decrease during indentation. This unexpected behavior is explained as follows: while indentation proceeds, the plastically-induced defects trap electrical charges (holes), thus causing a space charge to build up within the SiOCH film. This repelling space charge reduces Poole-Frenkel emission by moderating the lowering of barrier energy required for electrical conduction. This mechanism is modeled numerically by correcting the Poole-Frenkel conduction law with a strain-dependent factor. To do so, a threshold strain ϵ_{th} is introduced into the model: above ϵ_{th}, local Poole-Frenkel conduction is reduced by a factor that decreases exponentially with local plastic strain. Perfect matching of the experimental data over a wide range of electrical and mechanical stresses is thus obtained. A simple analytical model based on Gauss's law is then used to relate the local defect density to plastic strain. Finally, from independent experimental results, this threshold strain is identified as the driving criterion for the change in current line distribution within the dielectric during indentation: ϵ_{th} appears to be the percolation threshold above which current lines are repelled to the contact periphery. We believe that this case study of electrical/mechanical experimental monitoring and numerical modeling will have great significance in correlations between structural and functional properties that would be unachievable otherwise.

Chapter 4

Thermal Copper Oxide Thin Films: Microstructure, Mechanical/Electrical Properties and Impact on Copper Substrate Plasticity

This chapter is based on the following paper submitted to a peer-reviewed journal:

M. Rusinowicz, F. Volpi, G. Parry, C. Boujrouf, T. Bernard, M. Verdier, M. Braccini. Thermal copper oxide thin films: microstructure, mechanical/electrical properties and impact on copper substrate plastic behavior.

It reports a mechanical and electrical study of copper oxide (Cu_2O) layers grown by thermal oxidation from annealed copper (Cu) substrates. An enhancement of the mechanical size effects in the copper substrate induced by the presence of the barrier oxide layer against dislocation gliding is revealed and the mechanical/electrical properties of the oxide are determined.

All the work presented in this chapter was carried out within the framework of the present PhD: sample processing, physicochemical/microstructural analyses and mechanical/electrical characterizations.

4.1 Introduction

Copper oxide films and nanostructures are extensively studied for their disruptive functional properties: p-type conduction, tunable optical transparency or absorption in visible range, mechanical flexibility, catalytic behavior, ... [242–246]. Combined with their non-toxicity, abundant availability and low-cost production [247–250], these properties make copper oxides promising materials for advanced applications like heterojunction solar cells [243, 244, 251–253], thin film transistors [254], gas sensors [255], batteries [256], catalysts [245, 257], memristors [246, 258], photoelectrochemical cells [259], among others [260, 261]. Copper has two stable oxide phases: cuprous oxide or cuprite (Cu_2O) and cupric oxide or tenorite (CuO) [262]. In particular, Cu_2O is a p-type semiconductor thanks to the intrinsic defects (copper vacancies) present in its cubic crystallographic lattice [263, 264]. Its optoelectronic properties open the doors to its integration in devices such as efficient flexible solar cells [265–267], where it could become a prime substitution candidate to address the sustainability issues we face.

From a mechanical viewpoint, the integration of semiconductor thin films in advanced devices can generate important mechanical stresses leading to the device failure either during processing or operation [268, 269]. Nevertheless, only a few studies deal with the mechanical properties of Cu_2O, focusing mainly on the determination of its elastic modulus by nanoindentation [141, 270, 271]. The results of these works show a huge dispersion since Jian *et al.* [141] measure elastic modulus values in the 100-130 GPa range depending on the growth temperatures while Yuan *et al.* [270] and Lehmann *et al.* [271] find values in the 30-40 GPa range. Furthermore, the plastic response of the system is rarely discussed either in terms of the oxide layer plasticity or the potential effect of this layer on the metallic substrate behavior. Indeed, on the one hand, some microstructural defects may lead to plastic deformation under loading in oxide scales. This is for example the case of porosities as recently reported by Deng *et al.* [272] who performed nanoindentation tests on oxidized high speed steel. Using finite element method based simulations, with a Gurson model to describe the porous oxide film plasticity, they discuss the evolution of the load-depth curves according to plastic deformation in both the oxide layer and the metallic substrate. On the other hand, the presence of a hard adherent layer may affect plastic flow in the metallic substrate under nanoindentation in terms of incipient plasticity as measured for native oxide [108, 273–275] or also strain gradient plasticity as revealed for graphene single layer on copper [276]. These effects, often observed experimentally with low amplitude, have never been studied in the case of thermally grown oxide on copper.

From an electrical viewpoint, the resistivity of Cu_2O, its carrier density and mobility have been widely determined on thin films processed by various methods [247, 250, 260, 277], revealing a great dependency of those parameters on the processing conditions. Moreover, the conduction mechanisms of these oxides are rarely discussed.

This work proposes a comprehensive study of the microstructure and the mechanical/electrical behaviors of Cu_2O thin films obtained by simple thermal oxidation from bulk annealed copper. An approach coupling fine experimental measurements and multiphysics numerical models was used to meet a dual objective: (i) The determination of the elastic-plastic properties of cuprous oxide, also assessing its impact on the near-surface small-scale plasticity mechanisms of the copper substrate. (ii) The identification of the electrical transport mechanisms in cuprous oxide under mechanical loading.

To achieve these aims, the mechanical response of the system was monitored by nanoindentation [1, 2, 4], which is one of the most suitable nanomechanical testing methods for thin film

characterization [70, 278]. The nanoindentation experiments were coupled with fine electrical measurements allowing the monitoring of the current flowing through the oxide film induced by the substrate polarization during the mechanical loading. This advanced technique is referred to as "nano-ECR", "resistive-nanoindentation" or "electrical-nanoindentation" testing [12, 104, 106, 107], and is generally used to characterize local behaviors of various classes of materials such as piezoelectric materials [91, 110, 112, 279], shape memory alloys [280], metallic glasses [281], native oxides [108], dielectric thin films [113, 268], etc. Finally, numerical models using the Finite Element Method (FEM) was developed to fully describe the complex rheology of the system and to quantify the mechanical/electrical properties of Cu_2O by inverse methods.

4.2 Materials and method

4.2.1 Samples

Samples of 10 mm × 10 mm in size were cut in a 2 mm thick plate of Cuc1 OFHC copper (99.95 % purity). These platelets were mechanically ground using SiC abrasive papers down to the P4000 grade and then polished with 1 µm diameter diamond suspensions. After cleaning with acetone and ethanol, they were annealed for 30 min at 800 °C under an Ar/H_2 flow. A first sample of annealed copper was extracted at this stage (referred to as "ann-Cu"). Three other samples were then thermally oxidized under ambient air at 200 °C for 30, 60 and 120 min (referred to as "Ox30", "Ox60" and "Ox120" respectively). Finally, a last copper sample was oxidized in ambient air for 60 min at 200 °C without prior annealing treatment (referred to as "Ox60-h").

4.2.2 Nanoindentation set-ups

The electrical-nanoindentation experiments were conducted with a lab-made set-up that combines several commercial modules, in particular an InForce 50 actuator from Nanomechanics Inc./KLA-Tencor, and linear positioners from SmarAct GmbH for actuator and sample positioning. The tips used for electrical measurements are made of boron-doped diamond (BDD) with resistivity in the range of 0.2-2 Ω.cm supplied by Synton-MDP. The current is measured on the tip side with a highly-sensitive ammeter ("sub-femtoamp 6430" model from Keithley) which, coupled with a fully guarded measurement chain, achieves a current sensitivity in the fA range with an integration time of 40 ms. In this configuration, electrical bias is also applied with the sub-femtoamp 6430 to the sample. Further details of this set-up are described in previous papers [12, 112].

A second nanoindentation device was used essentially for the statistical measurements presented in Figure 4.5, which is a commercial nanoindenter MTS Nano Indenter XP.

Both devices are load-controlled, and are equipped with the Continuous Stiffness Measurement (CSM) mode which allows continuous extraction of hardness and elastic modulus during indentation [4]. All the experiments presented in this chapter were performed with Berkovich geometry tips and at a strain rate of 0.05 s^{-1} to be in conditions comparable to work already reported in the literature on copper oxides [141, 270, 271]. Tip geometry was systematically identified with the Oliver-Pharr method [4] by indenting a fused silica sample to obtain the so-called "shape function", relating the projected area A_c and the height h_c of the tip.

4.2.3 Physicochemical and microstructure characterization techniques

Top-surface observations were realized with an Olympus BX60M optical microscope and a Gemini SEM 500 Scanning Electron Microscope from Carl Zeiss. Cross-section views were taken after Focused Ion-Beam (FIB) milling, using a FIB Cross Beam NVision 40 from Carl Zeiss (Ga source with an acceleration voltage of 30 kV and current intensity of 300 pA).

The crystallographic orientation of copper grains was obtained by Electron Back Scattered Diffraction (EBSD) thanks to an EBSD detector on the Gemini SEM 500.

The characterization of the microstructure and phases of the oxide at a sub-micrometer scale was performed by Transmission Electron Microscopy (TEM) with a TEM FEG JEOL 2100 operating at 200 kV on thin foils prepared by FIB-milling. Orientation and phase mappings were obtained by the ACOM/TEM method and the hardware/software toolset ASTAR^{TM} from Nanomegas [282].

Residual nanoindentation imprints and surface roughness were characterized with a Veeco Dimension 3100 Atomic Force Microscope (AFM).

4.2.4 Finite element modeling

Numerical simulations were carried out using the Finite Element Method (FEM) under the commercial software ABAQUS®. The model was set-up in a 2D axisymmetric framework. The nanoindentation / electrical-nanoindentation experiments were modeled for both oxide-free annealed copper and oxidized annealed copper. In models with oxide film, the oxide/copper interface is set as fully tied. The film, the substrate and the tip are considered as deformable bodies. The tip geometry is modeled as the axisymmetric equivalent to the experimentally-used Berkovich tips (same area at a given height).

The simulations consist in applying a displacement on the top of the tip to bring it in contact with the sample while the bottom of the substrate is fixed. By extracting the reaction force, "load-depth" curves can be plotted and compared to experimental loading curves. The mechanical behavior of the tip is assumed to be isotropic linear elastic with an elastic modulus of 1140 GPa and a Poisson's ratio of 0.07. The elastic-plastic behavior of the film and substrate are described in this chapter. During the indentation step, an electrical potential difference is applied between the bottom of the substrate and the top of the tip. By extracting the current flowing through the tip, and dividing the applied voltage by this current, "resistance-depth" curves can be drawn and compared to experimental electrical curves. The electrical behavior of the tip and the copper substrate is assumed to be ohmic with conductivities of 1 and 10^6 S/cm respectively. However, the electrical behavior and properties of these two materials do not influence the results because the oxide film is much more resistive, which makes the resistances of the tip and copper negligible compared to the one in the film. Finally, the contact stiffness is extracted from the load-depth curves by calculating the slope at the first instants of the unloading step, and the contact area from an algorithm based on the contact pressure data.

The FEM mesh was optimized so that the results do not depend on it, leading to 5 nm size elements in the film and near the indenter/film and film/substrate interfaces. The mechanical equilibrium and electrical steady state equations were solved simultaneously with the ABAQUS®/Standard solver using an implicit scheme. The inverse analyses were conducted by adjusting the constitutive parameters until the maximum relative deviation between the numerical and experimental curves falls below 10 %.

A schematic of the numerical model is given in Figure 4.1 and all numerical details are similar to those described in previous papers [12, 268].

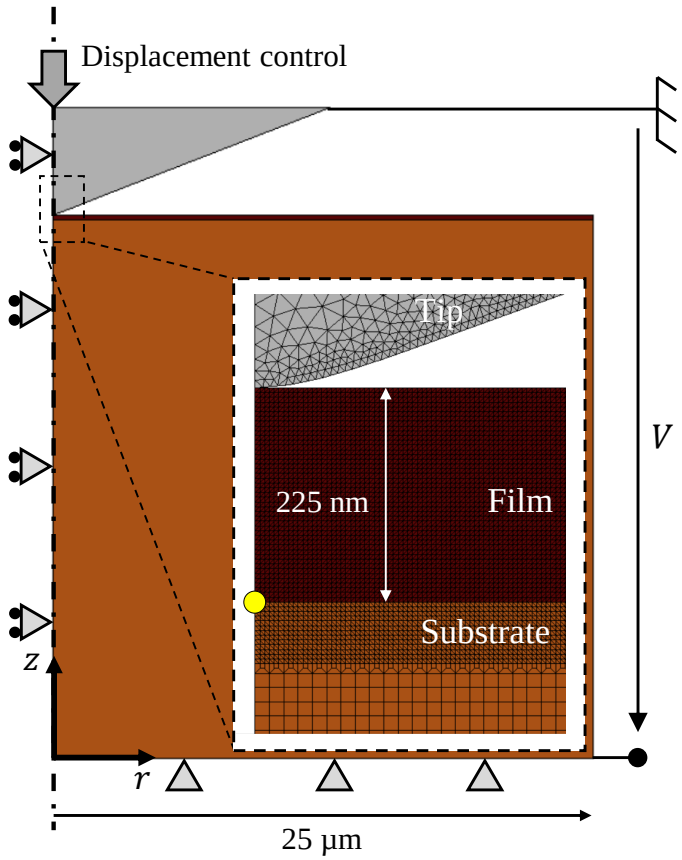

Figure 4.1. Schematic of the FEM numerical model, showing the system geometry, the mechanical/electrical boundary conditions, and the mesh.

4.3 Results

4.3.1 Physicochemical/microstructure analysis of oxidized samples

Figure 4.2 presents the physicochemical and microstructure analyses performed on the Ox60 sample. Figure 4.2a is an optical image of the sample surface showing the annealed copper grains under the oxide layer. Contrast between copper grains is due to the slight difference in oxide thickness related to the metal grain orientation dependence of the oxidation kinetics [283, 284]. As the annealing heat treatment is performed at high temperature (800 °C), the copper grains are very large, in the 0.1-1 mm range, with annealing twins. This implies that, at the scale of nanoindentation tests, the copper substrate is equivalent to a single crystal in the sense that the deformed volume under the indents is within a single copper grain and does not interact with grain boundaries. Figure 4.2b shows an SEM image of the oxide surface morphology. It reveals fine oxide grains of a few tens of nanometers, as reported by [285] under similar oxidation conditions (1 h at 200 °C). The oxide surface RMS roughness is determined to be 20 ± 2 nm by AFM on six different scans (not shown). The peak-to-peak height of these roughness is about 80 nm and their wavelength 100 nm, as shown in the AFM height profile in Figure 4.2c. Figures 4.2d and 4.2e are phase and orientation maps respectively, on a cross-section of the "*film on substrate*" system, obtained by the ACOM/TEM automated

electron diffraction pattern indexing technique with a spatial resolution of 2 nm. It can be seen that the oxide layer is composed mainly of cuprous oxide (Cu_2O) with equiaxed grains of size between 10 and 100 nm. Furthermore, these oxide grains do not seem to present a preferential crystallographic orientation. Voids are observed at the Cu_2O/Cu interface, which are attributed to a Kirkendall voiding mechanism [286] caused by the accumulation of cation vacancies at the oxide/metal interface, balancing the outward diffusion of copper cations [287]. Finally, the film thickness was measured at 225 ± 19 nm from four mappings made in different locations. The microstructure of the Ox30 and Ox120 samples was observed by SEM (not shown) and is similar to that of the Ox60 sample. The oxide thickness of these two samples is 167 ± 32 nm and 354 ± 44 nm respectively.

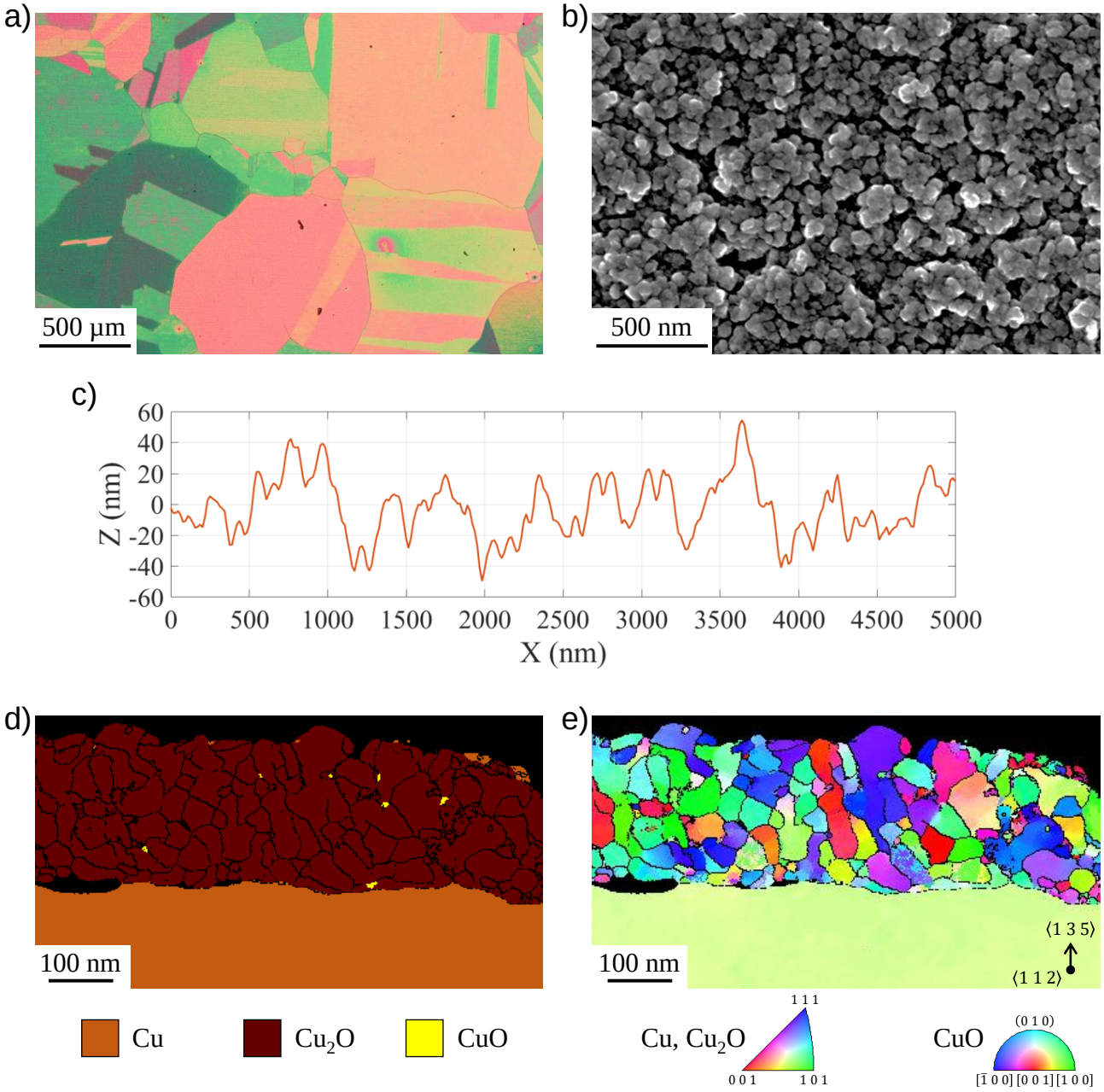

Figure 4.2. Physicochemical and microstructure analysis of the Ox60 thermally oxidized copper system. (a) Optical image of the surface. (b) SEM image of the surface. (c) AFM height profile showing the surface roughness. (d) ACOM/TEM phase and (e) orientation mappings on an oxide cross-section.

4.3.2 Electrical-nanoindentation experiments

Figure 4.3 presents the electrical-nanoindentation tests carried out on the Ox60 sample with a Berkovich tip. Figure 4.3a is a schematic of the experiment highlighting relevant parameters, especially: the film thickness t, the load L, the penetration depth h, the contact depth h_c and the contact area A_c which is defined as the projected surface of the tip in contact with the sample. To a contact area A_c corresponds a contact depth h_c (height of the sample in contact with the tip), depending on the material rheology. A contact radius a is defined by Equation 4.1 assuming an equivalent revolution-symmetric tip:

$$a = \sqrt{\frac{A_c}{\pi}} \tag{4.1}$$

Figure 4.3b shows the mechanical loading curves (load vs depth, at the top) and the electrical resistance curves (resistance vs depth, at the bottom) for a typical data set obtained with different voltages ranging from 1 to 5 V. These tests are performed up to 600 nm indentation depth, which leads to a maximum load of 6 mN and an electrical resistance between 10^5 and 10^{10} Ω.

Concerning the mechanical response, displacement jumps at constant load are observed on the loading curves for a critical depth/load couple of about (70 nm, 0.4 mN). These instabilities are called "pop-in" events and correspond to a sudden penetration of the tip into the material when the test is load-controlled [217, 288]. After the pop-in, the loading curves have a less pronounced inflection than before the pop-in. This inflection can be quantified by modeling the load-depth curves by a simple power law relation. Thus, before pop-in, the identified exponent is 2.1 ± 0.2 while after pop-in it becomes 1.53 ± 0.04.

Regarding the electrical response, the electrical resistance decreases for increasing applied voltage at a given penetration depth. The voltage dependence of the resistance is the signature of a non-linear conduction of the oxide film. In other words, oxide conduction cannot be modeled with a simple Ohm's law with a constant and intrinsic conductivity. Then, for a given voltage, the electrical resistance decreases with the indentation depth. This is consistent with the evolution of two key parameters during electrical-nanoindentation. The first one is the contact area A_c (see Figure 4.3a) which increases during indentation: this rise implies that the whole current should increase, which leads to a decrease of the electrical resistance. The second increasing parameter is the electric field which is defined at first order as the ratio of the applied voltage V to the local film thickness $t(h)$. When the film undergoes compression under the indentation tip, the electric field increases locally, resulting in a decrease of the resistance, regardless of the conduction mechanism. Nevertheless, the evolutions of these two geometrical parameters, contact area $A_c(h)$ and local film thickness $t(h)$, are unknown at this stage, and must be identified to quantitatively determine the electrical properties of the oxide. For this purpose, we propose a two-step methodology: 1/ description of the system rheology by identifying the mechanical constitutive laws and properties of the materials, 2/ identification of the electrical conduction law and properties of the cuprous oxide thin film.

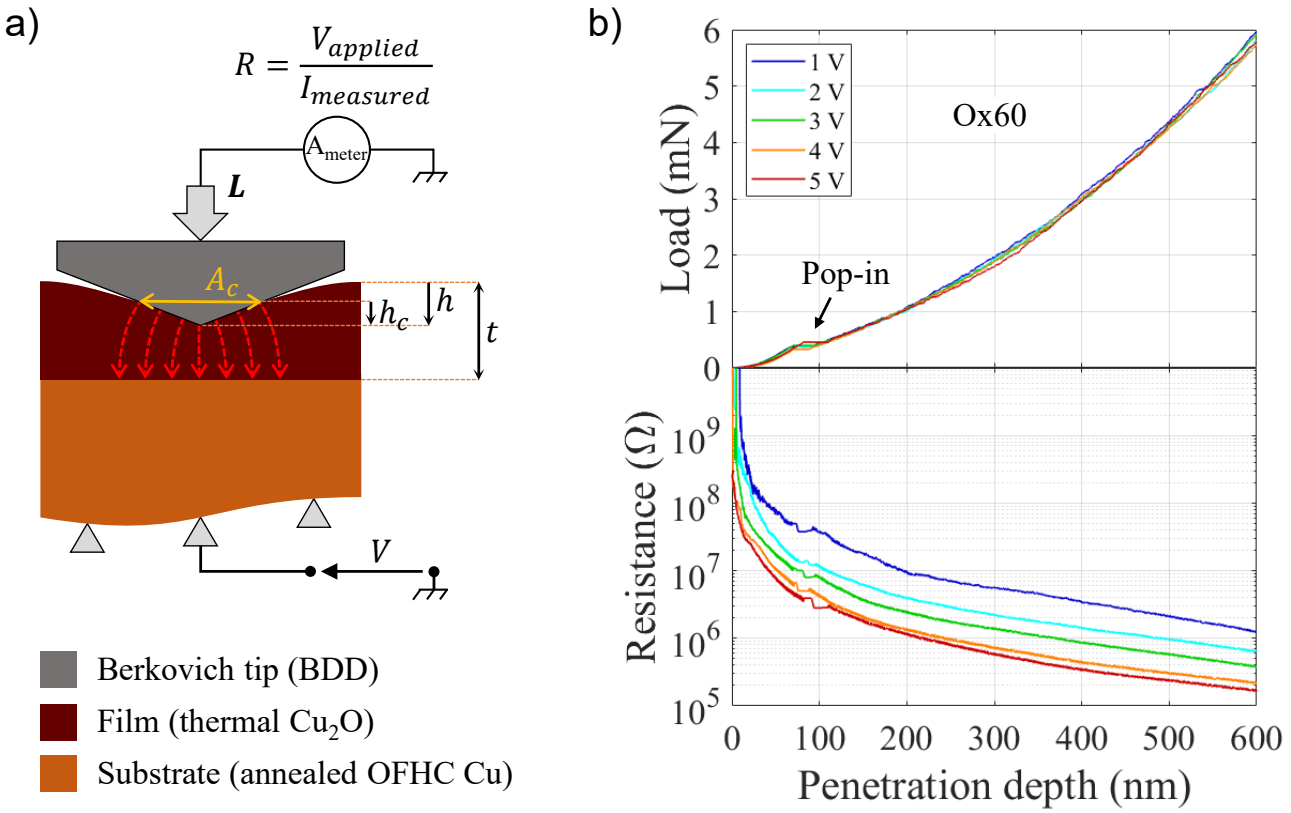

Figure 4.3. Electrical-nanoindentation tests. (a) Schematic of the test with relevant parameters. (b) Mechanical (top) and electrical (bottom) responses of the system during indentation.

4.4 Discussion

4.4.1 Plasticity-induced pop-in excursions

In the case of the Ox60 system, pop-in excursions observed on the loading curves in Figure 4.3b, and magnified in Figure 4.4a, can be mainly attributed to two possible phenomena: plastic burst in the copper substrate or oxide cracking.

- Plastic strain burst in the copper substrate is reported in several studies both experimentally and theoretically for this material [60, 276, 289–292]. The pop-in is linked to a collective nucleation and gliding (avalanche) of dislocations when the stress under the indenter exceeds the theoretical shear strength of the material. It occurs more likely and is more pronounced in low defect density metals, especially low dislocation density [293–295], but also large grains compared to the deformed volume (low grain boundary density) [296, 297]. Pop-in induced by incipient plasticity are found in many crystalline metals such as magnesium [298], aluminum [299], chromium [300], nickel [301], molybdenum [302], tantalum [303], tungsten [304], iron alloys [305–309], high-entropy alloys [310], but also in noble metals such as gold or platinum [217, 311–313], which proves that these plastic dynamic instabilities can occur without any link with the presence of a native oxide layer on the metal surface.
- Cracking of the oxide film can take place through two main mechanisms. The first one is the brittle cracking of the oxide either when stress reaches the fracture strength of the film or when pre-existing crack propagates. The second one occurs when the onset of plasticity has already initiated in the metallic substrate, as observed by Minor *et al.* [314]. In that case, pile-up of dislocations can be formed at the oxide/metal interface, leading to stress concentrations in the oxide and finally to its cracking at the head of the pile-up. Several

studies discuss these mechanisms as for example for grown aluminum oxide [274], native iron oxide [275, 288], native aluminum and chromium oxides [108], or native indium oxide [315].

To discriminate between substrate plasticity and crack formation mechanisms, three experiments were conducted. First, "interrupted indentation" tests were performed, consisting of several indents stopped right after the pop-in (Figure 4.4b), and of the observation of the residual imprints by SEM in plane and cross-section views (Figure 4.4c). As shown in Figure 4.4c, no cracking was observed, neither at the oxide surface nor in its thickness. Secondly, the Ox60 system was compared to the Ox60-h system which differs only in the copper substrate state. Indeed, since the Ox60-h sample has not been annealed prior to oxidation, it is work-hardened by both the processing and the mechanical polishing. Moreover, the grain size is about 30 µm, far from the millimetric size observed on the Ox60 system. Figure 4.4a gives representative loading curves obtained by indenting the Ox60 and Ox60-h samples with the same Berkovich tip. In contrast to the Ox60 system, the Ox60-h system shows no significant pop-in event. Furthermore, the loading curve inflexion of the Ox60-h is less pronounced than for the Ox60 in the first tens of nm of indentation. This is consistent with a perfectly elastic behavior of the substrate before pop-in for the Ox60 system, while the Ox60-h displays an elastic-plastic behavior from the earliest nanometers of indentation. Thirdly, nanoindentation tests were carried out on the ann-Cu sample, corresponding to the non-oxidized annealed copper substrate. A significant pop-in at a low load of $\sim$ 35 µN was observed on the corresponding load-depth curves, as evidenced by the representative loading curve shown in Figure 4.4a, confirming that these pop-in excursions are directly related to the substrate microstructure. All these observations lead to the conclusion that the observed pop-in events are induced by a plastic strain burst in the copper substrate, rather than by the cracking of the oxide film.

Figure 4.5 shows the results of a statistical analysis of the pop-in events carried out on the ann-Cu, Ox30, Ox60 and Ox120 samples by performing between 50 and 150 indents on each system, and by reporting critical load and length of pop-in on the collected load-depth curves. As a reminder, the only change between the Ox30, Ox60 and Ox120 samples are the oxidation time at 200 °C, and thus the film thickness. Figure 4.5a plots the pop-in length versus critical load for the four systems. The experimental curves were fitted with a linear relation in agreement with Shibutani *et al.* [290] who, using an energy balance, proposed that the critical load is proportional to the pop-in length, itself proportional to the number of dislocations needed to release the stored elastic energy. For a given critical load, the pop-in length is observed to decrease in the presence of an oxide film and when this film is thicker. Figure 4.5b shows the cumulative pop-in probability as a function of critical load. These curves were fitted with a Weibull distribution: parameters L_0 and m, given in Table 4.1, represent respectively the load at which the pop-in probability is 63 % and the Weibull modulus. Here, the critical load is found to increase in the presence of the oxide layer and when this layer is thicker, the latter case at constant Weibull modulus between 5.3 and 5.6. These observations reveal a twofold effect of the oxide film:

- *Pop-in length.* Applying the approach of Shibutani *et al.* [290] to our case, the number of dislocations involved in the plastic burst is found to be lower when the oxide film is thicker.
- *Pop-in onset.* Incipient plasticity is delayed as the film is thicker.

The present results could be seen as an increase in the equivalent size of the indenter by the hard film conforming to its surface, thus generating a late onset of plasticity in the copper substrate and a redistribution of stresses as known for spherical indentation [300].

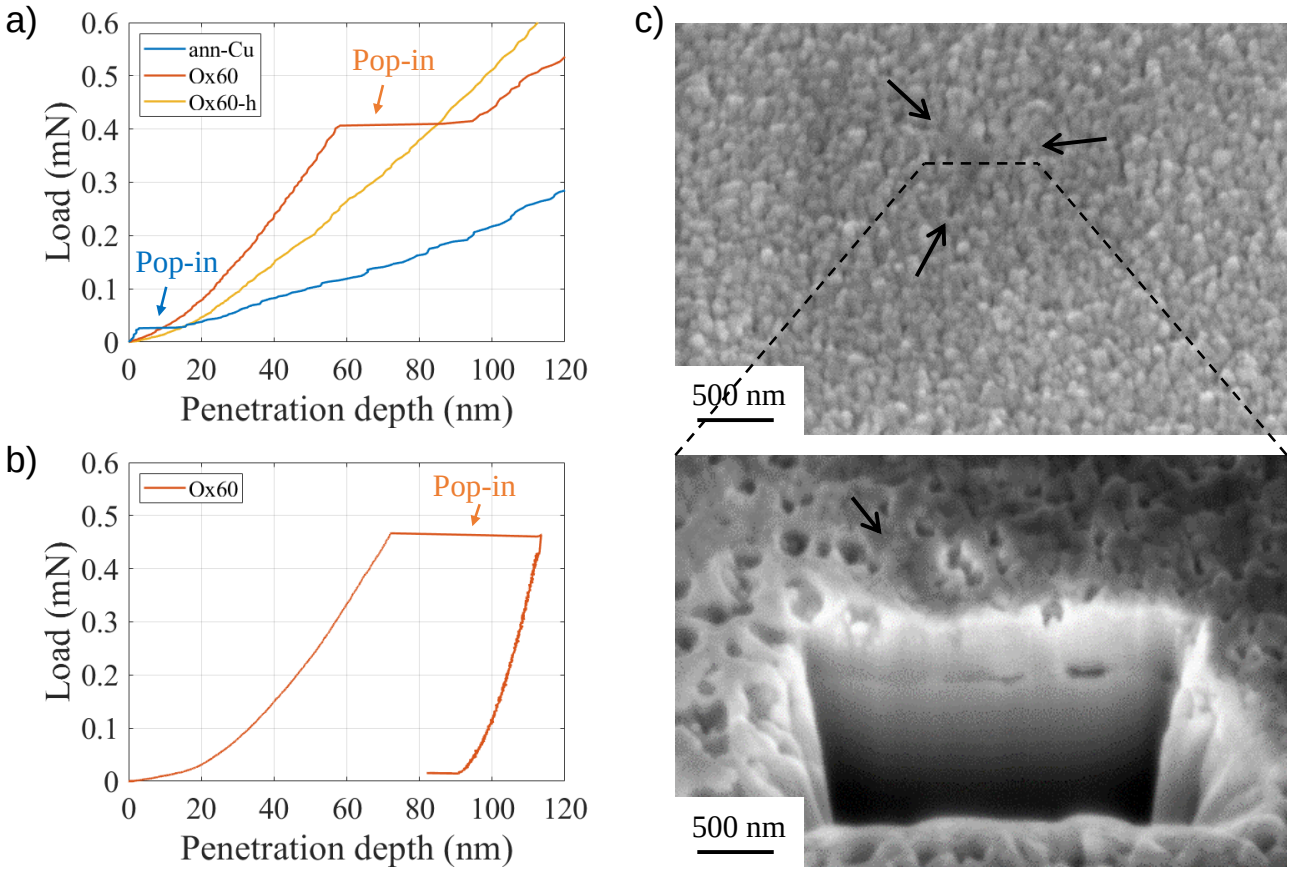

Figure 4.4. (a) Representative load-depth curves of the ann-Cu, Ox60 and Ox60-h samples. (b) Representative load-depth curve of a test stopped right after the pop-in and (c) the corresponding plane and cross-section views (arrows point to the imprints left by the tip edges).

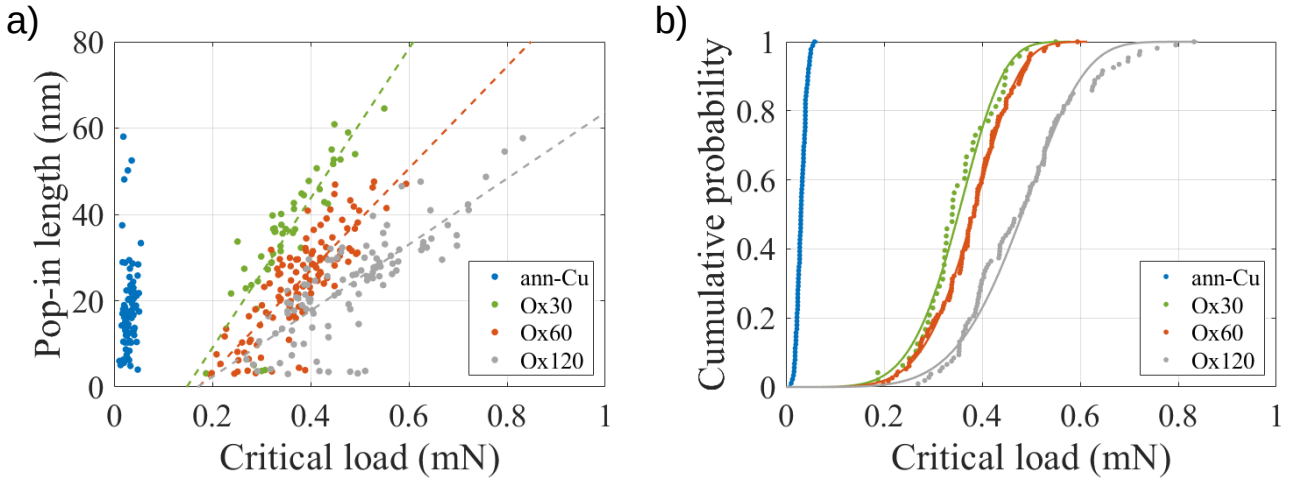

Figure 4.5. Pop-in events analysis. (a) Pop-in length versus pop-in critical load. (b) Pop-in distribution with the critical load and Weibull distribution fitting.

Sample	ann-Cu	Ox30	Ox60	Ox120
Film thickness (nm)	~ 0	167 ± 32	225 ± 19	354 ± 44
L_0 (mN)	0.035	0.377	0.407	0.516
m	3.67	5.33	5.59	5.30

Table 4.1. Weibull distribution law parameters identified on the different systems, with L_0 the load at which the pop-in probability is 63 % and m the Weibull modulus.

4.4.2 Mechanical properties of the oxide-free copper substrate

The analysis of the mechanical response of a "*film on substrate*" system under indentation requires the knowledge of the substrate properties before determining those of the film. This is why indentation tests were performed on the oxide-free ann-Cu sample. As already mentioned, indentation is achieved at the micron scale while the annealed copper substrate has a microstructure with grains of several hundred microns. This means that the copper substrate acts as a single crystal, as far as nanoindentation response is concerned. However, the mechanical properties of copper depend strongly on its crystallographic orientation: its uniaxial elastic modulus can vary from 66.7 to 191.1 GPa depending on the orientation of the crystal with respect to the loading axis [316]. Consequently, special attention was paid to perform indentation tests in grains with the same orientation in both the Ox60 and ann-Cu samples (see Figure 4.2e and Figure 4.6a, respectively). For this purpose, grain orientations were identified prior mechanical testing by EBSD analysis. The load-depth $L(h)$ and stiffness-depth $S(h)$ curves obtained on the ann-Cu sample are given in Figure 4.6b. The copper grain mechanical properties were determined by inverse analysis using a FEM numerical model of the indentation test (see Section 4.2.4). In the model, the elastic behavior of copper is assumed to be isotropic linear elastic with a Poisson's ratio fixed at 0.3, while the plastic behavior is described by an isotropic Hollomon-type hardening law (cf. Equation 4.2):

$$\sigma_f = \sigma_y \left(1 + \frac{E}{\sigma_y}\epsilon_{eq}^{pl}\right)^n \tag{4.2}$$

with σ_f and ϵ_{eq}^{pl} the flow stress and the equivalent plastic strain respectively, and E, σ_y, n three scalar parameters representing the elastic modulus, the initial yield stress and the strain hardening exponent respectively. These three constitutive parameters were identified so that not only the $L(h)$ curve but also the $S(h)$ curve from the numerical simulation match the experimental ones as shown in Figure 4.6b. Values of $E = 92$ GPa, $\sigma_y = 50$ MPa, $n = 0.26$ were obtained, in agreement with the literature for both elastic modulus [316] and plastic properties [317]. To confirm these results, the evolution of the contact area calculated numerically was validated experimentally by AFM measurements of the area of residual imprints left after indents at different depths (see Figure 4.6c).

4.4.3 Elastic properties of the cuprous oxide thin film

Once the properties of the oxide-free substrate are determined, the mechanical properties of the oxide film can be extracted. For the determination of its elastic modulus, the methodology followed relies on the Sneddon equation [7] which relates the contact stiffness S and contact radius a as presented in Equation 4.3:

$$S = 2E^* a \tag{4.3}$$

with E^* the reduced elastic modulus calculated from Equation 4.4:

$$\frac{1}{E^*} = \frac{1-\nu_s^2}{E_s} + \frac{1-\nu_i^2}{E_i} \tag{4.4}$$

where (E_s, ν_s) are the homogenized elastic modulus and Poisson's ratio of the sample respectively, and (E_i = 1140 GPa, ν_i = 0.07) are the elastic modulus and Poisson's ratio of the

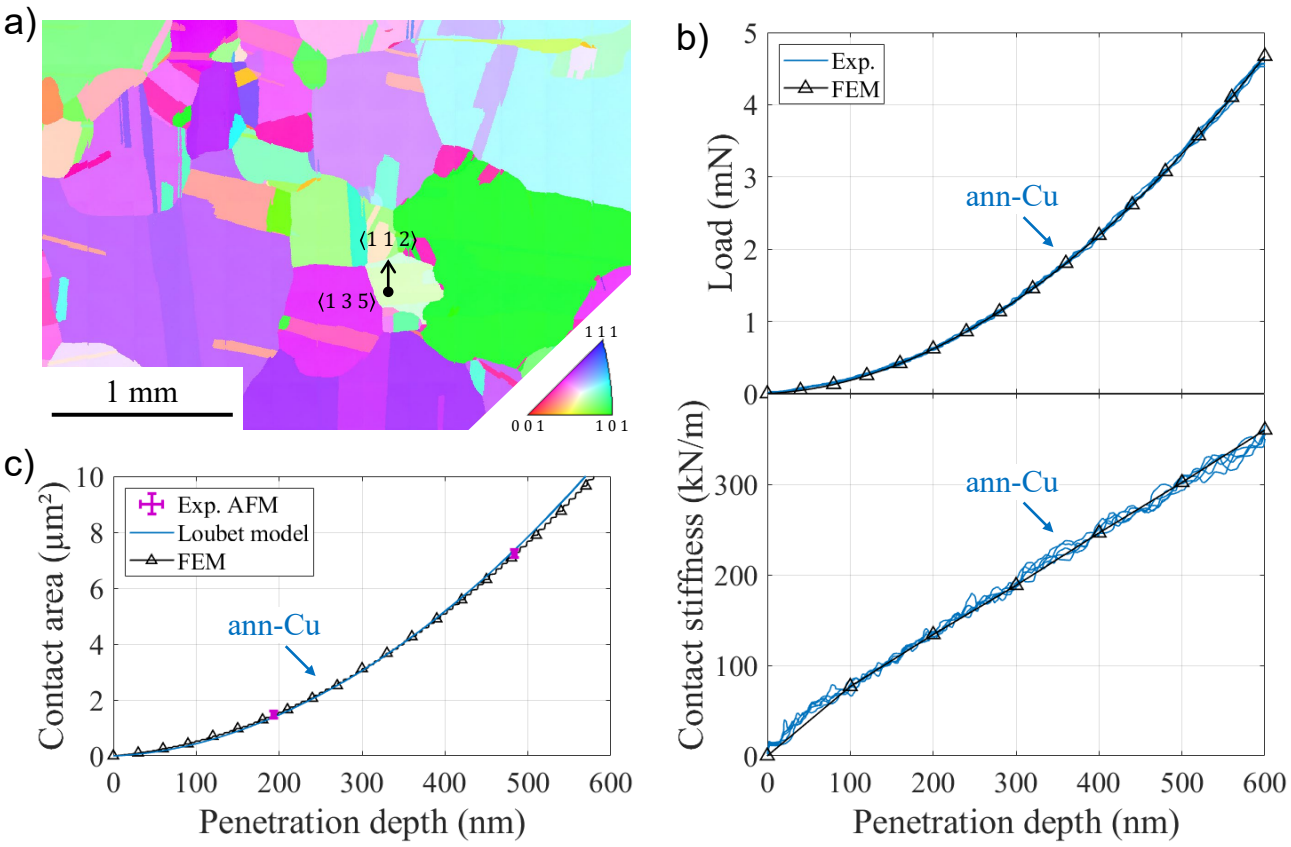

Figure 4.6. Identification of the copper substrate mechanical behavior on the ann-Cu sample. (a) EBSD mapping of the surface and selection of a grain with the desired orientation. (b) Load (top) and contact stiffness (bottom) plots with the penetration depth from experiments and FEM modeling. (c) Contact area plot with the penetration depth from AFM *post mortem* measurements, Loubet's analytical model and FEM modeling. Error bars on the experimental AFM point were calculated from the standard deviations on the measurements of 6 residual indents imprints.

indenter respectively. According to the Sneddon equation, the relation between contact stiffness and contact radius depends only on the elastic properties of the stressed materials and their contribution to E^*. As the properties of the tip and substrate are known, only those of the oxide film are missing. Thus, for a given oxide film thickness t, one experimental point on the $S(a/t)$ curve is enough to extract E^*. For this purpose, residual imprints left on the Ox60 system after indentations up to a maximum depth of 600 nm were measured by AFM, while the corresponding stiffnesses were extracted from the nanoindentation data (see Figure 4.7). Note that the experimental $S(a/t)$ point was chosen so that the a/t ratio is large enough to smooth the surface roughness observed in Figure 4.2c and therefore the whole tip surface is in contact with the oxide surface (verified by AFM measurements). Then, a 225 nm thick oxide film was added to the numerical indentation model and the evolution of the contact stiffness with the reduced contact radius a/t was established with varying film elastic properties [318]. The oxide is assumed to be isotropic linear elastic with a Poisson's ratio fixed at 0.3. The adjustment of its elastic modulus until the numerical $S(a/t)$ curve passes through the experimental point leads to a modulus of 22 GPa, bounded between 18 and 27 GPa taking into account the experimental errors. These values are in perfect agreement with the 20 GPa value of the theoretical Young's modulus recently derived by Živković *et al.* [319] using Density Functional Theory (DFT) calculations. However, they are on average ~ 30 % lower than those measured

by Yuan *et al.* [270] and Lehmann *et al.* [271] in the 30-40 GPa range, obtained from Berkovich indentation of thermal oxide films. This may be due to the difference in oxidation temperature between their studies (450 °C and 1000 °C for 1 h respectively) and ours (200 °C for 1 h) which led Yuan *et al.* to characterize a CuO/Cu_2O bilayer, CuO being at the top surface and having an elastic modulus at least 4 times larger than that of Cu_2O [319–322], while Lehmann *et al.* tried to remove the CuO layer by grinding it, potentially altering the measured surface properties. Considering these aspects, the Young's modulus of 22 GPa determined in our study is comparable to the few values estimated in the literature, with the notable exception of those of Jian *et al.* [141] who find very high elastic moduli in the 100-130 GPa range by Berkovich indentation of Cu_2O thin films deposited by magnetron sputtering on glass substrates.

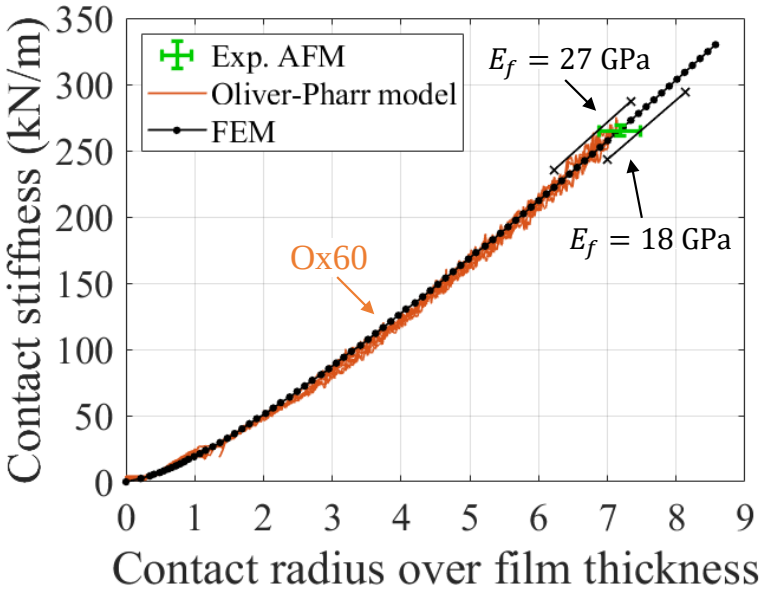

Figure 4.7. Contact stiffness vs reduced contact radius curve obtained on the Ox60 sample by coupling nanoindentation and AFM residual imprints measurements, by the Oliver-Pharr analytical model and by FEM modeling. Error bars on the experimental point were calculated from the standard deviations on the measurements of contact stiffness by nanoindentation, contact radius by AFM and film thickness by SEM cross-sections.

4.4.4 Plastic behavior of the cuprous oxide thin film

Figure 4.8 shows the load-depth curves of four representative indents performed on the Ox60 system at depths below the pop-in depth (60 nm maximum). The loading and unloading parts of these indentation curves do not superimpose, which is the signature of a non-reversible deformation of the system. However, it was shown in Section 4.4.1 that the pop-in event corresponds to the incipient plasticity in copper, meaning that before the pop-in depth, the substrate behavior is perfectly elastic. The observed non-reversible deformation is thus due to the plasticity of the oxide film, in agreement with the plane-view SEM image of Figure 4.4 on which appears imprints left by the edges of the Berkovich tip. Apart from damage mechanisms such as cracking, only a few studies address elementary deformation mechanisms in crystalline ceramic at room temperature as for example dislocation gliding [323], shear band formation [324], grain boundary sliding [325], amorphization [326] or densification [272], and no work reports those in Cu_2O to our best knowledge. To determine the homogenized plastic properties of the cuprous oxide, a Drucker-Prager yield criterion was chosen for modeling the plastic

behavior of the film in the FEM model, taking into account both shear plasticity and volumetric plasticity. The corresponding yield surface is written according to Equation 4.5:

$$\sigma_{eq} - p\tan(\beta) - \left(1 - \frac{1}{3}\tan(\beta)\right)\sigma_c = 0 \tag{4.5}$$

with σ_{eq} the equivalent Von Mises stress, p the hydrostatic pressure, β the friction angle of the material (slope of the linear yield surface in the $p - \sigma_{eq}$ stress plane) and σ_c the uniaxial compression yield stress. Furthermore, a linear hardening (cf. Equation 4.6) was introduced to reproduce the experimental data, as already known for amorphous silica [214, 215]:

$$\sigma_c = \sigma_{c0} + K\epsilon_{eq}^{pl} \tag{4.6}$$

with ϵ_{eq}^{pl} the equivalent plastic strain and σ_{c0}, K two scalar parameters.

A simulation of a perfectly elastic film on an elastic substrate is presented in Figure 4.8 ("FEM elastic film" curve). The load level is found to be overestimated from the earliest nanometers of indentation, suggesting that plastic deformation occurs as soon as contact is set. To account for this, the initial yield stress σ_{c0} was fixed at 100 MPa (this arbitrary value had no impact on the simulation results, as long as this yield stress was chosen low enough to enable early plasticity). The last two material properties (friction angle β and hardening modulus K) were chosen so that the numerical curve matched the experimental ones for both loading and unloading stages. As a result, $\beta = 20°$and $K = 8$ GPa are obtained. With these optimized parameters, the numerical curve ("FEM elastic-plastic film" on Figure 4.8) matches very well the experimental ones, which provides a simple quantitative approach for modeling the plastic behavior of such thermal oxide layers.

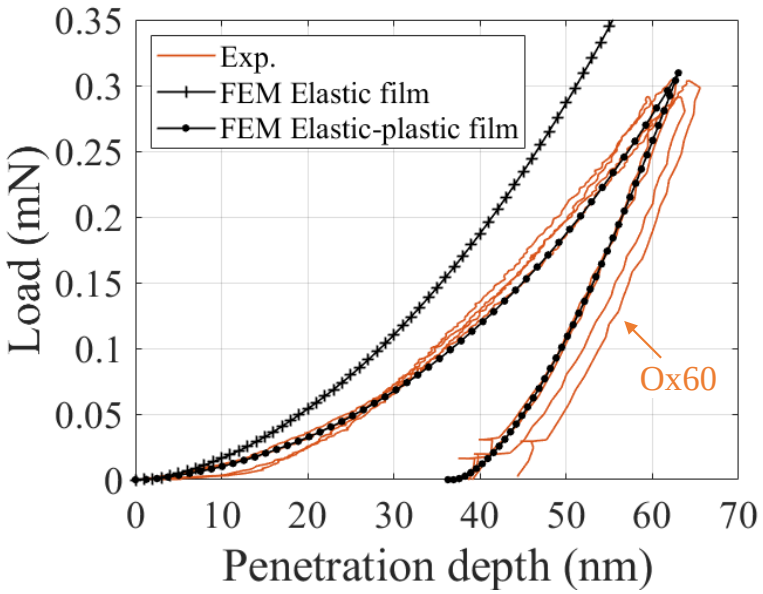

Figure 4.8. Representative experimental load-depth curves of the Ox60 system at depths below the pop-in depth (60 nm maximum) and numerical ones from the FEM model considering a perfectly elastic film and an elastic-plastic film.

4.4.5 Oxide film induced size effect enhancement in copper substrate

Figure 4.9 provides the loading curves (top) and hardness curves (bottom) from the ann-Cu and Ox60 samples. A numerical simulation was carried out on the complete system, integrating the mechanical properties of the oxide-free substrate, the elastic and the plastic properties of the oxide films determined in Sections 4.4.2, 4.4.3 and 4.4.4, respectively. In this simulation, the substrate was considered perfectly elastic up to the pop-in depth (70 nm) while the plastic behavior was introduced beyond this indentation depth. The loading curve obtained, labelled "Cu conventional plasticity" in Figure 4.9-top, is observed to match very well with the experimental curves of the oxidized sample up to the pop-in depth. However, from the pop-in depth, the numerical load is lower than the experimental load on the oxide/copper system, but closely matches the one achieved on the oxide-free substrate. This shows that after the pop-in excursion, the presence of the film is not expected to significantly impact the mechanical response of the system, which is largely driven by the copper substrate plasticity. The change in plastic behavior of the oxidized copper compared to the oxide-free copper can be explained by a strong back stress building up at the substrate near-surface: during deformation, the gliding dislocations cannot freely leave the substrate due to the non-penetrable oxide barrier and finally accumulate at the film/substrate interface, inducing copper hardening. To check if this change in boundary condition results in strain hardening and strain gradient plasticity effects, the evolution of hardness during indentation was plotted in Figure 4.9-bottom for both systems. Since the mechanical response after pop-in of the oxidized copper is controlled by the plastic flow in the substrate, the derived hardness for the Ox60 system is therefore to the first order the hardness of copper from $\sim$ 100 nm of indentation. The monitoring of contact area, necessary for the hardness H calculation according to Meyer's definition $H = L/A_c$, was performed by the Loubet model [5] for the ann-Cu sample and by the Oliver-Pharr model [4] for the Ox60 sample, which was validated by AFM *post mortem* indent measurements (see Figures 4.6c and 4.7 respectively). Figure 4.9-bottom shows that the hardness of the copper from the Ox60 sample is more than twice that of the copper from the ann-Cu sample after the pop-in, and then decreases until tending towards the same value around 0.5 GPa. This pronounced hardness gradient clearly reveals the contribution of the oxide film on enhancing size effects in the copper substrate. Similar results were found in the recent work of Bahrami *et al.* [276] by depositing a graphene single layer on an annealed copper surface. Simulations of the Berkovich indentation of this system by Discrete Dislocation Dynamics (DDD) method combined with a finite element code have unraveled the origin of these effects: the spreading and delocalization of the plasticity process by the generation of a large back stress induced by the barrier layer against dislocation gliding. Nevertheless, the discussed effects had a small amplitude experimentally compared to what they expected numerically, or to those presented in the present chapter. Bahrami *et al.* attributed this to the relaxation of the load by partial debonding of the graphene layer. In our case, no sign of delamination of the oxide layer was observed, which could explain why strong strain hardening and strain gradient plasticity effects were found.

Determining the properties of copper leading to the observed size effects is not the focus of this chapter. The objective is to describe the rheology of the Ox60 system by modeling the behavior of the substrate in the simplest possible way to accurately determine the electrical properties of Cu_2O in the next step. For this purpose, the strain gradient plasticity behavior of copper was phenomenologically integrated into the FEM model by scaling the initial yield

stress σ_y in Hollomon's law (see Equation 4.2) with the factor $\sqrt{1+l^*/d}$, similar to the one introduced in Nix-Gao type law [327], as written in Equation 4.7:

$$\sigma_f = \sigma_y \sqrt{1+\frac{l^*}{d}} \left(1 + \frac{E}{\sigma_y \sqrt{1+\frac{l^*}{d}}} \epsilon_{eq}^{pl} \right)^n \tag{4.7}$$

with d the displacement of the node on the top surface of the copper substrate coinciding with the axis of symmetry (see Figure 4.1) and l^* a fitting parameter so that the numerical curve matches the experimental ones. Although this last parameter does not make physical sense since the origin of the Nix-Gao strain gradient (accommodation of the deformation beneath the indent by geometrically necessary dislocations) is not the same as in our case (modification of the free surface condition of the copper crystal by the presence of a non-penetrable film), a value of $l^* = 400$ nm perfectly reproduces the experimentally observed mechanical response of the Ox60 system (see "Cu strain-gradient plasticity" curve in Figure 4.9-top).

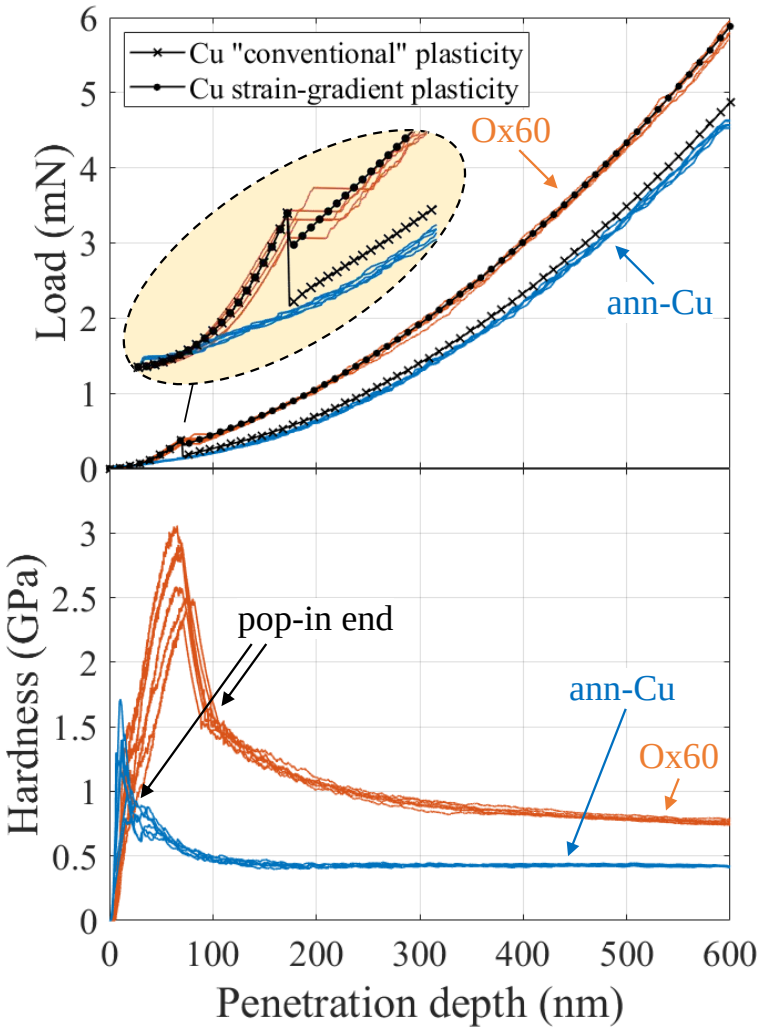

Figure 4.9. Loading curves (top) and hardness curves (bottom) from the ann-Cu and Ox60 samples. The loading curve "Cu conventional plasticity" corresponds to the simulated FEM curve considering the mechanical properties of the oxide-free copper determined in Section 4.4.2 while the loading curve "Cu strain-gradient plasticity" corresponds to the simulated FEM curve considering the Nix-Gao type factor introduced in Hollomon's law.

4.4.6 Electrical behavior of the oxide thin film

The conduction mechanisms in Cu_2O have been mainly studied on integrated devices such as resistive memory applications [328–334], but their chemistry and microstructure are little or not addressed. The most reported mechanisms identified in these works are ohmic conduction at low electric fields, Poole-Frenkel conduction at high electric fields and more rarely Space-Charge-Limited Conduction (SCLC). Ohmic conduction leads to a linear relationship between current density and electric field. In the present case, the voltage-dependence of resistance (see Section 4.3.2) allows us to rule out this mechanism. SCLC relies on a quadratic relationship between current density and voltage. To assess this possibility, $I-V$ characteristics at different depths were plotted in a log-log graph with slope = 2 marker lines (see Figure 4.10a). Under this representation, linear relationships are obtained but do not follow a slope of 2. The slopes of the $I-V$ characteristics were extracted for each depth between 0 and 600 nm in Figure 4.10b, resulting in an average value of about 2.5 between 50 and 500 nm, which excludes the SCLC mechanism. Finally, the Poole-Frenkel mechanism without compensation [227] relates the current density $\boldsymbol{J}$ to the electric field $\boldsymbol{F}$ following Equation 4.8:

$$\boldsymbol{J} = \sigma_{PF} \exp\left(\frac{-\Phi + q^{3/2}/\sqrt{\pi\varepsilon_0 k}}{2k_B T}\sqrt{\|\boldsymbol{F}\|}\right)\boldsymbol{F} \tag{4.8}$$

with σ_{PF} the Poole-Frenkel conductivity, Φ the zero-field trap barrier, k the dielectric constant, and ε_0, k_B, and T the vacuum permittivity, the Boltzmann constant and the temperature respectively.

According to this expression, the logarithm of the I/V ratio must vary linearly with the square root of V, which is the case over the range of electric fields probed in this study (see Figure 4.10c). This analytical expression was integrated into the numerical model as the electrical constitutive law for Cu_2O. Similarly to the mechanical properties, the electrical properties of the film were determined by inverse analysis, here from the resistance-depth curves shown in Figure 4.11. To ensure that the numerical and experimental results are compared for equal contact area, the resistance curves were plotted as a function of contact depth. Furthermore, since σ_{PF} and Φ are interdependent, σ_{PF} was set to 0.01 S/cm in agreement with the literature for thermal copper oxide grown at 200 °C [247, 250]. The choice to fix σ_{PF} rather than Φ is justified by the fact that we are much more sensitive to a variation of Φ because this parameter is in the exponential term. As a result of the inverse analysis, a dielectric constant of 7 and a trap barrier of 320 meV allow the numerical resistance curves to match perfectly the experimental ones (see Figure 4.11). The value of dielectric constant is in good agreement with the one reported for Cu_2O (~ 7.5) [335, 336] and that of trap barrier is perfectly compatible with a Poole-Frenkel emission mechanism ($\Phi < 1$ eV according to Chery [337]). Especially, the latter parameter is relatively close to the acceptor transition levels of copper vacancies derived by DFT calculations (280 meV) [338] and to the hole trap measured by deep level transient spectroscopy (250 meV) [339]. Besides validating our approach, this suggests that the structural defects driving the electrical transport in such low temperature processed thermal oxide layers are indeed simple copper vacancies, rather than split copper vacancies or oxygen interstitials [340].

All the mechanical and electrical properties of Cu_2O cuprous oxide obtained through this study are given in Table 4.2.

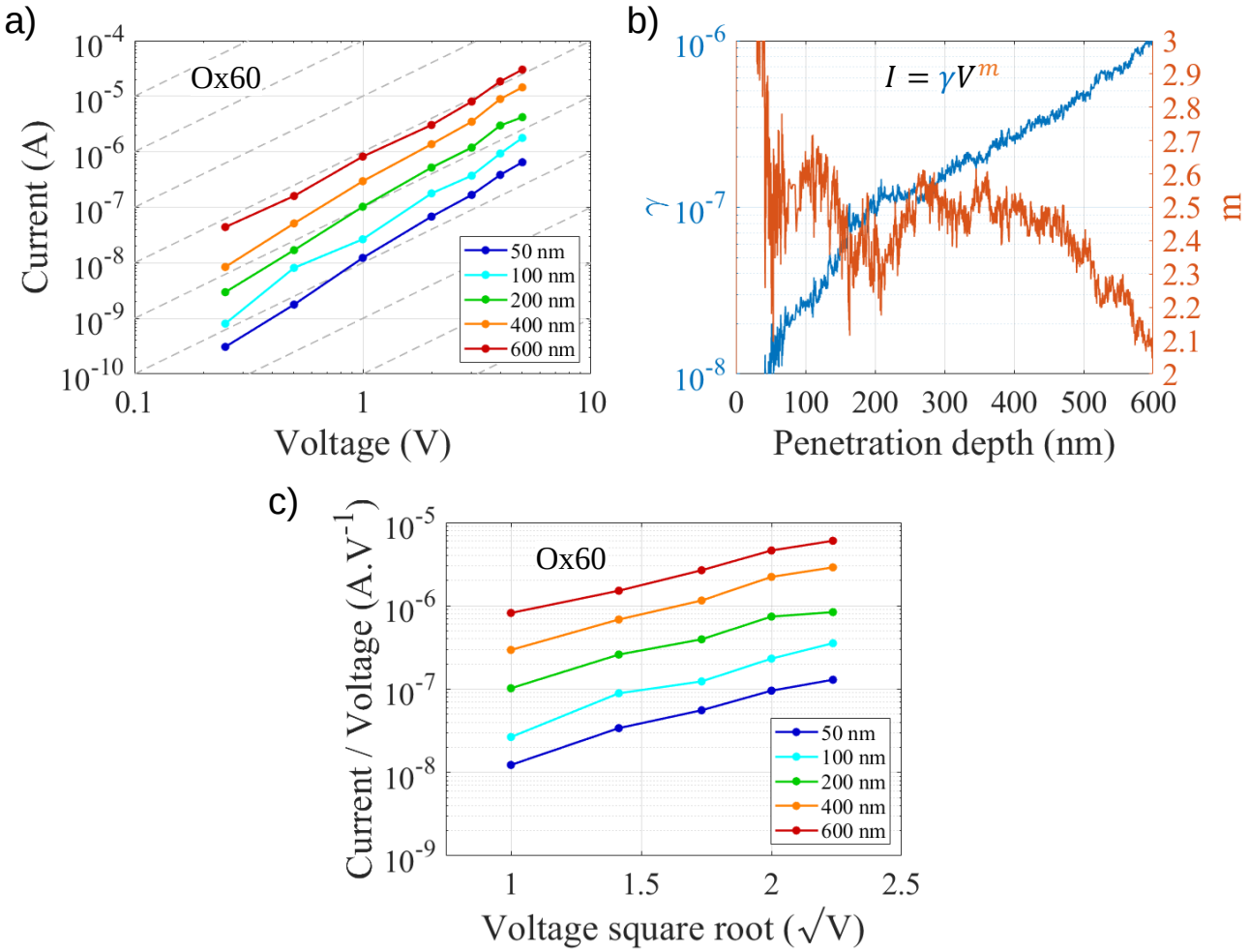

Figure 4.10. Identification of the oxide film electrical behavior on the Ox60 sample. (a) I vs V plot in log-log scale. (b) Power law fitting of $I-V$ characteristics as a function of indentation depth (γ is the pre-factor and m is the exponent). (c) I/V vs $\sqrt{V}$ plot in log-lin scale.

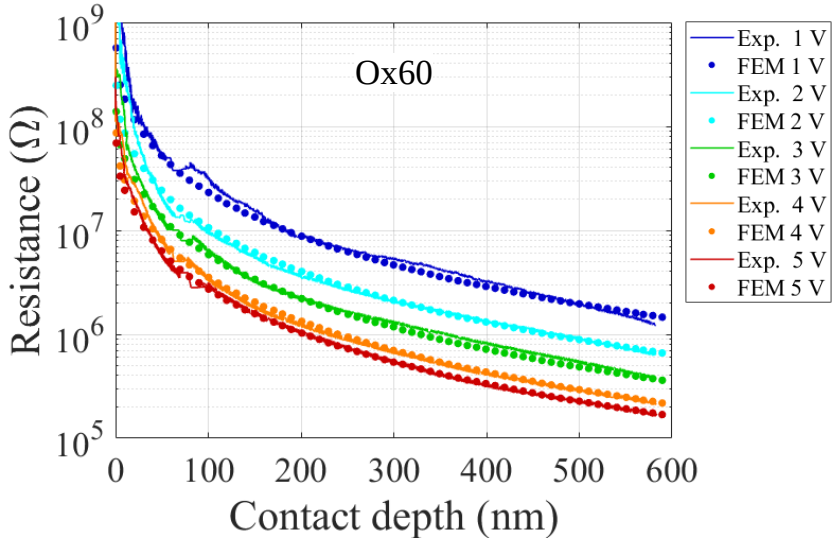

Figure 4.11. Resistance vs contact depth curves obtained by electrical-nanoindentation experiments and FEM modeling.

Elastic properties (Isotropic linear elastic)		Plastic properties (Drucker-Prager with linear hardening)			Electrical properties (Poole-Frenkel)		
E (GPa)	ν (-)	β (°)	σ_{c0} (MPa)	K (GPa)	σ_{PF} (S/cm)	Φ (eV)	k (-)
22	0.3	20	100	8	0.01	0.32	7

Table 4.2. Mechanical and electrical properties of Cu_2O cuprous oxide.

4.5 Conclusion

A comprehensive study of microstructure and mechanical/electrical properties of copper oxide thin films obtained by simple thermal oxidation from bulk annealed copper has been performed. The characterization of the properties was carried out through an approach combining nanoindentation experiments coupled with fine electrical measurements and multiphysics numerical simulations by the finite element method. The main findings of the work are the following:

- ACOM/TEM phase and orientation mappings from oxide cross-sections clearly revealed layers composed of Cu_2O, with 10-100 nm equiaxed grains, and some defects associated with the thermal oxidation process (surface roughness and interface voids).
- The elastic modulus of the oxide film was determined, and its plastic properties were evaluated by considering both the effect of shear and hydrostatic pressure using a Drucker-Prager yield criterion.
- FEM simulations highlight the contribution of the oxide film on enhancing size effects in the annealed copper substrate. Indeed, the oxide film can act as an non-penetrable barrier against dislocation gliding, inducing a strong back stress, and finally leading to extra strain hardening and strain gradient plasticity effects, as recently reported with a graphene single layer deposited on annealed copper [276].
- The electrical conduction mechanism of Cu_2O was identified as a Poole-Frenkel behavior. According to this law, constitutive parameters were determined. In particular, the level of trap barrier suggests that the structural defects driving the electrical transport in such low temperature processed thermal oxide layers are simple copper vacancies.
- Statistical analysis conducted on the pop-in event as a function of oxide film thickness led to another side results of this work: (i) The number of dislocations involved in the plastic burst is lower when the oxide film is thicker. (ii) Incipient plasticity is delayed as the film is thicker. These observations could be seen as an increase in the equivalent size of the indenter by the hard film conforming to its surface, thus generating a late onset of plasticity in the copper substrate and a redistribution of stresses as known for spherical indentation [300].

These results will contribute to the design of copper oxide thin films for integration into more sustainable advanced functional devices, to address their reliability issues, but also to tune the small-scale plastic behavior of metals by oxidation processes.

General Conclusion and Prospects

Within the framework of this PhD, the mechanical and electrical behaviors of three ceramic/dielectric thin films on conductive substrates (Si_3N_4-1.3µm/AlSiCu, SiOCH-330nm/Si, Cu_2O-225nm/Cu) have been described, and their properties determined. This was made possible by an approach coupling experiments with an advanced characterization tool and numerical simulations.

The experiments were carried out mainly by electrical-nanoindentation, which consisted in polarizing the sample and measuring the current flowing through the tip during a classical instrumented nanoindentation test. Experimental conditions were found to apply this technique to the monitoring of leakage currents in insulating thin films. This was a first challenge because of the high voltages to be applied (up to more than 100 V) and the very low currents to be measured (from fA) while limiting parasitic effects (capacitive couplings, set-up leakage, current transients, etc.). Thus, fine mechanical and electrical measurements at submicrometer scales could be performed. Associated with *post mortem* imaging of the residual imprints by different techniques (scanning electron microscopy, transmission electron microscopy, atomic force microscopy, ...), constitutive laws of the indented materials have been identified.

A second challenge was the processing of the raw load-depth and current-depth curves to extract the properties of the studied materials. Considering the complexity of the problem (geometry, loading conditions, constitutive laws, ...), numerical tools were essential to process the experimental results in a quantitative way. Several complex models were developed such as mechanical models of cracking/decohesion integrating cohesive laws, multiphysical models describing both the mechanical and electrical behavior of the systems, or a particularly noteworthy model coupling electrical conduction to plasticity in dielectric thin films. From these, the electrical-nanoindentation tests were simulated by the finite element method. Numerical curves were plotted with different sets of parameters and compared to the experimental ones. The material properties corresponded to the set of parameters leading to the closest simulated response to the experiment.

Finally, several original results of both academic and application interest were obtained from each system:

- Si_3N_4-1.3µm/AlSiCu: an energy-based methodology using features on the loading curves of "*brittle on ductile*" stacks has been developed to determine the damage properties of the brittle layer and to access the crack locations.
- SiOCH-330nm/Si: the classical Poole-Frenkel law driving the electrical transport of many dielectrics has been extended with the introduction of a phenomenological term modulating the conduction in the material as a function of its plastic deformation.
- Cu_2O-225nm/Cu: size effects already well known in crystalline metals (onset of plasticity, plasticity gradients) have been enhanced in the copper substrate by growing an oxide layer on their surface.

In addition to gaining a better understanding of the functional systems studied, which are at the heart of modern microelectronics, these results are probably generic enough to be applicable to other similar systems. In particular, they open very interesting perspectives on the reliability of advanced devices, which must ensure one or more functions while being subject to various mechanical stresses.

During this PhD, several other notable results were obtained on each of the three systems presented, but also on a recurrent question in electrical-nanoindentation: the effect of current density on thermal heating. An overview of these perspectives is given in the following.

Substrate influence on Si_3N_4 behavior

It was seen in Chapter 2 of this manuscript that the indentation of the Si_3N_4/AlSiCu/SiO_2/Si system (Figure 5.1a) led to the cracking of the nitride film (Figure 5.1b) and resulted in several pop-in on the loading curves (Figure 5.1c). Nanoindentation tests at the same maximum load (45 mN) were performed on the multilayer without depositing the ductile AlSiCu layer, i.e. on a brittle stack (Figure 5.1d).

The indented area was observed by SEM as shown in Figure 5.1e. It revealed plastic imprints of the Berkovich tip in the Si_3N_4 film with no apparent surface cracks. Concerning the load-depth curves, they do not show any pop-in, as evidenced by the representative indentation curve in Figure 5.1f.

To understand what mechanisms drive the irreversible deformation of the nitride film, the previously developed FEM model was adapted by removing the ductile AlSiCu layer. Several hypotheses were tested by changing the behavior of the materials (perfect elasticity, different plasticity laws, cracking with CZMs) and interfaces (fully tied, free, damaged with CZMs) and by comparing each time the resulting numerical curves to the experimental one. The only numerical load-depth curve that allowed to match the experimental data, with reasonable properties and agreement with the *post mortem* observations, was obtained by considering Si_3N_4 as elastic-perfectly plastic and the Si_3N_4/SiO_2 interface as damaged. Figure 5.1f shows the curve from the numerical simulation with a nitride yield strength of $\sigma_y = 15$ GPa and interface cohesive parameters of $T_n = T_t = 100$ MPa and $G_c = 1$ J/m^2.

The change in mechanical behavior of the nitride film as a function of the substrate is particularly interesting and deserves to be studied further. The substrate hardness at which this change in film behavior occurs could be estimated or the sensitivity to interface damage parameters could be evaluated. Especially, this work may have promising application perspectives, for example concerning the cutting of chips for microelectronic systems. It shows that to limit the damage of the device, the cutting path should be placed away from the metallic underlayers.

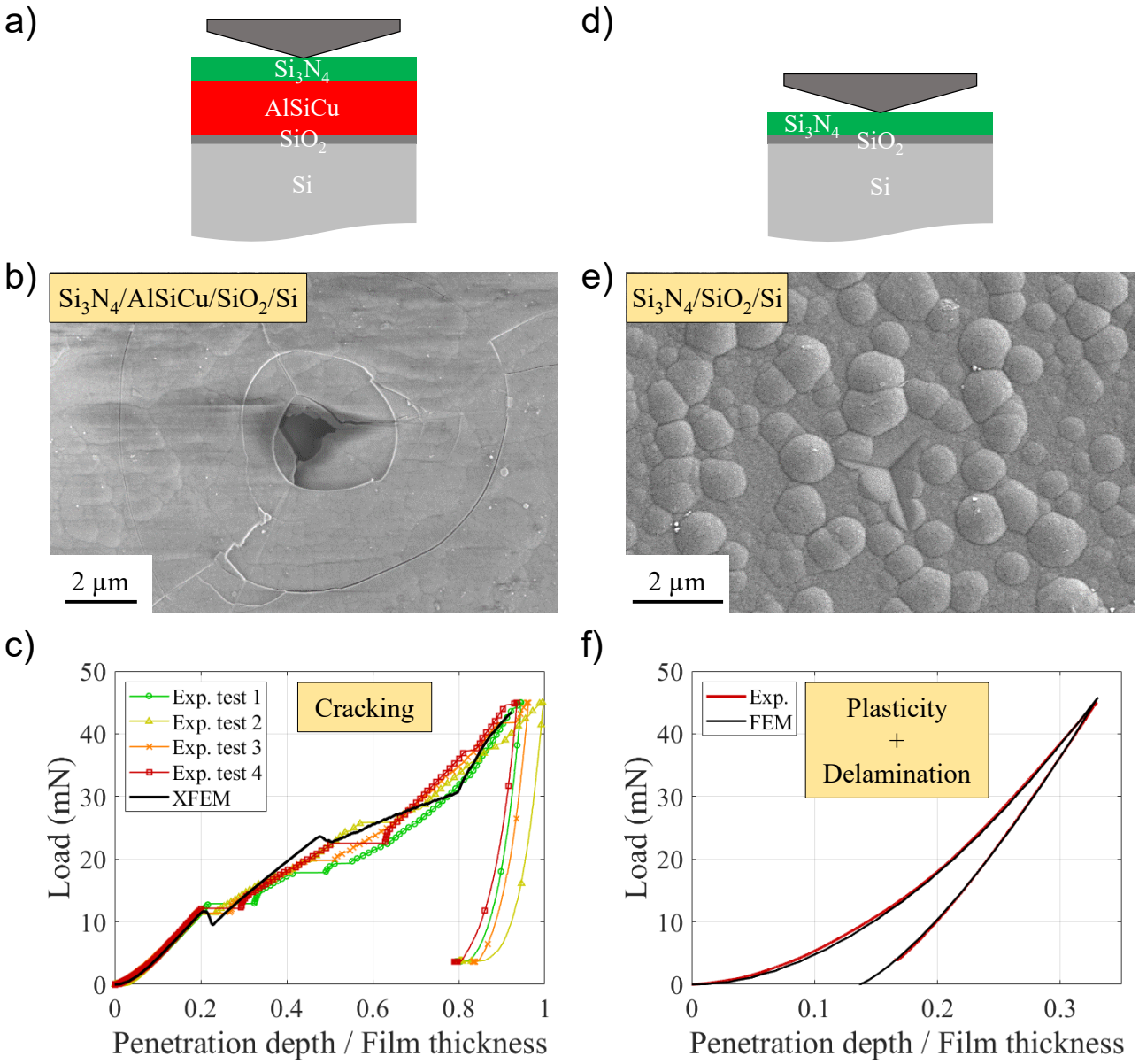

Figure 5.1. (a) Schematic of the nanoindentation tests performed on the Si_3N_4/AlSiCu/SiO_2/Si system. (b) SEM image of the residual imprint left with a maximum load of 45 mN. (c) Corresponding experimental and numerical indentation curves. (d) Schematic of the nanoindentation tests performed on the Si_3N_4/SiO_2/Si system. (e) SEM image of the residual imprint left with a maximum load of 45 mN. (f) Corresponding experimental and numerical indentation curves.

Electrically-induced mechanical failures in SiOCH

It was highlighted in Chapter 3 a drop in electrical conductivity of the nanoporous organosilicate glass film induced by mechanical deformation. Further electrical-nanoindentation tests were carried out on this SiOCH film with a flat punch of 2 µm diameter (the only experiments performed with another tip than the Berkovich ones in this thesis). The protocol consisted of maintaining a soft load of 300 µN ($\cong$ 20 nm) to ensure full contact, applying a constant voltage, and finally monitoring the current and contact stiffness responses over time. Figures 5.2a and 5.2b show a schematic of the tests and the results obtained respectively.

Up to 70 V, the current remains constant at a low base level of about 10 fA during the 20 min test as shown in Figure 5.2b. For these voltages, the contact stiffness is constant at

$\sim$ 28 kN/m, attesting to a steady mechanical strength of the system. Above 70 V, the current first increases as soon as the voltage is applied until it reaches a stationary state, then increases again very rapidly (the earlier the higher the voltage) until it saturates. Interestingly, the drastic electrical leakage is associated with a significant increase in contact stiffness, which is greater the higher the voltage. Furthermore, these events are simultaneous within the sensitivity range of the measurements, as shown in Figure 5.2c by calculating the derivatives of stiffness and current versus time on the test performed at 90 V. Figure 5.2d shows that the increase in stiffness corresponds to a sinking of the flat punch to maintain the constant applied load of 300 µN. This was confirmed by optical images of the indents (without polarizing filter) as seen in Figure 5.2e, which shows circular areas with different colors related to thickness variations measured by AFM (Figure 5.2f). However, the observed color changes extend over halos much larger than the diameter of the flat punch (more than 50 µm in diameter at 100 V for 10 min versus 2 µm respectively).

A noteworthy experiment was performed to verify that the sinking of the flat punch is not caused by the electrostatic force established between the tip and the silicon substrate. The nanoindenter was placed in a SEM to make the measurement under vacuum. The flat punch was positioned at a distance z from the film surface, a voltage of 100 V was then applied, and the load variation to maintain this z position was measured. By repeating this test at different tip/film distances (Figure 5.2g), the electrostatic force at contact was estimated as the ratio of the load variation ΔL just prior to contact by the dielectric constant k of SiOCH. A value of 6 µN was found which is much lower than the applied soft load of 300 µN. This hypothesis was therefore rejected.

A last type of experiments, similar to those presented in Figure 5.2b, were performed but with a polarization of opposite sign. Figure 5.2h shows the evolution of the contact stiffness (at a fixed load of 300 µN) and of the current (at a fixed voltage of -90 V) as a function of time. Contrary to the experiment carried out at +90 V for which the current increased drastically to more than 10 nA in 150 s, here the current remains stable at a low level of the pA. Moreover, the mechanical response of the system at -90 V remains also stable with a stiffness at a low level of $\sim$ 20 kN/m, contrary to the experiment performed at +90 V. The only difference between these two experiments lies in the current values since the electric field values are the same (the voltage drop in the silicon substrate in reverse polarity was estimated to be of the order of the V and is therefore negligible). This suggests that the observed phenomenon is driven by the current flowing through the SiOCH dielectric film rather than by the electric field.

Finally, thermal effects by self-heating seem an unlikely cause of the phenomenon given the low current densities flowing through SiOCH just before the drastic electrical leakage occurs, estimated at $\sim$ 10 µA/cm^2.

All these experiments reveal electrically-induced mechanical failures driven by current flow, which appear as a collapse of the SiOCH film over diameters much larger than that of the indenter. Fine physicochemical characterizations and/or atomic scale calculations could be particularly relevant to unravel the microscopic mechanisms involved in this damage process, such as electrochemical reactions that are currently being investigated. From an application viewpoint, these results are interesting for the reliability of dielectric materials, especially to understand the origin of some time-dependent dielectric breakdown phenomena.

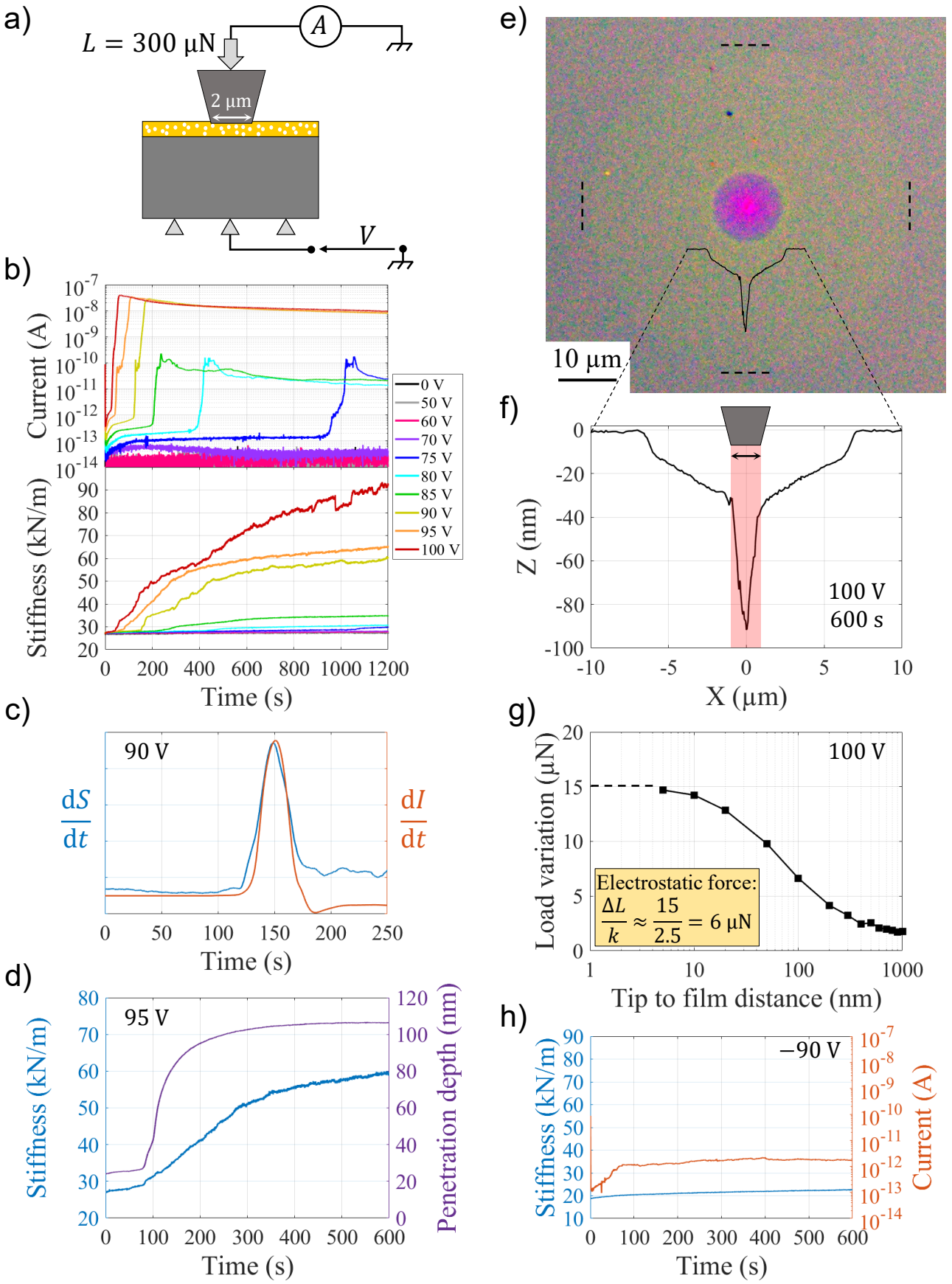

Figure 5.2. (a) Schematic of the electrical-nanoindentation tests. (b) Current (at constant voltage) and stiffness (at constant load) vs time. (c) Correlation between the increase in stiffness and the increase in current. (d) Correlation between the increase in stiffness and the sinking of the tip. (e) Optical image (without polarizing filter) of the indented area and its periphery. (f) AFM scan of this area. (g) Electrostatic force measurement with the electrical nanoindentation device integrated in a SEM. (h) Stiffness and current vs time at −90 V.

Microstructure/properties relations in copper oxide films

It was determined in Chapter 4 the mechanical and electrical properties of copper oxide films processed by thermal oxidation at 200 °C from annealed copper substrates. Two other systems were processed with different conditions and characterized by electrical-nanoindentation.

The first targeted system was a Cu_2O film processed at high temperature (typically at the annealing temperature of copper, 800 °C) with a thickness similar to the one processed at low temperature. Thus, a change in the microstructure of the oxide (larger grains, higher vacancy concentration, ...) affecting its properties could be expected. At 800 °C, the pressure-temperature diagram indicates that Cu_2O is thermodynamically stable if the oxygen partial pressure is below $\sim 10^{-3}$ atm. Above this pressure, the CuO phase is stable. The challenge was therefore to finely control the oxygen partial pressure to select the desired oxide phase. Preliminary oxidations were carried out at 800 °C for 5 h under primary vacuum with residual atmospheres of O_2 or O_2/H_2. They led to a discontinuous Cu_2O film, with a maximum thickness of about 1 µm, revealing copper islands (Figure 5.3a). This microstructure and morphology have been recently observed in the literature [341] and have been attributed to redox processes. Despite the difficulty to characterize the properties of this system, exploratory electrical-nanoindentation tests were performed (see the schematic in Figure 5.3b), *in situ* SEM to indent only the oxidized areas. The obtained load-depth and resistance-depth curves are presented in Figure 5.3c. Nevertheless, the dispersion of the results (discontinuous layer) and the range of electric field probed (same voltages applied as on Cu_2O-low temperature while the film is thicker) make it difficult to conclude about a change of properties caused by a microstructure effect.

A second objective was to characterize the properties of the CuO phase. Although this phase is thermodynamically stable in ambient air for oxidation temperatures between room temperature and 1000 °C, the CuO phase grows from the Cu_2O phase, leading to CuO/Cu_2O bilayers. Furthermore, for reasonable oxidation times ($\sim$ 1 h), the oxidation temperature must be higher than about 250 °C. Several systems were processed at temperatures between 250 and 500 °C in ambient air with durations between 15 min and 2 h. These conditions led to CuO/Cu_2O bilayers but with pronounced heterogeneities: non-uniformity of layer thickness, voids at the interfaces, pores in the layers and CuO whiskers on the surface. Figure 5.3d shows a SEM image of one of these systems, processed at 500 °C for 15 min. Exploratory electrical-nanoindentation tests were also performed on this sample (see the schematic in Figure 5.3e and the corresponding loading and resistance curves in Figure 5.3f). A notable result is the significant electrical sensitivity to whiskers and their degradation compared to the mechanical one before surface contact. However, the heterogeneities listed above make the quantitative exploitation of these curves difficult. Especially, the non-uniform thickness of the layers is an obstacle to the estimation of the electric field, and the whiskers prevent the evaluation of the contact area and thus the current density.

Further processing campaigns would be useful to obtain homogeneous Cu_2O and CuO layers at different temperatures. Thus, the properties of these systems could be extracted by methods coupling electrical-nanoindentation experiments and FEM simulations, as proposed in the present manuscript, for correlating them to their microstructure.

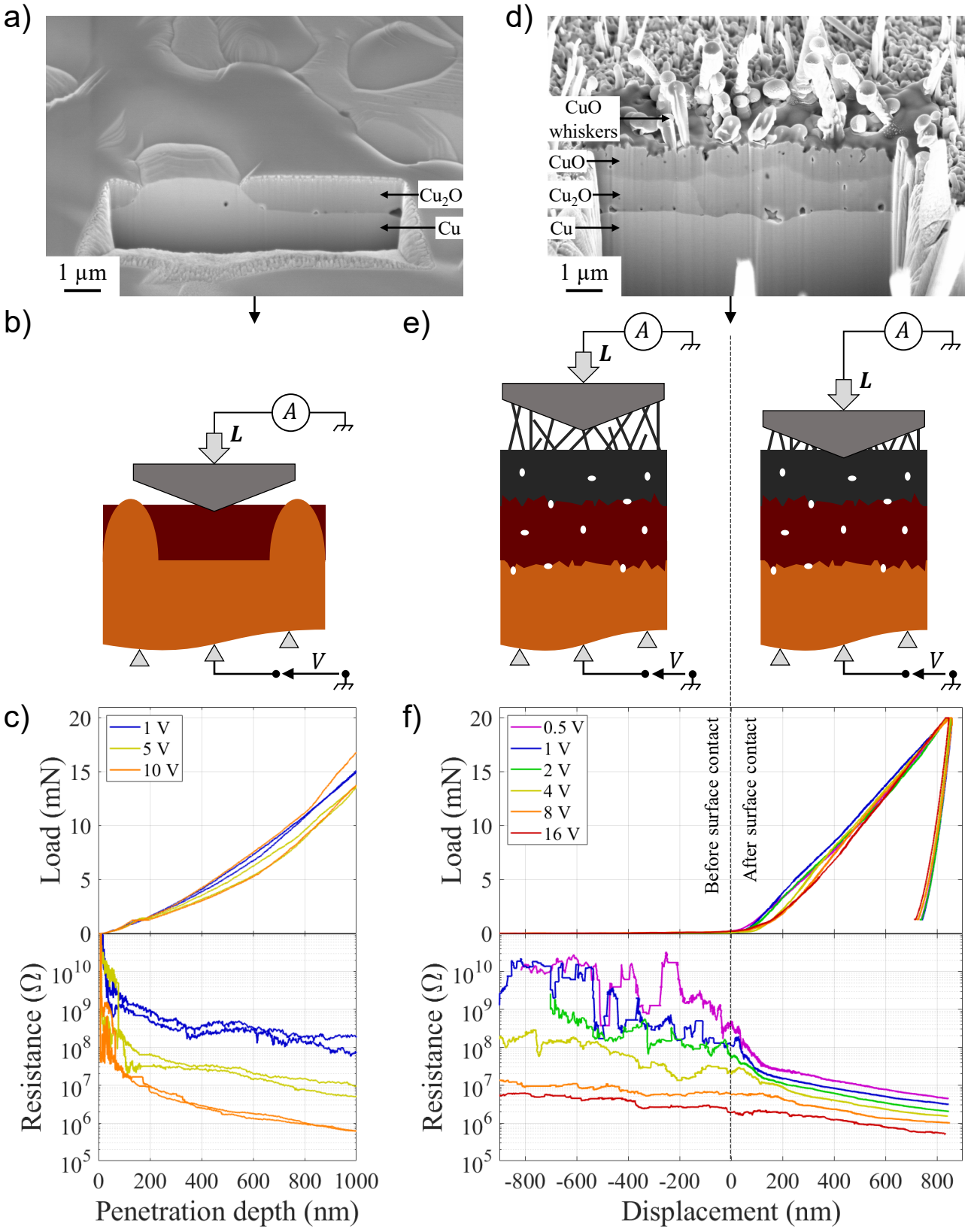

Figure 5.3. (a) Cross-sectional SEM image after FIB-slicing of the Cu_2O/Cu system processed by thermal oxidation of an annealed copper substrate, at 800 °C for 5 h under primary vacuum with residual O_2/H_2 atmosphere. (b) Schematic of the electrical-nanoindentation tests on this system. (c) Corresponding loading and electrical resistance curves. (d) Cross-sectional SEM image after FIB-slicing of the $CuO/Cu_2O/Cu$ system processed by thermal oxidation of an annealed copper substrate, at 500 °C for 15 min in ambient air. (e) Schematic of the electrical-nanoindentation tests on this system. (f) Corresponding loading and electrical resistance curves.

Self-heating in electrical-nanoindentation

A recurrent question in electrical-nanoindentation is about the effect of current density on thermal heating, which could affect the measurements. To estimate this Joule heating, electrical-nanoindentation tests were performed in a configuration maximizing the current density, i.e. on a 111-oriented single crystal gold sample (metal without oxide). The protocol consisted of maintaining the load corresponding to three depths (about 150, 500, 1000 nm), applying a voltage and monitoring the tip displacement over time. Durations of 4-6 min were left between the beginning of the load holding and the beginning of the voltage application to allow time for the system to thermalize and the sample to creep. Figures 5.4a and 5.4b show a schematic of the tests and the results obtained respectively.

From the application of a voltage, Figure 5.4b shows that the tip moves progressively in the direction of its withdrawal until it stabilizes at a new depth, lower than the depth measured without voltage. This phenomenon seems reversible since when the voltage is switched off, the tip returns to its initial position. Closer views of the three sets of curves in Figure 5.4b are shown in Figures 5.4c, 5.4d and 5.4e for initial depths of 150, 500 and 1000 nm respectively. They show that the higher the applied voltage, the greater the amplitude of the tip withdrawal. These displacement amplitudes were extracted just before the end of the voltage application, when the steady state is established, and plotted as a function of the applied voltage (Figure 5.4f). For each initial depth, the tip displacement Δl is found to vary as the square of the applied voltage ΔV.

All these observations are in perfect agreement with a Joule heating of the boron doped diamond tip, which by heat transfer would induce a thermal expansion of the gold sample around the contact, able to move back the tip. Indeed, by establishing a steady state flux balance and making strong simplifications, this assumption leads to the same dependence between the tip displacement and the applied voltage as the one observed experimentally: $\Delta l_{Au} \sim l_{Au}\alpha_{Au}\left(\sigma_{BDD}/\lambda_{BDD}\right)\Delta V^2$ where Δl_{Au} is the gold expansion, l_{Au} the thermal gradient length in the gold sample, α_{Au} the coefficient of thermal expansion of gold, σ_{BDD} the electrical conductivity of the BDD tip, λ_{BDD} its thermal conductivity and ΔV the applied voltage. As shown in Figure 5.4g, a multiphysics thermal-electrical-mechanical 3D FEM model has been built to fully validate the hypothesis, to access different information (size of the thermal gradient, temperature values, ...) and ultimately to predict the self-heating on other indented systems. Currently, the simulations give exactly the right experimental trends with the scenario just described but with ~ 50 times lower values.

Further experimental and numerical efforts are still needed to both be sure to understand the physics of the problem and to be able to capture it with a quantitative model. Thus, self-heating in electrical-nanoindentation and its consequences could be described for the first time.

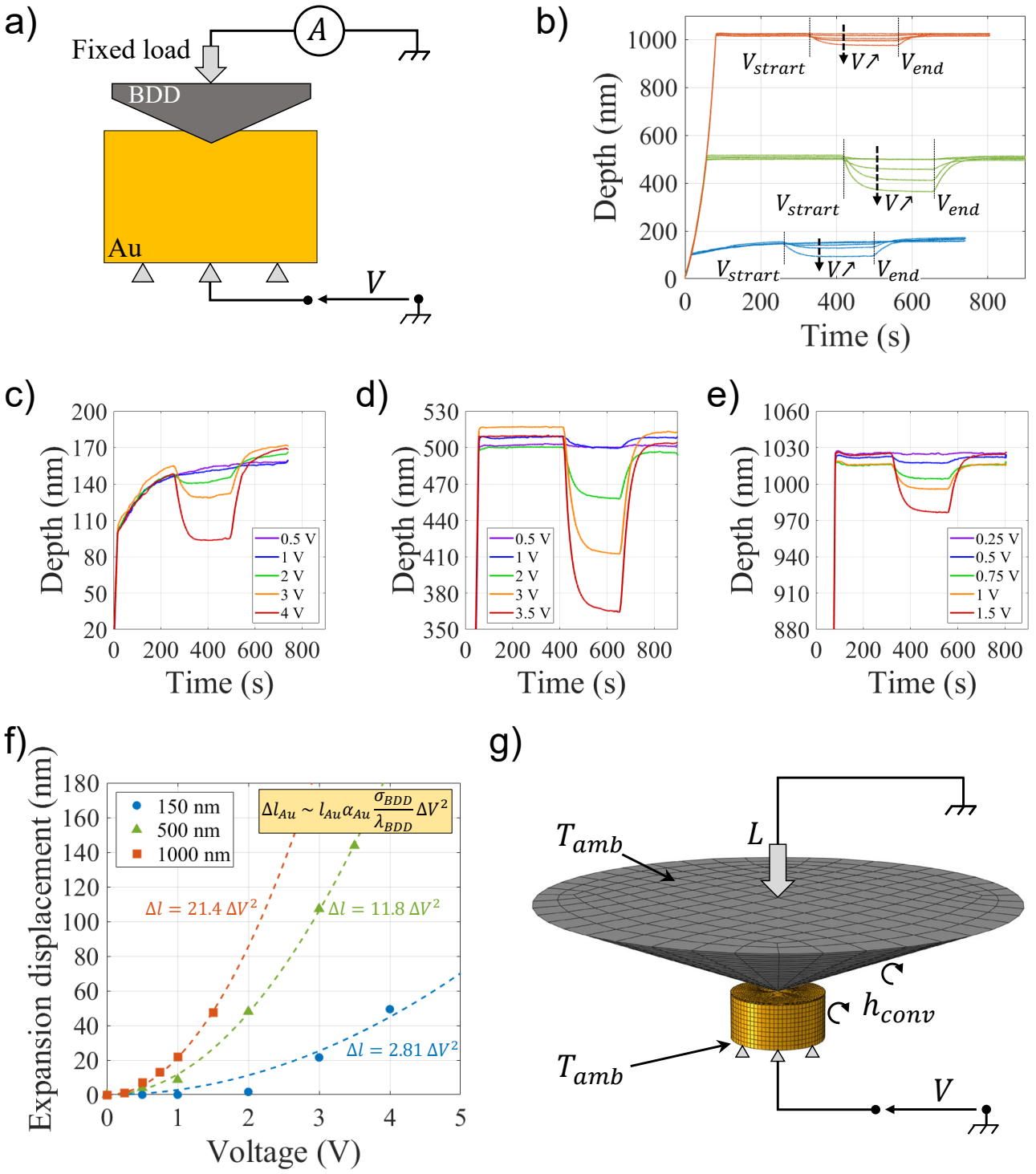

Figure 5.4. (a) Schematic of the electrical-nanoindentation tests on a 111-oriented gold single crystal. (b) Evolution of the tip depth over time at three fixed loads and several voltages. (c) Focus on Figure 5.4b for the set of curves obtained at an initial depth of 150 nm, (d) 500 nm and (e) 1000 nm. (f) Expansion displacement as a function of applied voltage for the three fixed loads. (g) Multiphysics thermal-electrical-mechanical 3D FEM model of the problem.

References

[1] J. B. Pethica, R. Hutchings, and W. C. Oliver. Hardness measurement at penetration depths as small as 20 nm. *Philosophical Magazine A* **48** (1983), 593–606.
DOI: 10.1080/01418618308234914.

[2] J. L. Loubet, J. M. Georges, O. Marchesini, and G. Meille. Vickers Indentation Curves of Magnesium Oxide (MgO). *Journal of Tribology* **106** (1984), 43–48.
DOI: 10.1115/1.3260865.

[3] J. B. Pethica and W. C. Oliver. Mechanical Properties of Nanometre Volumes of Material: use of the Elastic Response of Small Area Indentations. *MRS Proceedings* **130** (1988), 13.
DOI: 10.1557/PROC-130-13.

[4] W. Oliver and G. Pharr. An improved technique for determining hardness and elastic modulus using load and displacement sensing indentation experiments. *Journal of Materials Research* **7** (1992). Edition: 2011/01/31 Publisher: Cambridge University Press, 1564–1583.
DOI: 10.1557/JMR.1992.1564.

[5] J. L. Loubet, M. Bauer, A. Tonck, S. Bec, and B. Gauthier-Manuel. Nanoindentation with a Surface Force Apparatus. *Mechanical Properties and Deformation Behavior of Materials Having Ultra-Fine Microstructures*. Ed. by M. Nastasi, D. M. Parkin, and H. Gleiter. Dordrecht: Springer Netherlands, 1993, 429–447.
DOI: 10.1007/978-94-011-1765-4_28.

[6] E. Meyer. Untersuchungen über Härteprüfung und Härte Brinell Methoden. *Zeitschrift des Vereines Deutscher Ingenieure* **52** (1908).

[7] I. N. Sneddon. The relation between load and penetration in the axisymmetric boussinesq problem for a punch of arbitrary profile. *International Journal of Engineering Science* **3** (1965), 47–57.
DOI: 10.1016/0020-7225(65)90019-4.

[8] F. Lockett. Indentation of a rigid/plastic material by a conical indenter. *Journal of the Mechanics and Physics of Solids* **11** (1963), 345–355.
DOI: 10.1016/0022-5096(63)90035-8.

[9] M. Doerner and W. Nix. A method for interpreting the data from depth-sensing indentation instruments. *Journal of Materials Research* **1** (1986), 601–609.
DOI: 10.1557/JMR.1986.0601.

[10] G. Hochstetter, A. Jimenez, and J. L. Loubet. Strain-rate effects on hardness of glassy polymers in the nanoscale range. Comparison between quasi-static and continuous stiffness measurements. *Journal of Macromolecular Science, Part B* **38** (1999), 681–692.
DOI: 10.1080/00222349908248131.

[11] J. L. Bucaille, E. Felder, and G. Hochstetter. Identification of the viscoplastic behavior of a polycarbonate based on experiments and numerical modeling of the nano-indentation test. *Journal of Materials Science* **37** (2002), 3999–4011.
DOI: 10.1023/A:1019644630927.

[12] F. Volpi, M. Rusinowicz, S. Comby-Dassonneville, G. Parry, C. Boujrouf, M. Braccini, D. Pellerin, and M. Verdier. Resistive-nanoindentation on gold: Experiments and modeling of the electrical contact resistance. *Review of Scientific Instruments* **92** (2021), 035102.
DOI: 10.1063/5.0032682.

[13] R. King. Elastic analysis of some punch problems for a layered medium. *International Journal of Solids and Structures* **23** (1987), 1657–1664.
DOI: 10.1016/0020-7683(87)90116-8.

[14] Y.-G. Jung, B. R. Lawn, M. Martyniuk, H. Huang, and X. Z. Hu. Evaluation of elastic modulus and hardness of thin films by nanoindentation. *Journal of Materials Research* **19** (2004), 3076–3080.
DOI: 10.1557/JMR.2004.0380.

[15] S. Bec, A. Tonck, and J. L. Loubet. A simple guide to determine elastic properties of films on substrate from nanoindentation experiments. *Philosophical Magazine* **86** (2006), 5347–5358.
DOI: 10.1080/14786430600660856.

[16] G. Huajian, C. Cheng-Hsin, and L. Jin. Elastic contact versus indentation modeling of multi-layered materials. *International Journal of Solids and Structures* **29** (1992), 2471–2492.
DOI: 10.1016/0020-7683(92)90004-D.

[17] J. Mencik, D. Munz, E. Quandt, E. R. Weppelmann, and M. V. Swain. Determination of elastic modulus of thin layers using nanoindentation. *Journal of Materials Research* **12** (1997), 2475–2484.
DOI: 10.1557/JMR.1997.0327.

[18] A. Bhattacharya and W. Nix. Analysis of elastic and plastic deformation associated with indentation testing of thin films on substrates. *International Journal of Solids and Structures* **24** (1988), 1287–1298.
DOI: 10.1016/0020-7683(88)90091-1.

[19] D. Chicot and J. Lesage. Absolute hardness of films and coatings. *Thin Solid Films* **254** (1995), 123–130.
DOI: 10.1016/0040-6090(94)06239-H.

[20] A. Korsunsky, M. McGurk, S. Bull, and T. Page. On the hardness of coated systems. *Surface and Coatings Technology* **99** (1998), 171–183.
DOI: 10.1016/S0257-8972(97)00522-7.

[21] E. Puchi-Cabrera, J. Berrios, and D. Teer. On the computation of the absolute hardness of thin solid films. *Surface and Coatings Technology* **157** (2002), 185–196.
DOI: 10.1016/S0257-8972(02)00153-6.

[22] B. Jonsson and S. Hogmark. Hardness measurements of thin films. *Thin Solid Films* **114** (1984), 257–269.
DOI: 10.1016/0040-6090(84)90123-8.

[23] P. Burnett and D. Rickerby. The mechanical properties of wear-resistant coatings: I: Modelling of hardness behaviour. *Thin Solid Films* **148** (1987), 41–50.
DOI: 10.1016/0040-6090(87)90119-2.

[24] H. Yu, S. Sanday, and B. Rath. The effect of substrate on the elastic properties of films determined by the indentation test — axisymmetric boussinesq problem. *Journal of the Mechanics and Physics of Solids* **38** (1990), 745–764.
DOI: 10.1016/0022-5096(90)90038-6.

[25] A. Perriot and E. Barthel. Elastic contact to a coated half-space - Effective elastic modulus and real penetration. *Journal of Materials Research* **19** (2004), 600–608.
DOI: 10.1557/jmr.2004.0075.

[26] H. Li and J. J. Vlassak. Determining the elastic modulus and hardness of an ultra-thin film on a substrate using nanoindentation. *Journal of Materials Research* **24** (2009), 1114–1126.
DOI: 10.1557/jmr.2009.0144.

[27] X. Chen and J. J. Vlassak. Numerical study on the measurement of thin film mechanical properties by means of nanoindentation. *Journal of Materials Research* **16** (2001), 2974–2982.
DOI: 10.1557/JMR.2001.0408.

[28] C.-H. Hsueh and P. Miranda. Master curves for Hertzian indentation on coating/substrate systems. *Journal of Materials Research* **19** (2004), 94–100.
DOI: 10.1557/jmr.2004.19.1.94.

[29] Z.-H. Xu and D. Rowcliffe. Finite element analysis of substrate effects on indentation behaviour of thin films. *Thin Solid Films* **447-448** (2004), 399–405.
DOI: 10.1016/S0040-6090(03)01071-X.

[30] M. Sakai. Substrate-affected indentation contact parameters of elastoplastic coating/substrate composites. *Journal of Materials Research* **24** (2009), 831–843.
DOI: 10.1557/jmr.2009.0102.

[31] J. Hay and B. Crawford. Measuring substrate-independent modulus of thin films. *Journal of Materials Research* **26** (2011), 727–738.
DOI: 10.1557/jmr.2011.8.

[32] D. Tabor. A simple theory of static and dynamic hardness. *Proceedings of the Royal Society of London. Series A. Mathematical and Physical Sciences* **192** (1948), 247–274.
DOI: 10.1098/rspa.1948.0008.

[33] D. Tabor. *The Hardness of Metals*. Monographs on the physics and chemistry of materials. Clarendon Press, 1951.

[34] P.-L. Larsson. Investigation of sharp contact at rigid–plastic conditions. *International Journal of Mechanical Sciences* **43** (2001), 895–920.
DOI: 10.1016/S0020-7403(00)00056-4.

[35] K. Johnson. The correlation of indentation experiments. *Journal of the Mechanics and Physics of Solids* **18** (1970), 115–126.
DOI: 10.1016/0022-5096(70)90029-3.

[36] K. L. Johnson. *Contact Mechanics*. Cambridge: Cambridge University Press, 1985.
DOI: 10.1017/CBO9781139171731.

[37] D. Durban and R. Masri. Conical indentation of strain-hardening solids. *European Journal of Mechanics - A/Solids* **27** (2008), 210–221.
DOI: 10.1016/j.euromechsol.2007.05.007.

[38] G. Kermouche, J.-L. Loubet, and J.-M. Bergheau. An approximate solution to the problem of cone or wedge indentation of elastoplastic solids. *Comptes Rendus Mécanique* **333** (2005), 389–395.
DOI: 10.1016/j.crme.2005.04.001.

[39] B. Galanov, S. Ivanov, and V. Kartuzov. Improved core model of the indentation for the experimental determination of mechanical properties of elastic-plastic materials and its application. *Mechanics of Materials* **150** (2020), 103545.
DOI: 10.1016/j.mechmat.2020.103545.

[40] A. Giannakopoulos, P.-L. Larsson, and R. Vestergaard. Analysis of Vickers indentation. *International Journal of Solids and Structures* **31** (1994), 2679–2708.
DOI: 10.1016/0020-7683(94)90225-9.

[41] P.-L. Larsson, A. Giannakopoulos, E. SÖderlund, D. Rowcliffe, and R. Vestergaard. Analysis of Berkovich indentation. *International Journal of Solids and Structures* **33** (1996), 221–248.
DOI: 10.1016/0020-7683(95)00033-7.

[42] Y.-T. Cheng and C.-M. Cheng. Scaling approach to conical indentation in elastic-plastic solids with work hardening. *Journal of Applied Physics* **84** (1998), 1284–1291.
DOI: 10.1063/1.368196.

[43] Y.-T. Cheng and C.-M. Cheng. Effects of 'sinking in' and 'piling up' on estimating the contact area under load in indentation. *Philosophical Magazine Letters* **78** (1998), 115–120.
DOI: 10.1080/095008398178093.

[44] Y.-T. Cheng and C.-M. Cheng. Can stress–strain relationships be obtained from indentation curves using conical and pyramidal indenters? *Journal of Materials Research* **14** (1999), 3493–3496.
DOI: 10.1557/JMR.1999.0472.

[45] E. Buckingham. On Physically Similar Systems; Illustrations of the Use of Dimensional Equations. *Physical Review* **4** (1914), 345–376.
DOI: 10.1103/PhysRev.4.345.

[46] M. Dao, N. Chollacoop, K. Van Vliet, T. Venkatesh, and S. Suresh. Computational modeling of the forward and reverse problems in instrumented sharp indentation. *Acta Materialia* **49** (2001), 3899–3918.
DOI: 10.1016/S1359-6454(01)00295-6.

[47] J. H. Hollomon. Tensile Deformation. *Transactions of the Metallurgical Society of AIME* **162** (1945), 268–290.

[48] F. Kick. *Das Gesetz der proportionalen Widerstände und seine Anwendungen*. A. Felix, 1885.

[49] O. Casals and J. Alcala. The duality in mechanical property extractions from Vickers and Berkovich instrumented indentation experiments. *Acta Materialia* **53** (2005), 3545–3561.
DOI: 10.1016/j.actamat.2005.03.051.

[50] J. Bucaille, S. Stauss, E. Felder, and J. Michler. Determination of plastic properties of metals by instrumented indentation using different sharp indenters. *Acta Materialia* **51** (2003), 1663–1678.
DOI: 10.1016/S1359-6454(02)00568-2.

[51] N. Chollacoop, M. Dao, and S. Suresh. Depth-sensing instrumented indentation with dual sharp indenters. *Acta Materialia* **51** (2003), 3713–3729.
DOI: 10.1016/S1359-6454(03)00186-1.

[52] R. v. Mises. Mechanik der festen Korper im plastisch-deformablen Zustand. *Mathematisch-physikalische Klasse* **1** (1913), 582–592.

[53] D. C. Drucker and W. Prager. Soil mechanics and plastic analysis or limit design. *Quarterly of Applied Mathematics* **10** (1952), 157–165.
DOI: 10.1090/qam/48291.

[54] L. Charleux. Micromécanique de l'essai d'indentation : expériences et simulations. *PhD thesis* (2006).

[55] R. Seltzer, A. P. Cisilino, P. M. Frontini, and Y.-W. Mai. Determination of the Drucker–Prager parameters of polymers exhibiting pressure-sensitive plastic behaviour by depth-sensing indentation. *International Journal of Mechanical Sciences* **53** (2011), 471–478.
DOI: 10.1016/j.ijmecsci.2011.04.002.

[56] Y. Liu, B. Wang, M. Yoshino, S. Roy, H. Lu, and R. Komanduri. Combined numerical simulation and nanoindentation for determining mechanical properties of single crystal copper at mesoscale. *Journal of the Mechanics and Physics of Solids* **53** (2005), 2718–2741.
DOI: 10.1016/j.jmps.2005.07.003.

[57] N. Zaafarani, D. Raabe, R. Singh, F. Roters, and S. Zaefferer. Three-dimensional investigation of the texture and microstructure below a nanoindent in a Cu single crystal using 3D EBSD and crystal plasticity finite element simulations. *Acta Materialia* **54** (2006), 1863–1876.
DOI: 10.1016/j.actamat.2005.12.014.

[58] O. Casals, J. Ocenasek, and J. Alcala. Crystal plasticity finite element simulations of pyramidal indentation in copper single crystals. *Acta Materialia* **55** (2007), 55–68.
DOI: 10.1016/j.actamat.2006.07.018.

[59] J. Alcala, O. Casals, and J. Ocenasek. Micromechanics of pyramidal indentation in fcc metals: Single crystal plasticity finite element analysis. *Journal of the Mechanics and Physics of Solids* **56** (2008), 3277–3303.
DOI: 10.1016/j.jmps.2008.07.004.

[60] H.-J. Chang, M. Fivel, D. Rodney, and M. Verdier. Multiscale modelling of indentation in FCC metals: From atomic to continuum. *Comptes Rendus Physique* **11** (2010), 285–292.
DOI: 10.1016/j.crhy.2010.07.007.

[61] B. R. Lawn and M. V. Swain. Microfracture beneath point indentations in brittle solids. *Journal of Materials Science* **10** (1975), 113–122.
DOI: 10.1007/BF00541038.

[62] A. G. Evans and E. A. Charles. Fracture Toughness Determinations by Indentation. *Journal of the American Ceramic Society* **59** (1976), 371–372.
DOI: 10.1111/j.1151-2916.1976.tb10991.x.

[63] D. B. Marshall and B. R. Lawn. An Indentation Technique for Measuring Stresses in Tempered Glass Surfaces. *Journal of the American Ceramic Society* **60** (1977), 86–87.
DOI: 10.1111/j.1151-2916.1977.tb16106.x.

[64] B. R. Lawn, A. G. Evans, and D. B. Marshall. Elastic/Plastic Indentation Damage in Ceramics: The Median/Radial Crack System. *Journal of the American Ceramic Society* **63** (1980), 574–581.
DOI: 10.1111/j.1151-2916.1980.tb10768.x.

[65] G. Anstis, P. Chantikul, B. Lawn, and D. Marshall. A Critical Evaluation of Indentation Techniques for Measuring Fracture Toughness: I, Direct Crack Measurements. *Journal of the American Ceramic Society* **64** (1981), 533–538.
DOI: 10.1111/j.1151-2916.1981.tb10320.x.

[66] J. Malzbender, G. de With, and J. den Toonder. The P–h^2 relationship in indentation. *Journal of Materials Research* **15** (2000), 1209–1212.
DOI: 10.1557/JMR.2000.0171.

[67] J. D. Toonder, J. Malzbender, G. D. With, and R. Balkenende. Fracture Toughness and Adhesion Energy of Sol-gel Coatings on Glass. *Journal of Materials Research* **17** (2002), 224–233.
DOI: 10.1557/JMR.2002.0032.

[68] X. Li, D. Diao, and B. Bhushan. Fracture mechanisms of thin amorphous carbon films in nanoindentation. *Acta Materialia* **45** (1997), 4453–4461.
DOI: 10.1016/S1359-6454(97)00143-2.

[69] X. Li and B. Bhushan. Measurement of fracture toughness of ultra-thin amorphous carbon films. *Thin Solid Films* **315** (1998), 214–221.
DOI: 10.1016/S0040-6090(97)00788-8.

[70] S. J. Bull. Nanoindentation of coatings. *Journal of Physics D: Applied Physics* **38** (2005), R393–R413.
DOI: 10.1088/0022-3727/38/24/R01.

[71] J. Chen and S. J. Bull. A new method based on work-displacement curve to assess the toughness of coated system. *MRS Proceedings* **890** (2005), 0890–Y02–02.
DOI: 10.1557/PROC-0890-Y02-02.

[72] J. Chen and S. Bull. Assessment of the toughness of thin coatings using nanoindentation under displacement control. *Thin Solid Films* **494** (2006), 1–7.
DOI: 10.1016/j.tsf.2005.08.176.

[73] S. J. Bull. Analysis methods and size effects in the indentation fracture toughness assessment of very thin oxide coatings on glass. *Comptes Rendus Mécanique* **339** (2011), 518–531.
DOI: 10.1016/j.crme.2011.05.009.

[74] P. J. Wei, W. L. Liang, C. F. Ai, and J. F. Lin. A new method for determining the strain energy release rate of an interface via force–depth data of nanoindentation tests. *Nanotechnology* **20** (2009), 025701.
DOI: 10.1088/0957-4484/20/2/025701.

[75] J. Chen and S. J. Bull. Approaches to investigate delamination and interfacial toughness in coated systems: an overview. *Journal of Physics D: Applied Physics* **44** (2011), 034001.
DOI: 10.1088/0022-3727/44/3/034001.

[76] D. Dugdale. Yielding of steel sheets containing slits. *Journal of the Mechanics and Physics of Solids* **8** (1960), 100–104.
DOI: 10.1016/0022-5096(60)90013-2.

[77] G. Barenblatt. The Mathematical Theory of Equilibrium Cracks in Brittle Fracture. *Advances in Applied Mechanics*. **7**. Elsevier, 1962, 55–129.
DOI: 10.1016/S0065-2156(08)70121-2.

[78] V. Tvergaard and J. W. Hutchinson. The relation between crack growth resistance and fracture process parameters in elastic-plastic solids. *Journal of the Mechanics and Physics of Solids* **40** (1992), 1377–1397.
DOI: 10.1016/0022-5096(92)90020-3.

[79] G. Beltz and J. Rice. Dislocation nucleation at metal-ceramic interfaces. *Acta Metallurgica et Materialia* **40** (1992), S321–S331.
DOI: 10.1016/0956-7151(92)90291-L.

[80] X.-P. Xu and A. Needleman. Void nucleation by inclusion debonding in a crystal matrix. *Modelling and Simulation in Materials Science and Engineering* **1** (1993), 111–132.
DOI: 10.1088/0965-0393/1/2/001.

[81] J. P. McGarry, É. Ó Máirtín, G. Parry, and G. E. Beltz. Potential-based and non-potential-based cohesive zone formulations under mixed-mode separation and over-closure. Part I: Theoretical analysis. *Journal of the Mechanics and Physics of Solids* **63** (2014), 336–362.
DOI: 10.1016/j.jmps.2013.08.020.

[82] D. V. Kubair, D. J. Cole, L. C. Ciacchi, and S. M. Spearing. Multiscale mechanics modeling of direct silicon wafer bonding. *Scripta Materialia* **60** (2009), 1125–1128.
DOI: 10.1016/j.scriptamat.2009.02.058.

[83] T. Belytschko and T. Black. Elastic crack growth in finite elements with minimal remeshing. *International Journal for Numerical Methods in Engineering* **45** (1999), 601–620.
DOI: 10.1002/(SICI)1097-0207(19990620)45:5<601::AID-NME598>3.0.CO;2-S.

[84] A. Abdul-Baqi and E. Van der Giessen. Delamination of a strong film from a ductile substrate during indentation unloading. *Journal of Materials Research* **16** (2001), 1396–1407.
DOI: 10.1557/JMR.2001.0195.

[85] N. K. Fukumasu and R. M. Souza. Numerical evaluation of cohesive and adhesive failure modes during the indentation of coated systems with compliant substrates. *Surface and Coatings Technology* **260** (2014), 266–271.
DOI: 10.1016/j.surfcoat.2014.07.093.

[86] J. Albrecht, J. Auersperg, G. M. Reuther, P. W. Kudella, J. Brueckner, S. Rzepka, and R. Pufall. Brittle fracture and damage in bond pad stacks — A study of parameter influences in coupled XFEM and delamination simulation of nanoindentation. *2016 IEEE 18th Electronics Packaging Technology Conference (EPTC)*. Singapore, Singapore: IEEE, 2016, 724–728.
DOI: 10.1109/EPTC.2016.7861577.

[87] F. Lofaj and D. Németh. Multiple cohesive cracking during nanoindentation in a hard W-C coating/steel substrate system by FEM. *Journal of the European Ceramic Society* **37** (2017), 4379–4388.
DOI: 10.1016/j.jeurceramsoc.2017.03.051.

[88] E. Ovalle, M. Torres, J. Alvarado Orozco, S. Jimenez, D. Espinosa-Arbelaez, J. González, J. Zárate-Medina, J. González-Hernández, and G. Rodríguez. Theoretical-Experimental failure analysis of the c-Al0.66Ti0.33N-M2 steel system using nanoindentation instrumented and finite element analysis (2018).

[89] Z. Wang, X. Zhong, L. Jiang, F. Qi, X. Ouyang, J. Wang, B. Liao, and J. Luo. Effect of interfacial delamination on coating crack in thick diamond-like carbon coatings under indentation. *Acta Mechanica Sinica* **36** (2020), 524–535.
DOI: 10.1007/s10409-020-00930-x.

[90] K. Shu, C. Zhang, D. Zheng, S. Cui, P. Hou, and L. Gu. Analysis on the cracking of thin hard films considering the effects of interfacial delamination. *Surface and Coatings Technology* **402** (2020), 126284.
DOI: 10.1016/j.surfcoat.2020.126284.

[91] H. Nili, G. Cheng, T. Venkatesh, S. Sriram, and M. Bhaskaran. Correlation between nanomechanical and piezoelectric properties of thin films: An experimental and finite element study. *Materials Letters* **90** (2013), 148–151.
DOI: 10.1016/j.matlet.2012.09.036.

[92] R. Rabe, J.-M. Breguet, P. Schwaller, S. Stauss, F.-J. Haug, J. Patscheider, and J. Michler. Observation of fracture and plastic deformation during indentation and scratching inside the scanning electron microscope. *Thin Solid Films* **469-470** (2004), 206–213.
DOI: 10.1016/j.tsf.2004.08.096.

[93] J. D. Nowak, K. A. Rzepiejewska-Malyska, R. C. Major, O. L. Warren, and J. Michler. In-situ nanoindentation in the SEM. *Materials Today* **12** (2010), 44–45.
DOI: 10.1016/S1369-7021(10)70144-9.

[94] M. A. Wall and U. Dahmen. An in situ nanoindentation specimen holder for a high voltage transmission electron microscope. *Microscopy Research and Technique* **42** (1998), 248–254.
DOI: 10.1002/(SICI)1097-0029(19980915)42:4<248::AID-JEMT3>3.0.CO;2-M.

[95] A. M. Minor, E. T. Lilleodden, E. A. Stach, and J. W. Morris. In-situ transmission electron microscopy study of the nanoindentation behavior of Al. *Journal of Electronic Materials* **31** (2002), 958–964.
DOI: 10.1007/s11664-002-0028-4.

[96] A. Nafari, J. Angenete, K. Svensson, A. Sanz-Velasco, and P. Enoksson. MEMS sensor for *in situ* TEM-nanoindentation with simultaneous force and current measurements. *Journal of Micromechanics and Microengineering* **20** (2010), 064017.
DOI: 10.1088/0960-1317/20/6/064017.

[97] C. A. Schuh, C. E. Packard, and A. C. Lund. Nanoindentation and contact-mode imaging at high temperatures. *Journal of Materials Research* **21** (2006), 725–736.
DOI: 10.1557/jmr.2006.0080.

[98] Z. C. Duan and A. M. Hodge. High-temperature nanoindentation: New developments and ongoing challenges. *JOM* **61** (2009), 32–36.
DOI: 10.1007/s11837-009-0177-5.

[99] M. Conte, G. Mohanty, J. J. Schwiedrzik, J. M. Wheeler, B. Bellaton, J. Michler, and N. X. Randall. Novel high temperature vacuum nanoindentation system with active surface referencing and non-contact heating for measurements up to 800 °C. *Review of Scientific Instruments* **90** (2019), 045105.
DOI: 10.1063/1.5029873.

[100] S. Comby-Dassonneville, G. Tiphéne, A. Borroto, G. Guillonneau, L. Roiban, G. Kermouche, J.-F. Pierson, J.-L. Loubet, and P. Steyer. Real-time high-temperature scanning indentation: Probing physical changes in thin-film metallic glasses. *Applied Materials Today* **24** (2021), 101126.
DOI: 10.1016/j.apmt.2021.101126.

[101] A. Barnoush and H. Vehoff. Electrochemical nanoindentation: A new approach to probe hydrogen/deformation interaction. *Scripta Materialia* **55** (2006), 195–198.
DOI: 10.1016/j.scriptamat.2006.03.041.

[102] H. Zhou, Y. Pei, H. Huang, H. Zhao, F. Li, and D. Fang. Multi-field nanoindentation apparatus for measuring local mechanical properties of materials in external magnetic and electric fields. *Review of Scientific Instruments* **84** (2013), 063906.
DOI: 10.1063/1.4811779.

[103] S. Ruffell, J. E. Bradby, N. Fujisawa, and J. S. Williams. Identification of nanoindentation-induced phase changes in silicon by *in situ* electrical characterization. *Journal of Applied Physics* **101** (2007), 083531.
DOI: 10.1063/1.2724803.

[104] D. Sprouster, S. Ruffell, J. Bradby, D. Stauffer, R. Major, O. Warren, and J. Williams. Quantitative electromechanical characterization of materials using conductive ceramic tips. *Acta Materialia* **71** (2014), 153–163.
DOI: 10.1016/j.actamat.2014.02.028.

[105] R. Holm. *Electric Contacts*. Berlin, Heidelberg: Springer Berlin Heidelberg, 1967.
DOI: 10.1007/978-3-662-06688-1.

[106] J. George, S. Mannepalli, and K. S. R. N. Mangalampalli. Understanding Nanoscale Plasticity by Quantitative In Situ Conductive Nanoindentation. *Advanced Engineering Materials* **23** (2021), 2001494.
DOI: 10.1002/adem.202001494.

[107] S. Ruffell, J. Bradby, J. Williams, and O. Warren. An in situ electrical measurement technique via a conducting diamond tip for nanoindentation in silicon. *Journal of Materials Research* **22** (2007), 578–586.
DOI: 10.1557/jmr.2007.0100.

[108] D. D. Stauffer, R. C. Major, D. Vodnick, J. H. Thomas, J. Parker, M. Manno, C. Leighton, and W. W. Gerberich. Plastic response of the native oxide on Cr and Al thin films from in situ conductive nanoindentation. *Journal of Materials Research* **27** (2012), 685–693.
DOI: 10.1557/jmr.2011.432.

[109] H. H. Nguyen, P. J. Wei, and J. F. Lin. Electric contact resistance for monitoring nanoindentation-induced delamination. *Advances in Natural Sciences: Nanoscience and Nanotechnology* **2** (2011), 015007.
DOI: 10.1088/2043-6262/2/1/015007.

[110] M. Bhaskaran, S. Sriram, S. Ruffell, and A. Mitchell. Nanoscale Characterization of Energy Generation from Piezoelectric Thin Films. *Advanced Functional Materials* **21** (2011), 2251–2257.
DOI: 10.1002/adfm.201002663.

[111] E. Broitman, M. Y. Soomro, J. Lu, M. Willander, and L. Hultman. Nanoscale piezoelectric response of ZnO nanowires measured using a nanoindentation technique. *Physical Chemistry Chemical Physics* **15** (2013), 11113.
DOI: 10.1039/c3cp50915j.

[112] F. Volpi, C. Boujrouf, M. Rusinowicz, S. Comby-Dassonneville, F. Mercier, R. Boichot, M. Chubarov, R. C. Germanicus, F. Charlot, M. Braccini, G. Parry, D. Pellerin, and M. Verdier. Development of a multifunctional nanoindenter integrated in-situ Scanning Electron Microscope - application to the monitoring of piezoresponse and electro-mechanical failures. *Thin Solid Films* **735** (2021), 138891.
DOI: 10.1016/j.tsf.2021.138891.

[113] S. Comby-Dassonneville, F. Volpi, and M. Verdier. Electrically-functionalised nanoindenter dedicated to local capacitive measurements: Experimental set-up and data-processing procedure for quantitative analysis. *Sensors and Actuators A: Physical* **294** (2019), 185–193.
DOI: 10.1016/j.sna.2019.05.032.

[114] S. Comby-Dassonneville, F. Volpi, G. Parry, D. Pellerin, and M. Verdier. Resistive-nanoindentation: contact area monitoring by real-time electrical contact resistance measurement. *MRS Communications* **9** (2019), 1008–1014.
DOI: 10.1557/mrc.2019.74.

[115] F.-C. Chiu. A Review on Conduction Mechanisms in Dielectric Films. *Advances in Materials Science and Engineering* **2014** (2014), 1–18.
DOI: 10.1155/2014/578168.

[116] A. G. Aberle. Surface passivation of crystalline silicon solar cells: a review. *Progress in Photovoltaics: Research and Applications* **8** (2000), 473–487.
DOI: 10.1002/1099-159X(200009/10)8:5<473::AID-PIP337>3.0.CO;2-D.

[117] M.-B. Lin. *Introduction to VLSI systems: a logic, circuit, and system perspective*. Boca Raton, FL: CRC Press, 2012.
DOI: 10.1201/9781439897324.

[118] P. Morin, G. Raymond, D. Benoit, D. Guiheux, R. Pantel, F. Volpi, and M. Braccini. Study of stress in tensile nitrogen-plasma-treated multilayer silicon nitride films. *Journal of Vacuum Science & Technology A: Vacuum, Surfaces, and Films* **29** (2011), 041513.
DOI: 10.1116/1.3602082.

[119] A. E. Kaloyeros, F. A. Jové, J. Goff, and B. Arkles. Review - Silicon Nitride and Silicon Nitride-Rich Thin Film Technologies: Trends in Deposition Techniques and Related Applications. *ECS Journal of Solid State Science and Technology* **6** (2017), P691–P714.
DOI: 10.1149/2.0011710jss.

[120] C. Cazako, K. Inal, A. Burr, F. Georgi, and R. Cauro. Hypothetic impact of chemical bonding on the moisture resistance of amorphous SixNyHz by plasma-enhanced chemical vapor deposition. *Metallurgical Research & Technology* **115** (2018), 406.
DOI: 10.1051/metal/2018072.

[121] Z. Gan, C. Wang, and Z. Chen. Material Structure and Mechanical Properties of Silicon Nitride and Silicon Oxynitride Thin Films Deposited by Plasma Enhanced Chemical Vapor Deposition. *Surfaces* **1** (2018), 59–72.
DOI: 10.3390/surfaces1010006.

[122] D. Xiang, H. Xia, W. Yang, and P. Mou. Parametric study and residual gas analysis of large-area silicon-nitride thin-film deposition by plasma-enhanced chemical vapor deposition. *Vacuum* **165** (2019), 172–178.
DOI: 10.1016/j.vacuum.2019.04.017.

[123] J. Bustillo, R. Howe, and R. Muller. Surface micromachining for microelectromechanical systems. *Proceedings of the IEEE* **86** (1998), 1552–1574.
DOI: 10.1109/5.704260.

[124] T. Tekin. Review of Packaging of Optoelectronic, Photonic, and MEMS Components. *IEEE Journal of Selected Topics in Quantum Electronics* **17** (2011), 704–719.
DOI: 10.1109/JSTQE.2011.2113171.

[125] A. K. Sinha, H. J. Levinstein, and T. E. Smith. Thermal stresses and cracking resistance of dielectric films (SiN, Si3N4, and SiO2) on Si substrates. *Journal of Applied Physics* **49** (1978), 2423.
DOI: 10.1063/1.325084.

[126] J. Evans, J. Evans, P. Lall, and S. Cornford. Thermomechanical failures in microelectronic interconnects. *Microelectronics Reliability* **38** (1998), 523–529.
DOI: 10.1016/S0026-2714(97)00226-6.

[127] S. Raghavan, I. Schmadlak, G. Leal, and S. K. Sitaraman. Mixed-mode cohesive zone parameters for sub-micron scale stacked layers to predict microelectronic device reliability. *Engineering Fracture Mechanics* **153** (2016), 259–277.
DOI: 10.1016/j.engfracmech.2015.12.013.

[128] M. T. K. Soh, A. C. Fischer-Cripps, N. Savvides, C. A. Musca, and L. Faraone. Nanoindentation of plasma-deposited nitrogen-rich silicon nitride thin films. *Journal of Applied Physics* **100** (2006), 024310.
DOI: 10.1063/1.2217105.

[129] P. Scafidi and M. Ignat. Cracking and loss of adhesion of Si3N4 and SiO2:P films deposited on Al substrates. *Journal of Adhesion Science and Technology* **12** (1998), 1219–1242.
DOI: 10.1163/156856198X00407.

[130] Y. Lin, Y. Weng, D. Pen, and H. Li. Deformation model of brittle and ductile materials under nano-indentation. *Materials & Design* **30** (2009), 1643–1649.
DOI: 10.1016/j.matdes.2008.07.028.

[131] X. Li, B. Bhushan, K. Takashima, C.-W. Baek, and Y.-K. Kim. Mechanical characterization of micro/nanoscale structures for MEMS/NEMS applications using nanoindentation techniques. *Ultramicroscopy* **97** (2003), 481–494.
DOI: 10.1016/S0304-3991(03)00077-9.

[132] J.-n. Liu, B.-s. Xu, H.-d. Wang, X.-f. Cui, L.-n. Zhu, and G. Jin. Measurement for mechanical behavior and fatigue property of Cu films by nanoscale dynamic load method. *Materials & Design (1980-2015)* **65** (2015), 1136–1142.
DOI: 10.1016/j.matdes.2014.08.043.

[133] Q. Wang, F. Zhou, and J. Yan. Evaluating mechanical properties and crack resistance of CrN, CrTiN, CrAlN and CrTiAlN coatings by nanoindentation and scratch tests. *Surface and Coatings Technology* **285** (2016), 203–213.
DOI: 10.1016/j.surfcoat.2015.11.040.

[134] R. Saha and W. D. Nix. Effects of the substrate on the determination of thin film mechanical properties by nanoindentation. *Acta Materialia* **50** (2002), 23–38.
DOI: 10.1016/S1359-6454(01)00328-7.

[135] D. Beegan, S. Chowdhury, and M. Laugier. The nanoindentation behaviour of hard and soft films on silicon substrates. *Thin Solid Films* **466** (2004), 167–174.
DOI: 10.1016/j.tsf.2004.03.006.

[136] A. A. Pelegri and X. Huang. Nanoindentation on soft film/hard substrate and hard film/soft substrate material systems with finite element analysis. *Composites Science and Technology* **68** (2008), 147–155.
DOI: 10.1016/j.compscitech.2007.05.033.

[137] S. Zhang, D. Sun, Y. Fu, and H. Du. Toughness measurement of thin films: a critical review. *Surface and Coatings Technology* **198** (2005), 74–84.
DOI: 10.1016/j.surfcoat.2004.10.021.

[138] M. Kot, W. Rakowski, J. M. Lackner, and L. Major. Analysis of spherical indentations of coating-substrate systems: Experiments and finite element modeling. *Materials & Design* **43** (2013), 99–111.
DOI: 10.1016/j.matdes.2012.06.040.

[139] Y. Gaillard, C. Tromas, and J. Woirgard. Pop-in phenomenon in MgO and LiF: Observation of dislocation structures. *Philosophical Magazine Letters* **83** (2003), 553–561.
DOI: 10.1080/09500830310001594273.

[140] J. E. Bradby, J. S. Williams, J. Wong-Leung, M. V. Swain, and P. Munroe. Nanoindentation-induced deformation of Ge. *Applied Physics Letters* **80** (2002), 2651–2653.
DOI: 10.1063/1.1469660.

[141] S.-R. Jian, G.-J. Chen, and W.-M. Hsu. Mechanical Properties of Cu2O Thin Films by Nanoindentation. *Materials* **6** (2013), 4505–4513.
DOI: 10.3390/ma6104505.

[142] D. Mercier, V. Mandrillon, G. Parry, M. Verdier, R. Estevez, Y. Bréchet, and T. Maindron. Investigation of the fracture of very thin amorphous alumina film during spherical nanoindentation. *Thin Solid Films* **638** (2017), 34–47.
DOI: 10.1016/j.tsf.2017.07.040.

[143] K. Fu, Y. Yin, L. Chang, D. Shou, B. Zheng, and L. Ye. Analysis on multiple ring-like cracks in thin amorphous carbon film on soft substrate under nanoindentation. *Journal of Physics D: Applied Physics* **46** (2013), 505314.
DOI: 10.1088/0022-3727/46/50/505314.

[144] K. Fu, L. Chang, L. Ye, and Y. Yin. Indentation stress-based models to predict fracture properties of brittle thin film on a ductile substrate. *Surface and Coatings Technology* **296** (2016), 46–57.
DOI: 10.1016/j.surfcoat.2016.03.067.

[145] A. Needleman. A Continuum Model for Void Nucleation by Inclusion Debonding. *Journal of Applied Mechanics* **54** (1987), 525–531.
DOI: 10.1115/1.3173064.

[146] V. Yamakov, E. Saether, D. Phillips, and E. Glaessgen. Molecular-dynamics simulation-based cohesive zone representation of intergranular fracture processes in aluminum. *Journal of the Mechanics and Physics of Solids* **54** (2006), 1899–1928.
DOI: 10.1016/j.jmps.2006.03.004.

[147] Y. Leterrier, J. Andersons, Y. Pitton, and J.-A. E. Manson. Adhesion of silicon oxide layers on poly(ethylene terephthalate). II: Effect of coating thickness on adhesive and cohesive strengths. *Journal of Polymer Science Part B: Polymer Physics* **35** (1997), 1463–1472.
DOI: 10.1002/(SICI)1099-0488(19970715)35:9<1463::AID-POLB16>3.0.CO;2-4.

[148] F. Shieu and M. Shiao. Measurement of the interfacial mechanical properties of a thin ceramic coating on ductile substrates. *Thin Solid Films* **306** (1997), 124–129.
DOI: 10.1016/S0040-6090(97)00259-9.

[149] N. Nieva, C. Arreguez, R. Carrizo, C. S. Molé, and G. Lagarrigue. Bonding Strength Evaluation on Metal/Ceramic Interfaces in Dental Materials. *Procedia Materials Science* **1** (2012), 475–482.
DOI: 10.1016/j.mspro.2012.06.064.

[150] P. Alemany, R. S. Boorse, J. M. Burlitch, and R. Hoffmann. Metal-ceramic adhesion: quantum mechanical modeling of transition metal-alumina interfaces. *The Journal of Physical Chemistry* **97** (1993), 8464–8475.
DOI: 10.1021/j100134a016.

[151] Y. Jiang, Y. Wei, J. R. Smith, J. W. Hutchinson, and A. G. Evans. First principles based predictions of the toughness of a metal/oxide interface. *International Journal of Materials Research* **101** (2010), 8–15.
DOI: 10.3139/146.110254.

[152] A. D. Kiureghian and O. Ditlevsen. Aleatory or epistemic? Does it matter? *Structural Safety* **31** (2009), 105–112.
DOI: 10.1016/j.strusafe.2008.06.020.

[153] P. Castaldo, D. Gino, and G. Mancini. Safety formats for non-linear finite element analysis of reinforced concrete structures: discussion, comparison and proposals. *Engineering Structures* **193** (2019), 136–153.
DOI: 10.1016/j.engstruct.2019.05.029.

[154] D. C. Edelstein, G. A. Sai-Halasz, and Y. J. Mii. VLSI on-chip interconnection performance simulations and measurements. *IBM Journal of Research and Development* **39** (1995), 383–401.
DOI: 10.1147/rd.394.0383.

[155] M. Morgen, E. T. Ryan, J.-H. Zhao, C. Hu, T. Cho, and P. S. Ho. Low Dielectric Constant Materials for ULSI Interconnects. *Annual Review of Materials Science* **30** (2000), 645–680.
DOI: 10.1146/annurev.matsci.30.1.645.

[156] D. Shamiryan, T. Abell, F. Iacopi, and K. Maex. Low-k dielectric materials. *Materials Today* **7** (2004), 34–39.
DOI: https://doi.org/10.1016/S1369-7021(04)00053-7.

[157] A. Grill, S. M. Gates, T. E. Ryan, S. V. Nguyen, and D. Priyadarshini. Progress in the development and understanding of advanced low k and ultralow k dielectrics for very large-scale integrated interconnects - State of the art. *Applied Physics Reviews* **1** (2014), 011306.
DOI: 10.1063/1.4861876.

[158] A. Grill and D. A. Neumayer. Structure of low dielectric constant to extreme low dielectric constant SiCOH films: Fourier transform infrared spectroscopy characterization. *Journal of Applied Physics* **94** (2003), 6697–6707.
DOI: 10.1063/1.1618358.

[159] K. Maex, M. R. Baklanov, D. Shamiryan, F. lacopi, S. H. Brongersma, and Z. S. Yanovitskaya. Low dielectric constant materials for microelectronics. *Journal of Applied Physics* **93** (2003), 8793–8841.
DOI: 10.1063/1.1567460.

[160] A. Grill. Plasma enhanced chemical vapor deposited SiCOH dielectrics: from low-k to extreme low-k interconnect materials. *Journal of Applied Physics* **93** (2003), 1785–1790.
DOI: 10.1063/1.1534628.

[161] R. Hoofman, G. Verheijden, J. Michelon, F. Iacopi, Y. Travaly, M. Baklanov, Z. Tökei, and G. Beyer. Challenges in the implementation of low-k dielectrics in the back-end of line. *Microelectronic Engineering* **80** (2005), 337–344.
DOI: 10.1016/j.mee.2005.04.088.

[162] B. D. Hatton, K. Landskron, W. J. Hunks, M. R. Bennett, D. Shukaris, D. D. Perovic, and G. A. Ozin. Materials chemistry for low-k materials. *Materials Today* **9** (2006), 22–31.
DOI: 10.1016/S1369-7021(06)71387-6.

[163] X. Gu, H. Deng, Z. Tong, and X. Jing. Film deposition and UV curing process impact on ultralow-k dielectric for high performance Cu interconnects. *Japanese Journal of Applied Physics* **56** (2017), 07KF01.
DOI: 10.7567/JJAP.56.07KF01.

[164] C. A. Yuan, O. van der Sluis, G. Q. Zhang, L. J. Ernst, W. D. van Driel, A. E. Flower, and R. B. R. van Silfhout. Molecular simulation strategy for mechanical modeling of amorphous/porous low-dielectric constant materials. *Applied Physics Letters* **92** (2008), 061909.
DOI: 10.1063/1.2832639.

[165] M. R. Baklanov, E. A. Smirnov, and L. Zhao. Ultra Low Dielectric Constant Materials for 22 nm Technology Node and Beyond. *ECS Transactions* **35** (2011), 717–728.
DOI: 10.1149/1.3572315.

[166] V. Jousseaume, J. El Sabahy, C. Yeromonahos, G. Castellan, A. Bouamrani, and F. Ricoul. SiOCH thin films deposited by chemical vapor deposition: From low-$\varkappa$ to chemical and biochemical sensors. *Microelectronic Engineering* **167** (2017), 69–79.
DOI: 10.1016/j.mee.2016.10.003.

[167] J. B. Vella, A. A. Volinsky, I. S. Adhihetty, N. Edwards, and W. W. Gerberich. Nanoindentation of Silicate Low-K Dielectric Thin Films. *MRS Proceedings* **716** (2002), 1–6.
DOI: 10.1557/PROC-716-B12.13.

[168] A. A. Volinsky, J. B. Vella, and W. W. Gerberich. Fracture toughness, adhesion and mechanical properties of low-K dielectric thin films measured by nanoindentation. *Thin Solid Films* **429** (2003), 201–210.
DOI: 10.1016/S0040-6090(03)00406-1.

[169] R. Nay, O. Warren, D. Yang, and T. Wyrobek. Mechanical characterization of low-k dielectric materials using nanoindentation. *Microelectronic Engineering* **75** (2004), 103–110.
DOI: 10.1016/j.mee.2004.01.043.

[170] T. Wong, B. Liu, B. Narayanan, V. Ligatchev, and R. Kumar. Investigation of deposition temperature effect on properties of PECVD SiOCH low-k films. *Thin Solid Films* **462-463** (2004), 156–160.
DOI: 10.1016/j.tsf.2004.05.048.

[171] S. Takada, N. Hata, Y. Seino, N. Fujii, and T. Kikkawa. Dependences of Young's modulus of porous silica low dielectric constant films on skeletal structure and porosity. *Journal of Applied Physics* **100** (2006), 123512.
DOI: 10.1063/1.2401660.

[172] F. Ciaramella, V. Jousseaume, S. Maitrejean, M. Verdier, B. Remiat, A. Zenasni, and G. Passemard. Crosslinking impact of mesoporous MSQ films used in microelectronic interconnections on mechanical properties. *Thin Solid Films* **495** (2006), 124–129.
DOI: 10.1016/j.tsf.2005.08.291.

[173] M. Fujikane, S. Nagao, X. Liu, D. Chrobak, A. Lehto, S. Yamanaka, and R. Nowak. Evaluation of carbon-doped low-k multilayer structure by nanoindentation. *Journal of Alloys and Compounds* **448** (2008), 293–297.
DOI: 10.1016/j.jallcom.2006.10.089.

[174] V. Jousseaume, G. Rolland, D. Babonneau, and J. Simon. Influence of polymer porogens on the porosity and mechanical properties of spin coated Ultra Low k dielectrics. *Thin Solid Films* **517** (2009), 4413–4418.
DOI: 10.1016/j.tsf.2009.02.084.

[175] V. Gonda, J. Den Toonder, J. Beijer, G. Zhang, W. van Driel, R. Hoofman, and L. Ernst. Prediction of thermo-mechanical integrity of wafer backend processes. *Microelectronics Reliability* **44** (2004), 2011–2017.
DOI: 10.1016/j.microrel.2004.05.021.

[176] C. Hartfield, E. Ogawa, Y.-J. Park, T.-C. Chiu, and H. Guo. Interface Reliability Assessments for Copper/Low-k Products. *IEEE Transactions on Device and Materials Reliability* **4** (2004), 129–141.
DOI: 10.1109/TDMR.2004.831990.

[177] Y. Xiang, X. Chen, T. Tsui, J.-I. Jang, and J. Vlassak. Mechanical properties of porous and fully dense low-$\varkappa$ dielectric thin films measured by means of nanoindentation and the plane-strain bulge test technique. *Journal of Materials Research* **21** (2006), 386–395.
DOI: 10.1557/jmr.2006.0045.

[178] Y. Lin, Y. Xiang, T. Y. Tsui, and J. J. Vlassak. PECVD low-permittivity organosilicate glass coatings: Adhesion, fracture and mechanical properties. *Acta Materialia* **56** (2008), 4932–4943.
DOI: 10.1016/j.actamat.2008.06.007.

[179] W. Volksen, R. D. Miller, and G. Dubois. Low Dielectric Constant Materials. *Chemical Reviews* **110** (2010), 56–110.
DOI: 10.1021/cr9002819.

[180] T. K. Wong. Time Dependent Dielectric Breakdown in Copper Low-k Interconnects: Mechanisms and Reliability Models. *Materials* **5** (2012), 1602–1625.
DOI: 10.3390/ma5091602.

[181] J. Borja, J. L. Plawsky, T.-M. Lu, H. Bakhru, and W. N. Gill. Current leakage relaxation and charge trapping in ultra-porous low-k materials. *Journal of Applied Physics* **115** (2014), 084107.
DOI: 10.1063/1.4866692.

[182] J. R. Lloyd, E. Liniger, and T. M. Shaw. Simple model for time-dependent dielectric breakdown in inter- and intralevel low-k dielectrics. *Journal of Applied Physics* **98** (2005), 084109.
DOI: 10.1063/1.2112171.

[183] E. Van Besien, M. Pantouvaki, L. Zhao, D. De Roest, M. R. Baklanov, Z. Tőkei, and G. Beyer. Influence of porosity on electrical properties of low-k dielectrics. *Microelectronic Engineering* **92** (2012), 59–61.
DOI: 10.1016/j.mee.2011.04.015.

[184] E. Chery, X. Federspiel, D. Roy, F. Volpi, and J.-M. Chaix. Identification of the (sqrtE + 1/E)-dependence of porous low-k time dependent dielectric breakdown using over one year long package level tests. *Microelectronic Engineering* **109** (2013), 90–93.
DOI: 10.1016/j.mee.2013.03.085.

[185] Y.-L. Cheng, C.-Y. Lee, W.-J. Hung, G.-S. Chen, and J.-S. Fang. Electrical and reliability characteristics of dielectric stack with low dielectric constant SiCOH and capping SiCNH films. *Surface and Coatings Technology* **350** (2018), 57–63.
DOI: 10.1016/j.surfcoat.2018.06.071.

[186] S. Peng, H. Zhou, T. Kim, H.-B. Chen, and S. X.-D. Tan. Physics-Based Compact TDDB Models for Low-k BEOL Copper Interconnects With Time-Varying Voltage Stressing. *IEEE Transactions on Very Large Scale Integration (VLSI) Systems* **26** (2018), 239–248. DOI: 10.1109/TVLSI.2017.2764880.

[187] E. Y. Wu. Facts and Myths of Dielectric Breakdown Processes - Part I: Statistics, Experimental, and Physical Acceleration Models. *IEEE Transactions on Electron Devices* **66** (2019), 4523–4534. DOI: 10.1109/TED.2019.2933612.

[188] J. Palmer, G. W. Zhang, J. R. Weber, C.-Y. Lin, C. Perini, and R. Kasim. Intrinsic Reliability of BEOL interlayer dielectric. *2021 IEEE International Reliability Physics Symposium (IRPS)*. Monterey, CA, USA: IEEE, 2021, 1–2. DOI: 10.1109/IRPS46558.2021.9405089.

[189] K. Y. Yiang, W. J. Yoo, Q. Guo, and A. Krishnamoorthy. Investigation of electrical conduction in carbon-doped silicon oxide using a voltage ramp method. *Applied Physics Letters* **83** (2003), 524–526. DOI: 10.1063/1.1592618.

[190] H. Miyazaki, D. Kodama, and N. Suzumura. Phenomenological classification of stress-induced leakage current and time-dependent dielectric breakdown mechanism. *Journal of Applied Physics* **106** (2009), 104103. DOI: 10.1063/1.3259386.

[191] T. A. Pomorski, B. C. Bittel, P. M. Lenahan, E. Mays, C. Ege, J. Bielefeld, D. Michalak, and S. W. King. Defect structure and electronic properties of SiOC:H films used for back end of line dielectrics. *Journal of Applied Physics* **115** (2014), 234508. DOI: 10.1063/1.4882023.

[192] C. Wu, Y. Li, M. R. Baklanov, and K. Croes. Electrical Reliability Challenges of Advanced Low-k Dielectrics. *ECS Journal of Solid State Science and Technology* **4** (2015), N3065–N3070. DOI: 10.1149/2.0091501jss.

[193] Z.-J. Ding, Y.-P. Wang, W.-J. Liu, S.-J. Ding, M. R. Baklanov, and D. W. Zhang. Characterization of PECVD ultralow dielectric constant porous SiOCH films using triethoxymethylsilane precursor and cinene porogen. *Journal of Physics D: Applied Physics* **51** (2018), 115103. DOI: 10.1088/1361-6463/aaae79.

[194] J. Noguchi. Dominant Factors in TDDB Degradation of Cu Interconnects. *IEEE Transactions on Electron Devices* **52** (2005), 1743–1750. DOI: 10.1109/TED.2005.851849.

[195] F. Chen, O. Bravo, K. Chanda, P. McLaughlin, T. Sullivan, J. Gill, J. Lloyd, R. Kontra, and J. Aitken. A Comprehensive Study of Low-k SiCOH TDDB Phenomena and Its Reliability Lifetime Model Development. *2006 IEEE International Reliability Physics Symposium Proceedings*. San Jose, CA: IEEE, 2006, 46–53. DOI: 10.1109/RELPHY.2006.251190.

[196] S. Jeffery, C. J. Sofield, and J. B. Pethica. The influence of mechanical stress on the dielectric breakdown field strength of thin SiO2 films. *Applied Physics Letters* **73** (1998), 172–174. DOI: 10.1063/1.121745.

[197] T.-C. Yang and K. C. Saraswat. Effect of Physical Stress on the Degradation of Thin SiO2 Films Under Electrical Stress. *IEEE Transactions on Electron Devices* **47** (2000), 10.
DOI: 10.1109/16.830989.

[198] Y. S. Choi, H. Park, T. Nishida, and S. E. Thompson. Reliability of HfSiON gate dielectric silicon MOS devices under [110] mechanical stress: Time dependent dielectric breakdown. *Journal of Applied Physics* **105** (2009), 044503.
DOI: 10.1063/1.3074299.

[199] Y.-L. Wu, J.-J. Lin, B.-T. Chen, and C.-Y. Huang. Position-Dependent Nanoscale Breakdown Characteristics of Thin Silicon Dioxide Film Subjected to Mechanical Strain. *IEEE Transactions on Device and Materials Reliability* **12** (2012), 158–165.
DOI: 10.1109/TDMR.2011.2179804.

[200] T. Breuer, U. Kerst, C. Boit, E. Langer, and H. Ruelke. Ultra-Low-K dielectric degradation before breakdown. *2010 IEEE International Reliability Physics Symposium*. Garden Grove (Anaheim), CA, USA: IEEE, 2010, 890–894.
DOI: 10.1109/IRPS.2010.5488710.

[201] T. Tan, C. Gan, A. Du, Y. Tan, and C. Ng. Delamination-induced dielectric breakdown in Cu/low-k interconnects. *Journal of Materials Research* **23** (2008), 1802–1808.
DOI: 10.1557/JMR.2008.0222.

[202] Y.-L. Yang, T.-F. Young, T.-C. Chang, F.-Y. Shen, J.-H. Hsu, T.-M. Tsai, K.-C. Chang, and H.-L. Chen. Mechanical stress influence on electronic transport in low-k SiOC dielectric single damascene capacitor. *Applied Physics Letters* **102** (2013), 192912.
DOI: 10.1063/1.4807010.

[203] M. Alam, K. Maletto, J. Bielefeld, S. King, and M. Haque. Mechanical stress field assisted charge de-trapping in carbon doped oxides. *Microelectronics Reliability* **55** (2015), 846–851.
DOI: 10.1016/j.microrel.2015.02.017.

[204] S. Habermehl and R. T. Apodaca. Correlation of charge transport to intrinsic strain in silicon oxynitride and Si-rich silicon nitride thin films. *Applied Physics Letters* **84** (2004), 215–217.
DOI: 10.1063/1.1639132.

[205] N. Suzumura, S. Yamamoto, D. Kodama, H. Miyazaki, M. Ogasawara, J. Komori, and E. Murakami. Electric-field and temperature dependencies of TDDB degradation in Cu/Low-K damascene structures. *2008 IEEE International Reliability Physics Symposium*. Phoenix, AZ, USA: IEEE, 2008, 138–143.
DOI: 10.1109/RELPHY.2008.4558875.

[206] Shou-Chung Lee, A. S. Oates, and Kow-Ming Chang. Fundamental understanding of porous low-k dielectric breakdown. *2009 IEEE International Reliability Physics Symposium*. Montreal, QC, Canada: IEEE, 2009, 481–485.
DOI: 10.1109/IRPS.2009.5173300.

[207] K. Croes, C. J. Wilson, M. Lofrano, G. P. Beyer, and Z. Tőkei. Interconnect reliability – A study of the effect of dimensional and porosity scaling. *Microelectronic Engineering* **88** (2011), 614–619.
DOI: 10.1016/j.mee.2010.07.011.

[208] G. Abadias, E. Chason, J. Keckes, M. Sebastiani, G. B. Thompson, E. Barthel, G. L. Doll, C. E. Murray, C. H. Stoessel, and L. Martinu. Review Article: Stress in thin films and coatings: Current status, challenges, and prospects. *Journal of Vacuum Science & Technology A: Vacuum, Surfaces, and Films* **36** (2018), 020801.
DOI: 10.1116/1.5011790.

[209] V. Jousseaume, A. Zenasni, L. Favennec, G. Gerbaud, M. Bardet, J. P. Simon, and A. Humbert. Comparison Between E-beam and Ultraviolet Curing to Perform Porous a-SiOC:H. *Journal of The Electrochemical Society* **154** (2007), G103.
DOI: 10.1149/1.2667980.

[210] Y. Zheng, W. Zhu, T. F. Huang, S. Nemani, K. S. Yim, H. Amer, L. Q. Xia, and H. M'Saad. Proceedings of Advanced Metallization Conference 2003. *Advanced Metallization Conference 2003 (AMC 2003)*. Ed. by G. W. Ray, T. S. Smy, T. Ohta, and M. Tsujimura. **19**. Warrendale, Pa, 2004, 543–547.

[211] S. Jain, V. Zubkov, T. Nowak, A. Demos, and J. C. Rocha. Porous low-k dielectrics using ultraviolet curing. **48** (2005), 43–46.

[212] W. C. Oliver and G. M. Pharr. Measurement of hardness and elastic modulus by instrumented indentation: Advances in understanding and refinements to methodology. *J. Mater. Res.* **19** (2004), 19.
DOI: 10.1557/jmr.2004.19.1.3.

[213] W. Zhou, S. Bailey, R. Sooryakumar, S. King, G. Xu, E. Mays, C. Ege, and J. Bielefeld. Elastic properties of porous low-k dielectric nano-films. *Journal of Applied Physics* **110** (2011), 043520.
DOI: 10.1063/1.3624583.

[214] G. Kermouche, E. Barthel, D. Vandembroucq, and P. Dubujet. Mechanical modelling of indentation-induced densification in amorphous silica. *Acta Materialia* **56** (2008), 3222–3228.
DOI: 10.1016/j.actamat.2008.03.010.

[215] A. Perriot, D. Vandembroucq, E. Barthel, V. Martinez, L. Grosvalet, C. Martinet, and B. Champagnon. Raman Microspectroscopic Characterization of Amorphous Silica Plastic Behavior. *Journal of the American Ceramic Society* **89** (2006), 596–601.
DOI: 10.1111/j.1551-2916.2005.00747.x.

[216] K. Fu, Y. Tang, and L. Chang. Toughness Assessment and Fracture Mechanism of Brittle Thin Films Under Nano-Indentation. *Fracture Mechanics - Properties, Patterns and Behaviours*. Ed. by L. M. Alves. InTech, 2016.
DOI: 10.5772/64117.

[217] C. A. Schuh. Nanoindentation studies of materials. *Materials Today* **9** (2006), 32–40.
DOI: 10.1016/S1369-7021(06)71495-X.

[218] V. N. Sekhar, T. C. Chai, S. Balakumar, L. Shen, S. K. Sinha, A. A. O. Tay, and S. W. Yoon. Influence of thickness on nanomechanical behavior of Black Diamond™ low dielectric thin films for interconnect and packaging applications. *Journal of Materials Science: Materials in Electronics* **20** (2009), 74–86.
DOI: 10.1007/s10854-008-9610-8.

[219] S.-Y. Chang, H.-C. Tsai, J.-Y. Chang, S.-J. Lin, and Y.-S. Chang. Analyses of interface adhesion between porous SiOCH low-k film and SiCN layers by nanoindentation and nanoscratch tests. *Thin Solid Films* **516** (2008), 5334–5338.
DOI: 10.1016/j.tsf.2007.07.043.

[220] S. Sze and K. K. Ng. *Physics of Semiconductor Devices, 3rd Edition*. John Wiley & Sons, Ltd. 2006.
DOI: 10.1002/0470068329.

[221] K. A. Nasyrov and V. A. Gritsenko. Transport mechanisms of electrons and holes in dielectric films. *Uspekhi Fizicheskikh Nauk* **56** (2013), 999–1012.
DOI: 10.3367/UFNe.0183.201310h.1099.

[222] V. C. Ngwan, C. Zhu, and A. Krishnamoorthy. Dependence of leakage mechanisms on dielectric barrier in Cu–SiOC damascene interconnects. *Applied Physics Letters* **84** (2004), 2316–2318.
DOI: 10.1063/1.1688978.

[223] W. Vollmann. Poole-frenkel conduction in insulators of large impurity densities. *Physica Status Solidi (a)* **22** (1974), 195–203.
DOI: 10.1002/pssa.2210220122.

[224] D. Dergez, M. Schneider, A. Bittner, N. Pawlak, and U. Schmid. Mechanical and electrical properties of RF magnetron sputter deposited amorphous silicon-rich silicon nitride thin films. *Thin Solid Films* **606** (2016), 7–12.
DOI: 10.1016/j.tsf.2016.03.029.

[225] J. R. Yeargan and H. L. Taylor. The Poole-Frenkel Effect with Compensation Present. *Journal of Applied Physics* **39** (1968), 5600–5604.
DOI: 10.1063/1.1656022.

[226] R. Ongaro and A. Pillonnet. Generalized Poole Frenkel (PF) effect with donors distributed in energy. *Revue de Physique Appliquée* **24** (1989), 1097–1110.
DOI: 10.1051/rphysap:0198900240120109700.

[227] W. R. Harrell and J. Frey. Observation of Poole-Frenkel effect saturation in SiO2 and other insulating films. *Thin Solid Films* **352** (1999), 195–204.
DOI: 10.1016/S0040-6090(99)00344-2.

[228] B. Cheng, L. Xiong, Q. Cai, H. Shi, J. Zhao, X. Su, Y. Xiao, and S. Lei. Enhanced Giant Piezoresistance Performance of Sandwiched ZnS/Si/SiO2 Radial Heterostructure Nanotubes for Nonvolatile Stress Memory with Repeatable Writing and Erasing. *ACS Applied Materials & Interfaces* **8** (2016), 34648–34658.
DOI: 10.1021/acsami.6b10966.

[229] X. Guo, H. Zheng, S. W. King, V. V. Afanas'ev, M. R. Baklanov, J.-F. de Marneffe, Y. Nishi, and J. L. Shohet. Defect-induced bandgap narrowing in low-k dielectrics. *Applied Physics Letters* **107** (2015), 082903.
DOI: 10.1063/1.4929702.

[230] A. Kruv, B. Kaczer, A. Grill, M. Gonzalez, J. Franco, D. Linten, W. Goes, T. Grasser, and I. De Wolf. On the impact of mechanical stress on gate oxide trapping. *2020 IEEE International Reliability Physics Symposium (IRPS)*. Dallas, TX, USA: IEEE, 2020, 1–5.
DOI: 10.1109/IRPS45951.2020.9129541.

[231] P. V. Sushko, S. Mukhopadhyay, A. S. Mysovsky, V. B. Sulimov, A. Taga, and A. L. Shluger. Structure and properties of defects in amorphous silica: new insights from embedded cluster calculations. *Journal of Physics: Condensed Matter* **17** (2005), S2115–S2140.
DOI: 10.1088/0953-8984/17/21/007.

[232] S. Bonfanti, R. Guerra, C. Mondal, I. Procaccia, and S. Zapperi. Elementary plastic events in amorphous silica. *Physical Review E* **100** (2019), 060602.
DOI: 10.1103/PhysRevE.100.060602.

[233] F. Bamer, S. S. Alshabab, A. Paul, F. Ebrahem, B. Markert, and B. Stamm. Data-driven classification of elementary rearrangement events in silica glass. *Scripta Materialia* **205** (2021), 114179.
DOI: 10.1016/j.scriptamat.2021.114179.

[234] S. W. King, J. Brockman, M. French, M. Jaehnig, M. Kuhn, and B. French. Valence and conduction band offsets at low-k a-SiOxCy:H/a-SiCxNy:H interfaces. *Journal of Applied Physics* **116** (2014), 113703.
DOI: 10.1063/1.4895135.

[235] S. P. Ogden, Y. Xu, K. B. Yeap, T. Shen, T.-M. Lu, and J. L. Plawsky. Charge transport model to predict dielectric breakdown as a function of voltage, temperature, and thickness. *Microelectronics Reliability* **91** (2018), 232–242.
DOI: 10.1016/j.microrel.2018.10.005.

[236] S. King, B. French, and E. Mays. Detection of defect states in low-k dielectrics using reflection electron energy loss spectroscopy. *Journal of Applied Physics* **113** (2013), 044109.
DOI: 10.1063/1.4788980.

[237] M. A. Lampert. Volume-controlled current injection in insulators. *Reports on Progress in Physics* **27** (1964), 329–367.
DOI: 10.1088/0034-4885/27/1/307.

[238] J. Frenkel. On Pre-Breakdown Phenomena in Insulators and Electronic Semi-Conductors. *Physical Review* **54** (1938), 647–648.
DOI: 10.1103/PhysRev.54.647.

[239] D. J. DiMaria and J. H. Stathis. Ultimate limit for defect generation in ultra-thin silicon dioxide. *Applied Physics Letters* **71** (1997), 3230–3232.
DOI: 10.1063/1.120299.

[240] P. E. Nicollian. Insights on trap generation and breakdown in ultra thin SiO2 and SiON dielectrics from low voltage stress-induced leakage current measurements. *Microelectronics Reliability* **48** (2008), 1171–1177.
DOI: 10.1016/j.microrel.2008.07.011.

[241] J. U. Bhanu, G. R. Babu, and P. Thangadurai. Influence of Mg ion concentration in ZrO2 gate dielectric layered silicon based MOS capacitors for memory applications: Thorough understanding of conduction processes. *Materials Science in Semiconductor Processing* **89** (2019), 85–96.
DOI: 10.1016/j.mssp.2018.09.004.

[242] E. Fortunato, P. Barquinha, and R. Martins. Oxide Semiconductor Thin-Film Transistors: A Review of Recent Advances. *Advanced Materials* **24** (2012), 2945–2986.
DOI: 10.1002/adma.201103228.

[243] B. K. Meyer, A. Polity, D. Reppin, M. Becker, P. Hering, P. J. Klar, T. Sander, C. Reindl, J. Benz, M. Eickhoff, C. Heiliger, M. Heinemann, J. Bläsing, A. Krost, S. Shokovets, C. Müller, and C. Ronning. Binary copper oxide semiconductors: From materials towards devices. *physica status solidi (b)* **249** (2012), 1487–1509.
DOI: 10.1002/pssb.201248128.

[244] Y. Wang and J. F. Pierson. Binary copper oxides as photovoltaic absorbers: recent progress in materials and applications. *Journal of Physics D: Applied Physics* **54** (2021), 263002.
DOI: 10.1088/1361-6463/abf165.

[245] J. Zeng, M. Castellino, K. Bejtka, A. Sacco, G. Di Martino, M. A. Farkhondehfal, A. Chiodoni, S. Hernández, and C. F. Pirri. Facile synthesis of cubic cuprous oxide for electrochemical reduction of carbon dioxide. *Journal of Materials Science* **56** (2021), 1255–1271.
DOI: 10.1007/s10853-020-05278-y.

[246] G. Milano, S. Porro, I. Valov, and C. Ricciardi. Recent Developments and Perspectives for Memristive Devices Based on Metal Oxide Nanowires. *Advanced Electronic Materials* **5** (2019), 1800909.
DOI: 10.1002/aelm.201800909.

[247] C. Guillén and J. Herrero. Single-phase Cu2O and CuO thin films obtained by low-temperature oxidation processes. *Journal of Alloys and Compounds* **737** (2018), 718–724.
DOI: 10.1016/j.jallcom.2017.12.174.

[248] B. Maack and N. Nilius. Oxidation of polycrystalline copper films – Pressure and temperature dependence. *Thin Solid Films* **651** (2018), 24–30.
DOI: 10.1016/j.tsf.2018.02.007.

[249] S. Hussain, C. Cao, G. Nabi, W. S. Khan, M. Tahir, M. Tanveer, and I. Aslam. Optical and electrical characterization of ZnO/CuO heterojunction solar cells. *Optik* **130** (2017), 372–377.
DOI: 10.1016/j.ijleo.2016.10.099.

[250] V. Figueiredo, E. Elangovan, G. Gonçalves, P. Barquinha, L. Pereira, N. Franco, E. Alves, R. Martins, and E. Fortunato. Effect of post-annealing on the properties of copper oxide thin films obtained from the oxidation of evaporated metallic copper. *Applied Surface Science* **254** (2008), 3949–3954.
DOI: 10.1016/j.apsusc.2007.12.019.

[251] T. Wong, S. Zhuk, S. Masudy-Panah, and G. Dalapati. Current Status and Future Prospects of Copper Oxide Heterojunction Solar Cells. *Materials* **9** (2016), 271.
DOI: 10.3390/ma9040271.

[252] P. Sawicka-Chudy, M. Sibiński, E. Rybak-Wilusz, M. Cholewa, G. Wisz, and R. Yavorskyi. Review of the development of copper oxides with titanium dioxide thin-film solar cells. *AIP Advances* **10** (2020), 010701.
DOI: 10.1063/1.5125433.

[253] D. A. Fentahun, A. Tyagi, S. Singh, P. Sinha, A. Mishra, S. Danayak, R. Kumar, and K. K. Kar. Tunable optical and electrical properties of p-type Cu2O thin films. *Journal of Materials Science: Materials in Electronics* **32** (2021), 11158–11172.
DOI: 10.1007/s10854-021-05781-1.

[254] Z.-W. Shang, H.-H. Hsu, Z.-W. Zheng, and C.-H. Cheng. Progress and challenges in p-type oxide-based thin film transistors. *Nanotechnology Reviews* **8** (2019), 422–443.
DOI: 10.1515/ntrev-2019-0038.

[255] A. Rydosz. The Use of Copper Oxide Thin Films in Gas-Sensing Applications. *Coatings* **8** (2018), 425.
DOI: 10.3390/coatings8120425.

[256] J. Wu, J. Meng, Z. Yang, H. Chen, Y. Rong, L. Deng, and Z. Fu. Energy storage mechanism and electrochemical performance of Cu2O/rGO as advanced cathode for aqueous zinc ion batteries. *Journal of Alloys and Compounds* **895** (2022), 162653.
DOI: 10.1016/j.jallcom.2021.162653.

[257] H. Zhu, Y. Li, and X. Jiang. Room-temperature synthesis of cuprous oxide and its heterogeneous nanostructures for photocatalytic applications. *Journal of Alloys and Compounds* **772** (2019), 447–459.
DOI: 10.1016/j.jallcom.2018.09.092.

[258] L. Ortega-Reyes and A. Ávila-García. Memristors based on thermal copper oxide. *Journal of Materials Science: Materials in Electronics* **31** (2020), 7445–7454.
DOI: 10.1007/s10854-020-02963-1.

[259] I. S. Brandt, M. A. Tumelero, S. Pelegrini, G. Zangari, and A. A. Pasa. Electrodeposition of Cu2O: growth, properties, and applications. *Journal of Solid State Electrochemistry* **21** (2017), 1999–2020.
DOI: 10.1007/s10008-017-3660-x.

[260] R. D. Prabu, S. Valanarasu, V. Ganesh, M. Shkir, S. AlFaify, A. Kathalingam, S. Srikumar, and R. Chandramohan. An effect of temperature on structural, optical, photoluminescence and electrical properties of copper oxide thin films deposited by nebulizer spray pyrolysis technique. *Materials Science in Semiconductor Processing* **74** (2018), 129–135.
DOI: 10.1016/j.mssp.2017.10.023.

[261] A. Karapetyan, A. Reymers, S. Giorgio, C. Fauquet, L. Sajti, S. Nitsche, M. Nersesyan, V. Gevorgyan, and W. Marine. Cuprous oxide thin films prepared by thermal oxidation of copper layer. Morphological and optical properties. *Journal of Luminescence* **159** (2015), 325–332.
DOI: 10.1016/j.jlumin.2014.10.058.

[262] E. Alkoy and P. Kelly. The structure and properties of copper oxide and copper aluminium oxide coatings prepared by pulsed magnetron sputtering of powder targets. *Vacuum* **79** (2005), 221–230.
DOI: 10.1016/j.vacuum.2005.03.011.

[263] Y. Nishi, T. Miyata, and T. Minami. Electrochemically deposited Cu2O thin films on thermally oxidized Cu2O sheets for solar cell applications. *Solar Energy Materials and Solar Cells* **155** (2016), 405–410.
DOI: 10.1016/j.solmat.2016.06.013.

[264] A. O. Musa, T. Akomolafe, and M. J. Carter. Production of cuprous oxide, a solar cell material, by thermal oxidation and a study of its physical and electrical properties. *Solar Energy Materials and Solar Cells* **51** (1998), 305–316.
DOI: 10.1016/S0927-0248(97)00233-X.

[265] S. H. Wee, P.-S. Huang, J.-K. Lee, and A. Goyal. Heteroepitaxial Cu2O thin film solar cell on metallic substrates. *Scientific Reports* **5** (2015), 16272.
DOI: 10.1038/srep16272.

[266] M. Abdelfatah, J. Ledig, A. El-Shaer, A. Wagner, A. Sharafeev, P. Lemmens, M. M. Mosaad, A. Waag, and A. Bakin. Fabrication and characterization of flexible solar cell from electrodeposited Cu2O thin film on plastic substrate. *Solar Energy* **122** (2015), 1193–1198.
DOI: 10.1016/j.solener.2015.11.002.

[267] R. Jayakrishnan. Photovoltaic response of Cu2O/In2S3 hetero-structure grown on Cu substrate. *Materials Science in Semiconductor Processing* **16** (2013), 1608–1612.
DOI: 10.1016/j.mssp.2013.04.018.

[268] M. Rusinowicz, F. Volpi, G. Parry, M. Braccini, C. Boujrouf, and M. Verdier. Evidence of Plasticity-Driven Conductivity Drop in an Ultra-Low-k Dielectric Organosilicate Glass. *Advanced Functional Materials* **32** (2022), 2207354.
DOI: 10.1002/adfm.202207354.

[269] S.-M. Yi, I.-S. Choi, B.-J. Kim, and Y.-C. Joo. Reliability Issues and Solutions in Flexible Electronics Under Mechanical Fatigue. *Electronic Materials Letters* **14** (2018), 387–404.
DOI: 10.1007/s13391-018-0043-0.

[270] L. Yuan, X. Chen, S. Maganty, J. Cho, C. Ke, and G. Zhou. Enhancing the oxidation resistance of copper by using sandblasted copper surfaces. *Applied Surface Science* **357** (2015), 2160–2168.
DOI: 10.1016/j.apsusc.2015.09.203.

[271] J. S. Lehmann, R. Schwaiger, M. Rinke, and C. Greiner. How Tribo-Oxidation Alters the Tribological Properties of Copper and Its Oxides. *Advanced Materials Interfaces* **8** (2021), 2001673.
DOI: 10.1002/admi.202001673.

[272] G. Deng, A. Tieu, L. Su, H. Zhu, Q. Zhu, W. Zamri, and C. Kong. Characterizing deformation behaviour of an oxidized high speed steel: Effects of nanoindentation depth, friction and oxide scale porosity. *International Journal of Mechanical Sciences* **155** (2019), 267–285.
DOI: 10.1016/j.ijmecsci.2019.02.043.

[273] S. K. Venkataraman, D. L. Kohlstedt, and W. W. Gerberich. Continuous microindentation of passivating surfaces. *Journal of Materials Research* **8** (1993), 685–688.
DOI: 10.1557/JMR.1993.0685.

[274] N. G. Chechenin, J. Berttiger, and J. P. Krog. Nanoindentation of amorphous aluminum oxide films II. Critical parameters for the breakthrough and a membrane effect in thin hard films on soft substrates. *Thin Solid Films* **261** (1995), 228–235.
DOI: 10.1016/S0040-6090(94)06494-6.

[275] D. E. Kramer, K. B. Yoder, and W. W. Gerberich. Surface constrained plasticity: Oxide rupture and the yield point process. *Philosophical Magazine A* **81** (2001), 2033–2058.
DOI: 10.1080/01418610108216651.

[276] F. Bahrami, M. Hammad, M. Fivel, B. Huet, C. D'Haese, L. Ding, B. Nysten, H. Idrissi, J. Raskin, and T. Pardoen. Single layer graphene controlled surface and bulk indentation plasticity in copper. *International Journal of Plasticity* **138** (2021), 102936.
DOI: 10.1016/j.ijplas.2021.102936.

[277] C.-C. Hsu, C.-H. Wu, and S.-Y. Wang. Low power deposition of the polycrystalline CuxO film with a high mobility and a low hole concentration by radio-frequency magnetron sputtering of a Cu2O target. *Journal of Alloys and Compounds* **663** (2016), 262–269.
DOI: 10.1016/j.jallcom.2015.12.112.

[278] Y. I. Golovin. Nanoindentation and mechanical properties of solids in submicrovolumes, thin near-surface layers, and films: A Review. *Physics of the Solid State* **50** (2008), 2205–2236.
DOI: 10.1134/S1063783408120019.

[279] S. Sridhar, A. E. Giannakopoulos, S. Suresh, and U. Ramamurty. Electrical response during indentation of piezoelectric materials: A new method for material characterization. *Journal of Applied Physics* **85** (1999), 380–387.
DOI: 10.1063/1.369459.

[280] V. Shastry and U. Ramamurty. Simultaneous measurement of mechanical and electrical contact resistances during nanoindentation of NiTi shape memory alloys. *Acta Materialia* **61** (2013), 5119–5129.
DOI: 10.1016/j.actamat.2013.04.049.

[281] G. Singh, R. L. Narayan, A. M. Asiri, and U. Ramamurty. Discrete drops in the electrical contact resistance during nanoindentation of a bulk metallic glass. *Applied Physics Letters* **108** (2016), 181903.
DOI: 10.1063/1.4948540.

[282] E. Rauch and M. Véron. Automated crystal orientation and phase mapping in TEM. *Materials Characterization* **98** (2014), 1–9.
DOI: 10.1016/j.matchar.2014.08.010.

[283] C. Gattinoni and A. Michaelides. Atomistic details of oxide surfaces and surface oxidation: the example of copper and its oxides. *Surface Science Reports* **70** (2015), 424–447.
DOI: 10.1016/j.surfrep.2015.07.001.

[284] G. Zhou and J. C. Yang. Initial Oxidation Kinetics of Cu(100), (110), and (111) Thin Films Investigated by in Situ Ultra-high-vacuum Transmission Electron Microscopy. *Journal of Materials Research* **20** (2005), 1684–1694.
DOI: 10.1557/JMR.2005.0239.

[285] S.-K. Lee, H.-C. Hsu, and W.-H. Tuan. Oxidation Behavior of Copper at a Temperature below 300 °C and the Methodology for Passivation. *Materials Research* **19** (2016), 51–56.
DOI: 10.1590/1980-5373-MR-2015-0139.

[286] H. J. Fan, U. Gösele, and M. Zacharias. Formation of Nanotubes and Hollow Nanoparticles Based on Kirkendall and Diffusion Processes: A Review. *Small* **3** (2007), 1660–1671.
DOI: 10.1002/smll.200700382.

[287] Y. Unutulmazsoy, C. Cancellieri, L. Lin, and L. P. Jeurgens. Reduction of thermally grown single-phase CuO and Cu2O thin films by in-situ time-resolved XRD. *Applied Surface Science* **588** (2022), 152896.
DOI: 10.1016/j.apsusc.2022.152896.

[288] W. Gerberich, J. Nelson, E. Lilleodden, P. Anderson, and J. Wyrobek. Indentation induced dislocation nucleation: The initial yield point. *Acta Materialia* **44** (1996), 3585–3598.
DOI: 10.1016/1359-6454(96)00010-9.

[289] S. Suresh, T.-G. Nieh, and B. Choi. Nano-indentation of copper thin films on silicon substrates. *Scripta Materialia* **41** (1999), 951–957.
DOI: 10.1016/S1359-6462(99)00245-6.

[290] Y. Shibutani, T. Tsuru, and A. Koyama. Nanoplastic deformation of nanoindentation: Crystallographic dependence of displacement bursts. *Acta Materialia* **55** (2007), 1813–1822.
DOI: 10.1016/j.actamat.2006.10.055.

[291] Y. Sato, S. Shinzato, T. Ohmura, T. Hatano, and S. Ogata. Unique universal scaling in nanoindentation pop-ins. *Nature Communications* **11** (2020), 4177.
DOI: 10.1038/s41467-020-17918-7.

[292] T. Zhu. Predictive modeling of nanoindentation-induced homogeneous dislocation nucleation in copper. *Journal of the Mechanics and Physics of Solids* **52** (2004), 691–724. DOI: 10.1016/j.jmps.2003.07.006.

[293] A. Barnoush. Correlation between dislocation density and nanomechanical response during nanoindentation. *Acta Materialia* **60** (2012), 1268–1277. DOI: 10.1016/j.actamat.2011.11.034.

[294] P. Filippov and U. Koch. Nanoindentation of Aluminum Single Crystals: Experimental Study on Influencing Factors. *Materials* **12** (2019), 3688. DOI: 10.3390/ma12223688.

[295] H. Bei, Y. F. Gao, S. Shim, E. P. George, and G. M. Pharr. Strength differences arising from homogeneous versus heterogeneous dislocation nucleation. *Physical Review B* **77** (2008), 060103. DOI: 10.1103/PhysRevB.77.060103.

[296] T. Ohmura, L. Zhang, K. Sekido, and K. Tsuzaki. Effects of lattice defects on indentation-induced plasticity initiation behavior in metals. *Journal of Materials Research* **27** (2012), 1742–1749. DOI: 10.1557/jmr.2012.161.

[297] F. Javaid, H. Pouriayevali, and K. Durst. Dislocation–grain boundary interactions: recent advances on the underlying mechanisms studied via nanoindentation testing. *Journal of Materials Research* **36** (2021), 2545–2557. DOI: 10.1557/s43578-020-00096-z.

[298] H. Somekawa and C. A. Schuh. Effect of solid solution elements on nanoindentation hardness, rate dependence, and incipient plasticity in fine grained magnesium alloys. *Acta Materialia* **59** (2011), 7554–7563. DOI: 10.1016/j.actamat.2011.08.047.

[299] A. Gouldstone, H.-J. Koh, K.-Y. Zeng, A. Giannakopoulos, and S. Suresh. Discrete and continuous deformation during nanoindentation of thin films. *Acta Materialia* **48** (2000), 2277–2295. DOI: 10.1016/S1359-6454(00)00009-4.

[300] D. Wu, J. Morris, and T. Nieh. Effect of tip radius on the incipient plasticity of chromium studied by nanoindentation. *Scripta Materialia* **94** (2015), 52–55. DOI: 10.1016/j.scriptamat.2014.09.017.

[301] I. Salehinia, S. Lawrence, and D. Bahr. The effect of crystal orientation on the stochastic behavior of dislocation nucleation and multiplication during nanoindentation. *Acta Materialia* **61** (2013), 1421–1431. DOI: 10.1016/j.actamat.2012.11.019.

[302] J. R. Morris, H. Bei, G. M. Pharr, and E. P. George. Size Effects and Stochastic Behavior of Nanoindentation Pop In. *Physical Review Letters* **106** (2011), 165502. DOI: 10.1103/PhysRevLett.106.165502.

[303] M. M. Biener, J. Biener, A. M. Hodge, and A. V. Hamza. Dislocation nucleation in bcc Ta single crystals studied by nanoindentation. *Physical Review B* **76** (2007), 165422. DOI: 10.1103/PhysRevB.76.165422.

[304] A. Zbib and D. Bahr. Dislocation Nucleation and Source Activation during Nanoindentation Yield Points. *Metallurgical and Materials Transactions A* **38** (2007), 2249–2255. DOI: 10.1007/s11661-007-9284-5.

[305] D. F. Bahr, D. E. Wilson, and D. A. Crowson. Energy considerations regarding yield points during indentation. *Journal of Materials Research* **14** (1999), 2269–2275.
DOI: 10.1557/JMR.1999.0303.

[306] W. W. Gerberich, W. M. Mook, M. D. Chambers, M. J. Cordill, C. R. Perrey, C. B. Carter, R. E. Miller, W. A. Curtin, R. Mukherjee, and S. L. Girshick. An Energy Balance Criterion for Nanoindentation-Induced Single and Multiple Dislocation Events. *Journal of Applied Mechanics* **73** (2006), 327–334.
DOI: 10.1115/1.2125988.

[307] S. Pathak, J. Michler, K. Wasmer, and S. R. Kalidindi. Studying grain boundary regions in polycrystalline materials using spherical nano-indentation and orientation imaging microscopy. *Journal of Materials Science* **47** (2012), 815–823.
DOI: 10.1007/s10853-011-5859-z.

[308] L. Zhang and T. Ohmura. Plasticity Initiation and Evolution during Nanoindentation of an Iron–3% Silicon Crystal. *Physical Review Letters* **112** (2014), 145504.
DOI: 10.1103/PhysRevLett.112.145504.

[309] F. Pöhl. Pop-in behavior and elastic-to-plastic transition of polycrystalline pure iron during sharp nanoindentation. *Scientific Reports* **9** (2019), 15350.
DOI: 10.1038/s41598-019-51644-5.

[310] Y. Zhao, J.-M. Park, J.-i. Jang, and U. Ramamurty. Bimodality of incipient plastic strength in face-centered cubic high-entropy alloys. *Acta Materialia* **202** (2021), 124–134.
DOI: 10.1016/j.actamat.2020.10.066.

[311] S. G. Corcoran, R. J. Colton, E. T. Lilleodden, and W. W. Gerberich. Anomalous plastic deformation at surfaces: Nanoindentation of gold single crystals. *Physical Review B* **55** (1997), R16057–R16060.
DOI: 10.1103/PhysRevB.55.R16057.

[312] J. K. Mason, A. C. Lund, and C. A. Schuh. Determining the activation energy and volume for the onset of plasticity during nanoindentation. *Physical Review B* **73** (2006), 054102.
DOI: 10.1103/PhysRevB.73.054102.

[313] C. A. Schuh, J. K. Mason, and A. C. Lund. Quantitative insight into dislocation nucleation from high-temperature nanoindentation experiments. *Nature Materials* **4** (2005), 617–621.
DOI: 10.1038/nmat1429.

[314] A. M. Minor, S. A. Syed Asif, Z. Shan, E. A. Stach, E. Cyrankowski, T. J. Wyrobek, and O. L. Warren. A new view of the onset of plasticity during the nanoindentation of aluminium. *Nature Materials* **5** (2006), 697–702.
DOI: 10.1038/nmat1714.

[315] O. L. Warren, S. A. Downs, and T. J. Wyrobek. Challenges and interesting observations associated with feedback-controlled nanoindentation. *International Journal of Materials Research* **95** (2004), 287–296.
DOI: 10.3139/ijmr-2004-0064.

[316] A. Basavalingappa, M. Y. Shen, and J. R. Lloyd. Modeling the copper microstructure and elastic anisotropy and studying its impact on reliability in nanoscale interconnects. *Mechanics of Advanced Materials and Modern Processes* **3** (2017), 6.
DOI: 10.1186/s40759-017-0021-5.

[317] N. Wieczorek, G. Laplanche, J.-K. Heyer, A. Parsa, J. Pfetzing-Micklich, and G. Eggeler. Assessment of strain hardening in copper single crystals using in situ SEM microshear experiments. *Acta Materialia* **113** (2016), 320–334.
DOI: 10.1016/j.actamat.2016.04.055.

[318] S. Vu Hoang. Simulations numériques et mesures expérimentales du comportement mécanique de films minces. *PhD thesis* (2013).

[319] A. Živković, A. Roldan, and N. H. de Leeuw. Density functional theory study explaining the underperformance of copper oxides as photovoltaic absorbers. *Physical Review B* **99** (2019), 035154.
DOI: 10.1103/PhysRevB.99.035154.

[320] E. P. S. Tan, Y. Zhu, T. Yu, L. Dai, C. H. Sow, V. B. C. Tan, and C. T. Lim. Crystallinity and surface effects on Young's modulus of CuO nanowires. *Applied Physics Letters* **90** (2007), 163112.
DOI: 10.1063/1.2723654.

[321] B. Yao, X. Zhou, M. Liu, J. Yu, J. Cao, and L. Wang. First-principles calculations on phase transformation and elastic properties of CuO under pressure. *Journal of Computational Electronics* **17** (2018), 1450–1456.
DOI: 10.1007/s10825-018-1244-3.

[322] R. Sondors, J. Kosmaca, G. Kunakova, L. Jasulaneca, M. M. Ramma, R. Meija, E. Kauranens, M. Antsov, and D. Erts. Size Distribution, Mechanical and Electrical Properties of CuO Nanowires Grown by Modified Thermal Oxidation Methods. *Nanomaterials* **10** (2020), 1051.
DOI: 10.3390/nano10061051.

[323] X. Fang, H. Bishara, K. Ding, H. Tsybenko, L. Porz, M. Höfling, E. Bruder, Y. Li, G. Dehm, and K. Durst. Nanoindentation pop-in in oxides at room temperature: Dislocation activation or crack formation? *Journal of the American Ceramic Society* **104** (2021), 4728–4741.
DOI: 10.1111/jace.17806.

[324] H.-W. Hsiao, S. Li, K. A. Dahmen, and J.-M. Zuo. Shear banding mechanism in compressed nanocrystalline ceramic nanopillars. *Physical Review Materials* **3** (2019), 083601.
DOI: 10.1103/PhysRevMaterials.3.083601.

[325] D. Guo, S. Song, R. Luo, W. A. Goddard, M. Chen, K. M. Reddy, and Q. An. Grain Boundary Sliding and Amorphization are Responsible for the Reverse Hall-Petch Relation in Superhard Nanocrystalline Boron Carbide. *Physical Review Letters* **121** (2018), 145504.
DOI: 10.1103/PhysRevLett.121.145504.

[326] H. Idrissi, P. Carrez, and P. Cordier. On amorphization as a deformation mechanism under high stresses. *Current Opinion in Solid State and Materials Science* **26** (2022), 100976.
DOI: 10.1016/j.cossms.2021.100976.

[327] W. D. Nix and H. Gao. Indentation size effects in crystalline materials : a law for strain gradient plasticity. *Journal of the Mechanics and Physics of Solids* **46** (1998), 411–425.
DOI: 10.1016/S0022-5096(97)00086-0.

[328] A. E. Rakhshani, Y. Makdisi, and X. Mathew. The Poole–Frenkel conduction mechanism in Mo–Cu2O–Au thin film structures. *Journal of Materials Science: Materials in Electronics* **8** (1997), 207–211.
DOI: 10.1023/A:1018506516020.

[329] L. Hang-Bing, Z. Peng, F. Xiu-Feng, Y. Ming, S. Ya-Li, T. Li, T. Ting-Ao, and L. Yin-Yin. Polarity-Free Resistive Switching Characteristics of Cu $_x$ O Films for Non-volatile Memory Applications. *Chinese Physics Letters* **25** (2008), 1087–1090.
DOI: 10.1088/0256-307X/25/3/076.

[330] P. Zhou, H. B. Lv, M. Yin, L. Tang, Y. L. Song, T. A. Tang, Y. Y. Lin, A. Wu, S. Cai, H. Wu, C. Liang, and M. H. Chi. Performance improvement of CuOx with gradual oxygen concentration for nonvolatile memory application. *Journal of Vacuum Science & Technology B: Microelectronics and Nanometer Structures Processing, Measurement, and Phenomena* **26** (2008), 1030–1032.
DOI: 10.1116/1.2927922.

[331] Q. Zhou, Q. Lu, X. Zhang, Y. Song, Y. Y. Lin, and X. Wu. A study of copper oxide based resistive switching memory by conductive atom force microscope. *Applied Surface Science* **271** (2013), 407–411.
DOI: 10.1016/j.apsusc.2013.01.217.

[332] S. Yazdanparast. Resistance switching of electrodeposited cuprous oxide. *PhD thesis* (2015).

[333] K. Park and J.-S. Lee. Flexible resistive switching memory with a Ni/CuO $_x$ /Ni structure using an electrochemical deposition process. *Nanotechnology* **27** (2016), 125203.
DOI: 10.1088/0957-4484/27/12/125203.

[334] L. D. V. Sangani, C. R. Kumar, and M. G. Krishna. Interfacial Electrode-Driven Enhancement of the Switching Parameters of a Copper Oxide-Based Resistive Random-Access Memory Device. *Journal of Electronic Materials* **45** (2016), 322–328.
DOI: 10.1007/s11664-015-4074-0.

[335] C. Noguet, C. Schwab, C. Sennett, M. Sieskind, and C. Viel. Contribution à l'étude de la constante diélectrique de la cuprite. I. Détermination de la constante diélectrique par des méthodes optiques. *Journal de Physique* **26** (1965), 317–320.
DOI: 10.1051/jphys:01965002606031700.

[336] R. Kužel and F. L. Weichman. Hole mobility in Cu $_2$ O.I. Scattering by lattice vibrations. *Canadian Journal of Physics* **48** (1970), 2643–2656.
DOI: 10.1139/p70-328.

[337] E. Chery. Fiabilité des diélectriques low-k SiOCH poreux dans les interconnexions CMOS avancées. *PhD thesis* (2014).

[338] H. Raebiger, S. Lany, and A. Zunger. Origins of the p -type nature and cation deficiency in Cu 2 O and related materials. *Physical Review B* **76** (2007), 045209.
DOI: 10.1103/PhysRevB.76.045209.

[339] G. K. Paul, Y. Nawa, H. Sato, T. Sakurai, and K. Akimoto. Defects in Cu2O studied by deep level transient spectroscopy. *Applied Physics Letters* **88** (2006), 141901.
DOI: 10.1063/1.2175492.

[340] B. Huang. Intrinsic deep hole trap levels in Cu2O with self-consistent repulsive Coulomb energy. *Solid State Communications* **230** (2016), 49–53.
DOI: 10.1016/j.ssc.2016.01.008.

[341] J. Cao, A. Rinaldi, M. Plodinec, X. Huang, E. Willinger, A. Hammud, S. Hieke, S. Beeg, L. Gregoratti, C. Colbea, R. Schlögl, M. Antonietti, M. Greiner, and M. Willinger. In situ observation of oscillatory redox dynamics of copper. *Nature Communications* **11** (2020), 3554.
DOI: 10.1038/s41467-020-17346-7.

Abstract

Advanced devices (microelectronic systems, sensors, power sourcing or storage, photovoltaic cells, etc.) are complex architectures at small scales that integrate ever more heterogeneous stacks of thin films combining metals, semiconductors and dielectrics. Each material has the role of ensuring one or more functions for several years (signal transmission, energy conversion, insulation, ...) of which the most common are based on electrical conduction and dielectric properties. However, the functional reliability of devices is largely driven by the mechanical strength of these materials to the harsh stresses occurring both in the fabrication process and during operation. Knowing the local mechanical and electrical properties of thin film materials, but also their potential interaction, is therefore a major challenge.
In this context, the present PhD thesis consists in identifying the mechanical and electrical behaviors of three functional systems composed of dielectric thin films on conductive substrates. The characterization of these systems was performed by electrical-nanoindentation tests, coupling fine electrical measurements to nanoindentation tests. The processing of the experiments, being neither straightforward nor trivial for a quantitative approach, has been carried out essentially by using numerical simulations with the finite element method to extract material properties.
The first system studied is a silicon nitride layer on an aluminum-based alloy (Si_3N_4/AlSiCu). Its indentation led to the cracking of Si_3N_4 and to instabilities on the mechanical curves. From these features, a methodology based on the energy dissipation caused by the fracture has been developed, giving both an identification procedure of the damage properties of the brittle layer and the whole cracking process (location of the cracks, their shape, their length, etc.).
The second system is a nanoporous organosilicate glass thin film on a silicon substrate (SiOCH/Si). Its electrical indentation resulted in plastic deformation of the film, its cracking and electrical leakage. The correlation between mechanical and electrical failures has been fully described according to several regimes, one of which proved particularly interesting for identifying a conduction law of the SiOCH film under stress. Indeed, a plasticity-driven conductivity drop in the dielectric material has been clearly evidenced. An extension of the Poole-Frenkel conduction model was then proposed to account for plastic strain, and was supported by a physical mechanism.
The third system is a copper oxide thin film obtained from the thermal oxidation of an annealed copper substrate (Cu_2O/Cu). The mechanical behavior of the oxide, but also that of the copper substrate, was first fully described. In particular, size effects already well known in crystalline metals (onset of plasticity, plasticity gradients) have been observed to be enhanced in copper by the growth of an oxide layer on its surface. The fine description of the system rheology made it possible in a second step to determine its electrical properties.
Finally, these results are of both academic and application interest. In addition to gaining a better understanding of the functional systems studied, which are at the heart of modern microelectronics, they are probably generic enough to be transposed to other similar systems.

Résumé

Les dispositifs avancés (systèmes microélectroniques, capteurs, générateurs ou accumulateurs d'énergie, cellules photovoltaïques, etc.) sont des architectures complexes aux petites échelles qui intègrent des empilements toujours plus hétérogènes de couches minces combinant des métaux, des semi-conducteurs et des diélectriques. Chaque matériau a pour rôle d'assurer une ou plusieurs fonctions pendant plusieurs années (transmission de signaux, conversion d'énergie, isolation, ...) dont les plus courantes sont basées sur la conduction électrique et les propriétés diélectriques. Cependant, la fiabilité fonctionnelle des dispositifs est largement contrôlée par la résistance mécanique de ces matériaux aux contraintes sévères survenant tant au cours du processus de fabrication que pendant le fonctionnement du produit. Connaître les propriétés mécaniques et électriques locales des matériaux en couches minces, mais également leur potentielle interaction, est donc un enjeu majeur.
Dans ce contexte, cette thèse consiste à identifier les comportements mécaniques et électriques de trois systèmes fonctionnels, tous composés de couches minces diélectriques sur des substrats conducteurs. La caractérisation de ces systèmes a été réalisée par des essais de nanoindentation-électrique, couplant des mesures électriques fines à des essais de nanoindentation. Le traitement des expériences, n'étant ni direct ni trivial pour une approche quantitative, a été mené en utilisant des simulations numériques par la méthode des éléments finis afin d'extraire les propriétés des matériaux.
Le premier système étudié est une couche de nitrure de silicium sur un alliage d'aluminium (Si_3N_4/AlSiCu). Son indentation a conduit à la fissuration de Si_3N_4 ainsi qu'à des instabilités sur les courbes mécaniques. A partir de ces caractéristiques, une méthodologie basée sur la dissipation d'énergie causée par la rupture a été développée, donnant à la fois une procédure d'identification des propriétés d'endommagement de la couche fragile et le scénario de fissuration complet (position des fissures, leur forme, leur longueur, etc.).
Le deuxième système est une couche mince de verre organosilicate nanoporeuse sur un substrat de silicium (SiOCH/Si). Son indentation électrique a mené à la déformation plastique de la couche, à sa fissuration et à des fuites électriques. La corrélation entre les défaillances mécaniques et électriques a entièrement été décrite en fonction de plusieurs régimes dont un s'est avéré particulièrement intéressant pour identifier une loi de conduction de la couche de SiOCH sous contrainte. En effet, une chute de conductivité due à la plasticité dans le matériau diélectrique a clairement été mise en évidence. Une extension du modèle de conduction de Poole-Frenkel a alors été proposée pour tenir compte de la déformation plastique, et a été justifiée par un mécanisme physique.
Le troisième système est une couche mince d'oxyde de cuivre obtenue à partir de l'oxydation thermique d'un substrat de cuivre recuit (Cu_2O/Cu). Le comportement mécanique de l'oxyde, mais également celui du substrat de cuivre, ont été dans un premier temps complètement décrits. En particulier, des effets de taille déjà bien connus dans les métaux cristallins (amorce de la plasticité, gradients de plasticité) ont été observés comme renforcés dans le cuivre par la croissance d'une couche d'oxyde à sa surface. La description fine de la rhéologie de ce système a permis dans un second temps de déterminer ses propriétés électriques.
Finalement, ces résultats sont à la fois d'intérêt académique et applicatif. En plus d'accéder à une meilleure compréhension des systèmes fonctionnels étudiés, qui sont au cœur de la microélectronique moderne, ils sont probablement assez génériques pour être transposés à d'autres systèmes similaires.